



Review

Frequency down-conversion of solid-state laser sources to the mid-infrared spectral range using non-oxide nonlinear crystals

Valentin Petrov

Max-Born-Institute for Nonlinear Optics and Ultrafast Spectroscopy, 2A Max-Born-Str., D-12489 Berlin, Germany

Available online 11 April 2015

Abstract

The development of parametric devices down-converting the laser frequency to the mid-infrared (3–30 μm) based on non-oxide nonlinear optical crystals is reviewed. Such devices, pumped by solid-state laser systems operating in the near-infrared, fill in this spectral gap where no such lasers exist, on practically all time scales, from continuous-wave to femtosecond regime. All important results obtained so far with difference-frequency generation, optical parametric oscillation, generation and amplification are presented in a comparative manner, illustrating examples of recent achievements are given in more detail, and some special issues such as continuum and frequency comb generation or pulse shaping are also discussed. The vital element in any frequency-conversion process is the nonlinear optical crystal and this represents one of the major limitations for achieving high energies and average powers in the mid-infrared although the broad spectral tunability seems not to be a problem. Hence, an overview of the available non-oxide nonlinear optical materials, emphasizing new developments such as wide band-gap, engineered (mixed), and quasi-phase-matched crystals, is also included.

© 2015 Elsevier Ltd. All rights reserved.

Keywords: Mid-infrared coherent sources; Frequency down-conversion; Non-oxide nonlinear crystals; Parametric nonlinear processes; Solid-state laser systems

Contents

1. Introduction. 2
2. Second-order nonlinear processes in noncentrosymmetric crystals. 3

E-mail address: petrov@mbi-berlin.de

3.	Difference-frequency generation vs. parametric amplification: gain and spectral bandwidths.	11
4.	Down-conversion of the laser frequency: systematics of processes and devices	17
5.	The mid-infrared spectral range: non-oxide nonlinear materials	25
6.	Down-conversion to the mid-IR using non-oxide nonlinear materials	34
6.1.	Down-conversion of cw radiation	36
6.1.1.	DFG of cw radiation	36
6.1.2.	OPOs in cw regime.	38
6.2.	Down-conversion of ns pulses	38
6.2.1.	DFG of ns pulses	38
6.2.2.	OPOs in ns regime	41
6.3.	Down-conversion of ultrashort pulses.	64
6.3.1.	DFG of ps and fs pulses	64
6.3.2.	SPOPOs	78
6.3.3.	OPGs	82
7.	Miscellaneous down-conversion using non-oxide nonlinear materials	90
	Acknowledgments	93
	References	94

1. Introduction

This work reviews the achievements in nonlinear optical frequency conversion of laser radiation to longer wavelengths in the last more than 40 years. The consideration is restricted to second-order nonlinear processes (three-wave interactions) in noncentrosymmetric non-oxide crystals. The definition of the mid-infrared (mid-IR) spectral range is to some extent arbitrary. The limits of 3–30 μm (100–10 THz) adopted here are most useful for the coverage of this review. They are often found in the literature and there are few arguments in support of their choice: (i) this is the spectral range defined by the upper limits of clear transmission of the more popular oxide type nonlinear materials and the non-oxide materials considered here, respectively, in both cases determined by the onset of (multi-)phonon absorption; (ii) both limits can be related to the availability of good or less good sensors (e.g. non-thermal detectors can be used up to $\sim 30 \mu\text{m}$); and (iii) mature solid-state laser (SSL) sources exist only up to $\sim 3 \mu\text{m}$ and the methods and devices discussed here aim to show how nonlinear optics can help to extend this limit to longer wavelengths. Generation of far-IR (or THz) radiation (30–3000 μm) at frequencies below the lowest phonon resonance is outside the scope of the present review, although in many cases similar laser sources, nonlinear materials, processes and methods can be employed.

The next two sections are devoted to fundamental theoretical backgrounds, conventions, notations, definitions and parameters used when describing down-conversion of the frequency (generation of longer wavelengths). Many of the references here have textbook or handbook character, or include essential theoretical or modeling results and predictions valid in any spectral region. The difference to up-conversion (generation of shorter wavelengths) which is outside the scope of this review is emphasized as well as the role of the temporal regime. A systematic classification of the corresponding methods and devices applicable on different time scales is given in [Section 4](#). Whenever possible a parallel is

drawn with laser processes and devices. Section 5 presents all relevant nonlinear materials in comparison emphasizing the essential advantages and limitations. The present review deals solely with inorganic non-oxide nonlinear crystals because they offer the extended clear transparency into the mid-IR essential for frequency down-conversion of existing high-power SSL sources.

Section 6 gives an overview of experimental results with such crystals in all types of parametric down-conversion devices and on all possible time scales. Sometimes wavelengths above 3 μm have been generated by down-conversion with the more widespread oxides but the spectral extension is limited and such results are outside the scope of the present review. The same holds for up-conversion processes in non-oxide noncentrosymmetric crystals: such have been studied to produce e.g. the harmonics of infrared gas lasers or to up-convert weak radiation to shorter wavelengths for better detection but these experiments are also left aside. Thus, while the consideration is not strictly confined to the defined wavelength limits, it covers *only* non-oxide inorganic materials and *only* phase-matched or quasi-phase-matched second-order frequency down-conversion nonlinear processes. Some special issues such as continuum and frequency comb generation or pulse shaping are discussed in the corresponding places. A concluding Section 7 summarizes related experiments and topics which do not fall into any of the adopted categories and explicitly explains which of them remained unconsidered and why.

The author has tried to present a complete picture of the past and ongoing research with all the important publications cited. A great deal of the results remained unfortunately unpublished in peer-reviewed journals. Many important contributions were presented at the OSA topical meetings Advanced Solid-State Lasers/Photonics (ASSL/ASSP); other results related primarily to defense applications appeared only in SPIE Proceedings of conferences. To limit the number of references strongly overlapping publications are suppressed and priority is given to journal publications, followed by Proc. SPIE, and finally ASSL/ASSP post-conference editions (OSA Proc. or TOPS) indicated by the pagination. Only in exceptional cases when such proceedings did not appear, the conference edition or other OSA conferences such as CLEO, QELS, AIOM, and NLO are cited (OSA Technical Digest, paper edition and/or CD) indicated by the paper code.

2. Second-order nonlinear processes in noncentrosymmetric crystals

At the relatively low light intensities that normally occur in nature, which are far weaker than the fields inside atoms and molecules, the optical properties of materials do not depend on the light intensity and co-propagating waves do not interact with each other. However, if the light intensity is sufficiently high, the optical properties begin to depend on it and light waves may interact with a transparent dielectric medium and with each other. The observation of such nonlinear effects with optical fields and their investigation became possible only after the invention of the laser. Nowadays, however, they are widely used in nonlinear-optical devices and techniques to convert the wavelength of existing lasers.

When an electric field \vec{E} is applied to a dielectric medium the separation of bound charges results in induced microscopic dipole moments. The electric polarization \vec{P} is defined as the net average dipole moment vector per unit volume. Microscopic polarizability may have different origin but only the so-called electronic polarizability, due to displacement of the electron cloud, is fast enough to follow fast oscillating optical fields. The most general constitutive relation

between the dielectric polarization and the electric field takes the form:

$$\begin{aligned}\vec{P}(t) &= \vec{P}_L(t) + \vec{P}_{NL}(t) \\ &= \varepsilon_0 \int_{-\infty}^t \chi^{(1)}(t; t_1) \vec{E}(t_1) dt_1 + \varepsilon_0 \int \int_{-\infty}^t \chi^{(2)}(t; t_1, t_2) \vec{E}(t_1) \vec{E}(t_2) dt_1 dt_2 \\ &\quad + \varepsilon_0 \int \int \int_{-\infty}^t \chi^{(3)}(t; t_1, t_2, t_3) \vec{E}(t_1) \vec{E}(t_2) \vec{E}(t_3) dt_1 dt_2 dt_3 \dots\end{aligned}\quad (1)$$

where ε_0 is the dielectric constant in vacuum, $\chi^{(1)}$ denotes the linear susceptibility, and $\chi^{(2)}$, $\chi^{(3)}$ etc. are the nonlinear susceptibilities of 2nd, 3rd and higher orders represented by tensors of 3rd, 4th, etc. rank. Assuming interaction far from resonances, no losses and no dispersion (instantaneous medium response), the above relation simplifies and the susceptibilities become time-independent constants:

$$\vec{P} = \vec{P}_L + \vec{P}_{NL} = \varepsilon_0(\chi^{(1)} \vec{E} + \chi^{(2)} \vec{E} \vec{E} + \chi^{(3)} \vec{E} \vec{E} \vec{E} + \dots)\quad (2)$$

In anisotropic materials Eqs. (1)–(2) take vector-tensor form. When dispersion cannot be ignored, a relation similar to Eq. (2) can be written in the frequency domain for the corresponding Fourier components. The Fourier transform of the fully time-dependent dielectric response is in general a complex function of frequency [1]. The linear polarization term $\vec{P} = \varepsilon_0 \chi^{(1)} \vec{E}$ describes the classical linear optical effects, the real part of $\chi^{(1)}$ being related to the linear refractive index $n = \sqrt{1 + \chi_r^{(1)}}$ and its imaginary part - to the linear absorption $\alpha = \omega \chi_i^{(1)} / nc$ (ω : frequency, c : speed of light). The lowest (second-) order nonlinear processes, the so-called three-wave interactions, are described by the real part of the second term $\chi^{(2)}$ in Eq. (2). It is obvious that in the presence of two waves with different carrier frequencies this term will cause the polarization to have terms oscillating at the sum- and difference-frequencies and, under certain conditions, light can be re-emitted at such frequencies. It can be shown that $\chi^{(2)}$ is non-zero only in media without an inversion center [1], acentric or noncentrosymmetric crystals.

Second-harmonic generation (SHG), also called frequency doubling, is the simplest second-order nonlinear optical process, in which photons interacting with a nonlinear material (noncentrosymmetric crystal) are effectively “combined” to form new photons with twice the energy, and therefore twice the frequency and half the wavelength of the initial photons. SHG was also the first nonlinear optical process demonstrated in 1961 by Franken et al. [2], just one year after the discovery of the ruby laser by Maiman. It was this SSL that was employed in the first SHG experiment with quartz as the nonlinear optical crystal. While 10^{-8} photon conversion efficiency was achieved at that time, at present the improvement using engineered nonlinear devices, in terms of % per W, is by more than 13 orders of magnitude.

Soon afterwards the general theory of optical parametric three-wave interactions was developed [3]. The generation of a photon at frequency ω_1 when photons at frequencies ω_3 and ω_2 are incident on a crystal with non-zero $\chi^{(2)}$, such that $\omega_1 = \omega_3 - \omega_2$ (assuming $\omega_3 > \omega_2$), is called Difference-Frequency Generation (DFG). In order for energy conservation to hold, this additionally implies that, for every photon generated at the difference frequency ω_1 , a photon at ω_2 must also be created, while a photon at the higher frequency ω_3 must be annihilated.

The wave equation, derived from Maxwell's equations considering electrically neutral and nonconducting medium and neglecting magnetic effects, contains the nonlinear polarization term as a perturbation. Thus, the optical waves are coupled through the nonlinear polarization, which acts as a source term in the wave equation for each monochromatic or quasi-monochromatic

wave. Because of the linearity of the wave equation, each frequency component of the field satisfies the wave equation independently, with the source term being the Fourier component of the nonlinear polarization corresponding to the frequency of that optical field.

Working with laser beams it can be assumed that waves are propagating primarily in the z -direction, representing them as $\vec{E}(\vec{r}, t) = \vec{e} \{A(\vec{r}, t)\exp(kz - \omega t) + c.c.\}$ so that the intensity is $I = 2\varepsilon_0 n c |A|^2$ in SI units, with a similar expression for the electric polarization. Here \vec{e} is the unit polarization vector, $k = k(\omega)$ is the wave vector (in this case number) of propagation depending on the circular frequency of the rapidly oscillating wave. The amplitude A is slowly varying in space and time compared to the exponential factor (i.e. it changes only slightly over a wavelength in space and a period in time). In general, A is complex to include the possibility of phase modulation. Very often, the waves can be assumed to be of infinite extent and constant in amplitude and phase in a plane transverse to the direction of propagation, i.e. they are plane waves with $A = A(z, t)$. For the majority of cases, the interacting waves are with linear and parallel or orthogonal to each other polarization vectors, i.e. only a single component of the vectors has to be considered in the laboratory frame. For simplicity, also the spatial effect of the birefringence (the walk-off angle between the wave and Poynting vectors) can be ignored although its incorporation is straightforward [3]. While propagation of ultrashort pulses has to be regarded as wave packages traveling with their group velocities, for pulses longer than ~ 100 ps it can be assumed that the temporal walk-off over the nonlinear crystal (NLC) length L is negligible (i.e., all three waves travel with the same group velocity) which is equivalent to consideration of monochromatic plane waves, i.e. $A = A(z)$, for which phase and group velocities coincide. Note that dispersive broadening of ultrashort pulses, relevant for durations below ~ 100 fs, is also neglected for the moment as an even higher order effect called group-velocity dispersion (GVD). Considering three waves and the corresponding polarizations, under the so-called slowly varying amplitude approximation, the truncated coupled amplitude steady-state equations for a lossless medium are obtained [1,3–6]:

$$\begin{aligned} \frac{dA_1(z)}{dz} &= i \frac{2\omega_1 d_{\text{eff}}}{n_1 c} A_3(z) A_2^*(z) e^{i\Delta k z} \\ \frac{dA_2(z)}{dz} &= i \frac{2\omega_2 d_{\text{eff}}}{n_2 c} A_3(z) A_1^*(z) e^{i\Delta k z} \\ \frac{dA_3(z)}{dz} &= i \frac{2\omega_3 d_{\text{eff}}}{n_3 c} A_1(z) A_2(z) e^{-i\Delta k z} \end{aligned} \quad (3)$$

where the subscripts refer to the three waves with the standard convention that $\omega_1 \leq \omega_2 < \omega_3$ ($\lambda_1 \geq \lambda_2 > \lambda_3$), and $\Delta k = k_3 - k_2 - k_1$ is the so-called wave-vector mismatch (in this case a scalar). For the nonlinear processes, to take place with an appreciable efficiency of frequency conversion, phase-matching (PM) must occur, i.e. $\Delta k = 0$. For the simple collinear (scalar) interaction considered, this equation is equivalent to $n_1 \omega_1 = n_3 \omega_3 - n_2 \omega_2$ in terms of DFG. In the more general case of noncollinear (vector) interaction the same condition can be written as $\vec{k}_1 = \vec{k}_3 - \vec{k}_2$, i.e. as conservation of photon momentum. The PM condition is impossible to satisfy in isotropic (cubic) materials but the dispersion can be balanced by birefringence in anisotropic crystals. This most common method to satisfy the above relation by using waves of different polarization is called birefringent or angle PM because the index of refraction of the extraordinary wave can be adjusted by the propagation direction defined in the dielectric frame [4–6].

As can be seen from Eq. (3) the conversion efficiency will be determined by the coupling constants which are proportional to the so-called effective nonlinearity d_{eff} . Whenever dispersion of the susceptibility tensor $\chi^{(2)}$ can be neglected (for field frequencies much lower than the

resonant frequencies of the material system when the medium is necessarily lossless) the frequency arguments can be suppressed, the system responds instantaneously and the consideration can be in the time domain. In these conditions the susceptibility tensor components obey full permutation symmetry, known as Kleinman symmetry condition [1,6], and the same d_{eff} enters all Eq. (3), which are not restricted to DFG but, depending on the initial conditions and the input waves, describe also the reverse process of Sum-Frequency Generation (SFG). Moreover, in this case it follows from Eq. (3) that $dI_1/dz + dI_3/dz + dI_2/dz = 0$ for the corresponding intensities (Manley–Rowe relation), i.e. the total intensity in a lossless medium is conserved [1,6].

The notation commonly used by experimentalists is the nonlinearity tensor $d_{ijk} = \chi_{ijk}^{(2)}/2$ which is related to the symmetry in the two last indices (intrinsic permutation symmetry) under more general assumptions [1,6]. Consequently, a contracted (3×6) matrix d_{il} is introduced which has 18 components. When the Kleinman condition is explicitly introduced, i.e. all three d_{ijk} indices can be freely permuted, the independent components of d_{il} remain only 10 [1,6]. This number is further reduced by the crystallographic symmetry (point group) of the nonlinear material, except for the triclinic noncentrosymmetric class 1. The effective nonlinearity d_{eff} is obtained by summation of relevant contributions [1,4–7], i.e., it is some linear combination of the non-zero components of the contracted nonlinearity tensor d_{il} determined by the propagation direction, which is derived from the PM condition, and the corresponding polarizations. This is so because d_{il} are not defined in the laboratory frame but in an orthogonal crystallo-physical frame, which is fixed to the crystallographic frame but differs from the orthogonal dielectric frame of the optical indicatrix (principal optical axes) in which the polar angle θ and azimuthal angle φ determine the propagation direction. In uniaxial crystals, PM direction depends only on the polar angle θ , in biaxial crystals – on both θ and φ . However, d_{eff} always depends on both angles. Explicit expressions in the general case (without Kleinman symmetry) for d_{eff} in the 13 uniaxial acentric classes were presented in [7]; when Kleinman symmetry is applied, for two of them $d_{\text{eff}} \equiv 0$. Correct expressions for biaxial crystals belonging to the orthorhombic $mm2$ class can be found in [5,8] for arbitrary propagation direction and without Kleinman symmetry. For the orthorhombic class 222, and the monoclinic m and 2 classes, such expressions were published in [9,10], respectively, only for the case of Kleinman symmetry. In general, the expressions for d_{eff} are greatly simplified in the principal planes of biaxial crystals where the latter behave like uniaxial. From the 21 noncentrosymmetric classes, the remaining 3 are isotropic, for one of them $d_{\text{eff}} \equiv 0$ while for the other two, the high symmetry reduces d_{il} to a single component d_{14} even without the Kleinman condition [1,4].

As already mentioned PM can be achieved in birefringent crystals for specific propagation direction, which can be calculated using exact or approximate analytic expressions and the Sellmeier equations for a given crystal [4,5,8]. However, some deviation of the critical angle (polar in uniaxial and polar and/or azimuthal in biaxial crystals), at the expense of decreased conversion efficiency, is tolerable. The value of Δk is a function of crystal temperature T , frequencies of the interacting waves ν , and deviation from the PM angle $\phi = \varphi$ or θ . In a first (linear) approximation, the dependence is determined by the first derivatives:

$$\Delta k(\phi, T, \nu) = \Delta k_0 + \frac{\partial(\Delta k)}{\partial \phi} d\phi + \frac{\partial(\Delta k)}{\partial T} dT + \frac{\partial(\Delta k)}{\partial \nu} d\nu \quad (4)$$

where PM means that $\Delta k_0 = 0$. Very often the so-called fixed-field approximation can be applied, according to which the input plane waves remain unchanged (in amplitude and phase) at the NLC exit while the generated wave amplitude is much smaller. In the case of DFG, neglecting

effects such as absorption, diffraction, anisotropy, group-velocity mismatch (GVM) and GVD, this approximation leads to the following expression for the generated wave intensity:

$$I_{1,2} = \frac{8\pi^2 d_{\text{eff}}^2 L^2 I_{2,1} I_3}{\epsilon_0 c n_1 n_2 n_3 \lambda_{1,2}^2} \text{sinc}^2\left(\frac{|\Delta k|L}{2}\right) \quad (5)$$

The $\text{sinc}^2(x) = \sin^2(x)/x^2$ dependence accounts for the unequal phase velocities of the interacting waves and the product $|\Delta k|L$ quantifies the difference in phase accumulated over a distance L which leads to a reduction in the conversion efficiency. The conversion efficiency can be defined from Eq. (5) with respect to either of the input waves intensity or their geometrical average but the $\text{sinc}^2(x)$ dependence always holds. The distance over which the desired frequency is still generated is defined as the coherence length, for collinear interaction $L_c = \pi/|\Delta k|$. In the absence of PM, energy flows back and forth with a period of $2L_c$ and not in the desired direction. The function $\text{sinc}^2(x)$ drops to 1/2 at $|\Delta k| = 0.886\pi/L$. From this relation and Eq. (4), one obtains, e.g. for the angle acceptance bandwidth:

$$\Delta\phi = 1.772 \frac{\pi}{L} \left[\frac{\partial(\Delta k)}{\partial\phi} \right]_{\phi = \phi_{\text{PM}}}^{-1} \quad (6)$$

The angle acceptance bandwidth is defined as FWHM of the dependence of the process efficiency on the critical (PM) angle. It can be shown that it is inversely proportional to the spatial walk-off angle due to birefringence. The angle acceptance bandwidth becomes extremely large in uniaxial crystals when PM can be achieved at 90° to the optical axis, or in biaxial crystals when this is possible along one of the three principal dielectric axes [4,5]. In this case the derivative in Eq. (6) vanishes and the next order (quadratic) term with respect to the critical angle has to be considered in Eq. (4) which leads to:

$$\Delta\phi_{\phi = 90^\circ} = 2 \left[1.772 \frac{\pi}{L} \left(\frac{\partial^2(\Delta k)}{\partial\phi^2} \right)^{-1} \right]^{1/2} \quad (7)$$

In this particular case, the dependence on L is weaker and there is no spatial walk-off of the interacting waves, hence, tight focusing can be utilized with long NLCs, essential for low power, e.g., continuous-wave (cw) operation. This is the so-called noncritical PM (NCPM) condition, which is often compatible with maximum d_{eff} . Expressions for calculating the critical and noncritical angle acceptance in terms of refractive indices are tabulated in the literature [4,5].

In a similar manner temperature and spectral acceptances can be defined and such expressions are tabulated in the literature, too [4,5,8]. Changing the temperature is often used to adjust the birefringence for a specific nonlinear process, however, it is most attractive for NCPM when the wavelengths are tuned. It should be outlined that wide angle acceptance facilitates tight focusing but restricts the practical tuning capability for a fixed NLC cut. Similarly, wide temperature acceptance is attractive for stable operation especially when some residual absorption loss is present but in the same time restricts the tuning capability by temperature (in practice this is typically possible from room temperature up to $\sim 200^\circ\text{C}$).

The calculation of the frequency conversion efficiency has been generalized in few cases: In the undepleted approximation, this includes linear absorption losses α_i at all three wavelengths, birefringence (spatial walk-off) and focusing (i.e. diffraction) [4,5,8]. The essential consequence in the last two cases when the plane wave approximation is not fulfilled is that the L^2 dependence in Eq. (5) for $\Delta k=0$, is substituted by a weaker factor when these effects start to play a role [11].

Keeping the infinite plane wave approximation, it is possible to derive analytic expressions for the conversion efficiency including depletion [3,4]. In the case of perfectly phase-matched DFG, it is given in terms of Jacobi elliptic sine function with imaginary argument and modulus. When the number of input photons at ω_2 is much less than at ω_3 , both ω_2 and ω_1 waves (recall that $\omega_1 \leq \omega_2 < \omega_3$) grow exponentially with the propagation distance. When these numbers are approximately equal, the two waves at ω_2 and ω_1 still grow, though not so fast, at the expense of the wave at ω_3 until it is depleted, a phase reversal takes place and energy flows back to it. Effects of phase-mismatch can be incorporated in the consideration of the depleted case, too [3,4]. The same holds for the linear losses provided they exhibit no dispersion ($\alpha_i = \alpha$) since transformation of variables/coordinates leaves the system of equations (Eq. (3)) unchanged [8].

With noncollinear (vector) PM it is possible to spatially decouple the beams in the remaining optical elements (though they remain overlapped in the NLC) which can be very useful in different parametric devices. More important, one can optimize some characteristics of the interaction, most notably the spectral acceptance in ultrashort pulse (or in general broadband radiation) down-conversion which means that the interaction length is increased, and/or the compensation of the spatial walk-off. Noncollinear vs. collinear type-I PM in an optically negative uniaxial crystal is illustrated in Fig. 1 by the k -vectors.

The critical PM angle $\theta_c = \theta_3$ between the propagation direction z and the optical axis Z in the collinear case is determined by the intersection of the circle with a radius corresponding to the sum of the wave numbers k_1 and k_2 with the ellipse corresponding to $k_3(\theta)$. The notation ooe for the polarizations (ordinary and extraordinary) follows the convention for the sequence $\omega_1\omega_2\omega_3$. In negative uniaxial crystals $n_o \geq n_e(\theta) \geq n_e$ where n_o and n_e are the principal values (light polarization perpendicular or parallel to the optical axis Z). Type-I according to the nomenclature

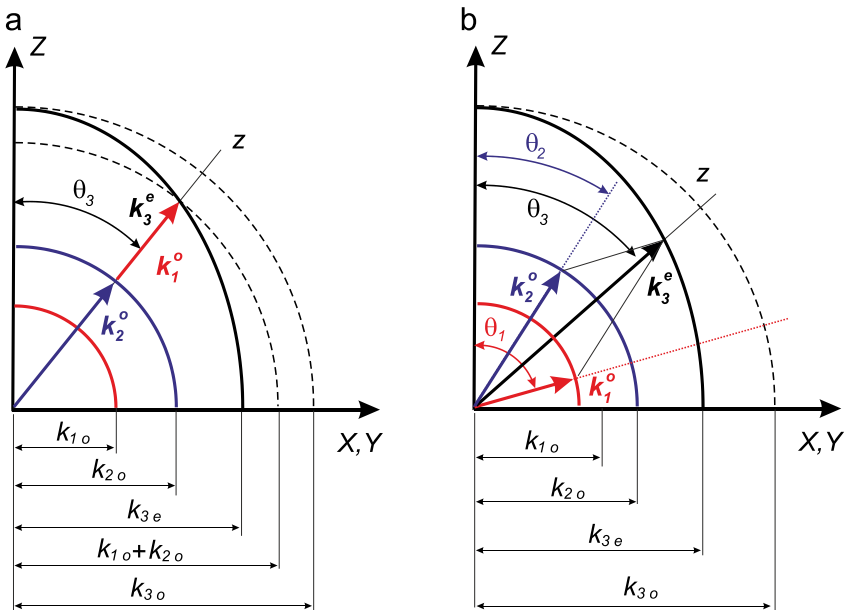


Fig. 1. Collinear (a) and noncollinear (b) type-I (ooe) PM for non-degenerate three-wave interaction. The subscripts o,e are related to principal values of the refractive indices whereas the superscripts o,e in the wave vectors are related to the angle dependent refractive indices, in this case $k_1^o(\theta) = k_{1o}$, $k_2^o(\theta) = k_{2o}$, and $k_3^e = k_{3e}^e$.

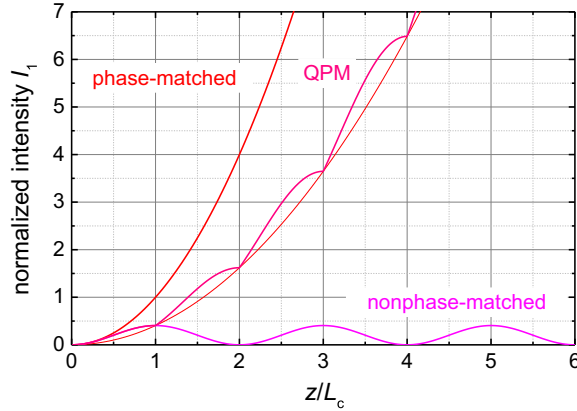


Fig. 2. Comparison of the DFG intensity I_1 calculated in the fixed-field plane-wave approximation for exact PM, 1st order QPM and in the absence of PM. The asymptotic QPM dependence is quadratic in z or L as Eq. (5) but the efficiency is $(2/\pi)^2$ times lower.

means that the polarization of the two lower frequency waves is the same (o in negative and e in positive uniaxial crystals). The value of the PM angle $\theta_c = \theta_3$ in the case of noncollinear PM is larger because the absolute value of the k_3 vector as a vector sum of k_1 and k_2 is smaller and this is achieved with smaller $n_e(\theta)$ value on the ellipse.

There is another possibility to keep the energy flow “almost” in the same direction, in fact suggested as a method earlier [3], by the so-called quasi-PM (QPM). If the NLC is divided into segments each a coherence length thick and then rotated relative to its neighbors by 180° about the axis of propagation, because of the lack of inversion symmetry, this has the effect of changing the sign of all components d_{il} and hence of d_{eff} . Bonding of such plates into a stack is obviously one possible realization of QPM but a more elegant way in the case of ferroelectric materials is electric field poling where the sign of the nonlinear coefficient in alternating domains is flipped simply switching the orientation of permanent dipoles in the material using a patterned electrode with the desired grating period $\Lambda = 2L_c$ [4,8,12]. Momentum is again conserved, however, with the help of an additional contribution from the wave vector of the periodic structure. Hence, in principle, any polarization configuration is possible and noncollinear interaction can be utilized as well, as long as the energy conservation condition is satisfied. This offers the possibility to optimize certain characteristics of the nonlinear process, e.g., to utilize diagonal elements of d_{il} which are in general larger. QPM not only enables the use of highly nonlinear isotropic (or in general weakly or too highly birefringent) NLCs, it is in principle NCPM. For short wavelengths, L_c could be very small and one can use odd multiple m of L_c for each slab, albeit at lower ($\sim m^{-2}$) efficiency. However, in the infrared this is not necessary and the nonlinearity of the process for the lowest (first) order grating is given simply by $(2/\pi)d_{\text{eff}}$ (see Fig. 2) while the wave-vector mismatch is $\Delta k = k_3 - k_2 - k_1 - 2\pi/\Lambda$ [4,8,12]. It should be noted here that lithographic methods offer great flexibility for the grating design, such as multi-grating, chirped, fan-out, etc.

This review deals only with down-conversion second-order nonlinear processes, i.e. such processes, which exhibit gain like DFG but not SFG. Nevertheless, an important limiting factor will be mentioned here, which has its origin in the imaginary part of the next, 3rd order nonlinear susceptibility. Two-photon absorption (TPA) involves a transition from the ground state of a system to a higher-lying state by the simultaneous absorption of two photons from an incident field or fields. The transition does not involve a real intermediate state. In the simplest case of

two equal photons, i.e. a single beam, the differential equation governing the optical loss reads:

$$\frac{dI}{dz} = -\alpha I - \beta I^2 - \sigma_c N_c(I)I \quad (8)$$

where α is the residual linear absorption coefficient and $\beta = (3\pi/\varepsilon_0 n^2 c \lambda) \text{Im}[\chi^{(3)}]$ is the TPA coefficient [4]. This detrimental loss mechanism is more important in the mid-IR because (i) non-oxide crystals are mostly semiconductors in which the magnitude of the TPA coefficient increases notably when the added energy of two photons approaches the band-gap, and (ii) in down-conversion nonlinear processes, the wave at ω_3 (with the highest photon energy) is normally also with the highest intensity, often much higher than the two other waves.

Once free carriers are generated by residual linear absorption in such semiconductors, they may experience also phonon-assisted absorption to higher-lying (lower-lying) states in the conduction (valence) band. This process is called free-carrier absorption. In the weak absorption regime, the attenuation may be described by the additional nonlinear term in Eq. (8) [4] where $N_c(I)$ is the intensity dependent carrier density, and σ_c is the free-carrier cross-section which has the $1/\omega^2$ dependence of a high-frequency conductivity (ω is the optical angular frequency) and thus is most important for infrared radiation in semiconductors. It is essential that nonlinear crystals do not exhibit free-carrier absorption.

Table 1

Systematics of $\chi^{(2)}$ - or three-photon-processes: lowest order nonlinear effects in noncentrosymmetric media. The convention $\omega_1 \leq \omega_2 < \omega_3$ ($\lambda_1 \geq \lambda_2 > \lambda_3$) is used. The third column summarizes the characteristics of up- and down-conversion parametric devices.

SFG (sum-frequency generation)	$\omega_3 = \omega_2 + \omega_1$ (energy conservation) $\hbar\omega_1, \hbar\omega_2$ annihilated, $\hbar\omega_3$ created	SFG (Mixing): feasible on all time scales (from cw to fs); requires two laser sources, synchronization, but there is no threshold. Particular case of SFG
SHG (second-harmonic generation)	$\omega_3 = 2\omega_1 \equiv \text{SFG } (\omega_1 = \omega_2)$	
DFG (difference-frequency generation)	$\omega_1 = \omega_3 - \omega_2$ (or $\omega_2 = \omega_3 - \omega_1$) $\hbar\omega_3$ annihilated, $\hbar\omega_2, \hbar\omega_1$ created, input wave at ω_2 (or ω_1) is amplified (parametric amplification)	DFG (Mixing): feasible on all time scales (from cw to fs); requires two laser sources, synchronization.
OPG (optical parametric generation)	Only pump wave at ω_3 present and two new waves at ω_1 and ω_2 (idler and signal) generated from parametric noise	OPG (Generator): no input signal; requires high intensity (ps or fs pulses) but has high gain and can tolerate certain losses (e.g., residual absorption, Fresnel reflections).
OPA (optical parametric amplification) \equiv DFG	\equiv OPG+(weak) seed at ω_2 or ω_1 . Gain (DFG) ~ 1 e.g. at ω_2 Gain (OPA) $\gg 1$ e.g. at ω_2	OPA (Amplifier): input seed reduces threshold and improves spectral, temporal and spatial properties; otherwise like OPG.
OPO (optical parametric oscillation)	\equiv (OPG or OPA)+resonator	OPO (Oscillator): SRO or DRO; pump: single pass, double pass, resonated, or intracavity pumped; from ns to cw (many round trips); seeding reduces threshold and improves spectral and spatial properties.
SPOPO (synchronously pumped OPO)	Requires cw or long (typically μs) train of ultrashort (ps or fs) pulses from a mode-locked laser oscillator in the steady-state or burst mode	SPOPO: low threshold average power; synchronized outputs at two wavelengths; high gain possible, can oscillate with high idler loss; cascaded SPOPOs practical.

3. Difference-frequency generation vs. parametric amplification: gain and spectral bandwidths

DFG is the fundamental nonlinear process for down-conversion, i.e. the transfer of power (energy) from a strong laser field at ω_3 to lower frequencies (longer wavelengths). The opposite process, SFG, see Table 1, is used for up-conversion and SHG is a particular case of SFG. Since the mid-IR spectral range can be accessed with SSL sources only starting from shorter wavelengths, this is achieved primarily by down-conversion. Note that down-conversion devices (see Table 1) are in principle more difficult to realize because there is a certain threshold for the field at ω_3 which is not the case for SFG, however, DFG offers in general also broader wavelength tunability of the resulting lower-frequency fields.

In many DFG experiments, the wave at ω_3 is an intense pump, while the wave at ω_2 (or ω_1) is a weak seed, commonly called signal. DFG yields amplification of the ω_2 (or ω_1) wave along with generation of another field at ω_1 (or ω_2), commonly called idler. Thus, this process/device is termed also optical parametric amplification/amplifier (OPA). In the notations adopted here, however, independent of which wavelength is available at the input of the NLC, signal will always be associated with the wave at ω_2 and idler with the wave at ω_1 , recalling that $\omega_2 \geq \omega_1$. To avoid confusion, the following examples will be for situations when the two conventions are univocal, i.e., the second wave at the input is at ω_2 and the wave generated in the process is at ω_1 .

The parametric gain depends on the NLC length L , d_{eff} and the pump intensity I_3 . The last factor is related to the temporal regime because average power of any SSL is limited by thermal or damage constraints and high intensities are only possible with pulsed sources. That is why it is important to explain here the terms spectral acceptance bandwidth, used in DFG, and parametric gain bandwidth, used in OPA, although these represent essentially the same nonlinear process (Table 1). This is in line with the growing number of frequency conversion experiments with ultrashort (ps and fs) pulses or broadband radiation, including continuum generation, also in the mid-IR spectral range.

OPA is normally considered for plane waves, assuming that the pump wave (at ω_3) remains undepleted, i.e. the intensities of signal (at ω_2) and idler (at ω_1) are much lower, and that there is only signal but no idler at the input ($z=0$). Under these simplifications, the Jacobi elliptic sine solution [3] of Eq. (3) is reduced to hyperbolic functions [13]:

$$I_2(L) = I_{20} \left[1 + \frac{\Gamma^2}{g^2} \sinh^2(gL) \right] = GI_{20} \quad (9a)$$

$$I_1(L) = I_{20} \frac{\omega_1}{\omega_2} \frac{\Gamma^2}{g^2} \sinh^2(gL) \quad (9b)$$

where G is the steady-state parametric gain for the signal (intensity), $g = \sqrt{\Gamma^2 - (\Delta k/2)^2}$, and the exponential gain coefficient Γ is defined by

$$\Gamma^2 = \frac{8\pi^2 d_{\text{eff}}^2 I_3}{\varepsilon_0 c n_1 n_2 n_3 \lambda_1 \lambda_2} \quad (10)$$

From Eq. (10) it can be seen that the parametric gain is maximum at degeneracy; as will be shown later this can be accompanied by extreme spectral bandwidths. In addition to Eq. (9), there is an equation governing the relative phase [3,13]. When only signal is applied as seed at the input, the parametric gain does not depend on the signal phase relative to the pump phase since the generated idler assumes a proper phase for maximum gain. However, if both waves ω_1 and

ω_2 are present at the input, simulations show that the gain depends on their phases relative to the pump and this situation is important in experiments [13].

When $\Gamma < \Delta k/2$, g is imaginary and the hyperbolic functions become trigonometric with oscillatory behavior. Then, at low gain, one obtains from Eq. (9b) the conversion efficiency $I_1(L)/I_{20}$ for DFG according to Eq. (5) with the $\text{sinc}^2(x)$ -dependence which tends to $\Gamma^2 L^2$ when $\Delta k \rightarrow 0$. When $\Gamma > \Delta k/2$, however, the equations support the exponential growth of both signal and idler with the effective gain coefficient g . In the limit of high gain ($gL \gg 1$) G is given by:

$$G \cong \frac{1}{4} \exp(2gL) \tag{11}$$

and this is the main difference between OPA and DFG. In order to obtain analytic expressions for the parametric gain bandwidth, the wave mismatch is expanded in series as a function of frequency, assuming in a first approximation that the pump is monochromatic,

$$\begin{aligned} \Delta k = \Delta k_0 + \left(\frac{\partial k_2}{\partial \omega_2} - \frac{\partial k_1}{\partial \omega_1} \right) \Delta \omega + \frac{1}{2!} \left(\frac{\partial^2 k_2}{\partial \omega_2^2} + \frac{\partial^2 k_1}{\partial \omega_1^2} \right) (\Delta \omega)^2 \\ + \frac{1}{3!} \left(\frac{\partial^3 k_2}{\partial \omega_2^3} - \frac{\partial^3 k_1}{\partial \omega_1^3} \right) (\Delta \omega)^3 + \frac{1}{4!} \left(\frac{\partial^4 k_2}{\partial \omega_2^4} + \frac{\partial^4 k_1}{\partial \omega_1^4} \right) (\Delta \omega)^4 \dots \end{aligned} \tag{12}$$

where $\Delta \omega = \Delta \omega_2$ denotes the frequency change of the signal wave and, by energy conservation, the idler frequency change will be $\Delta \omega_1 = -\Delta \omega$. Again, the PM condition means that $\Delta k_0 = 0$. The individual terms in Eq. (12) are used to evaluate the points, in terms of frequency, where the gain function G in Eq. (11) drops to 1/2 of its maximum value, which corresponds to the wave vector mismatch $\Delta k_{1/2} \approx \pm 2(\ln 2)^{1/2} (\Gamma/L)^{1/2}$. The results, when using the first derivative (GVM approximation), and the second derivative (GVD approximation), were derived in [14] and read, in terms of FWHM for $\Delta \nu = \Delta \omega/2\pi$:

$$\Delta \nu = \frac{2(\ln 2)^{1/2}}{\pi} \left(\frac{\Gamma}{L} \right)^{1/2} \left| \frac{\partial k_2}{\partial \omega_2} - \frac{\partial k_1}{\partial \omega_1} \right|^{-1} \tag{13a}$$

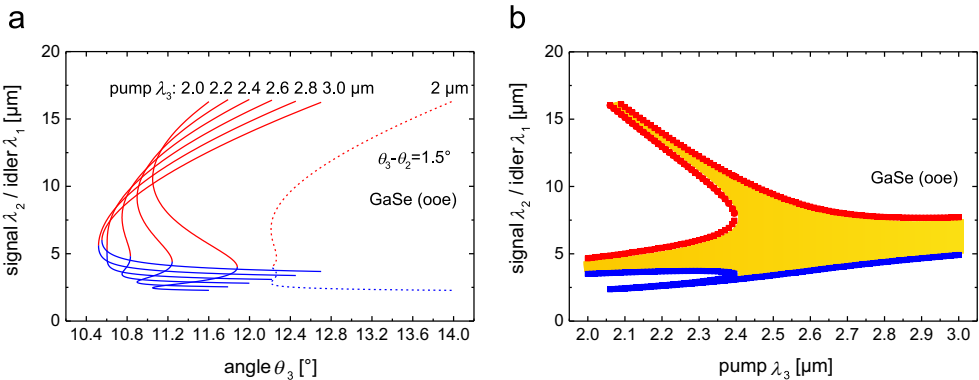


Fig. 3. Retracing behavior in GaSe for type-I (ooe) PM and effect of noncollinear propagation shown by dotted line (a). The signal and idler wavelengths are plotted vs. PM angle θ_3 for different pump wavelengths. The Sellmeier equations used [21] are valid up to 16.2 μm . The calculated spectral acceptance bandwidth is presented in (b) by red and blue symbols corresponding to wavelengths where $\text{sinc}^2(x) = 1/2$.

$$\Delta\nu = \frac{2(\ln 2)^{1/4}}{\pi} \left(\frac{\Gamma}{L}\right)^{1/4} \left| \frac{\partial^2 k_2}{\partial \omega_2^2} + \frac{\partial^2 k_1}{\partial \omega_1^2} \right|^{-1/2} \quad (13b)$$

The next two terms were obtained in [15,16]:

$$\Delta\nu = \frac{(144 \ln 2)^{1/6}}{\pi} \left(\frac{\Gamma}{L}\right)^{1/6} \left| \frac{\partial^3 k_2}{\partial \omega_2^3} - \frac{\partial^3 k_1}{\partial \omega_1^3} \right|^{-1/3} \quad (13c)$$

$$\Delta\nu = \frac{2(9 \ln 2)^{1/8}}{\pi} \left(\frac{\Gamma}{L}\right)^{1/8} \left| \frac{\partial^4 k_2}{\partial \omega_2^4} + \frac{\partial^4 k_1}{\partial \omega_1^4} \right|^{-1/4} \quad (13d)$$

The denominator in Eq. (13a) vanishes (group-velocity matching) at the turning point(s) of the tuning curve (dependence of the signal/idler wavelength on PM angle at fixed pump wavelength, see Fig. 3a) and it vanishes at degeneracy ($\omega_2 = \omega_1$) for type-I OPA (which is always such a turning point), i.e., when the polarizations of the signal and idler waves are the same. At degeneracy ($\omega_3 = 2\omega_2 = 2\omega_1$), it is possible that the denominator in Eq. (13b) also vanishes, however, this happens only for a certain “magic” pump wavelength. Such “magic” pump wavelengths have been identified in [15] for a number of oxide crystals. In [17] also some typical non-oxide crystals have been considered for which the signal and idler wavelengths lie in the mid-IR. This situation is very important for fs laser pulses because at such zero GVD wavelengths they will propagate without dispersive spreading. Unfortunately, for a given crystal, there is no guarantee that the “magic” pump wavelength coincides with some popular laser source. It is clear that in degenerate type-I OPA also the denominator of the third-order term, Eq. (13c) vanishes which makes it necessary to consider the fourth-order term, Eq. (13d). This can be formulated as a condition to generate continuum by an ultra-broadband degenerate OPA [18]. It is related to the occurrence of more than one pair of signal and idler that are simultaneously phase-matched at a given angle, so-called retracing behavior, Fig. 3a. In the general case, from the four approximations in Eq. (13) one should use, depending on how far the signal wavelength is from degeneracy, the term which predicts the smallest gain bandwidth.

Similar analysis can be performed in the low gain limit ($\Gamma L \ll 1$), i.e. based on the $\text{sinc}^2(x)$ -dependence of the DFG efficiency in Eq. (5). This is the so-called spectral acceptance bandwidth. It does not depend on the gain any more but can be expressed solely through the dispersive properties (refractive indices in different polarization configurations) of the NLC. The first order approximation, e.g., when the pump wave at ω_3 is chosen to be narrowband, reads $\Delta\nu = 0.886/(L|\Delta_{21}|)$ where $\Delta_{21} = 1/u_2 - 1/u_1$ is the inverse GVM between signal and idler. Comparing with Eq. (13a), the parametric gain bandwidth is $\approx 0.6\sqrt{\Gamma L}$ times larger. Thus, until $\Gamma L \sim 3$, there will be no substantial gain broadening of the bandwidth. The dependence of this ratio on ΓL gets even weaker for the higher order terms, see Eqs. (13b)–(13d) [18]. Nevertheless, gain increases the bandwidth unlike in lasers where broadband operation is associated with decreased gain.

Fig. 3a shows the retracing behavior in type-I (ooe) GaSe crystal. For a pump wavelength of $\lambda_3 = 2.6 \mu\text{m}$ a large portion of the curve is vertical, i.e. an ultra-broad spectrum (signal and idler) is phase-matched at a constant angle. This can be seen in Fig. 3b where the yellow area between the symbols is the range limited by the 50% drop in the DFG conversion efficiency from its maximum value. The left part of this figure corresponds to the retracing behavior in Fig. 3a, where “satellites” appear corresponding to the second pair of signal and idler. The largest

spectral acceptance in Fig. 3b is at $\lambda_3 \sim 2.4 \mu\text{m}$ where the three branches related to the three turning points in Fig. 3a already exist but still overlap well.

“Vertical” portions in the PM curves indicate vanishing GVM between signal and idler. The existence of the retracing phenomenon in the PM curves, which can be characterized by three or more turning points [19], is in fact determined by the existence of a turning point in the SHG tuning curve which is attributed to anomalous dispersion (the second pole in the Sellmeier equations related to phonon absorption) [20]. This same property is also characteristic of periodically poled materials, where QPM is realized by suitable choice of the poling period. Note that retracing behavior (and the spectral bandwidth) can also be controlled by varying the crystal temperature. Operating near degeneracy and pumping at the “magic” λ_3 means that the PM point is very close to the SHG turning point. This automatically leads to very low GVM with the pump as well which in OPA means broad spectral acceptance combined with long interaction length with the pump, i.e., high conversion efficiency. Therefore, this regime is very attractive when all three waves are ultrashort, in particular fs pulses. However, in QPM the separation between the two points is larger due to the same polarization of all three waves and the GVM with the pump is roughly one order of magnitude larger at the “magic” λ_3 [15]. This means that such materials are more suitable for chirped-pulse OPA (CPOPA, see below). Continuum is supported in both cases but with QPM efficient generation will be possible only on the ps time scale. Note that if the ultra-broad bandwidths near degeneracy are utilized in OPA, e.g., seeding it with white light continuum, a slight angle to the pump shall be introduced so that each branch of the spectrum (signal and idler) produces a noncollinear secondary beam but seeding at both wavelengths is avoided for each pair.

Type-II PM also can exhibit retracing behavior [19], i.e., multiple signal/idler solutions, but this is not relevant for ultra-broad parametric bandwidths because signal and idler have orthogonal polarizations. The signal and idler have their individual turning points where the GVM between them vanishes but there is no inflection point near degeneracy to obtain behavior like the $\lambda_3 = 2.6 \mu\text{m}$ curve in Fig. 3a and the GVM with the pump is not minimized. Thus OPA is broadband only for spectrally separated signal or idler.

Considering the first order GVM approximation for the spectral acceptance and parametric gain bandwidths it should be outlined that there is remarkable difference between type-I and type-II interaction (the same holds for their tuning behavior). Normally, the bandwidth is smaller for type-II interaction and stays more or less constant over the tuning range, while for type-I interaction the bandwidth increases towards degeneracy. Thus, type-I PM is attractive for ultimately short pulses, while type-II PM provides relatively narrow bandwidths over broad tuning ranges, which is interesting for many spectroscopic applications. The condition for group-velocity matching can be modified, however, by noncollinear PM. This represents an additional degree of freedom which can be utilized when operation away from degeneracy is required [22]. For instance this can be the angle between the pump and signal wave vectors $\theta_3 - \theta_2$ while the angle between the idler and signal wave vectors $\theta_1 - \theta_2$ (see Fig. 1) will depend on λ_2 (spatial dispersion of the idler). In this case the PM condition becomes a vector equation and both components (e.g. perpendicular and parallel to the signal wave vector) have to vanish. The result for the spectral acceptance bandwidth in the first order approximation is again $\Delta\nu = 0.886/(L|\Delta_{21}|)$ but this time $\Delta_{21} = \cos(\theta_1 - \theta_2)/u_2 - 1/u_1$ [22]. The GVM parameter Δ_{21} can vanish if only $u_1 > u_2$ but this is always the case in the normal dispersion region of a type-I NLC. The effect of introducing slight noncollinearity between signal and idler is illustrated in Fig. 3a by the dotted line. Ultra-broad bandwidth is achieved for a λ_3 for which collinear interaction cannot yield this. The broadband OPA is given for the signal in this case and for practical

implementation it is more convenient to derive from the above condition an expression for the angle between the signal and pump wave-vectors [22]. This approach, however, does not ensure that the GVM with the pump is minimized, too. It is possible to make all three group velocities equal by introducing noncollinearity and pulse phase-front slant as two independent degrees of freedom [23]. Noncollinear interaction and such ultimate group-velocity matching are applicable to both type-I and type-II non-degenerate PM but OPA is only broadband and not ultra-broadband if signal and idler are spectrally separated.

Expressions for the spectral acceptance bandwidth (as well as such for the related tuning behavior) depending on the refractive indices in different polarization configurations can be tabulated for any choice of the narrowband wave [5]. When the pump is narrowband, in view of the instantaneous nature of the nonlinear process (it is assumed that the electronic nonlinearity has a response time ~ 1 fs) and its intensity dependence, this will mean that the idler energy produced by DFG will be very low. In the limit of cw pump radiation at ω_3 and ultrashort signal pulse at ω_2 the result will be extremely low idler energy generated at ω_1 since the peak power of the pulses will be limited by the cw power level at ω_3 .

It can be questioned if similar limitation does not apply also for OPA with narrowband pump. In principle, the answer is positive but a powerful approach has been developed, the CPOPA, in which seed (signal) is first temporally stretched (adding linear chirp to the phase) and then parametrically amplified overlapping optimally with the much longer pump pulse before being recompressed [16]. In this case, it is essential to have sufficient parametric gain bandwidth so that the recompressed pulse can maintain the initial pulse duration or even get shorter. Noncollinear interaction plays an essential role in CPOPA because it offers the possibility to increase the parametric gain bandwidth when the wavelengths are already selected (basically from the limited number of existing suitable pump and seed signal laser sources) and they are away from degeneracy. This concerns mostly the GVM approximation, Eq. (13a), but also the higher order terms [17]. Other methods to increase the (CP) OPA gain bandwidth include chirping of the pump pulse, multi-beam pumping, etc. [16,24]. The tuning capability of parametric down-conversion devices is a major advantage because it can be not only much broader than any tunable laser but can cover wavelength ranges inaccessible to SSLs. Similarly, the achievable parametric gain bandwidths in (CP)OPA exceed the gain bandwidth of any broadband SSL, including Ti:sapphire (Ti:Sa).

It should be also emphasized that analytic expressions for the spectral acceptance or parametric gain bandwidths are based on Eq. (4) which in the case of DFG has its origin in Eq. (5). The latter equation is in turn derived in the fixed-field limit from the system Eq. (3), which is strictly valid only for monochromatic plane waves or when GVM is negligible. It is a kind of misleading paradox that these bandwidths in first approximation are then expressed in terms of GVM. Thus, though often used in the literature on ultrafast pulses, the meaning of such bandwidths is strictly speaking that one of the input wavelengths is fixed while the other is tuned, generating a tunable third wavelength while certain PM is maintained in some wavelength range but nevertheless all three waves are narrowband (quasi-monochromatic).

When dealing with ultrashort (ps or fs) pulses additional terms have to be included in Eq. (3) to describe correctly the non-stationary pulse evolution [25]. In Eq. (14), these are the first and second time derivatives of the amplitudes where the GVD factor is the second derivative of the wave vector $k_i'' = \partial^2 k_i / \partial \omega_i^2$. For completeness, loss coefficients α_i are also included for each wave. Often, even higher order dispersion terms or terms representing higher order nonlinear effects such as TPA or self-phase modulation have to be added to these equations [26]. Whether dispersion terms have to be taken into account depends on the pulse duration, the separation of the wavelengths and the ratio of their photon energies to the band-gap. In the mid-IR, GVM

effects start to play a role for durations less than ~ 1 ps and GVD for sub-100 fs pulses.

$$\frac{\partial A_1(z, t)}{\partial z} + \frac{1}{u_1} \frac{\partial A_1(z, t)}{\partial t} + \frac{i}{2} k_1'' \frac{\partial^2 A_1(z, t)}{\partial t^2} = -\frac{\alpha_1}{2} A_1(z, t) + i \frac{2\omega_1 d_{\text{eff}}}{n_1 c} A_3(z, t) A_2^*(z, t) e^{i\Delta k z} \quad (14a)$$

$$\frac{\partial A_2(z, t)}{\partial z} + \frac{1}{u_2} \frac{\partial A_2(z, t)}{\partial t} + \frac{i}{2} k_2'' \frac{\partial^2 A_2(z, t)}{\partial t^2} = -\frac{\alpha_2}{2} A_2(z, t) + i \frac{2\omega_2 d_{\text{eff}}}{n_2 c} A_3(z, t) A_1^*(z, t) e^{i\Delta k z} \quad (14b)$$

$$\frac{\partial A_3(z, t)}{\partial z} + \frac{1}{u_3} \frac{\partial A_3(z, t)}{\partial t} + \frac{i}{2} k_3'' \frac{\partial^2 A_3(z, t)}{\partial t^2} = -\frac{\alpha_3}{2} A_3(z, t) + i \frac{2\omega_3 d_{\text{eff}}}{n_3 c} A_1(z, t) A_2(z, t) e^{-i\Delta k z} \quad (14c)$$

Even with only the GVM terms added in Eq. (14), the analytical treatment is extremely difficult [25,27]. As already shown, it might happen that for certain crystal and polarization configurations all three group velocities are equal (group-velocity matching in addition to PM) but obviously this will not correspond to the available and/or desired wavelengths in the general case [28]. In such special conditions, the treatment at each time moment can rely on the steady-state Eq. (3), written in a frame moving with the common group velocity ($\eta = t - z/u$) while in some experiments OPA is more practical than CPOPA [28].

If pump depletion and GVM are negligible, it is easy to see from Eq. (11) that in the high gain limit the signal and idler pulses are shortened in the field of the pump. For a Gaussian pump pulse at exact PM, e.g., the signal pulse evolves also into a Gaussian shape with duration $\tau_2(z) = \tau_3/(\Gamma z)^{1/2}$ independent of its initial shape [25,29]. The pulse narrowing which is proportional to the $z^{-1/2}$ factor continues until limited by GVM. Even for $\Gamma z \sim 10$, the compression factor of 3 is modest. Analytical treatment in the general case, however, requires further simplifications. Considering the degenerate type-I PM (i.e., only a single GVM parameter) in the fixed-field approximation, the signal/idler pulses get shorter compared to the pump pulse due to the temporal gain narrowing effect [25,29] but this proceeds only as long as the temporal walk-off is small, at larger NLC lengths, the GVM effect will lengthen the pulses. Temporal walk-off decreases the parametric gain and the conversion efficiency.

Analytical work taking into account GVM predicted also interesting steady-state (solitonic) solutions and giant signal/idler pulse formation with intensity higher than the pump intensity and much higher compression factor, as a result of strong energy exchange, however, such phenomena occur in the field of a long (stationary) pump pulse [25,27,29,30] and thus are not relevant to efficient frequency down-conversion in practical OPAs. Nowadays, mostly numerical methods are used to treat the parametric amplification (OPA and CPOPA) in the presence of dispersion [16,24]. One of the early numerical simulations, e.g., predicted exponential, though decreased parametric gain for signal/idler in the undepleted pump approximation when the temporal walk-off of these pulses relative to the pump has opposite signs [16]. Using split-step Fourier algorithm approach to model pulse propagation in the presence of both nonlinearities and dispersion [24], allows one to take into account a lot of additional effects, such as the finite pump bandwidth, GVM among all three interacting pulses, pump depletion, dispersive broadening of the pulses due to GVD, noncollinear interaction, spatial walk-off, wave-front slant, phase modulation (chirp) of the interacting pulses,

higher order dispersion and nonlinear effects, as well as (asymmetric) dependence on the transversal coordinates.

4. Down-conversion of the laser frequency: systematics of processes and devices

OPA can also occur in the absence of an applied signal field; under these circumstances, it is called spontaneous parametric fluorescence. The cavity-free device, called Optical Parametric Generator (OPG), Fig. 4, operates due to its extremely high gain ($GL \sim 20$) capable to amplify spontaneous (quantum) noise to incident pump power levels [31]. In OPG, the frequencies of the generated photons are determined by the PM condition for the particular crystal orientation. According to the $\approx 0.6\sqrt{TL}$ dependence the bandwidth will be roughly 3 times larger than in the low gain case. It depends on the angle collected and increases at larger angles due to noncollinear PM. This leads to complex spatio-spectral distribution of the intensity. Normally OPG is followed by OPA to reduce the divergence and simultaneously the bandwidth.

If the OPA process occurs within an optical cavity with resonance frequency ω_2 , and the gain exceeds the cavity loss so that oscillation starts, the device is called Optical Parametric Oscillator (OPO). If the cavity has modes at both ω_2 and ω_1 , and the feedback is at both wavelengths, the device is a Doubly-Resonant OPO or DRO, see Fig. 5. The first OPO, based on LiNbO_3 , was demonstrated in 1965 by Giordmaine and Miller [32]. It utilized the high power of a short (ns) pulse Nd:CaWO_4 laser operating in the Q-switched (giant-pulse) regime. OPOs operating in the cw mode were realized in the following years: at first doubly-resonant to reduce the pump threshold and later singly-resonant (SRO) – to avoid the instabilities and complex tuning, Fig. 6.

The OPO threshold can be reduced by retro-reflecting the pump, then the signal (SRO) or both signal and idler (DRO) are amplified also in the back direction. Another option to reduce the threshold in OPOs is intracavity pumping: the OPO cavity or a part of it containing the NLC is inside the laser cavity. It is also possible to make the OPO cavity resonant for the pump: Such pump-enhanced OPOs can be of the SRO or DRO type, in the latter case they are also called Triply-Resonant OPO or TRO. This can be especially useful for the cw regime. Below only SRO, DRO and pump retro-reflection will be considered in more detail [31,33]; extensive information on pump enhancement cavities and intracavity pumped OPOs can be found in [34]. In the so-called non-resonant OPO, called NRO, the signal is totally outcoupled by one of the

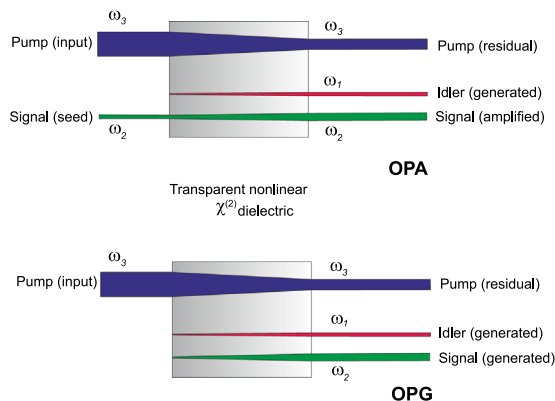


Fig. 4. OPA (top) vs. OPG (bottom).

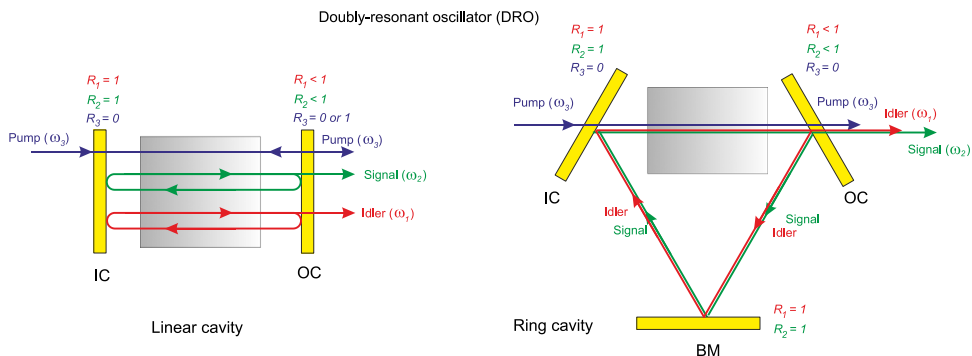


Fig. 5. Doubly-resonant OPO or DRO: linear (left) and ring (right) cavity where IC, OC, and BM denote input coupler, output coupler and bending mirror, respectively. In the linear cavity the pump can be transmitted by the OC (single pump pass, $R_3=0$), retro-reflected (double pump pass, $R_3=1$) or resonated in the OPO cavity (triply-resonant OPO, not shown here). In the ring cavity parametric amplification occurs only in the forward direction and the pump can be either transmitted by the OC (single pump pass, $R_3=0$) or resonated for triply-resonant OPO, not shown here.

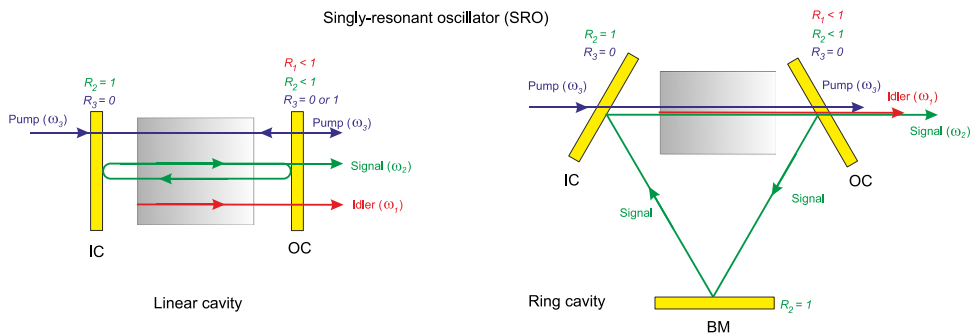


Fig. 6. Singly-resonant OPO or SRO: linear (left) and ring (right) cavity where IC, OC, and BM denote input coupler, output coupler and bending mirror, respectively. In the linear cavity the pump can be transmitted by the OC (single pump pass, $R_3=0$), retro-reflected (double pump pass, $R_3=1$) or resonated in the OPO cavity (case not shown here). In the ring cavity parametric amplification occurs only in the forward direction and the pump can be either transmitted by the OC (single pump pass, $R_3=0$) or resonated in the OPO, case not shown here.

end mirrors and idler – by the other, while “oscillation” is ensured by the retro-reflected pump although there is no resonated wave [8]. The term NRO is used sometimes also for OPOs with single output coupler when it reflects only a very small portion of both resonated waves.

While OPO is a feasible concept from ns time scale to cw operation, the parametric down-conversion of ultrashort (ps and fs) laser pulses is realized normally in “single pass” schemes, OPG and/or OPA. When OPA is employed as a second stage, it is seeded by one of the waves (in rare cases by both) from the OPG. OPG presents the simplest approach but offers less control on the output properties and requires high pump intensities, which are often close to the NLC damage threshold. As already explained OPA is in fact not different from DFG except that the input wave at ω_2 is weak and is to be strongly amplified while in DFG the main interest is in the generated idler wave at ω_1 and the input signal wave at ω_2 can be comparable in power or even stronger than the pump.

DFG is applicable on any time scale (from fs to cw) but requires two wavelengths. The OPA regime (i.e., high parametric gain) is reached as a rule only with ultrashort pulses. OPA, OPO and

OPG can produce output levels resulting in depletion of the pump power. In these devices, Q-switched ns lasers/amplifiers or ultrafast amplifiers are normally used for high-energy parametric down-conversion of ns, ps and fs pulses while the repetition rate varies from a few Hz up to ~ 1 MHz (more typically from 10 Hz to 100 kHz). Low energy ps and fs pulses directly from mode-locked laser oscillators can be down-converted employing an OPO cavity with a length matched to the repetition rate of the pump source (typically from ~ 40 MHz to ~ 1 GHz); in rare cases, the repetition rate is a multiple or some fraction of the pump repetition rate. These devices, called Synchronously-Pumped OPO (SPOPO), can be singly-resonant or doubly-resonant linear and ring cavities as shown in Figs. 5 and 6, and pump retro-reflection, enhancement or intracavity pumping are all possible options. However, typically SPOPOs are singly resonant for the signal, pumped in single pass (SP), and the idler is generated in a SP DFG and then out-coupled. Moreover, SPOPOs can be operated in the burst mode, i.e. pumped by macropulses at low repetition rate, which consist of few tens or hundreds of micropulses at high repetition rate. This helps to avoid damage originating from high average focused intensities, which are necessary to achieve sufficient parametric gain in a steady-state SPOPO.

It should be emphasized that in all down-conversion devices operating with ultrashort (i.e. ps or fs) pulses, the NLC length must be short enough so that GVM does not separate pump, signal and idler pulses (in some special cases GVM might have the opposite effect of compressing the pulse duration but this does not correspond to optimum conversion efficiency). In SPOPO group-velocity matching is essential only in a single pass, hence, matching pump and signal round trip times pulse narrowing can be achieved because the SPOPO is equivalent to OPA in a very long NLC with compensated GVM. Moreover, while other parametric devices are tuned either by the NLC rotation at fixed pump wavelength or at fixed crystal angle (e.g., NCPM) by temperature or by the pump wavelength, the SPOPO can be tuned also by variation of the cavity length because the resonated wave cavity round trip time depends on wavelength due to dispersion but must always equal the fixed period of the pump source. Thus, to maintain the synchronism, the signal and consequently the non-resonant idler experience wavelength change.

All the above parametric down-conversion processes and devices whose characteristics are compared in Table 1 have their laser analogs and there are many similarities with the operation of a laser. However, there are also essential differences: (i) parametric devices require coherent pump sources, i.e. lasers, and parametric fluorescence and gain occur in the direction of the pump beam (no analog of side-pumped lasers), there is a finite range of pump wave directions at which the signal wave is amplified and multimode pump sources can be used (brightness enhancement); (ii) their wavelength is determined and tuning is realized by changing the PM conditions (change of crystal tilt or temperature, or grating period in the case of QPM), the signal-idler tuning is very broad with possibility to access wavelengths where no lasers exist such as mid-IR or far-IR, and the spectral gain bandwidth is defined by the dispersive properties of the NLC and its length; (iii) no heat is deposited in a NLC unless there is some residual absorption at some of the three wavelengths involved, there is no energy exchange with the nonlinear medium – only exchange between the interacting waves; (iv) there is no gain/energy storage in the NLC because no levels are occupied and the dynamics is completely different due to the instantaneous nature of the nonlinear process: gain is only present while pump is present and as a consequence the temporal profile of the output is determined to a great extent by the temporal profile of the pump and seed (signal) radiation as well as by the dispersive properties of the NLC; (v) gain is produced at two wavelengths – two outputs; (vi) gain is determined by peak pump intensity and very high gain is possible with ultrashort pump pulses.

To increase the parametric gain beams are often focused. For practical purposes one has to transform Eqs. (9) and (10) to measurable integral powers. Assuming fundamental Gaussian modes the result in the near field is that in the expression for I^2 (Eq. (9)) the plane wave intensity I_3 has to be substituted by $4M^2w_3^2I_{3m}$ where w_3 is the Gaussian waist radius, I_{3m} the axial intensity, i.e. the pump power is $P_3 = (1/2)\pi w_3^2I_{3m}$, and $M = (w_1w_2w_3)/(w_1^2w_2^2 + w_1^2w_3^2 + w_2^2w_3^2)$ [31]. If the signal and idler beam waists are fixed $M_{\max}^2 = 1/(4w_1^2 + 4w_2^2)$ for $1/w_3^2 = (1/w_1^2) + (1/w_2^2)$ (optimum confocal near-field beams). For equal waists of signal and idler (degeneracy) this gives $w_3 = w_1/\sqrt{2}$ and $M_{\max}^2 = 1/8w_1^2$; then $4M^2w_3^2I_{3m} = I_{3m}/4$. This means that in terms of average power Γ is 2 times lower compared to a plane wave consideration with intensity equal to the peak (axial) pump intensity. However, keeping the geometry confocal means that the waists have to be increased when the NLC length is increased, e.g., $w_3^2 = \lambda_3 L / 2\pi n_3$. Substituting this expression in the gain at degeneracy yields $(\Gamma L)^2 = 2\pi^2 d_{\text{eff}}^2 LP_3 / \varepsilon_0 c n_1^2 \lambda_3^3$, i.e. linear instead of quadratic dependence on L [31]. As already mentioned, generalizations taking into account the birefringence can be found in [11]. The arguments above hold, however, strictly speaking for a DRO [31]. In DFG, or in a SRO where the idler is not resonated it will assume a radial distribution defined by the driving polarization, $1/w_1^2 = (1/w_3^2) + (1/w_2^2)$ where w_3 is determined by the pump focusing and w_2 by the OPO cavity [31].

The threshold and conversion efficiency of an OPO are normally analyzed in the steady-state regime (strictly speaking applicable only to cw OPOs) when the parametric gain balances the round trip cavity loss (transmission of mirrors, absorption and scatter loss for the signal and idler) [31,33]. In this regime, the parametric gain can be considered as in low gain OPA, i.e. DFG. For plane waves assuming small single pass intensity losses a_1 and a_2 for idler and signal, the calculated DRO threshold at exact PM is $(\Gamma L)^2 \approx a_1 a_2$ [31,33]; for simplicity, if the reflectivities $R_{1,2}$ for the two waves are considered to be the same for the two mirrors then $a_{1,2} = 1 - R_{1,2} \exp(-\alpha_{1,2} L)$. This result is strictly valid, however, only for single-frequency (SF) operation which requires SF pump source and precise cavity control (in fact more than one pair of signal and idler modes cannot be stable because the longitudinal mode interval is different at signal and idler frequencies due to dispersion). When the pump is totally reflected by the output coupler of the linear cavity and there are no phase shifts upon this reflection, the double pump pass reduces the DRO threshold in the ideal case 4 times [31,33]. The threshold is lower because parametric amplification takes place in the forward and backward direction.

As in a cw laser, the gain in a steady state OPO is clamped to its threshold value. The signal and idler waves are nearly constant across the cavity while the pump wave is strongly depleted. The conversion efficiency of a DRO, $\eta = (P_2 + P_1)/P_{30}$, where the splitting between the powers P_1 and P_2 is according to the photon energies, is normally expressed as a function of the parameter N which is the number of times the pump power exceeds the threshold value. In the plane wave approximation for a single pump pass it is $\eta = 2(\sqrt{N} - 1)/N$, hence, $\eta_{\max} = 50\%$ at $N=4$ [31,33]. The transmitted pump power in this case is clamped to the threshold value; the excess pump power is converted into signal and idler powers which can be calculated [4,33], and retro-reflected (in fact regenerated) pump as a result of the SFG process during the backward propagation. At $N=4$ the pump depletion is 50%, 25% of the incident pump are transmitted and 25% are retro-reflected. In the case of double pump pass DRO the regenerated pump power in the backward pass adds to the reflected pump power. Then, under ideal conditions, $\eta = 4(\sqrt{N} - 1)/N$, hence, $\eta_{\max} = 100\%$ at $N=4$ when the retro-reflection of the pump vanishes. This result is the same for the ring DRO shown in Fig. 5, where obviously a double pump pass cannot be realized, however, there is never “retro-reflection” of the pump beam due to SFG. Thus, the ring DRO is an option to reduce the back conversion and double the conversion efficiency. In addition, it eliminates feedback into the

pump laser which may cause instability. However, in contrast to the double pump pass it does not reduce the threshold.

As already mentioned, it is difficult to ensure stability and realize tuning in the DRO. This is so because cavity length fluctuations due to temperature and vibrations shift the cavity modes of both signal and idler in the same direction and the energy conservation law for a given pair is no more satisfied; it is satisfied or approximately satisfied then for other modes (clustering effect) and this leads to power and frequency instability of the output. That is why, when threshold can be reached below the NLC damage threshold, SRO is always preferable.

In the SRO, Fig. 6, only the signal is resonant while the idler is produced by DFG and if the cavity modes fluctuate the fluctuations can be accommodated by the idler frequency. For plane waves, assuming low gain and $a_1 \gg a_2$, the calculated SRO threshold at exact PM is $(\Gamma L)^2 \approx 2a_2$. This means that the threshold is reduced 200 times in a DRO if $a_1 = 1\%$ but only 20 times if $a_1 = 10\%$. The SRO can be also used with double pump pass, see Fig. 6, then the threshold is reduced 2 times in the ideal case [31,33]. If the idler is also retro-reflected, the reduction is 4 times in the best case [31,33]. There are two basic practical realizations of such OPOs, shown in Fig. 7.

Dielectric mirrors as in Fig. 7a reflecting in the mid-IR have low damage resistivity; it is also difficult to cover broad spectral ranges in the mid-IR with such mirrors. This is easier in transmission, e.g. using ZnSe substrates, as in Fig. 7b. A metallic total reflector (e.g. Au) can have even lower damage resistivity but is preferable as a mirror for the three waves because its dispersion is lower and the relative phase shift upon reflection will be minimized. Even if the main interest is in the idler, the output coupler normally transmits some portion of the signal, too. This is due to the increased damage risk for the NLC when the signal is fully resonated.

In the SRO, only the signal is nearly constant across the cavity while the pump and idler waves may vary. In the plane wave approximation, for low gain and exact PM, the conversion efficiency of the SRO, $\eta = (P_2 + P_1)/P_{30}$, can be calculated from an implicit relation for the signal intensity $\text{sinc}^2 BL = 1/N$ [31] where $B^2 = 8\pi^2 d_{\text{eff}}^2 I_2 / \epsilon_0 c n_1 n_2 n_3 \lambda_1 \lambda_3$ is a coupling constant analogous to Eq. (10). There is no “reflected” pump wave in the SRO and the pump is totally depleted ($\eta = 100\%$) for $N = (\pi/2)^2$. At higher pump levels it is rebuilt again in the forward direction (there is no clamping at threshold). When the pump is totally retro-reflected for a double pass in the SRO, under ideal conditions, the expression for the signal intensity reads $\text{sinc}^2 BL = 2 / ((1 + \cos BL)N)$ and the pump is totally depleted for $\eta_{\text{max}} = 100\%$ at $N = 2(\pi/2)^2$. In this case there is no pump wave propagating backward to the pump source. Thus, although the

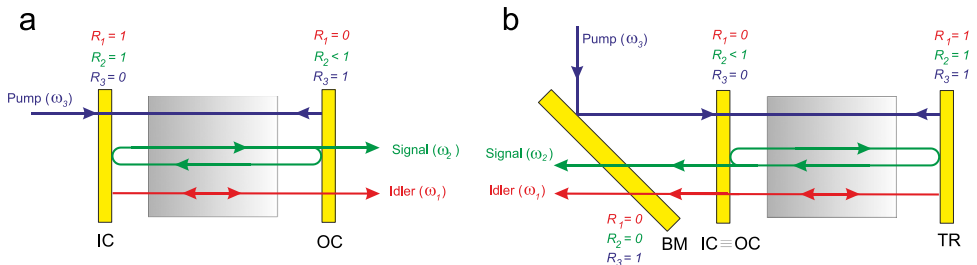


Fig. 7. Singly-resonant OPO, SRO with double pass for the pump and the idler. In (a) dielectric mirrors are used as input coupler (IC) and output coupler (OC). In (b) IC and OC coincide while the total reflector (TR) is a metallic mirror or a sequence of dielectric mirrors.

threshold is reduced by the double pump pass, maximum conversion is attained at the same pump intensity. Nevertheless, the region of high conversion is much broader compared to the single pump pass SRO; it covers $2.5 \leq N \leq 8.5$ for $\eta > 90\%$.

For more realistic Gaussian radial distribution of the pump beam, the results are quite different [31]. For the single pump pass DRO, $\eta = 4(\sqrt{N} - \ln \sqrt{N} - 1)/N$, hence, $\eta_{\max} = 41\%$ at $N = 12.5$. The transmitted pump power (in a single pump pass) in this case is no more clamped to the threshold value but increases with N . For the ring DRO shown in Fig. 5 the result reads $\eta = 8(\sqrt{N} - \ln \sqrt{N} - 1)/N$, hence, $\eta_{\max} = 82\%$ at $N = 12.5$. 100% conversion is impossible because of the low pump intensity far from the cavity axis. Similar calculation performed for SRO yields a solution only in an integral form since the resonant signal wave is not solved for explicitly [31]. Again 100% conversion is impossible, the maximum is $\eta_{\max} = 71\%$ at $N = 6.5$.

Tabulated expressions for estimating the threshold, conversion efficiency, and output power of different OPOs can be found in [4] for plane waves and near field Gaussian beams, and also birefringence can be accounted for. However, the low-gain steady-state conditions assumed are only a rough approximation for pulsed OPOs. In practice, most OPOs are pumped by ns pulses and steady state is achieved only after a finite build-up time. Thus, the energy conversion efficiency is lower than the power conversion efficiency while the build-up time will depend not only on the pump power but also on the pump duration and the cavity round trip time. The build-up time is the time required to amplify the quantum noise (i.e. the spontaneous parametric fluorescence) to a steady-state signal power of the order of the pump power. The process starts when the steady-state threshold is reached but the parametric gain is modest and more or less cavity round trips are required until the signal grows and pump depletion can be observed. The build-up time for DRO and SRO is discussed in detail in [31] and formulae for different cases are tabulated in [4]. It can be regarded as additional equivalent loss that has to be exceeded to reach threshold and this loss, for fixed round-trip time, is higher for shorter pulse durations and for the SRO compared to the DRO [31]. It depends only weakly (logarithmic) on the amount of gain needed to amplify the signal/idler from quantum noise to the steady-state level. Shorter cavities always reduce this build-up time and can increase the efficiency. The build-up time as a fraction of the pump pulse duration increases for shorter pump pulses and for smaller N numbers with respect to the steady state. For Gaussian pump pulses it may also decrease with the cavity losses. Thus the actual threshold can be expressed as the number of times the steady-state threshold has to be exceeded [31]. This number increases with the cavity length and for shorter pump pulse durations but decreases with the round-trip losses which emphasizes the fact that the latter are more detrimental in the steady-state regime. The finite build-up time means that certain energy must be accumulated and thus the actual (observable) threshold of a pulsed OPO can be expressed in terms of energy (fluence) instead of power (intensity) as in the steady-state regime. A widely accepted model for Gaussian pump pulse shape and spatial distributions, developed by Brosnan and Byer [35], gives expressions for the threshold fluence of SRO in the collinear configuration. Using a time-dependent gain analysis the threshold condition is derived from the solution of the coupled-wave equations in the limit of low pump depletion and zero input idler field, by allowing the resonant signal wave to be amplified from the initial parametric noise power to a detectable level in successive transits through the SRO cavity. By defining the observable SRO threshold as a signal energy of $\sim 100 \mu\text{J}$, corresponding to a threshold signal power to parametric noise power of $\ln(P_{2\text{th}}/P_n) = 33$, the threshold pump fluence is derived. The model includes also birefringence walk-off effects but this is omitted in the following expressions, reproduced here for the single and double pump pass SRO, respectively, assuming

that the effective gain length is equal to the actual crystal length L :

$$F_{3th} = \frac{1.91\tau}{\kappa_2\gamma L^2} \left\{ \frac{l\sqrt{\ln 2/2}}{c\tau} \ln\left(\frac{P_{2th}}{P_n}\right) + \alpha L + \ln\left(\frac{1}{\sqrt{R_2}}\right) + \ln 2 \right\}^2 \tag{15a}$$

$$F_{3th} = \frac{1.91\tau}{4\kappa_2\gamma L^2} \left\{ \frac{l\sqrt{\ln 2/2}}{c\tau} \ln\left(\frac{P_{2th}}{P_n}\right) + \alpha L + \ln\left(\frac{1}{\sqrt{R_2}}\right) + \ln 4 \right\}^2 \tag{15b}$$

Here τ is the pump pulse duration (FWHM intensity), l is the linear cavity optical length, $\kappa_2 = w_3^2/(w_2^2 + w_3^2)$ is the signal mode-coupling coefficient, R_2 is the output coupler reflectivity at the signal wavelength, and at degeneracy $\gamma = 8\pi^2 d_{eff}^2/\epsilon_0 c n_2^2 n_3 \lambda_2^2$ and $\alpha_1 = \alpha_2 = \alpha$. The main conclusions of the time-dependent model relate to the strong dependence of the threshold on the build-up time.

In pulsed OPO, it is essential that the build-up time is shorter than the pump pulse duration in order to reach the threshold but for efficient operation it must be also minimized (as an effective loss factor). In practice, this is achieved by minimizing the OPO cavity length in order to increase the number of round trips over the pump pulse length and by using longer pump pulses.

One of the greatest challenges in scaling ns OPOs to high energy is the output beam quality. On one hand, because of damage threshold constraints, OPO energy scaling implies increasing the beam diameters while keeping the pump fluence unchanged. On the other hand, as already explained, the cavity length should be as short as possible. The result is a high-Fresnel-number cavity ($N_F = 4w_2^2/\lambda_2 l$) that supports many transverse modes, often resulting in poor beam quality. As the beam diameters are increased to large Fresnel numbers, different portions of the beams uncouple and develop more or less independently of one another in cavities with flat mirrors. Thus uncorrelated phase and amplitude variations occur across the beam profile, resulting in poor beam quality. To improve the beam quality all regions of the signal or the idler beams or both have to communicate in a way that establishes more nearly uniform phase and amplitude across the beams. One of the methods developed exploits the spatial walk-off in the birefringent crystal between signal and idler, combined with image rotation [36] which resulted in development of three-dimensional cavity designs, Fig. 8.

Spatial walk-off tends to smooth the phase of the signal beam over regions that interact with a particular portion of the idler beam. Without image rotation uniform phase can be achieved parallel to the walk-off direction. By rotating the image by 90° on each cavity pass, one can induce a uniform phase across the entire beam with correlation in both transverse directions.

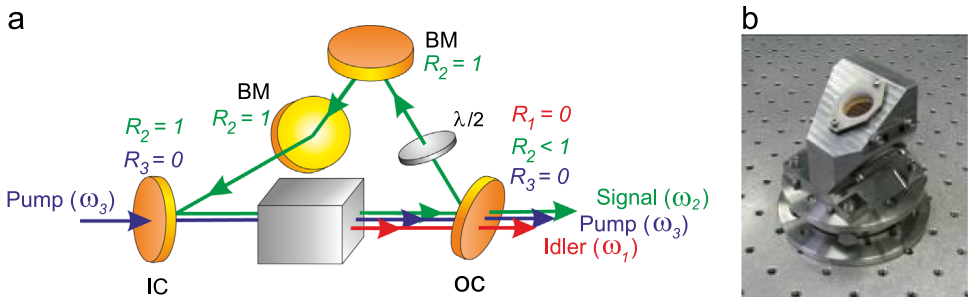


Fig. 8. Rotated Image Singly-Resonant Twisted-RectAngle (RISTRA) 3D OPO cavity (a) and photograph of a monolithic construction (b) developed at ISL (France).

Image rotation can be accomplished in different ways; one compact design is a three-dimensional four-mirror ring, named Rotated Image Singly-Resonant Twisted-RectAngle (RISTRA). Such non-planar geometry is insensitive to small tilts of the cavity mirrors, thus RISTRA requires no cavity mirror adjustments and can be engineered as a monolithic block, see Fig. 8b. Each image rotation causes also the polarization of the resonated signal to rotate, hence, a half-wave plate is introduced to compensate for this effect in each round-trip.

Initially, RISTRA was proposed for type-II PM (nonparallel Poynting vectors of signal and idler) in the crystal. Numerical simulations showed that the walk-off effect improves also the beam quality of the non-resonated idler [36]. As will be seen later the RISTRA concept turned out to be effective also for type-I PM. According to numerical modeling RISTRA shall be most effective for SF OPOs (where the pump should be also SF) and for pump beams in the fundamental mode. Most experiments have been performed, however, not in SF regime. With low-quality pump beams, i.e., not in the fundamental TEM₀₀ mode, and large pump diameters, good signal quality required decoupling of signal by walk-off not only from idler but also from pump while idler is supposed to carry away phase distortions of the pump [37]. Exactly in such high Fresnel number OPOs, where the pump beam sometimes is transformed into nearly top-hat spatial profile to overcome NLC damage limitations, RISTRA seems to be a very useful concept.

OPO tuning is normally achieved by critical angle variation, temperature variation or variation of the pump wavelength when the pump source is tunable, the last two methods used primarily at NCPM. The spectral properties are determined by the gain bandwidth which can be considered as in low-gain OPA or DFG, the pump laser bandwidth and the cavity properties. Narrowband operation requires additional cavity elements such as gratings (recently volume Bragg gratings, VBG), birefringent filters, etalons, or injection seeding. Injection seeding can reduce the build-up time. However, it has to be tunable. A narrowband low power OPO can serve as a seeder to a powerful OPO: master oscillator – power oscillator (MOPO) concept. Except for equal cavity length with the pump laser, which is not usually achievable, only a single longitudinal pump laser mode is effective in driving the DRO [31]. In the general case, energy conservation in a DRO is satisfied for a cluster of modes which leads to instabilities [31]. In a SRO the full pump power may couple into a single longitudinal mode of the signal because the idler frequency is free to adjust itself as in DFG, provided the pump bandwidth is smaller than the spectral acceptance bandwidth. Holding ω_2 fixed one can vary ω_1 and calculate the pump bandwidth acceptance. When no additional cavity elements are employed for spectral narrowing or SF operation of the signal, its spectrum is narrower than the gain bandwidth because multiple cavity round trips increase the spectral narrowing effect similar to a longer crystal. In this case the spectrum of the non-resonated idler is broader than the pump and signal spectra and in a first approximation can be estimated as a convolution of the latter. Like in a homogeneously saturated system, spectral narrowing is not expected to reduce the OPO output power. Far above threshold the bandwidths of both resonated signal and non-resonated idler approach the parametric gain bandwidth. The OPO bandwidth is also affected by the pump divergence. This effect can be estimated from Eq. (4) if both angle and frequency terms are preserved at exact PM.

More complex OPO layouts are used: (i) for noncollinear interaction and when the pump is retro-reflected, separate mirrors are needed for the noncollinear resonated wave(s), (ii) when additional tuning or spectral narrowing elements are implemented, (iii) when two or more NLCs are used for spatial walk-off compensation and to relax damage and thermal problems, (iv) when multiple dielectric mirrors are necessary to ensure tuning or avoid damage (e.g. when separate cavities are used for resonating signal and idler in collinear DRO or a separate mirror is used to retro-reflect the pump), (v) when the OPO is fully or partly inside the pump laser or other nonlinear processes, e.g. SHG, are performed inside the OPO cavity, (vi) when small size cavity

waists are necessary in the low power regime, e.g. in ultrafast SPOPOs for which also intracavity GVD compensation can be arranged [34].

SPOPOs pumped by a continuous train of ultrashort pulses can be treated similarly to true cw OPOs but with the parametric gain defined by the peak pump pulse intensity. Pulsed SPOPOs in the burst mode on the other hand can be treated similar to pulsed OPOs and besides the peak pump pulse intensity also the finite build-up time has to be taken into account. Additional effects important in any SPOPO are related to cavity length detuning, and, depending on the pulse durations, GVM and GVD. When these effects can be ignored, pulse narrowing relative to the pump pulse can be expected until pump depletion occurs. These effects are taken into account in the developed round-trip models which are numerically investigated [38]. The results for a singly-resonant non-degenerate SPOPO show that above the threshold the generated pulses are intrinsically stable against pump power fluctuations; for good efficiency and to maintain narrow pulses, the output coupler should be selected so that the peak pump intensity is at approximately two-times the pump threshold; with respect to cavity length fluctuations one has the choice between power stability and stability of the signal frequency; and that a trade-off in the NLC length is required related to the desire to have simultaneously high gain and broad bandwidth.

Since the pioneering work of Franken et al. on SHG, parametric down-conversion and up-conversion processes in NLCs as well as combinations of them have been widely used to fill in gaps in the optical spectrum where lasers do not exist or certain operational regimes are impossible: from the vacuum ultraviolet (UV) to the far-IR. The main progress took place in the last two decades following the advancement in near-IR SSL technology and NLCs.

5. The mid-infrared spectral range: non-oxide nonlinear materials

The entire mid-IR spectral range from 3 to 30 μm represents a very wide “gap”, where gas lasers emitting at discrete lines are well-known but SSLs are scarce. Indeed, the upper limit of practical SSLs, such as Er^{3+} or Cr^{2+} , extends to about 3 μm [39]. Other transitions at longer wavelengths exist but temperature quenching of the mid-IR fluorescence (e.g. Fe^{2+}) or the lack of suitable pump sources represent basic limitations. Note that above $\sim 3 \mu\text{m}$, low-phonon non-oxide host materials have to be used [39]. In many cases operation at low temperature and/or using pulsed pumping is required. The recent progress in tunable transition-metal mid-IR lasers is impressive [40], nevertheless, it is hard to imagine that all temporal regimes (from cw down to fs) will be ever realized with mid-IR SSLs which often exhibit only narrowband emission (e.g., Pr^{3+}). Still, as it will be seen later, in some temporal regimes nonlinear frequency down conversion faces severe competition from the emerging quantum-cascade lasers (QCLs) [41].

At present the main approach to cover the mid-IR spectral range on the basis of all-SSL technology is down-conversion employing NLCs. There are oxide crystals that are partially transparent in the mid-IR but not more than 4–5 μm . Indeed, the performance of oxide based crystals is affected by multi-phonon absorption starting in the best case from about 4 μm and thus non-oxide materials have to be used, such as unary, binary, ternary and quaternary phosphides, arsenides, or chalcogenides (sulfides, selenides and tellurides). Some of these inorganic crystals transmit up to 20–30 μm before multi-phonon absorption sets on as an intrinsic limit. In contrast to the oxides, which can be grown by well mastered and harmless hydrothermal, flux or Czochralski methods, the more complex Bridgman-Stockbarger growth technique in sealed (high atmosphere) ampoules, with volatile and chemically reactive starting components, is the only method used to produce large-size single-domain non-oxide crystals of such compounds, and this certainly hampered their development all the more that special post-growth treatments are needed to restore

stoichiometry and improve their optical quality. As a matter of fact such materials exhibit more defects, the residual losses (absorption and scatter) are more than one order of magnitude higher than in the best oxide crystals, and the damage threshold is lower.

Note that the longer the long-wave transmission limit the smaller the band-gap E_g of such non-oxides. In fact, there are some exceptions from this rule. Some acentric fluorides, a good example is the ferroelectric MgBaF_4 [42] which has been well optically characterized, exhibit extended transparency both in the UV and mid-IR direction as compared to oxides: In these wide band-gap materials, however, the nonlinearity is too low to be useful for down-conversion to the mid-IR. Many halides have been suggested for the mid-IR [43] and some of them have a short-wave cut-off in the UV, too. Active research on such compounds is ongoing [44], with the main objective to discover new mid-IR NLCs with improved damage resistivity thanks to wider band-gap. However, as explained below, this condition normally leads to low nonlinear coefficients. Indeed, no experimental evidence (beyond powder SHG tests, which are essentially qualitative) of nonlinear coefficients > 1 pm/V can be found in the literature for such halides. Below, only non-oxide NLCs which have been optically characterized (i.e., dispersion relations and nonlinear coefficients have been derived from measurements on single crystals) will be discussed.

Using typical non-oxide NLCs, down-conversion will require laser pump sources operating at longer wavelengths compared to oxides, or if such do not exist, cascaded schemes based on oxides in the first stage. This restriction is even more pronounced when short (ns) and ultrashort (ps or fs) pulses are used for pumping non-oxide materials because of the detrimental role of TPA, which sets the limit for λ_3 to half the band-gap value $\sim E_g/2$. Thus, e.g. only very few materials can be used for direct conversion of fs pulses from Ti:Sa laser systems operating near 800 nm and cascaded parametric down-conversion schemes are required. Even for wavelengths in the 1- μm spectral range, where powerful Nd^{3+} or Yb^{3+} short and ultrashort pulse laser systems exist, limitations related to the upper transmission cut-off wavelength, residual loss, nonlinearity, PM, thermo-mechanical properties, or simply growth and availability, often restrict the usefulness of a given NLC and especially its capability to generate high single pulse energies and/or average powers in the mid-IR. In such cases pumping at longer wavelengths (e.g., by Er^{3+} lasers near 1.5 μm , Tm^{3+} and Ho^{3+} lasers near 2 μm , and Cr^{2+} and Er^{3+} lasers up to ~ 3 μm or cascaded schemes) is more promising.

Such typical mid-IR NLCs exhibit nonlinear coefficients on the order of 10 pm/V or above, in the best cases few tens of pm/V, with the record value of ~ 600 pm/V for Te [5,45]. There are fundamental laws relating the nonlinearity and the index of refraction and although d_{il} may vary a lot, the quantity $\delta = d_{il}/(n^2 - 1)^3 = d_{il}/(\chi^{(1)} - 1)^3$ (Miller's delta) remains almost constant (e.g. within one order of magnitude, Miller's empirical rule) [46]. This means that the high nonlinearity of non-oxide NLCs is due to the increased linear susceptibility. Such NLCs have $n > 2$ and empirical formulae indicate that the index of refraction depends on the material band-gap as $\sim E_g^{-1/4}$ [46], hence, at $n \gg 1$, $d \sim E_g^{-3/2}$ (here d is some average nonlinearity). However, it should be kept in mind that such general considerations are over-simplified and sometimes even crystals with the same symmetry show deviation from such dependence. The index of refraction also enters the expression for the parametric gain (Eq. (10)) and it is not the d -tensor that should be compared for different materials but rather some figure of merit, such as $\text{FM} \sim d^2/n^3$, which determines the conversion efficiency. Therefore, at $n \gg 1$, $\text{FM} \sim n^9 \sim E_g^{-9/4}$ [46]. Comparing operation at different wavelengths one should keep in mind the weak dependence (dispersion) of the d_{il} components which can be estimated from Miller's rule on the basis of the refractive index dispersion. The direct wavelength dependence of the parametric gain is, however, much stronger

and the figure of merit can be redefined as $FM^* \sim d^2 / (n^3 \lambda_1 \lambda_2 \lambda_3)$. Thus, operation at longer (idler) wavelengths in general means lower conversion efficiency.

The NLCs combining transmission extending beyond $\sim 5 \mu\text{m}$ (the upper limit of oxide materials), $d > 1 \text{ pm/V}$, and large-enough birefringence to permit PM over their transparency ranges are not so many. Their FM is plotted in Fig. 9 vs. transparency range. The list of crystals in Fig. 9 can be considered as complete in the sense that all non-oxide NLCs for which a second-order nonlinear process has been phase-matched by birefringence are included although in some cases the materials have not been completely characterized (e.g. individual nonlinear tensor components are still unknown). Most of the data used for calculating the figure of merit can be found in [5,45]. Some exceptions are ZnSiAs₂ (ZSA) [47], InPS₄ [48], and Sn₂P₂S₆ [49] for which phase-matched processes have not been realized (except in the near-IR for Sn₂P₂S₆) but the linear and nonlinear optical properties were well characterized. Note that roughly one third of these materials are already archived [50] and their development abandoned, and only about another third are commercially available. Proustite (Ag₃AsS₃) and pyrargyrite (Ag₃SbS₃) which are difficult to grow in large sizes, have already lost their importance being completely replaced by AgGaS₂ (AGS) while the growth technology of ZSA, HgS (mineral) and InPS₄ (obtained by chemical vapor transport) was never developed [5,47,48]. The monoclinic (biaxial) Sn₂P₂S₆ is included in Fig. 9 for completeness: it is the only one of the materials presented that possesses ferroelectric properties but a phase transition at 338 K to a centrosymmetric phase makes it impractical [49]. Few other

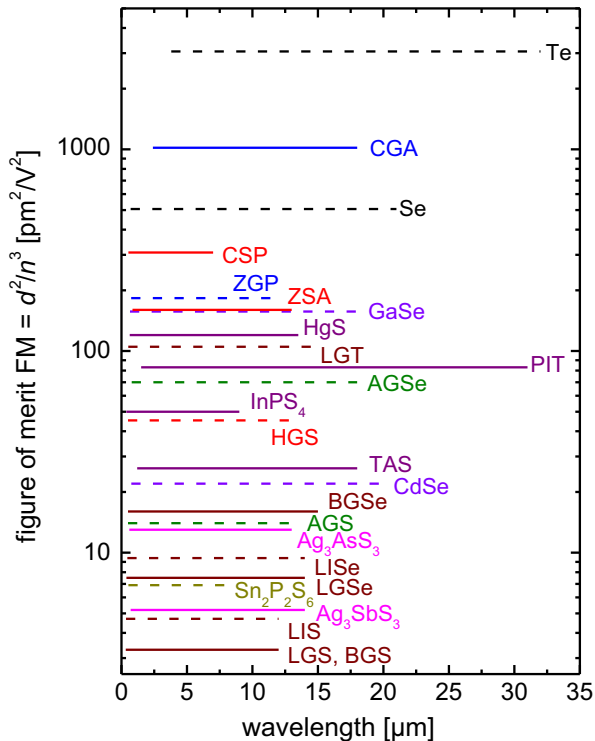


Fig. 9. Nonlinear figure of merit of non-oxide birefringent NLCs vs. transparency range. The data on HgS, TAS, and Se is very old and the FM error in this diagram is $\pm 50\%$. Only rough data exists on BGSe and it is assumed that $d(\text{BGSe}) = 2.5 \times d(\text{BGS})$. Oxide NLCs typically possess much lower FM, in the best cases (e.g. KNbO_3) $\sim 10 \text{ pm}^2/\text{V}^2$.

compounds show high nonlinearity and have been optically characterized but they are not included in Fig. 9 since their birefringence is insufficient for PM. Isotropic semiconductors useful for QPM, are considered separately below.

As already mentioned, non-oxide NLCs exhibit higher nonlinearity but smaller band-gap in comparison to oxides and their refractive index is also higher. Ternary chalcopyrite semiconductors are the most widely used non-oxide NLCs. Many such compounds have been investigated in the early 1970s and 11 of them were optically characterized [51]. Of these 11 compounds, only 5 exhibit sufficient birefringence: the optically negative AGS and AgGaSe_2 (AGSe) which belong to the I-III-VI₂ family, and the optically positive ZnGeP_2 (ZGP), ZSA, and CdGeAs_2 (CGA), which belong to the II-IV-V₂ family. The optically positive LiGaTe_2 (LGT) [52] and the optically negative CdSiP_2 (CSP) [53], were developed in the 2000s and added to the first and second group, respectively. AGS and AGSe have modest FM but low residual absorption. Poor thermal conductivity and anisotropic thermal expansion with different sign represent serious disadvantages of these I-III-VI₂ chalcopyrites while the surface of LGT is in addition not chemically stable. The II-IV-V₂ chalcopyrites exhibit in general much higher FM and better thermo-mechanical properties although the level of residual losses is also higher, in the best case of the order of 1%/cm in the clear transparency ranges of CSP and ZGP. Intrinsic multi-phonon and residual near band-gap absorption additionally restrict the useful transparency range from both sides. Thus, AGS can be pumped near 1 μm without TPA, CSP exhibits very low TPA at this wavelength, observable only with ultrashort pulses, AGSe requires pump wavelengths of at least $\sim 1.5 \mu\text{m}$ to avoid TPA, while in ZGP, residual near band-gap absorption sets the lower limit for λ_3 at $\sim 2 \mu\text{m}$ (which is less than 1/3 of its band-gap). Residual absorption and TPA set this limit at $\sim 4.6 \mu\text{m}$ for CGA (its band-gap corresponds to $\sim 2.3 \mu\text{m}$). CGA possesses extremely high FM (Fig. 9) but exhibits also absorption features and low temperatures may be required to avoid the much higher residual losses. Thus, CGA is impractical for pumping by existing high-power SSLs and in particular for power scaling based on laser-diode (LD) pumping. On the other hand the practical upper cut-off wavelengths are

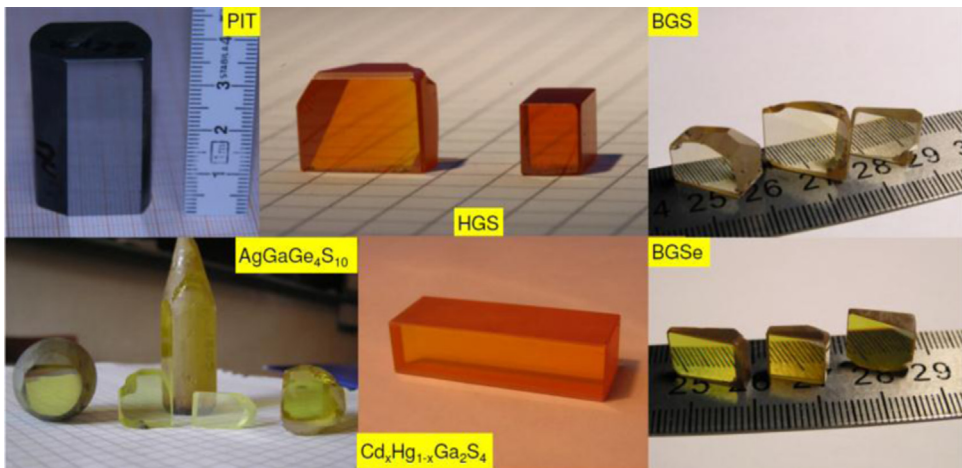


Fig. 10. Polished part of a $\text{PbIn}_6\text{Te}_{10}$ (PIT) boule, HgGa_2S_4 (HGS) optical elements with different color, samples of quaternary $\text{AgGaGe}_4\text{S}_{10}$, extra wide optical element of $\text{Cd}_x\text{Hg}_{1-x}\text{Ga}_2\text{S}_4$ (11 mm length and $30.6 \times 8 \text{ mm}^2$ aperture), for tuning by composition, and prisms of BaGa_4S_7 (BGS) and BaGa_4Se_7 (BGSe) for refractive index measurements. All crystals were grown by the Bridgman-Stockbarger method (courtesy of V. Badikov, Kuban State University).

relatively short in phosphides: $\sim 6.5 \mu\text{m}$ (CSP) and $\sim 8.5 \mu\text{m}$ (ZGP). They are longer for the arsenides, while in the I-III-VI₂ family the transparency window shifts to longer wavelengths from S to Se and to Te.

The defect chalcopyrite (the term has nothing to do with “defects” but reflects the presence of a vacancy sublattice) HgGa₂S₄ (HGS), Fig. 10, is a single representative of a whole class of related compounds; it competes directly with AGS since the transparency window is very similar. The main advantage of HGS over AGS is the ~ 1.8 times higher nonlinear coefficient d_{36} [54]. However, HGS is very difficult to grow in large sizes because several phases exist and oriented seeds cannot be used.

Tl₃AsSe₃ (TAS) exhibits rather low losses in its transparency range but its FM is modest and the thermal conductivity, similar to Ag₃AsS₃ and Ag₃SbS₃, is extremely low [45]. GaSe has large FM but it is a soft, cleaving compound, with low damage threshold and low thermal conductivity normal to the layers; it is difficult for polishing and coating. Its unique property is the very large birefringence capable to phase-match any three-wave process but the related spatial walk-off is simultaneously a limiting factor when tight focusing is required. CdSe exhibits modest birefringence and nonlinearity but its growth technology is mature, the residual losses are very low and the available sizes are quite large.

As can be seen from Fig. 9 only few arsenides, selenides, and tellurides show transparency extending beyond 15 μm . CGA transmits up to $\sim 18 \mu\text{m}$ but multi-phonon absorption peaks are seen already at 12.5 and 13.5 μm [55]. Unary, binary, ternary and quaternary (mixed) selenides in many cases are transparent above 15 μm . The long-wave transmission cut-off of the binary GaSe and CdSe as well as the ternary TAS and AGSe is affected by strong absorption bands, starting in the best case from $\sim 18 \mu\text{m}$ (CdSe). Unary trigonal Te with 32 point group symmetry is transparent from 3.5 to 36 μm and possesses the highest known nonlinear coefficient for an inorganic birefringent material, $\sim 600 \text{ pm/V}$. Its highest energy phonon band is at 24.3 μm compared to 15 μm for trigonal Se [56] which shows the third highest nonlinear coefficient, $\sim 100 \text{ pm/V}$. However, elemental Te, similar to elemental Se, exhibits high linear (free carrier absorption) losses within the transparency window which do not permit real applications apart from some diagnostics (e.g., of ultrashort pulses) in the mid-IR [57].

The extension of the NLC long-wave transmission limit beyond 15- μm , up to $\sim 25\text{--}30 \mu\text{m}$ is a challenging task and the candidates shall be searched among the tellurides which show the lowest phonon energies. Recently, PbIn₆Te₁₀, (PIT), Fig. 10, belonging to a new class of β -Mn structure type compounds, was grown and characterized [58]. It presents a unique combination of high FM and extended transparency without free carrier absorption but it seems very difficult to control the homogeneity of the boule composition.

Some of the crystals mentioned above are known for quite a long time, for some of them (e.g. AGS, AGSe, ZGP, CGA, TAS, GaSe, CdSe) improvement of growth technology, reduction of residual losses etc. still continue after few decades of development, others were never developed (HgS, ZSA, InPS₄) or abandoned (Ag₃AsS₃ and Ag₃SbS₃) in favor of more promising ones. Improved NLCs, however, will be crucial for advancing mid-IR coherent source development and in particular for higher conversion efficiency and output power. Important challenges include also compatibility with powerful 1 μm pump sources (Nd and Yb laser systems) or, in the fs domain, even with 800 nm Ti:Sa laser systems, which means relatively wide band-gap. As already mentioned, this unfortunately contradicts the basic requirement for high nonlinear coefficients. Other desirable properties include low residual losses, high damage threshold, high thermal conductivity and the possibility for NCPM. Problems that occur include the already mentioned TPA (except for the cw regime), the available sizes (especially for OPO), the homogeneity of the

Table 2

Summary of important properties of birefringent NLCs that can be pumped at 1.064 μm to generate 6.45 μm light: The effective nonlinearity d_{eff} (column 3) is calculated at the corresponding PM angle θ or φ (column 2), the nonlinear tensor components, d_{ij} , used for this calculation were derived from the literature (column 6) applying Miller's rule (column 7). The wavelength λ_F (fundamental) at which the nonlinear coefficients have been estimated by SHG is also shown in column 6. For $\text{Sn}_2\text{P}_2\text{S}_6$, d_{eff} is taken directly from the literature [49].

Crystal Point group	Plane θ/φ [°] (Interaction)	d_{eff} [pm/V]	Thermal conductivity [W/mK]	Band- gap E_g [eV]	Miller's δ [pm/V] or d_{ij} [pm/V] @ λ_F for SHG	+Miller's correction [pm/V]																																																																																																																																															
AgGaS ₂ ^a $\bar{4}2m$	40.50 (ooe)	8.86	1.4//c	2.70	$\delta_{36}=0.12$	$d_{36}=13.65$																																																																																																																																															
	45.53 (eoe)	13.65	1.5 \perp c				HgGa ₂ S ₄ ^a $\bar{4}$	45.87 (ooe)	15.57	2.49–2.85//c	2.79	$d_{36}=27.2$ @ 1.064 μm	$d_{36}=24.56$	51.21 (eoe)	21.18	2.36–2.31 \perp c	Cd _x Hg _{1-x} Ga ₂ S ₄ ^a ($\theta=90^\circ$, $x=0.55$) $\bar{4}$	90.00 (ooe)	24.94	1.8–1.92//c 1.62–1.81 \perp c ($x=0.27-0.3$)	3.22 ($x=0.55$)	$d_{36}=27.2$ @ 1.064 μm	$d_{36}=24.94$	LiGaS ₂ ^a $mm2$	XZ 47.77 (ooe)	4.23	NA	3.76	$d_{31}=5.8$ $d_{24}=5.1$ @ 2.3 μm	$d_{31}=5.71$ $d_{24}=5.21$	XY 40.36 (eoe)	5.50		LiInS ₂ $mm2$	XZ 40.01 (ooe)	4.65	6.2//x	3.57	$d_{31}=7.25$ $d_{24}=5.66$ @ 2.3 μm	$d_{31}=7.23$ $d_{24}=5.93$	XY 36.37 (eoe)	6.77	6.0//y 7.6//z	LiGaSe ₂ $mm2$	XZ 51.45 (ooe)	7.82	NA	3.65	$d_{31}=9.9$ $d_{24}=7.7$ @ 2.3 μm	$d_{31}=10$ $d_{24}=8.16$	XY 37.61 (eoe)	9.31		LiInSe ₂ ^a $mm2$	XZ 36.97 (ooe)	7.26	4.7–4.5//x	2.86	$d_{31}=11.78$ $d_{24}=8.17$ @ 2.3 μm	$d_{31}=12.08$ $d_{24}=8.65$	XY 41.62 (eoe)	10.57	4.7–4.8//y 5.5–5.8//z	LiGaTe ₂ $\bar{4}2m$	36.38 (eoo)	46.20	NA	2.41	$d_{36}=43$ @ 4.6 μm	$d_{36}=48.37$	40.05 (eoo)	31.12		BaGa ₄ S ₇ ^a $mm2$	XZ 10.47 (ooe)	4.99	1.68//x 1.58//y 1.45//z	3.54	$d_{31}=5.1$ @ 2.26 μm	$d_{31}=5.07$	BaGa ₄ Se ₇ m	YZ 33.47 (eoo)	~ 1	0.56–0.74	2.64	$d_{23}=20$ @ 1.8 μm	$d_{23}=18.14$ $d_{24}=3.70$	XZ 45.68 (eoo)	~ 9.3		XZ 49.17 (eoo)	2.8		InPS ₄ $\bar{4}$	38.80 (eoo)	34.40	NA	3.2	$\delta_{31}=0.39$ $\delta_{36}=0.30$	$d_{31}=27.87$ $d_{36}=21.53$	42.67 (eoo)	23.87		Sn ₂ P ₂ S ₆ m	... (ssf) ^b	≈ 4	0.4–0.55	2.35 (fsf) ^b	≈ 2		GaS _{0.4} Se _{0.6} $\bar{6}2m$	22.31 (ooe)	45.80	1.3//c	2.4	$d_{22}=44.1$ @ 4.65 μm	$d_{22}=49.51$	24.67 (eoe)	40.88	10 \perp c	CdSiP ₂ ^a $\bar{4}2m$	80.46 (ooe)	90.99	13.6	2.2–2.45	$d_{36}=84.5$ @ 4.56 μm	$d_{36}=92.27$	AgGaGeS ₄ $mm2$	XZ 53.99 (ooe)	3.32	0.399	3.0	$d_{32}=6.2$ $d_{31}=10.2$ @ 1.064 μm	$d_{32}=5.65$ $d_{31}=9.30$	XY 35.74 (ooe)	5.43		Ag ₃ AsS ₃ ^a $3m$	22.04 (ooe)	22.89	0.113//c,	2.2	$d_{31}=10.4$ $d_{22}=16.6$ @ 10.6 μm	$d_{31}=12.34$ $d_{22}=19.70$	24.01 (eoe)	16.44
HgGa ₂ S ₄ ^a $\bar{4}$	45.87 (ooe)	15.57	2.49–2.85//c	2.79	$d_{36}=27.2$ @ 1.064 μm	$d_{36}=24.56$																																																																																																																																															
	51.21 (eoe)	21.18	2.36–2.31 \perp c				Cd _x Hg _{1-x} Ga ₂ S ₄ ^a ($\theta=90^\circ$, $x=0.55$) $\bar{4}$	90.00 (ooe)	24.94	1.8–1.92//c 1.62–1.81 \perp c ($x=0.27-0.3$)	3.22 ($x=0.55$)	$d_{36}=27.2$ @ 1.064 μm	$d_{36}=24.94$	LiGaS ₂ ^a $mm2$	XZ 47.77 (ooe)	4.23	NA	3.76	$d_{31}=5.8$ $d_{24}=5.1$ @ 2.3 μm	$d_{31}=5.71$ $d_{24}=5.21$	XY 40.36 (eoe)	5.50		LiInS ₂ $mm2$	XZ 40.01 (ooe)	4.65	6.2//x	3.57	$d_{31}=7.25$ $d_{24}=5.66$ @ 2.3 μm	$d_{31}=7.23$ $d_{24}=5.93$	XY 36.37 (eoe)	6.77	6.0//y 7.6//z	LiGaSe ₂ $mm2$	XZ 51.45 (ooe)	7.82	NA	3.65	$d_{31}=9.9$ $d_{24}=7.7$ @ 2.3 μm	$d_{31}=10$ $d_{24}=8.16$	XY 37.61 (eoe)	9.31		LiInSe ₂ ^a $mm2$	XZ 36.97 (ooe)	7.26	4.7–4.5//x	2.86	$d_{31}=11.78$ $d_{24}=8.17$ @ 2.3 μm	$d_{31}=12.08$ $d_{24}=8.65$	XY 41.62 (eoe)	10.57	4.7–4.8//y 5.5–5.8//z	LiGaTe ₂ $\bar{4}2m$	36.38 (eoo)	46.20	NA	2.41	$d_{36}=43$ @ 4.6 μm	$d_{36}=48.37$	40.05 (eoo)	31.12		BaGa ₄ S ₇ ^a $mm2$	XZ 10.47 (ooe)	4.99	1.68//x 1.58//y 1.45//z	3.54	$d_{31}=5.1$ @ 2.26 μm	$d_{31}=5.07$	BaGa ₄ Se ₇ m	YZ 33.47 (eoo)	~ 1	0.56–0.74	2.64	$d_{23}=20$ @ 1.8 μm	$d_{23}=18.14$ $d_{24}=3.70$	XZ 45.68 (eoo)	~ 9.3			XZ 49.17 (eoo)	2.8					InPS ₄ $\bar{4}$	38.80 (eoo)	34.40	NA	3.2	$\delta_{31}=0.39$ $\delta_{36}=0.30$	$d_{31}=27.87$ $d_{36}=21.53$	42.67 (eoo)	23.87		Sn ₂ P ₂ S ₆ m	... (ssf) ^b	≈ 4	0.4–0.55	2.35 (fsf) ^b	≈ 2		GaS _{0.4} Se _{0.6} $\bar{6}2m$	22.31 (ooe)	45.80	1.3//c	2.4	$d_{22}=44.1$ @ 4.65 μm	$d_{22}=49.51$	24.67 (eoe)	40.88	10 \perp c	CdSiP ₂ ^a $\bar{4}2m$	80.46 (ooe)	90.99	13.6	2.2–2.45	$d_{36}=84.5$ @ 4.56 μm	$d_{36}=92.27$	AgGaGeS ₄ $mm2$	XZ 53.99 (ooe)	3.32	0.399	3.0	$d_{32}=6.2$ $d_{31}=10.2$ @ 1.064 μm	$d_{32}=5.65$ $d_{31}=9.30$	XY 35.74 (ooe)	5.43		Ag ₃ AsS ₃ ^a $3m$	22.04 (ooe)	22.89	0.113//c,	2.2	$d_{31}=10.4$ $d_{22}=16.6$ @ 10.6 μm		$d_{31}=12.34$ $d_{22}=19.70$	24.01 (eoe)	16.44				0.092 \perp c	65.63 (eoe)
Cd _x Hg _{1-x} Ga ₂ S ₄ ^a ($\theta=90^\circ$, $x=0.55$) $\bar{4}$	90.00 (ooe)	24.94	1.8–1.92//c 1.62–1.81 \perp c ($x=0.27-0.3$)	3.22 ($x=0.55$)	$d_{36}=27.2$ @ 1.064 μm	$d_{36}=24.94$																																																																																																																																															
	LiGaS ₂ ^a $mm2$	XZ 47.77 (ooe)	4.23				NA	3.76	$d_{31}=5.8$ $d_{24}=5.1$ @ 2.3 μm	$d_{31}=5.71$ $d_{24}=5.21$																																																																																																																																											
XY 40.36 (eoe)		5.50		LiInS ₂ $mm2$	XZ 40.01 (ooe)	4.65	6.2//x				3.57	$d_{31}=7.25$ $d_{24}=5.66$ @ 2.3 μm	$d_{31}=7.23$ $d_{24}=5.93$	XY 36.37 (eoe)	6.77	6.0//y 7.6//z	LiGaSe ₂ $mm2$	XZ 51.45 (ooe)	7.82	NA	3.65	$d_{31}=9.9$ $d_{24}=7.7$ @ 2.3 μm	$d_{31}=10$ $d_{24}=8.16$	XY 37.61 (eoe)	9.31		LiInSe ₂ ^a $mm2$	XZ 36.97 (ooe)	7.26	4.7–4.5//x	2.86	$d_{31}=11.78$ $d_{24}=8.17$ @ 2.3 μm	$d_{31}=12.08$ $d_{24}=8.65$	XY 41.62 (eoe)	10.57	4.7–4.8//y 5.5–5.8//z	LiGaTe ₂ $\bar{4}2m$	36.38 (eoo)	46.20	NA	2.41	$d_{36}=43$ @ 4.6 μm	$d_{36}=48.37$	40.05 (eoo)	31.12		BaGa ₄ S ₇ ^a $mm2$	XZ 10.47 (ooe)	4.99	1.68//x 1.58//y 1.45//z	3.54	$d_{31}=5.1$ @ 2.26 μm	$d_{31}=5.07$	BaGa ₄ Se ₇ m	YZ 33.47 (eoo)	~ 1	0.56–0.74	2.64	$d_{23}=20$ @ 1.8 μm	$d_{23}=18.14$ $d_{24}=3.70$	XZ 45.68 (eoo)	~ 9.3		XZ 49.17 (eoo)	2.8		InPS ₄ $\bar{4}$	38.80 (eoo)	34.40	NA	3.2	$\delta_{31}=0.39$ $\delta_{36}=0.30$	$d_{31}=27.87$ $d_{36}=21.53$	42.67 (eoo)	23.87		Sn ₂ P ₂ S ₆ m	... (ssf) ^b	≈ 4	0.4–0.55	2.35 (fsf) ^b	≈ 2		GaS _{0.4} Se _{0.6} $\bar{6}2m$	22.31 (ooe)	45.80	1.3//c	2.4	$d_{22}=44.1$ @ 4.65 μm	$d_{22}=49.51$	24.67 (eoe)	40.88	10 \perp c	CdSiP ₂ ^a $\bar{4}2m$	80.46 (ooe)	90.99	13.6	2.2–2.45	$d_{36}=84.5$ @ 4.56 μm	$d_{36}=92.27$	AgGaGeS ₄ $mm2$	XZ 53.99 (ooe)	3.32	0.399	3.0	$d_{32}=6.2$ $d_{31}=10.2$ @ 1.064 μm	$d_{32}=5.65$ $d_{31}=9.30$	XY 35.74 (ooe)	5.43		Ag ₃ AsS ₃ ^a $3m$	22.04 (ooe)	22.89	0.113//c,	2.2	$d_{31}=10.4$ $d_{22}=16.6$ @ 10.6 μm	$d_{31}=12.34$ $d_{22}=19.70$	24.01 (eoe)	16.44	0.092 \perp c	65.63 (eoe)	3.35																								
LiInS ₂ $mm2$	XZ 40.01 (ooe)	4.65	6.2//x		3.57	$d_{31}=7.25$ $d_{24}=5.66$ @ 2.3 μm	$d_{31}=7.23$ $d_{24}=5.93$																																																																																																																																														
	XY 36.37 (eoe)	6.77	6.0//y 7.6//z	LiGaSe ₂ $mm2$				XZ 51.45 (ooe)	7.82	NA	3.65	$d_{31}=9.9$ $d_{24}=7.7$ @ 2.3 μm	$d_{31}=10$ $d_{24}=8.16$	XY 37.61 (eoe)	9.31		LiInSe ₂ ^a $mm2$	XZ 36.97 (ooe)	7.26	4.7–4.5//x	2.86	$d_{31}=11.78$ $d_{24}=8.17$ @ 2.3 μm	$d_{31}=12.08$ $d_{24}=8.65$	XY 41.62 (eoe)	10.57	4.7–4.8//y 5.5–5.8//z	LiGaTe ₂ $\bar{4}2m$	36.38 (eoo)	46.20	NA	2.41	$d_{36}=43$ @ 4.6 μm	$d_{36}=48.37$	40.05 (eoo)	31.12		BaGa ₄ S ₇ ^a $mm2$	XZ 10.47 (ooe)	4.99	1.68//x 1.58//y 1.45//z	3.54	$d_{31}=5.1$ @ 2.26 μm	$d_{31}=5.07$	BaGa ₄ Se ₇ m	YZ 33.47 (eoo)	~ 1	0.56–0.74	2.64	$d_{23}=20$ @ 1.8 μm	$d_{23}=18.14$ $d_{24}=3.70$	XZ 45.68 (eoo)	~ 9.3			XZ 49.17 (eoo)	2.8					InPS ₄ $\bar{4}$	38.80 (eoo)	34.40	NA	3.2	$\delta_{31}=0.39$ $\delta_{36}=0.30$	$d_{31}=27.87$ $d_{36}=21.53$	42.67 (eoo)	23.87		Sn ₂ P ₂ S ₆ m	... (ssf) ^b	≈ 4	0.4–0.55	2.35 (fsf) ^b	≈ 2		GaS _{0.4} Se _{0.6} $\bar{6}2m$	22.31 (ooe)	45.80	1.3//c	2.4	$d_{22}=44.1$ @ 4.65 μm	$d_{22}=49.51$	24.67 (eoe)	40.88	10 \perp c	CdSiP ₂ ^a $\bar{4}2m$	80.46 (ooe)	90.99	13.6	2.2–2.45	$d_{36}=84.5$ @ 4.56 μm	$d_{36}=92.27$	AgGaGeS ₄ $mm2$	XZ 53.99 (ooe)	3.32	0.399	3.0	$d_{32}=6.2$ $d_{31}=10.2$ @ 1.064 μm	$d_{32}=5.65$ $d_{31}=9.30$	XY 35.74 (ooe)	5.43		Ag ₃ AsS ₃ ^a $3m$	22.04 (ooe)	22.89	0.113//c,	2.2	$d_{31}=10.4$ $d_{22}=16.6$ @ 10.6 μm		$d_{31}=12.34$ $d_{22}=19.70$	24.01 (eoe)	16.44				0.092 \perp c	65.63 (eoe)	3.35																										
LiGaSe ₂ $mm2$	XZ 51.45 (ooe)	7.82	NA		3.65	$d_{31}=9.9$ $d_{24}=7.7$ @ 2.3 μm	$d_{31}=10$ $d_{24}=8.16$																																																																																																																																														
	XY 37.61 (eoe)	9.31		LiInSe ₂ ^a $mm2$				XZ 36.97 (ooe)	7.26	4.7–4.5//x	2.86	$d_{31}=11.78$ $d_{24}=8.17$ @ 2.3 μm	$d_{31}=12.08$ $d_{24}=8.65$	XY 41.62 (eoe)	10.57	4.7–4.8//y 5.5–5.8//z	LiGaTe ₂ $\bar{4}2m$	36.38 (eoo)	46.20	NA	2.41	$d_{36}=43$ @ 4.6 μm	$d_{36}=48.37$	40.05 (eoo)	31.12		BaGa ₄ S ₇ ^a $mm2$	XZ 10.47 (ooe)	4.99	1.68//x 1.58//y 1.45//z	3.54	$d_{31}=5.1$ @ 2.26 μm	$d_{31}=5.07$	BaGa ₄ Se ₇ m	YZ 33.47 (eoo)	~ 1	0.56–0.74	2.64	$d_{23}=20$ @ 1.8 μm	$d_{23}=18.14$ $d_{24}=3.70$	XZ 45.68 (eoo)	~ 9.3			XZ 49.17 (eoo)	2.8					InPS ₄ $\bar{4}$	38.80 (eoo)	34.40	NA	3.2	$\delta_{31}=0.39$ $\delta_{36}=0.30$	$d_{31}=27.87$ $d_{36}=21.53$	42.67 (eoo)	23.87		Sn ₂ P ₂ S ₆ m	... (ssf) ^b	≈ 4	0.4–0.55	2.35 (fsf) ^b	≈ 2		GaS _{0.4} Se _{0.6} $\bar{6}2m$	22.31 (ooe)	45.80	1.3//c	2.4	$d_{22}=44.1$ @ 4.65 μm	$d_{22}=49.51$	24.67 (eoe)	40.88	10 \perp c	CdSiP ₂ ^a $\bar{4}2m$	80.46 (ooe)	90.99	13.6	2.2–2.45	$d_{36}=84.5$ @ 4.56 μm	$d_{36}=92.27$	AgGaGeS ₄ $mm2$	XZ 53.99 (ooe)	3.32	0.399	3.0	$d_{32}=6.2$ $d_{31}=10.2$ @ 1.064 μm	$d_{32}=5.65$ $d_{31}=9.30$	XY 35.74 (ooe)	5.43		Ag ₃ AsS ₃ ^a $3m$	22.04 (ooe)	22.89	0.113//c,	2.2	$d_{31}=10.4$ $d_{22}=16.6$ @ 10.6 μm	$d_{31}=12.34$ $d_{22}=19.70$	24.01 (eoe)	16.44	0.092 \perp c		65.63 (eoe)	3.35																																							
LiInSe ₂ ^a $mm2$	XZ 36.97 (ooe)	7.26	4.7–4.5//x		2.86	$d_{31}=11.78$ $d_{24}=8.17$ @ 2.3 μm	$d_{31}=12.08$ $d_{24}=8.65$																																																																																																																																														
	XY 41.62 (eoe)	10.57	4.7–4.8//y 5.5–5.8//z	LiGaTe ₂ $\bar{4}2m$				36.38 (eoo)	46.20	NA	2.41	$d_{36}=43$ @ 4.6 μm	$d_{36}=48.37$	40.05 (eoo)	31.12		BaGa ₄ S ₇ ^a $mm2$	XZ 10.47 (ooe)	4.99	1.68//x 1.58//y 1.45//z	3.54	$d_{31}=5.1$ @ 2.26 μm	$d_{31}=5.07$	BaGa ₄ Se ₇ m	YZ 33.47 (eoo)	~ 1	0.56–0.74	2.64	$d_{23}=20$ @ 1.8 μm	$d_{23}=18.14$ $d_{24}=3.70$	XZ 45.68 (eoo)	~ 9.3			XZ 49.17 (eoo)	2.8					InPS ₄ $\bar{4}$	38.80 (eoo)	34.40	NA	3.2	$\delta_{31}=0.39$ $\delta_{36}=0.30$	$d_{31}=27.87$ $d_{36}=21.53$	42.67 (eoo)	23.87		Sn ₂ P ₂ S ₆ m	... (ssf) ^b	≈ 4	0.4–0.55	2.35 (fsf) ^b	≈ 2		GaS _{0.4} Se _{0.6} $\bar{6}2m$	22.31 (ooe)	45.80	1.3//c	2.4	$d_{22}=44.1$ @ 4.65 μm	$d_{22}=49.51$	24.67 (eoe)	40.88	10 \perp c	CdSiP ₂ ^a $\bar{4}2m$	80.46 (ooe)	90.99	13.6	2.2–2.45	$d_{36}=84.5$ @ 4.56 μm	$d_{36}=92.27$	AgGaGeS ₄ $mm2$	XZ 53.99 (ooe)	3.32	0.399	3.0	$d_{32}=6.2$ $d_{31}=10.2$ @ 1.064 μm	$d_{32}=5.65$ $d_{31}=9.30$	XY 35.74 (ooe)	5.43		Ag ₃ AsS ₃ ^a $3m$	22.04 (ooe)	22.89	0.113//c,	2.2	$d_{31}=10.4$ $d_{22}=16.6$ @ 10.6 μm	$d_{31}=12.34$ $d_{22}=19.70$	24.01 (eoe)	16.44	0.092 \perp c		65.63 (eoe)	3.35																																																	
LiGaTe ₂ $\bar{4}2m$	36.38 (eoo)	46.20	NA		2.41	$d_{36}=43$ @ 4.6 μm	$d_{36}=48.37$																																																																																																																																														
	40.05 (eoo)	31.12		BaGa ₄ S ₇ ^a $mm2$				XZ 10.47 (ooe)	4.99	1.68//x 1.58//y 1.45//z	3.54	$d_{31}=5.1$ @ 2.26 μm	$d_{31}=5.07$	BaGa ₄ Se ₇ m	YZ 33.47 (eoo)	~ 1	0.56–0.74	2.64	$d_{23}=20$ @ 1.8 μm	$d_{23}=18.14$ $d_{24}=3.70$	XZ 45.68 (eoo)	~ 9.3			XZ 49.17 (eoo)	2.8					InPS ₄ $\bar{4}$	38.80 (eoo)	34.40	NA	3.2	$\delta_{31}=0.39$ $\delta_{36}=0.30$	$d_{31}=27.87$ $d_{36}=21.53$	42.67 (eoo)	23.87		Sn ₂ P ₂ S ₆ m	... (ssf) ^b	≈ 4	0.4–0.55	2.35 (fsf) ^b	≈ 2		GaS _{0.4} Se _{0.6} $\bar{6}2m$	22.31 (ooe)	45.80	1.3//c	2.4	$d_{22}=44.1$ @ 4.65 μm	$d_{22}=49.51$	24.67 (eoe)	40.88	10 \perp c	CdSiP ₂ ^a $\bar{4}2m$	80.46 (ooe)	90.99	13.6	2.2–2.45	$d_{36}=84.5$ @ 4.56 μm	$d_{36}=92.27$	AgGaGeS ₄ $mm2$	XZ 53.99 (ooe)	3.32	0.399	3.0	$d_{32}=6.2$ $d_{31}=10.2$ @ 1.064 μm	$d_{32}=5.65$ $d_{31}=9.30$	XY 35.74 (ooe)	5.43		Ag ₃ AsS ₃ ^a $3m$	22.04 (ooe)	22.89	0.113//c,	2.2	$d_{31}=10.4$ $d_{22}=16.6$ @ 10.6 μm	$d_{31}=12.34$ $d_{22}=19.70$	24.01 (eoe)	16.44	0.092 \perp c		65.63 (eoe)	3.35																																																											
BaGa ₄ S ₇ ^a $mm2$	XZ 10.47 (ooe)	4.99	1.68//x 1.58//y 1.45//z		3.54	$d_{31}=5.1$ @ 2.26 μm	$d_{31}=5.07$																																																																																																																																														
	BaGa ₄ Se ₇ m	YZ 33.47 (eoo)	~ 1	0.56–0.74				2.64	$d_{23}=20$ @ 1.8 μm	$d_{23}=18.14$ $d_{24}=3.70$																																																																																																																																											
XZ 45.68 (eoo)		~ 9.3																																																																																																																																																			
XZ 49.17 (eoo)		2.8		InPS ₄ $\bar{4}$	38.80 (eoo)	34.40	NA				3.2	$\delta_{31}=0.39$ $\delta_{36}=0.30$	$d_{31}=27.87$ $d_{36}=21.53$	42.67 (eoo)	23.87		Sn ₂ P ₂ S ₆ m	... (ssf) ^b	≈ 4	0.4–0.55	2.35 (fsf) ^b	≈ 2		GaS _{0.4} Se _{0.6} $\bar{6}2m$	22.31 (ooe)	45.80	1.3//c	2.4	$d_{22}=44.1$ @ 4.65 μm	$d_{22}=49.51$	24.67 (eoe)	40.88	10 \perp c	CdSiP ₂ ^a $\bar{4}2m$	80.46 (ooe)	90.99	13.6	2.2–2.45	$d_{36}=84.5$ @ 4.56 μm	$d_{36}=92.27$	AgGaGeS ₄ $mm2$	XZ 53.99 (ooe)	3.32	0.399	3.0	$d_{32}=6.2$ $d_{31}=10.2$ @ 1.064 μm	$d_{32}=5.65$ $d_{31}=9.30$	XY 35.74 (ooe)	5.43		Ag ₃ AsS ₃ ^a $3m$	22.04 (ooe)	22.89	0.113//c,	2.2	$d_{31}=10.4$ $d_{22}=16.6$ @ 10.6 μm	$d_{31}=12.34$ $d_{22}=19.70$	24.01 (eoe)	16.44	0.092 \perp c	65.63 (eoe)	3.35																																																																																				
InPS ₄ $\bar{4}$	38.80 (eoo)	34.40	NA		3.2	$\delta_{31}=0.39$ $\delta_{36}=0.30$	$d_{31}=27.87$ $d_{36}=21.53$																																																																																																																																														
	42.67 (eoo)	23.87																																																																																																																																																			
Sn ₂ P ₂ S ₆ m	... (ssf) ^b	≈ 4	0.4–0.55	2.35																																																																																																																																															
	... (fsf) ^b	≈ 2					GaS _{0.4} Se _{0.6} $\bar{6}2m$	22.31 (ooe)	45.80	1.3//c	2.4	$d_{22}=44.1$ @ 4.65 μm	$d_{22}=49.51$	24.67 (eoe)	40.88	10 \perp c	CdSiP ₂ ^a $\bar{4}2m$	80.46 (ooe)	90.99	13.6	2.2–2.45	$d_{36}=84.5$ @ 4.56 μm	$d_{36}=92.27$	AgGaGeS ₄ $mm2$	XZ 53.99 (ooe)	3.32	0.399	3.0	$d_{32}=6.2$ $d_{31}=10.2$ @ 1.064 μm	$d_{32}=5.65$ $d_{31}=9.30$	XY 35.74 (ooe)	5.43		Ag ₃ AsS ₃ ^a $3m$	22.04 (ooe)	22.89	0.113//c,	2.2	$d_{31}=10.4$ $d_{22}=16.6$ @ 10.6 μm	$d_{31}=12.34$ $d_{22}=19.70$	24.01 (eoe)	16.44	0.092 \perp c	65.63 (eoe)	3.35																																																																																																								
GaS _{0.4} Se _{0.6} $\bar{6}2m$	22.31 (ooe)	45.80	1.3//c	2.4	$d_{22}=44.1$ @ 4.65 μm	$d_{22}=49.51$																																																																																																																																															
	24.67 (eoe)	40.88	10 \perp c				CdSiP ₂ ^a $\bar{4}2m$	80.46 (ooe)	90.99	13.6	2.2–2.45	$d_{36}=84.5$ @ 4.56 μm	$d_{36}=92.27$	AgGaGeS ₄ $mm2$	XZ 53.99 (ooe)	3.32	0.399	3.0	$d_{32}=6.2$ $d_{31}=10.2$ @ 1.064 μm	$d_{32}=5.65$ $d_{31}=9.30$	XY 35.74 (ooe)	5.43		Ag ₃ AsS ₃ ^a $3m$	22.04 (ooe)	22.89	0.113//c,	2.2	$d_{31}=10.4$ $d_{22}=16.6$ @ 10.6 μm	$d_{31}=12.34$ $d_{22}=19.70$	24.01 (eoe)	16.44	0.092 \perp c		65.63 (eoe)	3.35																																																																																																																	
CdSiP ₂ ^a $\bar{4}2m$	80.46 (ooe)	90.99	13.6	2.2–2.45	$d_{36}=84.5$ @ 4.56 μm	$d_{36}=92.27$																																																																																																																																															
	AgGaGeS ₄ $mm2$	XZ 53.99 (ooe)	3.32				0.399	3.0	$d_{32}=6.2$ $d_{31}=10.2$ @ 1.064 μm	$d_{32}=5.65$ $d_{31}=9.30$																																																																																																																																											
XY 35.74 (ooe)		5.43		Ag ₃ AsS ₃ ^a $3m$	22.04 (ooe)	22.89	0.113//c,				2.2	$d_{31}=10.4$ $d_{22}=16.6$ @ 10.6 μm	$d_{31}=12.34$ $d_{22}=19.70$	24.01 (eoe)	16.44	0.092 \perp c	65.63 (eoe)	3.35																																																																																																																																			
Ag ₃ AsS ₃ ^a $3m$	22.04 (ooe)	22.89	0.113//c,		2.2	$d_{31}=10.4$ $d_{22}=16.6$ @ 10.6 μm	$d_{31}=12.34$ $d_{22}=19.70$																																																																																																																																														
	24.01 (eoe)	16.44	0.092 \perp c																																																																																																																																																		
	65.63 (eoe)	3.35																																																																																																																																																			

Table 2 (continued)

Crystal Point group	Plane θ/φ [°] (Interaction)	d_{eff} [pm/V]	Thermal conductivity [W/mK]	Band-gap E_g [eV]	Miller's δ [pm/V] or d_{il} [pm/V] @ λ_F for SHG	+Miller's correction [pm/V]
Ag ₃ SbS ₃ 3m	47.14 (ooe)	14.34	~0.1 //c,	2.2	$d_{31}=7.8$	$d_{31}=9.90$
	52.84 (eoe)	3.80	~0.09 $\perp c$		$d_{22}=8.2$ @ 10.6 μm	$d_{22}=10.41$

NA: not available.

^aCrystals for which OPO with $\sim 1 \mu\text{m}$ pump wavelength has been already demonstrated.

^bMore general notations outside the principal planes of biaxial crystals [5], angles and d_{il} components omitted for simplicity (...).

grown crystals, the surface (chemical) stability, and the damage resistivity of the anti-reflection (AR) coatings necessary when cavities are employed.

Some trends can be observed in the development of new non-oxide NLCs in the last decade, related to the development of SSL pump sources. The first one is in fact a rather old idea of doping or mixing binary or ternary NLCs to obtain new, more complex ternary NLCs such as GaS_xSe_{1-x} [59] or quaternary NLCs such as AgIn_xGa_{1-x}S(e)₂, Cd_xHg_{1-x}Ga₂S₄ or Ag_xGa_xGe_{1-x}S(e)₂ [54,60], see Fig. 10. Adding S to GaSe (possible only up to 40% since GaS exhibits a different symmetry) not only improves the thermo-mechanical properties (the same does In in Ga_{1-x}In_xSe) but increases the band-gap thus helping to avoid TPA at 1.064 μm (see Table 2). Mixing AGS(e) or HGS compounds with the isostructural but low-birefringence AgInS(e)₂ or CdGa₂S₄ crystals, respectively, permits NCPM with maximized d_{eff} . In decreases the band-gap and slightly improves the nonlinearity of AGS(e) crystals while Cd has the opposite effect on HGS. Indeed, the latter enables NCPM in Cd_xHg_{1-x}Ga₂S₄ at $\lambda_3=1.064 \mu\text{m}$ (Table 2). In-doping can shift the long-wave cut-off of AGSe, e.g., by $\sim 1 \mu\text{m}$ to longer wavelengths. Mixing AGS(e) compounds with GeS(e)₂ produces new orthorhombic (biaxial) structure, different from the chalcopyrite structure of AGS(e), and the resulting quaternary compounds (see Fig. 10) exhibit increased band-gap and improved damage resistivity. CdS_xSe_{1-x}, CdGe(As_{1-x}P_x)₂ and AgGa(Se_{1-x}S_x)₂ have also been studied; they are quaternary compounds isostructural to their parent ternary compounds and mixing permits to engineer band-gap, nonlinearity and birefringence (PM properties). CdS and CdGeP₂ do not possess enough birefringence for PM. Doping with P, similar to doping with S, shifts the transmission window to shorter wavelengths.

The main problem with such mixed crystals is the varying composition along the grown boule and also in radial direction. It seems that it is easier to achieve stable composition when the two parent compounds exhibit different crystallographic structure, e.g. Ag_xGa_xGe_{1-x}S(e)₂ and GaS_xSe_{1-x} (Figs. 10 and 11). An elegant way to utilize the variation of the composition for tuning of an OPO, has been demonstrated with Cd_xHg_{1-x}Ga₂S₄ and this experiment will be presented in Section 6.2.2.1 – the active element used is shown in the lower part of Fig. 10.

As already mentioned, one of the major limitations of non-oxide NLCs is related to the lower damage resistivity. Thus, another trend is the search for mid-IR compounds with wider band-gap. Considerable progress has been made with four such ternary chalcogenides, LiInS₂ (LIS), LiInSe₂ (LISE), LiGaS₂ (LGS), and LiGaSe₂ (LGSe) [61–64], see Fig. 11. In contrast to all other NLCs discussed so far which are uniaxial (except for Sn₂P₂S₆), the Li ternary compounds are biaxial (orthorhombic). They exhibit wider band-gap than their Ag-analogs (AGS, AGSe, etc.). Their wurtzite type structure leads to better thermo-mechanical and damage properties. However,

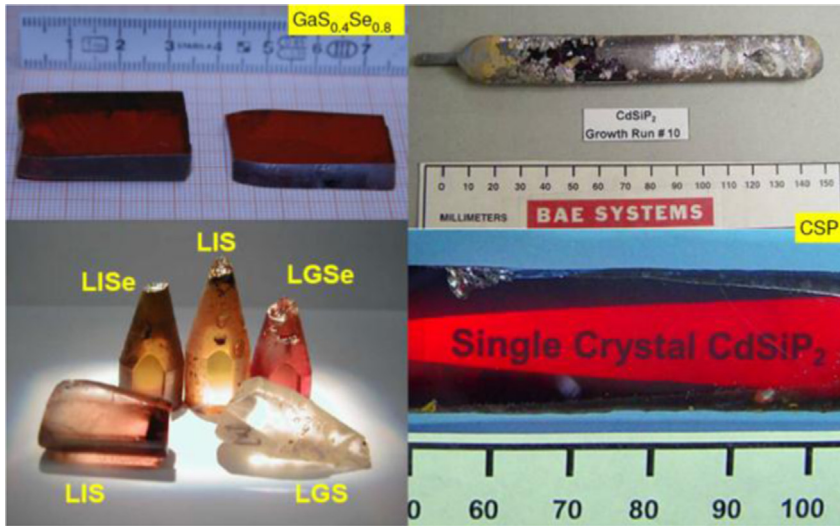


Fig. 11. Layered crystal of GaS_{0.4}Se_{0.6}, the maximum S-content maintaining noncentrosymmetric structure of the mixed compound (the transmission in the visible is obviously improved in comparison with GaSe), boule and polished sample demonstrating the transparency of CdSiP₂ (CSP) in the visible, ingots of orthorhombic Li-compounds after annealing, (courtesy of V. Panyutin, Kuban State University, P. Schunemann, BAE Systems, and L. Isaenko and A. Yelissev, Institute of Geology and Mineralogy).

the nonlinearity of the Li-compounds is lower compared to their Ag-analogs and their FMs are among the lowest, comparable to some oxide NLCs. Nevertheless, LGS, LIS, and LGSe are among the very few non-oxide NLCs that can be pumped by fs Ti:Sa laser systems operating near 800 nm without TPA. They also can be mixed in all combinations.

Two related compounds, BaGa₄S₇ (BGS) and BaGa₄Se₇ (BGSe), Fig. 10, were recently added to this group [65]. BGS is orthorhombic and also free of TPA at 800 nm, however, BGSe is monoclinic. Other properties are similar to their Li analogs but it seems that these crystals are easier to grow in larger sizes with reduced residual absorption in the clear transparency range.

Table 2 summarizes the properties of all non-oxide NLCs that can be phase-matched for down-conversion by birefringence at $\lambda_3 = 1.064 \mu\text{m}$ (Nd:YAG laser) with negligible TPA. For proper comparison, $\lambda_1 = 6.45 \mu\text{m}$ (target wavelength for surgical applications) is selected.

CSP (Fig. 11) occupies a unique position in Table 2 since it is the only crystal that can offer NCPM for a 1.064 μm pumped OPO with idler output in the 6 μm range. As can be seen from Fig. 9, CSP has a very high FM but its main limitation is the $\sim 6.5 \mu\text{m}$ upper wavelength limit which is the shortest in Table 2. The other crystals in Table 2 are mainly sulfides, however, among the wide band-gap Li- and Ba-compounds, there are also selenides and even LGT can be pumped at 1.064 μm without TPA.

At present, from the birefringent non-oxide NLCs, only AGS, AGSe, ZGP, GaSe, CdSe, TAS and Te can be considered to be commercially available (HGS, CGA, LIS, LSe, LGS and LGSe – available from some institutes in limited sizes/quantity).

The third and most important trend is the introduction of NLCs with cubic structure, which are transparent in the mid-IR. The zincblende semiconductors, such as the binary GaP, InP, GaAs, InAs, ZnSe, and few other phosphides, arsenides, antimonides, and chalcogenides, exhibit large nonlinear susceptibilities, very good thermal conductivity, higher purity levels, very low losses

when grown from the vapor phase, and good transparency well into the mid-IR as opposed to their ferroelectric oxide counterparts. However, their optical isotropy precludes birefringent PM, which has severely limited the applicability of these materials. Nevertheless, they had been used in the past for frequency conversion without PM. CdTe, which e.g., shows low dispersion and clear transparency up to 30 μm , was used for temporal diagnostics of ultrashort pulses by non-phase-matched SHG up to 37 μm [66]. In the mid-IR, such type of interaction is facilitated by the relatively long coherence lengths.

The chief obstacle to achieving QPM and NCPM in such materials is the process of creating a modulated structure from a non-ferroelectric material. A number of QPM techniques based on diffusion bonding of stacks of crystal plates with alternating orientation have been explored for such cubic crystals, but fabrication proved to be challenging, Fig. 12a. More recently, epitaxial growth of orientation-patterned structures of GaAs, with lithographically controlled patterns, has greatly opened the range of applicability of these materials [67]. The orientation-patterned crystal growth requires template for the growth of the structure, Fig. 12b. Molecular beam epitaxy (MBE) was used to grow a thin (5 nm) layer on a wafer which, under the proper growth conditions, had the opposite or “inverted” polarity relative to the substrate [67]. The resulting layer was then photolithography patterned with the desired grating structure for QPM, and alternating domains were etched down to the original substrate orientation. The wafer was then loaded into the MBE chamber for regrowth: layers which nucleate and grow on the etched-back gratings propagate the orientation of the original substrate, while those that grow on the inverted layer domains have the opposite polarity. The MBE or metal-organic vapor phase epitaxy (MOVPE) grown templates have a thickness up to a few microns. Alternatively, the wafer bonding method followed by the photolithography and etching steps, can be used to fabricate the template [68,69]. The templates are then used for growth by hydride vapor phase epitaxy (HVPE), a technique capable of much higher growth rates (over 200 $\mu\text{m}/\text{h}$) to produce bulk

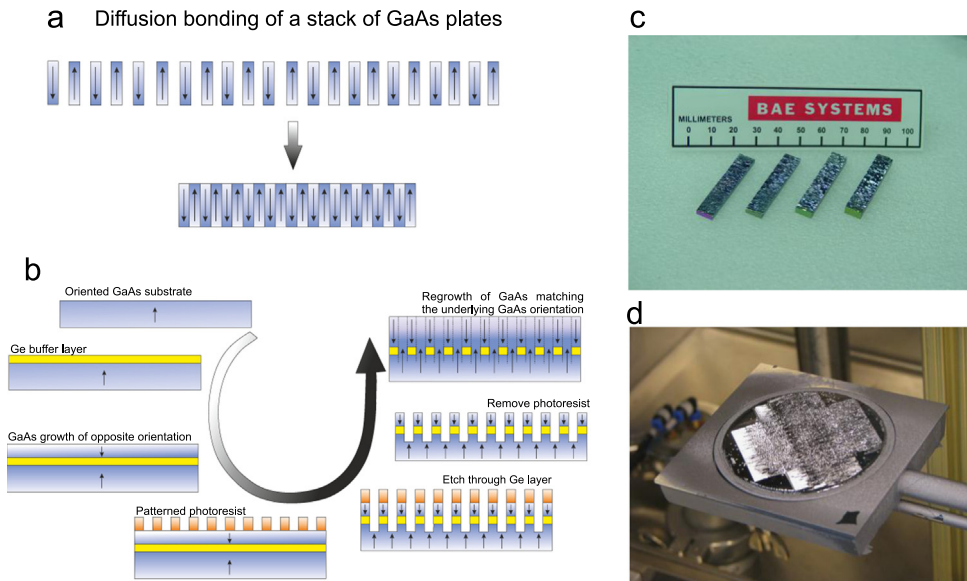


Fig. 12. Diffusion bonding of GaAs plates for QPM (a), procedure for fabrication of OPGaAs template (b), manufactured by HVPE OPGaAs elements with thickness of up to 3.5 mm (c), and HVPE grown, as removed from reactor multi-grating OPGaP on 3" wafer (d) (courtesy of P. Schunemann, BAE Systems).

Table 3

Important properties of cubic semiconductor NLCs investigated for QPM. A lot of data but also a lot of scatter in the values exist in the corresponding literature. The table is compiled on a best effort basis using some values from [70,71]. Only for GaAs the d_{14} value has been refined from SHG measurements with OPGaAs.

Crystal Point group	Transparency range [μm] at 3 cm^{-1} level	Thermal conductivity [W/mK]	Band-gap E_g [eV]	d_{14} [pm/V] SHG @ $10.6\ \mu\text{m}$	FM = $(2d_{14}/\pi)^2/n^3$ [pm^2/V^2]
GaAs $\bar{4}3m$	0.85–18.5	55	1.42–1.435 Direct	83–86	78–83
GaP $\bar{4}3m$	0.57–13.2	110	2.23–2.78 Indirect/direct	37	20.6
ZnSe (cubic form) $\bar{4}3m$	0.55–20	18–19	2.58–2.7 Direct	26.4	20

structures of orientation-patterned GaAs (OPGaAs) scalable to hundreds of microns (and ultimately several mm). The advantages of this process include the possibility to set the period by photolithography, the parallel fabrication process, the large sample lengths achievable and the short periods that are equally possible. The development profits from already mature processes including MBE, MOVPE, and HVPE; automated equipment for precision dicing and polishing; extremely high purity solid, liquid, and gas sources; low-cost, epi-ready substrates [70].

OPGaAs was the first material to demonstrate the potential of QPM semiconductors. In addition to it, the present interest is focused on GaN, GaP, and ZnSe. GaN exhibits the highest thermal conductivity but in view of its transparency range (not very different from LiNbO_3), its potential for the mid-IR is limited although highest damage threshold can be expected due to its large band-gap in the UV (nitrides are short-wavelength shifted compared to phosphides) [70]. Some relevant properties of GaAs, GaP, and ZnSe are compared in Table 3.

The thermal conductivity of GaAs and GaP is superior compared to all the birefringent non-oxide NLCs shown in Fig. 9. GaP and ZnSe exhibit lower nonlinearity compared to GaAs but they can be pumped at shorter wavelengths while TPA sets a lower limit of $1.73\text{--}1.75\ \mu\text{m}$ for GaAs (see Table 3) which is its only essential principle limitation [66]. Obviously GaP and ZnSe can be added then to Table 2 for $1\text{-}\mu\text{m}$ pumping. GaP and ZnSe in addition, due to lower dispersion, will require larger grating periods in QPM structures compared to GaAs. Unfortunately ZnSe lacks viable template technology. On the other hand much of the template and HVPE growth technology developed for OPGaAs can be directly applied to OPGaP with relatively straightforward modifications, which contributed to the faster advancement with OPGaP [72,73]. The state-of-the-art can be summarized as HVPE growth on $3''$ -wafers, excellent vertical domain propagation over few mm in OPGaAs (Fig. 12c) and $>0.5\ \text{mm}$ in OPGaP (Fig. 12d) with record low measured losses of $<0.5\%/ \text{cm}$ (OPGaAs).

In noncentrosymmetric NLCs of the cubic class, the high symmetry of the nonlinear tensor and the isotropy of the refractive index enable nonlinear interactions with an unusual variety of polarization combinations. As a result, they can be used in polarization-insensitive OPA or in OPA that is pumped with an unpolarized laser [67].

6. Down-conversion to the mid-IR using non-oxide nonlinear materials

Experimental results achieved on all times scales, from cw to ns and ultrashort (ps and fs) pulses will be reviewed here in this sequence.

Table 4

DFG of cw laser sources in non-oxide NLCs. ESEC: external signal enhancement cavity, ESPEC: external signal and pump enhancement cavity, IS: intracavity with respect to signal, TT: temperature tuning, DL: discrete lines, SFR: tunable spin flip Raman laser, NA: not available. Powers are not corrected for NLC Fresnel losses.

Crystal-type, $\theta(\varphi)_{\text{cut}}, \Delta$	L [mm]	Pump and Signal sources	λ_1 [μm], Bandwidth	Idler power @ Wavelength	Refs.
AGSe-I, NA	6	CO+CO ₂ , DL	12.2–13, 0.5 MHz	200 nW @ 12.2 μm	[74]
CGA-II, NA	9	CO+CO ₂ , DL	11.4–16.8, 0.5 MHz	4 μW @ 12.87 μm	[75]
CGA-II, 50°	10	CO+CO ₂ , DL	15.5–16.5, NA	2.5 W in 2 μs^a	[76]
Te-I, 0°	3	SFR+1/5 duty cycle CO ₂ , DL	~11, <300 MHz	10 μW^a	[77]
AGS-I, 90°	20	SF dye+SF dye	7–9, 0.5 MHz, NCPM	>1 μW @ 7–9 μm	[78]
AGS-I, 90°	15	SF dye+SF dye	7.8–9, <1.5 MHz, NCPM	~30 nW @ 8.4 μm	[79]
AGS-I, 90°	45	SF dye+SF Ti:Sa	4.76–6.35, <1 MHz, NCPM	~20 μW @ 5.26 μm	[80]
AGS-I, 90°	45	Ti:Sa+SF ampl. LD	~4.26, ~1 GHz, NCPM	47 μW / 89 μW in 50 μs^a	[81]
AGS-I, 90°	45	SF Ti:Sa+SF LD SF Ti:Sa+SF LD	4.73, ~30 MHz, NCPM 5.12, ~120 MHz, NCPM	1.4 μW 1.2 μW	[82]
AGS-I, 90°	5–5.5	SF LD+SF Nd:YAG/ESEC	4.73, ~120 MHz, NCPM	3.3 nW	
AGS-I, 90°	5–5.5	SF LD+SF Nd:YAG/ESEC	3.14–3.42, 0.5 MHz, incl. NCPM	6 μW @ 3.2 μm	[83,84]
AGS-I, 75°	5	Ti:Sa+Nd:YAG/IS	3.35–3.39, NA	>1 mW @ 3.39 μm	[85,86]
AGS-I, 74°	1	Ti:Sa+SF Nd:YAG/IS	3.1–4.3, NA	300 μW @ 3.2 μm	[86]
AGS-I, 90°	42.5	SF dye+SF Ti:Sa	3.8–6.2, <1 MHz, NCPM	17.4 μW @ ~4 μm	[87,88]
AGS-I, 90°	30	SF LD+SF LD	4.9–5.1, 360 MHz, NCPM, TT	100–200 nW	[89,90]
AGS-I, 90°	40	SF LD+SF LD	~4.76, <30 MHz, NCPM	>100 nW	[91,92]
AGS-I, 90°	25	SF dye+SF LD	4.95–5.21, ~30 MHz, NCPM	~15 nW	[93]
AGS-I, 43°	15	SF LD+SF LD/ESPEC	10.2, ~0.2 MHz	40 nW	[94]
AGS-I, 90°	15	SF LD+SF LD	4.76–4.86, NA, NCPM, TT	~7 nW	[95]
AGS-II, 50°	10	SF ampl. LD+SF ampl. LD	6.8–12.5, <4 MHz	1.3 μW @ 8 μm	[96]
AGS-II, 59°	10	SF Ti:Sa+SF ampl. LD	5–12.5, ~1.5 MHz	~55 nW @ 8.06 μm	[97]
AGSe-I, 65°	10	SF Nd:YAG+SF Er fiber ampl. LD	8.7, NA	~300 nW	[98]
AGSe-I, 90°	40	SF LD+SF LD	~7.2, ~60 MHz, NCPM	10 nW	[99]
GaSe-I, 0°	5	SF Ti:Sa+SF Ti:Sa	8–19, ~1 MHz	100 nW	[88,100,101]
GaSe-I, 0°	5	SF Ti:Sa+SF Ti:Sa	8.8–15, ~2 MHz	30 nW	[102]
GaSe-I, 0°	5	SF LD+SF LD	11.8–16.1, ~70 MHz	100 nW @ 12.5 μm	[103]
LIS-II, 42°	10	SF Ti:Sa+SF Ti:Sa	5.5–11.3, ~1 MHz	138 nW @ 6.7 μm	[63,104]
LISe-II, 55°	9	SF Ti:Sa+SF Ti:Sa	5.9–8.1, ~1 MHz	154 nW @ 6.7 μm	[63]
OPGaAs, 26.3 μm	19	SF LD+SF Er fiber ampl. LD	~7.9, <1 MHz, NCPM	38 nW	[105]
OPGaAs, 26.3 μm	19	SF Pr fiber ampl. LD+SF Er fiber ampl. LD	7.9–8.7, <1 MHz, NCPM, TT	2 μW	[106]

Table 4 (continued)

Crystal-type, $\theta(\varphi)_{\text{cut}}, \Lambda$	L [mm]	Pump and Signal sources	λ_1 [μm], Bandwidth	Idler power @ Wavelength	Refs.
OPGaAs, 38.6 μm	33	SF Er fiber ampl. LD+SF Tm fiber laser	7.6–8.2, NA, NCPM, TT	500 μW	[107]
OPGaAs, 63.5 μm	25.7	Tm fiber+OPO (idler)	6.46–7.517, 30 GHz, NCPM, TT	51.1 mW @ 6.79 μm	[108]

^aPeak powers in quasi-cw regime.

6.1. Down-conversion of cw radiation

Compared to the pulsed regime, parametric down-conversion of cw laser radiation offers ultra-narrow spectral bandwidths (down to the 100 kHz range) with SF operation possible, better frequency stability, and continuous scan options at the expense of lower conversion efficiency. It can be realized by DFG and OPO.

6.1.1. DFG of cw radiation

DFG has been realized in non-oxide NLCs with various, mostly SF pump sources but the conversion efficiency is extremely low, see Table 4. In general at least one of the input waves has to be tunable in order to obtain idler tunability but if NCPM is utilized and temperature tuning is not feasible, both input waves have to be tuned.

Tight focusing and long NLC are crucial for cw DFG. The first cw DFG with non-oxide NLC was reported in 1973, mixing discrete lines of SF CO and CO₂ lasers in AGSe to produce mid-IR radiation between 12.2 and 13 μm [74]. In the 1970s, such angle tuned critical PM in AGSe, CGA, and Te was used but from the beginning of the 1990s AGS and especially type-I (ooe) NCPM, with L up to 45 mm, became the primary choice [109]. In earlier experiments, pairs of two dye lasers or dye and Ti:Sa lasers were employed for mixing because NCPM requires typically relatively short input wavelengths (600–1100 nm). Later on all-SSL systems became available and two LDs, or (amplified) LDs and Ti:Sa lasers were mixed in AGS.

The bandwidth (resolution) achieved in the mid-IR when mixing two SF sources ranges from 1 to 100 MHz. It is determined by the convolution of the input bandwidths and as such depends on the time scale considered. The values in the literature and in Table 4 are often estimated from the specifications of the input sources which depend on their stability (time interval). Scans can be performed with one of the input wavelengths fixed because the DFG spectral acceptance is much larger, from 1 to 10 cm^{-1} (30–300 GHz), depending on the AGS crystal length. In the case of LDs also the mode-hop free tuning range should be taken into account. Broader spectral ranges ($> 70 \text{ cm}^{-1}$) can be covered with NCPM in type-I AGS by changing its temperature [90].

Typically the DFG powers in the mid-IR achieved with SF LDs were much less than 1 μW ; powers exceeding 1 μW were obtained by mixing different lasers. The highest power reported for SF operation mixing dye and Ti:Sa lasers was 20 μW at 5.26 μm [80]. Critical PM with type-I AGS was realized in external enhancement cavities or in intracavity (with respect to the signal) DFG; in these cases relatively short crystals could be employed. Powers exceeding 100 μW were obtained with AGS only with intracavity DFG schemes, however, not in SF regime, Table 4. The longest DFG wavelength reached with type-I AGS was 10.2 μm [94].

If angle tuning is necessary because the NCPM condition is not fulfilled for the available input sources, type-II (eoe) PM in AGS is preferable for its higher d_{eff} . Fig. 13 shows the results

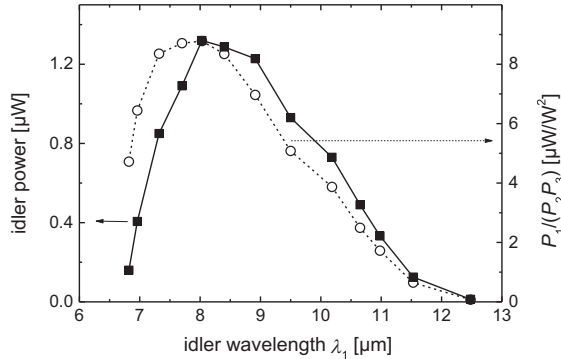


Fig. 13. Idler power and external conversion efficiency vs. idler wavelength for type-II DFG in AGS [96].

obtained when mixing two 500 mW amplified, tunable, SF (short-term bandwidth < 200 kHz) LDs in such a AGS ($L = 10$ mm) [96]. DFG tuning was possible for $6.8 < \lambda_1 < 12.5$ μm (the longest wavelength demonstrated with AGS). The maximum power was 1.3 μW at 8 μm . Piezoelectric scanning provided mode-hop-free electronic tuning range of 67 GHz (> 2.2 cm^{-1}), about three times smaller than the measured spectral acceptance bandwidth. Spectral resolution < 4 MHz was estimated taking into account the frequency jitter specifications of the LDs [96].

For extension to longer input wavelengths ($\lambda_3, \lambda_2 > 1.1$ μm) it was proposed to substitute AGS by AGSe [110] but longer idler wavelengths (up to 19 μm) were achieved in fact mixing two SF Ti:Sa lasers in GaSe [88]. PM is always critical in this crystal that can only be cleaved at $\theta = 0^\circ$ and the DFG powers did not exceed 0.1 μW . Other crystals employed for DFG with SF Ti:Sa lasers were LIS and LISe [62,63]. As with GaSe, angle tuning had to be used with them. Their essential advantage over AGS is the better thermal conductivity and damage resistivity. One of the problems observed with AGS is the low surface damage threshold with visible cw radiation (as low as 3 kW/cm^2 [78]). A major limitation for all crystals discussed above is the fact that temperature tuning is quite restricted and QPM is not feasible.

Narrowband mid-IR sources based on cw DFG in non-oxide NLCs were losing their importance in the 2000s. On the one hand, in the wavelength range up to 5 μm similar devices based on oxide materials, e.g., periodically-poled LiNbO₃ (PPLN), periodically poled KTiOPO₃ (PPKTP) and similar, delivered 1–2 orders of magnitude higher (\sim mW) DFG power while cw OPOs based on such materials produced even powers on the watt level. On the other hand, strong competition emerged from narrowband and tunable mid-IR QCLs [41] although a single device can tune only over a narrow range. The situation seems to change after the invention of OPGaAs. NCPM through QPM relaxes the constraints on the input wavelengths and $\lambda_3, \lambda_2 > 1.25$ μm were applied with OPGaAs. It is also possible to use unpolarized laser sources (from fibers) because of the cubic symmetry of GaAs. In the first such experiment, LDs (one of them amplified in Er-fiber) were mixed in a 0.5 thick OPGaAs ($L = 19$ mm) [105]. The system performance was subsequently improved, with two LDs amplified in Er- and Pr-fiber amplifiers before mixing them in a similar OPGaAs, tuning in the 8 μm range by both λ_3 and temperature [106]. Finally, output powers as high as 0.5 mW were obtained with tuning in the 7.6 – 8.2 μm range [107]. In this case, Er-fiber amplifier seeded by a LD and Tm-fiber laser-amplifier served as high power sources to be mixed in a 0.45 mm thick OPGaAs ($L = 33$ mm) crystal, Table 4. Without restriction to SF operation, powers > 50 mW (6.79 μm) were obtained in [108] using a 2.1 -mm thick OPGaAs ($L = 25.7$ mm) and mixing a Tm-fiber module with the idler of a cw OPO.

6.1.2. OPOs in cw regime

Much higher cw powers can be expected in principle from cw OPOs. However, for a long time, there was only a single demonstration of a cw OPO based on a non-oxide NLC [111]. Essential for this achievement was the NCPM in type-I AGS ($L = 15$ mm) and the tight focusing in the 30 mm long cavity consisting of two highly-reflecting (HR) concave mirrors with -5 cm radius of curvature (RC). The NCPM condition required rather short pump wavelength, $\lambda_3 = 845$ nm (from a SF, grating-tuned extended cavity GaAlAs LD with a typical short-term bandwidth of ~ 100 kHz and a tapered GaAlAs amplifier) and the resulting $\lambda_2 \sim 1.267$ μm and $\lambda_1 \sim 2.535$ μm were in the near-IR. The triple-band AR-coated AGS had $\sim 1\%$ /cm absorption loss at λ_3 and $\sim 0.5\%$ /cm loss at λ_2 . The (external) pump threshold power for this DRO with weak pump enhancement (weakly triply resonant OPO) was in the 60–70 mW range. The output power saturated at ~ 2 mW from each cavity side which corresponds to $\sim 2\%$ efficiency for 200 mW of pump power but only 5% of the SF output power was in the idler wave because of the much smaller residual transmission of the mirrors at 2.535 μm . Further studies of this OPO with different crystals and cavities [112,113] identified strong thermal effects due to residual absorption as the main limiting factor and confirmed that low intracavity losses ($\leq 1\%$ per round trip) are needed to balance the weak cw parametric gain.

The first mid-IR cw OPO based on a non-oxide NLC was reported in 2012 [114] but the progress was indeed impressive. The NLC used for this experiment was a 1.7 mm thick OPGaAs ($L = 39.9$ mm, $\Lambda = 63.5$ μm) designed for conversion of $\lambda_3 = 2.09$ μm to the mid-IR by temperature tuning across 20 to 100 $^\circ\text{C}$. It was AR-coated for the three wavelengths and pumped in SP. The master-oscillator power-amplifier (MOPA) laser source based on Ho:YAG was capable of up to 60 W average power with a beam quality factor of $M^2 \sim 1.3$. The oscillator also contained an etalon to narrow the spectral bandwidth to ~ 0.3 nm. The pump beam was focused to $2w_3 = 126$ μm in the centre of the OPGaAs crystal. The ring SP-SRO (~ 87 cm physical length) had a 2% OC for the signal while the idler was totally transmitted through one of the $\text{RC} = -10$ cm focusing mirrors surrounding the NLC. Threshold was measured near 11.5 W and maximum total (signal and idler) conversion efficiency of 23.6% occurred at 1.8 times threshold. At a pump level of 25 W the idler power exceeded 4 W at 4.7 μm for OPGaAs temperature of ~ 41 $^\circ\text{C}$. The idler spectral bandwidth amounted to 9.5 nm and the beam M^2 was ~ 1.4 [114]. The results clearly demonstrate the advantages of OPGaAs for cw OPOs, especially the superior thermo-mechanical properties and the low residual losses (0.4%/cm loss measured at 2.4 μm [114]).

6.2. Down-conversion of ns pulses

This part describes DFG experiments with ns input pulses, ns OPOs and some related OPAs in the ns regime. Some more exotic ns OPG experiments are included in [Section 6.3.3](#).

6.2.1. DFG of ns pulses

DFG with pulsed sources (e.g., Q-switched lasers generating ns pulses or free running lasers generating ns or μs pulses) is less demanding than OPO and less prone to optical damage because there is no resonated wave. Also much longer idler wavelengths were demonstrated, extending deep into the phonon absorption region of the NLC which is impossible in OPOs because of the decreasing parametric gain.

Some long pulse (μs) DFG experiments were included in [Table 4](#) but the pulsed temporal regime is most often accessed with Q-switched laser systems (oscillator or MOPA). The first ever DFG experiment in a non-oxide NLC from 1965 was without PM, utilizing the long coherence

length in CdS when pumped by a Q-switched Nd:glass laser near 1 μm [115]. The signal beam was derived from the same source via stimulated Raman scattering in C_6D_6 and the 944 cm^{-1} beat frequency detected behind the CdS crystal corresponded to $\lambda_1 \sim 10.6\ \mu\text{m}$. The first phase-matched DFG ($\lambda_1 = 4.9\ \mu\text{m}$, $10.1\text{--}12.7\ \mu\text{m}$) in a non-oxide NLC was reported in 1971 with type-I Ag_3AsS_3 ($L = 5\ \text{mm}$) mixing a Q-switched ruby laser and a gain-switched dye laser pumped by the same ruby laser [116]. Most of the earlier ns DFG experiments relied on combinations of a ruby or Nd:YAG with a dye laser, two dye lasers, dual-wavelength Nd:YAG or CO_2 lasers, using Ag_3AsS_3 , AGS, GaSe, CGA, and Te as NLCs. However, gain-switched dye lasers are characterized by build-up time which makes the synchronization between two of them or with the pump laser problematic. It was soon realized that mixing the output of an OPO offers synchronized in time signal and idler, and convenient tuning capability. Thus, in [117], the signal and idler pulses from a Ag_3AsS_3 DRO were mixed in a second Ag_3AsS_3 crystal. In the 1970s, ns OPOs based on Ag_3AsS_3 or LiNbO_3 were used for DFG in Ag_3AsS_3 , AGSe, CdSe, and GaSe. OPOs were pumped also at the second harmonic (SH) of the pump laser mixing the tunable idler output with the fixed wavelength fundamental in the DFG NLC [118].

In the following decades, the OPOs employed as sources for DFG were mostly based on LiNbO_3 [119–126] and KTiOPO_4 (KTP) [127–132] (type-II interaction in KTP provides narrower bandwidths for the mixing process). As the gain-switched lasers, these OPOs were pumped at the fundamental or SH by Q-switched SSLs. OPOs based on $\beta\text{-BaB}_2\text{O}_4$ (BBO) were pumped also at the third harmonic (TH) of Nd:YAG [133–135]. Nevertheless, the use of various gain-switched or pump and gain-switched laser combinations, such as ruby with dye [136], Nd with dye [121,137–141], two dye lasers [142], two Ti:Sa [143], alexandrite with color centre [144], Nd:YAG with Cr:forsterite [145,146] lasers, etc. continued and yielded also DFG energies on the μJ level. In the 2000s PPLN started to play a major role in the OPOs employed [147–153] though when larger apertures were required for power scaling, bulk LiNbO_3 and KTP remained the crystals of choice. The use of two independently tunable lasers [142–144,154], OPOs [148,151,153] or their combination [152] offers more flexibility with respect to PM, in particular for NCPM [151,154] or operation at a fixed angle [143,148,153].

Often, more complex approaches were needed to provide the suitable input wavelengths for DFG in non-oxide NLCs for which TPA is negligible, or to ensure the desired output wavelengths, energies or bandwidths. A MOPO was employed in [124] for narrowband operation where the first LiNbO_3 OPO, containing wavelength selective elements, injection seeded the second LiNbO_3 OPO, to produce the two wavelengths for DFG in AGSe. In [127], to achieve SF operation, the signal (700–920 nm) of a SF KTP OPO pumped by the SH of a SF Nd:YAG laser, was first amplified in a KTP NRO, generating radiation between 1.3 and 2.2 μm which was then used as a seed for a KTP OPA pumped by the fundamental, to produce the two input wavelengths for DFG in AGSe. A mixed approach without OPO was employed in [140] to achieve narrow and constant bandwidth: A tunable dye laser pumped by the SH of a Nd:YAG laser was first mixed with the fundamental to produce tunable radiation between 1.4 and 2.13 μm , which was amplified as a signal in a LiNbO_3 OPA, generating simultaneously idler radiation in the 2.13–4 μm range, and then both were used for DFG in AGS and CdSe. A similar approach was presented in [141]: The SH of an injection seeded Nd:YAG laser pumped a narrowband dye laser whose output was mixed with the fundamental to produce narrowband radiation between 2.5 and 2.74 μm , which was then amplified as an idler in a LiNbO_3 OPA, generating simultaneously signal radiation in the 1.74–1.85 μm range, and finally both were used for DFG in AGSe.

The DFG energy exceeded the 100 μJ level only in few of the systems described in the literature [122,124,125,128,138,139,141,145,152]. The bandwidth is determined by the input bandwidths

and typically varies from 0.5 to 50 cm⁻¹ (15 GHz–1.5 THz). These are the rough limits in standard OPO-DFG or related schemes when wavelength selective elements are present or not [120,123,125,140]. However, it is difficult to obtain narrow bandwidths with high (> 100 μJ) energy. Spectral narrowing of the OPO output, in relation to the spectral acceptance of the DFG process, was shown to increase the efficiency [124]: Thus injection seeding of the OPO helped to increase the energy at 7.5 μm from 380 to 630 μJ but the bandwidth was still 8 cm⁻¹ (240 GHz) in this case. The SF system described in [127] yielded a bandwidth of <1 GHz but it was rather complex and the output energy level was max. 100 μJ. Using synchronized narrowband laser sources without OPO it is easier to achieve narrower mid-IR bandwidths [143]. The system presented in [141] indeed combined narrow bandwidth of ~0.1 cm⁻¹ (3 GHz) with higher DFG energy (440 μJ at ~6.1 μm).

The highest DFG energies obtained on the ns time scale exceeded 1 mJ. 1.44 mJ at 10 Hz (λ₁=6 μm) were reported in [139] mixing the Nd:YAG pump laser and a near-IR dye MOPA in type-II AGS. Over 1 mJ at 5 Hz (λ₁=8.2 μm) were reported in [128] mixing the signal and idler pulses from a Nd:YAG laser pumped KTP OPO in type-I AGSe. 1.4 mJ at 10 Hz (λ₁=5.5 μm) were achieved in [145] mixing a Cr:forsterite gain-switched laser with a second Nd:YAG pump laser in type-II AGS. The record DFG energy so far was produced employing PPLN based OPO (with VBG and etalon for spectral narrowing) and OPA pumped by the same Nd:YAG laser in the one (pump) arm at 2.128 μm and a commercial narrowband system comprising a dye-laser pumped by the SH of another Nd:YAG laser, followed by DFG in LiNbO₃ in the second (signal) arm, tunable from 2.6 to 4 μm [152]: With type-I ZGP in the final DFG stage, 2 mJ at 10 Hz (λ₁=5.1 μm) were obtained with a bandwidth of 1.6 cm⁻¹, with tunability from 4.6 to 11.2 μm.

The repetition rate of ns DFG systems is usually low (1–50 Hz) in order to achieve higher energy, the “standard” being 10 Hz. In few cases operation at kHz repetition rates was described but without data on the DFG energy. In [153] DFG energy ~1.21 μJ at 8 μm was reported for a repetition rate of 4 kHz; this system was based on mixing the signal and idler outputs of two independent narrowband PPLN OPOs in type-I ZGP and was tunable from 7.27 to 10 μm.

The DFG tuning range depends on the NLC used, which included Ag₃AsS₃, CGA, Te, AGS, AGSe, ZGP, CdSe, LIS, and GaSe. DFG operation beyond the peaks of the multi-phonon absorption bands was reported for few of them, e.g., λ₁ > 18 μm in AGS [154], much longer than its “standard” limit of 10–12 μm, but this regime is accompanied by strong absorption and heating of the crystal, and tuning is not continuous. The typical long-wave limit for ZGP is similar while AGSe, GaSe and CdSe are used beyond ~10 μm. Longest wavelengths (typically > 20 μm) were mostly achieved with CdSe (transmitting up to ~25 μm) but the record of 38.4 μm was reached with GaSe due its 3-times higher nonlinearity [135]. Obviously, such operation in the deep absorption regime is only possible by DFG in a thin layer at the exit face of the crystal. It is very inefficient, by almost 4 orders of magnitude compared to idler wavelengths where the crystal shows good transmission. NCPM was exploited only in CdSe [133]; however, In-doped AGS is also interesting for NCPM and temperature tuning [155,156]. Some other doped NLCs with improved properties like S-doped GaSe were also studied [142]. In a few cases, dual-crystal set-ups were used [145,152], in a spatial walk-off compensation scheme. Finally, the first application of GaAs for DFG was with diffusion bonded stacks (DBGaAs) in third order QPM, mixing the idler outputs of two independently tunable 20 kHz PPLN OPOs [151] or the signal and idler of a 50 Hz LiNbO₃ OPO [126] to generate λ₁ > 10 μm under NCPM.

Some DFG experiments mixing CO₂ and CO lasers to produce discrete mid-IR lines were included in Table 4. With synchronous Q-switching the efficiency can be greatly enhanced. Such DFG in GaSe and AGSe was reported in [157], reaching idler wavelengths as long as 16.57 μm.

DFG can be used to convert an optical vortex, i.e. beam carrying orbital angular momentum, from the near- to the mid-IR. With ns pulses at 50 Hz, an optical vortex created at 1.064 μm was converted to the 6.3–12 μm range by DFG in ZGP using a KTP OPO intermediate stage [158].

Angle/temperature DFG tuning is too slow for some real time applications. Rapid random-access switching and continuous tuning in the mid-IR (5–12 μm) were achieved by DFG in AGS with electronically tuned dual-wavelength pulsed Ti:Sa lasers applying an acousto-optic tunable filter (AOTF) [159]. The technique was later extended to kHz repetition rates [156,160,161].

As already explained, there is no strict borderline between DFG and OPA. In DFG experiments, often only the generated idler is characterized and the gain experienced by the signal, which is low for ns pulses, is not evaluated. Gain estimations are complicated by the fact that it is difficult to know the actual seed energy, which depends on spatial and temporal overlaps. In this section, the designations in the cited literature were followed concerning DFG. True OPA experiments with ns pulses will be mentioned in the next sections since some of them are closely related to a combination with an OPO, i.e. they present parametric MOPA.

6.2.2. OPOs in ns regime

OPOs are typically pumped by Q-switched (often amplified) or gain-switched lasers generating ns pulses. Pulsed flash-lamp pumping was employed in the past with electro-optic Q-switching providing typically 5–10 ns pulses, e.g., from Nd:YAG lasers, at repetition rates of the order of 10 Hz (typically <50 Hz), or cw pumping with acousto-optic Q-switching providing 50–400 ns pulses at 1–30 kHz. Modern commercial LD-pumped systems operate typically at repetition rates from 0.1 up to 300 kHz and are cw pumped though amplifier modules normally require pulsed pumping. Pulse durations vary from few ns to ~ 100 ns depending on the repetition rate.

6.2.2.1. OPOs pumped near 1 μm . The shortest wavelength at which ns OPOs based on non-oxide NLCs can be pumped without the onset of TPA is about 1 μm , corresponding to Nd- or Yb-laser systems. This is simultaneously a very desirable pump wavelength range because exactly such Nd-laser based systems are most advanced at present and offer power scaling through LD-pumping. However, at the same time, TPA represents a more stringent limitation on the choice of non-oxide NLCs at such short wavelengths. Until now all such OPOs were pumped by Nd-lasers, see Table 5 [162].

The list of NLCs successfully employed in $\sim 1\text{-}\mu\text{m}$ pumped OPOs is quite short, see Tables 2 and 5, the main reason for this is that often damage threshold is lower than OPO threshold. In the first demonstrations from the beginning of the 1970s, Ag_3AsS_3 was the crystal of choice and in fact it was only the very first report [163] in which 2 kHz repetition rate was used – cumulative surface damage problems made it necessary to further operate such systems mostly at 10 Hz. Only in these early attempts was it necessary to employ a DRO in order to reach the threshold. Further realizations relied on SROs, predominantly with double pump pass indicated as DP in Table 5, to reduce the threshold, and more rarely with SP. The pump pulse duration of the Nd-lasers used for pumping was mostly in the 10–30 ns range (with longer pulses it becomes increasingly difficult to reach threshold before surface damage occurs) and in most of the cases the pump was in the TEM_{00} fundamental mode but not SF.

AGS successfully substituted Ag_3AsS_3 in subsequent experiments (Table 5) offering better thermal conductivity and availability. The highest idler energy obtained with AGS reached 1.2 mJ at 8.2 μm for a repetition rate of 3.3 Hz [168]. The substantially higher FM of HGS compared to AGS, Fig. 9, allowed one to use active elements as short as 6 mm while for AGS the

Table 5

OPOs based on non-oxide NLCs pumped by ns Nd-lasers near 1 μm . Except for [163,164] all other OPOs are SROs. SP/DP: single/double pump pass, ND: near degeneracy, TT: temperature tuning, NA: not available.

Crystal-type, $\theta(\varphi)_{\text{cut}}, \text{A}$	L [mm]	Pump source: λ_3 , duration, repetition rate, pump mode	λ_1 [μm]	Idler energy @ Wavelength	Refs.
Ag ₃ AsS ₃ -I, 30°	3.8	1.064 μm , 200 ns, 2 kHz, SP, TEM ₀₀	ND	NA	[163]
Ag ₃ AsS ₃ -I, 29.5°	10	1.065 μm , 26 ns, 2 Hz, SP, TEM ₀₀ , SF	2.13–2.56	> 10 μJ	[164]
Ag ₃ AsS ₃ -I, 28°	10	1.065 μm , 25 ns, 2 Hz, SP, TEM ₀₀	2.13–8.5	< 2.5 μJ @ 4.5 μm	[165]
AGS-I, 50.5°	20	1.064 μm , 20 ns, 10 Hz, SP, TEM ₀₀	2.128–4	250 μJ @ 2.128 μm	[166]
AGS-I, 49°	20	1.064 μm , 10.9 ns, 10 Hz, DP	2.77–4.2	120 μJ @ 3.5 μm	[167]
AGS-II, 39.9°	25	1.064 μm , 10 ns, 3.3 Hz, DP	6.7–9.8	1.2 mJ @ 8.2 μm	[168]
AGS-II, 45.1°	20	1.064 μm , 20–30 ns, 10 Hz, DP, TEM ₀₀	3.9–11.3	372 μJ @ 6 μm	[169]
AGS-I, 47°	20	1.064 μm , 10–30 ns, < 10 Hz, DP, TEM ₀₀	2.6–5.3	620 μJ @ 4 μm	[170– 172]
HGS-II, 67.5°	8	1.064 μm , NA, 10 Hz, DP	~ 3.7–4.5	NA	[173]
HGS-II, 67.5°	8	1.064 μm , 5 ns, 30 Hz, DP	4.18–4.311, TT	2.67 mJ @ 4.18 μm	[174]
HGS-I, 52°	6	1.064 μm , 30 ns, 10 Hz, SP, TEM ₀₀	2.3–4.4	360 μJ @ 2.37 μm	[175]
HGS-I, 52.7°	10.1	1.064 μm , 4.5 ns, 20 Hz, SP	3.69–5.69	3.3 mJ @ 4.03 μm	[176]
HGS-I, 52.7°	13.4	1.064 μm , 8 ns, 100 Hz, DP	2.8–8.1	6.1 mJ @ 4.03 μm	[177]
HGS-I, 52°	6	1.064 μm , 15 ns, 10 Hz, DP, TEM ₀₀	3.75–4.65, TT	< 250 μJ @ 4.3 μm	[178]
HGS-II, 50.2°	10.76	1.064 μm , 8 ns, 10 Hz, DP	4.5–9	3 mJ @ 6.3 μm	[179]
HGS-II, 50.3°	13.4– 17.9	1.064 μm , 8 ns, 10 Hz, RISTRA	6.3	0.8 mJ @ 6.3 μm	[180]
Cd _x Hg _{1-x} Ga ₂ S ₄ -I, $x=0.21$ – 0.56 , 74–90°	10.9– 11.6	1.064 μm , 22–30 ns, 10 Hz, SP, TEM ₀₀	2.85–8.9, in part NCPM	400 μJ @ 3.03 μm 270 μJ @ 5.76 μm 110 μJ @ 8.9 μm	[181, 182]
LISe-II, 72°	17	1.064 μm , 10 ns, 10 Hz, DP	3.34–3.82	92 μJ @ 3.457 μm	[183]
LISe-II, 41.6°	17.6	1.064 μm , 14 ns, 100 Hz, DP	4.65–7.5	282 μJ @ 6.514 μm	[184– 186]
LISe-II, 34°	24.5		5.45–8.7	116 μJ @ 8.428 μm	[186]
CSP-I, 90°	8	1.064 μm , 14 ns, 10–20 Hz, DP	6.2, NCPM	470 μJ @ 6.193 μm	[187]
CSP-I, 90°	9.5	1.064 μm , 1 ns, 1 kHz, DP	6.117–6.554, NCPM, TT	24 μJ @ 6.125 μm	[188]
CSP-I, 90°	7	1.064 μm , 0.4 ns, 1–10 kHz, DP, TEM ₀₀ , SF	6.15	4.3 μJ @ 6.137 μm	[189]
CSP-I, 90°	9.5	1.064 μm , 14 ns, 100 Hz, RISTRA	6.125, NCPM	64 μJ @ 6.125 μm	[190]
LGS-II, 40.6°	8	1.064 μm , 8 ns, 100 Hz, DP	5.46	134 μJ @ 5.46 μm	[191]
LGS-II, 40.6°	8.2	1.064 μm , 1 ns, 1 kHz, DP	4.046–6.014	1.1 μJ @ 5.46 μm	[191]
BGS-I, 9.2°	14.05	1.064 μm , 8 ns, 100 Hz, DP	5.5–7.3	483 μJ @ 6.217 μm	[192]
OPGaP, 20.8 μm	16.5	1.064 μm , 3.3 ns, 10 kHz, SP	4.591–4.876, NCPM, TT	0.4 μJ @ 4.624 μm	[193]

crystal length as a rule was 20 mm (Table 5). In [174,176] single pulse energy as high as 2.67 and 3.3 mJ at 30 and 20 Hz, respectively, was achieved with HGS OPOs near 4 μm . Indeed, most of the reported AGS and HGS OPOs generated rather short idler wavelengths, with one exceptional case of impressive tunability from 3.9 to 11.3 μm in [169] with AGS at 10 Hz.

Recently, the performance of HGS-based OPOs was greatly improved using a LD-pumped laser at 1.064 μm [177,179]. The pump system comprised a Q-switched Nd:YAG laser and amplifier, with a bandwidth of 30 GHz (1 cm^{-1}) and $M^2 \sim 1.4$. The laser emitted pulses of 8 ns duration at 100 Hz with energy as high as 200 mJ but an external shutter could reduce the repetition rate. A telescope expanded the pump beam to a diameter of $2w_3 = 9.6$ and 8.45 mm in

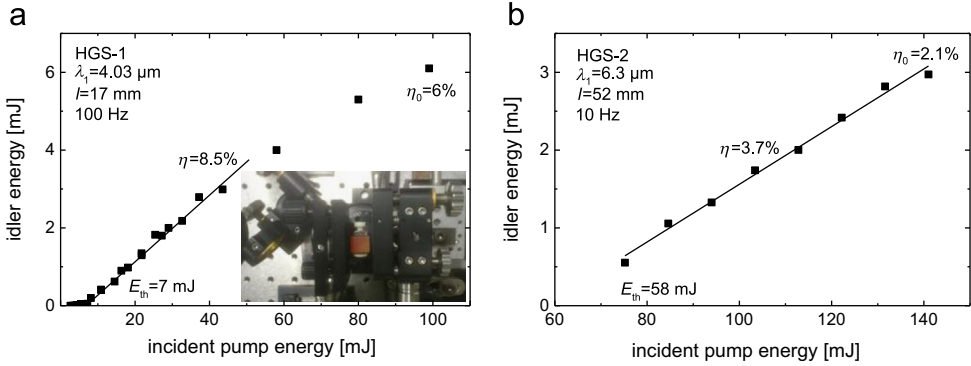


Fig. 14. Input–output OPO characteristics for HGS-1 (a) and HGS-2 (b). In this and all following figures l is the cavity length, η_0 is the idler conversion efficiency at maximum pump level, η is the slope efficiency determined from a linear fit, and E_{th} is the extrapolated pump threshold from this linear fit. The inset in (a) shows a photograph of the HGS-1 OPO from above with the NLC in the centre between the two cavity mirrors and the bending mirror on ZnSe substrate seen on the left, see Fig. 7b.

the two planes, respectively. The HGS samples used were a 13.4-mm-long one with an aperture of $\sim 10 \times 13.6 \text{ mm}^2$ cut at $\theta = 52.7^\circ$ and $\varphi = 45^\circ$ for type-I (ooe) interaction in the 4- μm idler range (HGS-1), and a 10.76-mm-long one with an aperture of $\sim 9.5 \times 9.5 \text{ mm}^2$, cut at $\theta = 50.2^\circ$ and $\varphi = 0^\circ$ for type-II (eoe) interaction in the 6.3- μm idler range (HGS-2), in both cases utilizing only the d_{36} component of the nonlinear tensor. Type-II HGS has higher d_{eff} (Table 2). Both HGS crystals were AR-coated for the resonated signal but showed low residual reflectivity also for the pump.

The linear SRO was built according to the retro-reflection scheme for all waves (see Fig. 7b). The OC was partly transmitting for the signal wave as well, in order to avoid crystal damage. There were some differences in this mirror and in the cavity length l for the two cases discussed below, Fig. 14. For HGS-1, the plane OC had a transmission of 29% at the signal and 79% at the idler wavelength. The OC used with HGS-2 had $RC = -2 \text{ m}$ and transmission of $\sim 30\%$ for the signal wave and 92% for the idler, and was AR-coated on its rear surface for improved idler extraction. In this case the OPO cavity was also lengthened, for better output beam quality.

Input–output characteristics at normal incidence are shown in Fig. 14. Since the experimental OPO threshold depends on the detection, extrapolated pump threshold values E_{th} from a linear fit of the input–output curves (slope efficiency η) are used for better comparison of the results. The extrapolated threshold with HGS-1 in the 4 μm idler range (Fig. 14a) corresponds to an axial pump fluence of 22 mJ/cm^2 or a peak intensity of $\sim 2.7 \text{ MW/cm}^2$. This is a much lower value than with HGS-2 which can be attributed to the higher parametric gain closer to degeneracy, the shorter cavity and the longer crystal. The extrapolated threshold at 6.3 μm with HGS-2 (Fig. 14b) corresponds to an axial pump fluence of $\sim 180 \text{ mJ/cm}^2$ or a peak intensity of $\sim 23 \text{ MW/cm}^2$.

Although highest idler energies (of any 1- μm pumped non-oxide OPO) were obtained, as shown in Fig. 14a, and damage-free operation far above (> 10 times) threshold was possible with the HGS-1 OPO, maximum conversion to the idler of $\sim 7.5\%$ occurred in fact around 40 mJ pump energy (compared to $\eta_0 = 6\%$ at maximum pump level) which indicates that yet higher output idler energies and average power could be possible with larger apertures of the NLC. The peak intensity applied (see Fig. 14a) did not exceed 40 MW/cm^2 (axial pump fluence of 320 mJ/cm^2). At highest pump levels some depletion of the pump in its maximum occurred.

The idler energy presented in Fig. 14b is the highest for such a 1- μm pumped OPO above 5 μm (the upper limit of oxide NLCs). No saturation is seen due to back conversion because it was impossible to reach 3-times above threshold operation. The maximum pump level applied was higher, axial fluence of 442 mJ/cm^2 or peak intensity $\sim 55 \text{ MW}/\text{cm}^2$, and the conversion efficiency was lower compared to HGS-1. Operation was safe for HGS-2 only at lower (10 Hz) repetition rates. Damage developed immediately at 100 Hz for pump levels > 2 times threshold.

Angle tuning showed excellent agreement with calculations, from $\lambda_1 = 2.8$ to 8.1 μm (HGS-1) and from $\lambda_1 = 4$ to 9 μm (HGS-2), see Fig. 15. Typical pulse durations were ~ 5 ns at 4 μm (HGS-1) and ~ 7 ns at 6.3 μm (HGS-2). The spectral bandwidth was measured only for the signal pulses: 1.9 cm^{-1} at 1.446 μm (HGS-1) and $\sim 2.3 \text{ cm}^{-1}$ at 1.28 μm (HGS-2). The M^2 factor, measured for the idler, was in the range 180–190 in the two planes for HGS-1 and improved to ~ 30 with the longer cavity used for the HGS-2 OPO.

The solid solution $\text{Cd}_x\text{Hg}_{1-x}\text{Ga}_2\text{S}_4$ should possess even higher potential than HGS because it exhibits better damage resistivity [195] although the FM is unchanged. The main problem with it is the control of the homogeneity in the growth process [54]. Nevertheless, this solid solution enabled for the first time NCPM in a ~ 1 - μm pumped mid-IR OPO [181,182], which is possible with AGS or HGS only at shorter pump wavelengths where TPA will be detrimental.

The 11-mm thick, AR-coated for the signal wave active element shown in Fig. 10, was studied with 22 ns long pump pulses at 1.064 μm , see Fig. 16. The aperture of the $\text{Cd}_x\text{Hg}_{1-x}\text{Ga}_2\text{S}_4$ sample ($\theta = 90^\circ$, $\varphi = 45^\circ$) was 30.6 mm \times 8 mm with the composition varying from $x = 0.21$ to 0.25 along the 30.6 mm y -dimension (parallel to the crystal c -axis). The SP-SRO was linear with both plane mirrors reflecting $> 95\%$ at λ_2 , and parametric amplification took place only in forward direction so that the generated idler was completely extracted by the OC. With $2w_3 = 2$ mm, the OPO threshold in Fig. 16a corresponds to an axial pump fluence of $\sim 250 \text{ mJ}/\text{cm}^2$ or a peak intensity of $\sim 11 \text{ MW}/\text{cm}^2$. The maximum axial pump fluence applied was 580 mJ/cm^2 (peak intensity $> 26 \text{ MW}/\text{cm}^2$). The asymmetry in the idler spatial distribution (insets Fig. 16a) was likely due to different angular acceptance with respect to θ and φ . The scatter of the measured energy and slope efficiencies in Fig. 16b in dependence on the position y indicates rather smooth variation of the crystal composition except for one of the end positions. Translation of the crystal over a range from $y = 0$ to 28 mm permitted smooth tuning of λ_1 from 2.85 to 3.27 μm (Fig. 16b).

In the last decade, using LD-pumped Nd-laser systems, few new NLCs were employed for the first time in SROs. On the first place LISe, the compound with the highest nonlinear coefficient

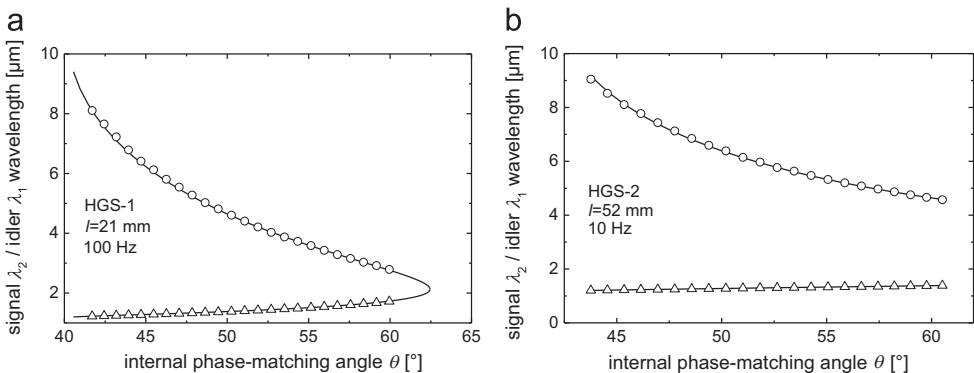


Fig. 15. Experimental signal (triangles) and idler (circles) OPO wavelengths vs. internal PM angle θ compared with calculations (lines) based on Sellmeier equations [194] for type-I (a) and type-II (b) HGS.

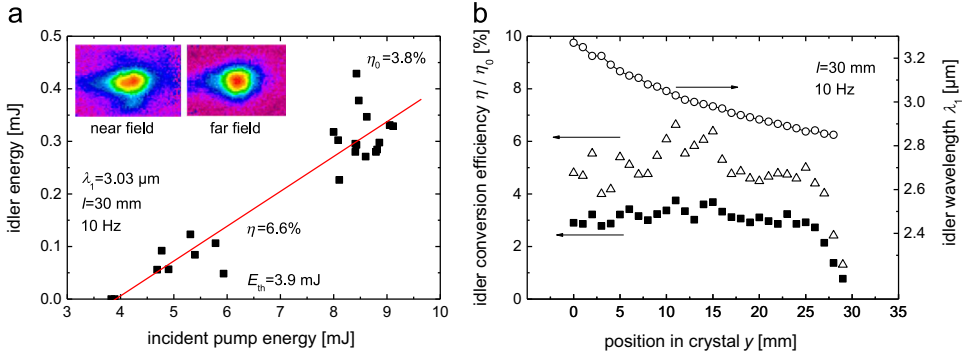


Fig. 16. Idler vs. pump energy of the tunable $\text{Cd}_x\text{Hg}_{1-x}\text{Ga}_2\text{S}_4$ -OPO for crystal position corresponding to $y=11$ mm (measured along the 30.6 mm dimension) (a). The insets show the spatial distribution of the idler intensity. Idler wavelength (circles), conversion efficiency η_0 (squares) and slope efficiency η (triangles) vs. position y (b). (Courtesy of K. V. Mitin, ASTROPHYSICA, National Center for Laser Systems & Complexes, from [181]).

of the four wide band-gap orthorhombic crystals belonging to this family, was studied, see Table 2 and Fig. 11. The idea was to demonstrate advantages over AGS due to better thermal conductivity and damage threshold and the initial results were quite promising, Table 5 [183–186]. Maximum energies of 282 μJ at 6.514 μm and 116 μJ at 8.428 μm , were achieved at a repetition rate of 100 Hz. The idler conversion efficiency in the 6- μm wavelength range was comparable to HGS. Although the output idler energy was much lower, compared to HGS, the maximum average idler power of ~ 28 mW was very similar due to the 100 Hz repetition rate. In comparison to AGS (operating at 10 Hz, restricted by cumulative damage) the improvement in terms of average power was 7-fold [168,169]. With two different LISe samples, tunable OPO operation was achieved from $\lambda_1=4.7$ to 8.7 μm for the idler.

Unfortunately, the surface chemical instability hampered the development of reproducible AR-coatings and surface damage problems always limited the performance of LISe OPOs. This shifted the interest to LGS [191] and BGS [192], which exhibit the largest band-gaps (Table 2), are colorless (Fig. 10), and possess much higher damage threshold than LISe, AGS or HGS, exceeding 3 J/cm^2 in terms of axial fluence at 1.064 μm for 14 ns long pulses, i.e. peak intensity > 200 MW/cm^2 . OPO operation was achieved with both of them although d_{eff} is roughly two times lower compared to LISe (Table 2). However, the OPO threshold was quite high for $L < 10$ mm [191] and operation far above threshold was impossible because of damage to the cavity optics. Thus, the main challenge for LGS and BGS will be the availability of samples longer than 20 mm for higher parametric gain. At present the development of BGS seems faster (in terms of sizes and reduction of residual losses) and notwithstanding the low idler conversion efficiency the maximum energy obtained with ~ 14 -mm long BGS reached 483 μJ at 6.217 μm which translates into an average power of ~ 48 mW at 100 Hz [192]. The idler tunability of the BGS OPO extended from ~ 5.5 to ~ 7.3 μm . No surface damage was observed in BGS for axial pump fluence exceeding 440 mJ/cm^2 (peak intensity > 55 MW/cm^2) [192].

An important milestone in 1- μm pumped OPO development has been the introduction of CSP [187–189], the first and only NLC which, without being a solid solution, enabled NCPM for type-I (ooe) configuration ($\theta=90^\circ$, $\varphi=45^\circ$). In this configuration the idler wavelength falls luckily in the spectral range just before the onset of multi-phonon absorption at ~ 6.5 μm which is interesting for medical applications and where fine tuning is possible by temperature. The first such CSP sample available for an OPO test had a length of 8 mm and an aperture of 6 mm (along

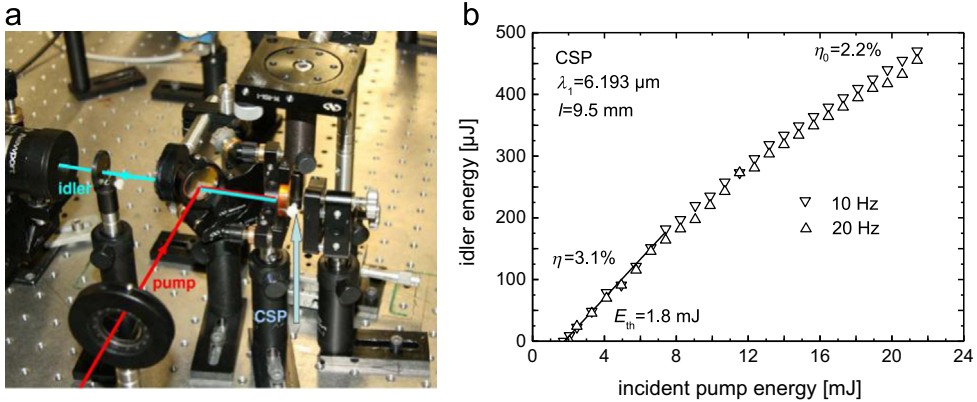


Fig. 17. Photograph showing the compact NCPM CSP OPO pumped by 14-ns pulses at 1.064 μm and the beam path of the pump and idler following the design shown in Fig. 7b (a), and idler energy vs. pump energy at normal incidence for two repetition rates (b).

the c -axis) \times 6.75 mm. It was AR-coated for all three wavelengths. The compact SRO cavity was 9.5 mm long and the OC had a transmission of 20% at the signal and 75% at the idler wavelength, see Fig. 17a. The pump system was similar to the one used for pumping HGS, see Fig. 14, but with duration of 14 ns and higher M^2 , while $2w_3 \sim 3.8$ mm in the position of the NLC.

The OPO threshold in Fig. 17b corresponds to an axial pump fluence of ~ 32 mJ/cm² which translates into a peak intensity of only ~ 2.3 MW/cm². The maximum idler energy measured at 10 Hz repetition rate was 470 μJ at 6.193 μm , Fig. 17b [187]. However, this was the maximum pump level (~ 377 mJ/cm² axial fluence or ~ 27 MW/cm² peak intensity) that could be safely applied, slightly above it surface/AR-coating damage was observed. The maximum average idler power amounted to 9.1 mW at 20 Hz. The slightly degrading OPO performance at 20 Hz could be attributed to residual crystal absorption at 1.064 μm . The input-output OPO characteristics in Fig. 17b show no real saturation and power scaling can be expected even without increasing the pump beam diameter. The OPO threshold is very low but the slope efficiency is low, too. The limiting factor for CSP at present is the low damage resistivity which is the major aspect that has to be improved in the future because it seems to be a defect related feature [196]. The spectral bandwidth of the CSP OPO at 1.285 μm (signal) amounted to ~ 1.7 cm⁻¹.

Furthermore, CSP enabled two innovations [188]: (i) the exceptionally high FM (Fig. 9) permits the use of rather short crystal/cavity lengths, and consequently pumping with relatively short pump pulses, achieving, for the first time with any OPO, sub-ns signal and idler pulse durations, (ii) the good thermo-mechanical properties (Table 2) enabled for the first time stable and long term kHz repetition rate operation with a non-oxide NLC pumped at 1.064 μm . The 90°-cut CSP used had the same AR-coating and aperture as the one described before but $L=9.5$ mm. The SRO cavity was only slightly longer, $l=10$ mm, but the cavity mirrors were the same. This SRO was pumped by a Q-switched 1 ns, 1 kHz Nd:YVO₄ microlaser, amplified in a cw pumped Nd:YVO₄ regenerative amplifier and a double pass Nd:YAG post amplifier. Maximum energy of 1.15 mJ at 1.064 μm was incident on the CSP sample at $2w_3 \sim 3$ mm.

In these conditions, the extrapolated SRO threshold (Fig. 18a) corresponded to an axial pump fluence of 10.8 mJ/cm² or a peak intensity of 10.8 MW/cm². The maximum idler energy reached 24 μJ at 6.125 μm which translates into an average power of 24 mW at 1 kHz. Temperature

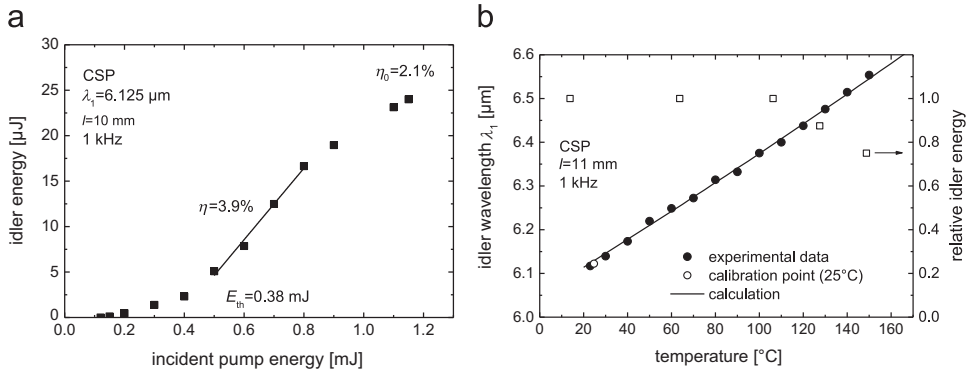


Fig. 18. Input-output characteristics of the NCPM CSP OPO pumped by 1 ns, 1 kHz, 1.064 μm pulses at room temperature (a), and temperature tuning: experimental data (symbols) and calculation using the Sellmeier equations from [197] (line) (b). Note that the thermo-optic coefficients in [197] were refined using these experimental data.

tuning is feasible for CSP providing an extension of the NCPM range to the long-wave transmission limit, which covers $\lambda_1 = 6.45 \mu\text{m}$, essential for surgical applications. Thus, λ_1 changed from 6.117 to 6.554 μm when the crystal was heated from room temperature to 150 $^\circ\text{C}$, Fig. 18b. The spectral bandwidth was 1.8 cm^{-1} at $\lambda_2 = 1.288 \mu\text{m}$. The output idler energy was almost constant when changing the temperature, slightly decreasing above 6.4 μm , partially due to the idler absorption. The signal pulse duration amounted to 0.75 ns, shorter, as expected, than the pump pulse duration and the idler pulse duration should be similar [188]. Moreover, CSP seems to be more damage resistant at such short pump pulse durations. No damage was observed up to the maximum applied axial pump fluence of $\sim 32 \text{ mJ/cm}^2$ (peak intensity $\sim 32 \text{ MW/cm}^2$).

These studies were extended to even shorter pump pulses [189]. A 7-mm long 90° -cut CSP crystal (same aperture and AR-coating) was pumped in an 8-mm long SRO cavity with $\sim 0.4 \text{ ns}$ pulses at 1.064 μm . The OC transmitted 93% at the idler wavelength, reflecting $\sim 70\%$ at the signal wavelength. The pump source for this experiment was SF, single mode ($M^2 = 1.1$), LD-pumped laser system consisting of a gain-switched/passively Q-switched $\text{Cr}^{4+}:\text{YAG}/\text{Nd}^{3+}:\text{YAG}$ oscillator and a double pass, side-pumped $\text{Nd}^{3+}:\text{YVO}_4$ bounce amplifier. The repetition rate could be varied from 1 to 10 kHz through the pulsed regime of the pump LDs. The pump beam had $2w_3 \sim 1.16 \text{ mm}$ in the position of the OPO.

The SRO threshold at 1 kHz in Fig. 19a corresponds to an axial pump fluence of 14 mJ/cm^2 or a peak intensity of $\sim 35 \text{ MW/cm}^2$. At maximum pump energy of 310 μJ at 1 kHz the idler output energy reached 4.3 μJ at 6.137 μm . No damage occurred to the crystal surface for peak pump intensities 5–6 times higher than the limit observed with 14-ns long pump pulses. The maximum axial pump fluence applied with the $\sim 0.4 \text{ ns}$ pulses was 59 mJ/cm^2 (peak intensity of 147 MW/cm^2). The spectral bandwidth of this CSP SRO at $\lambda_2 \sim 1.287 \mu\text{m}$ was larger, $\sim 3.9 \text{ cm}^{-1}$ due to the small number of cavity round-trips. From measurements of the signal pulse duration one can conclude that $< 300 \text{ ps}$ is a reasonable estimate for the idler pulses at $\lambda_1 = 6.137 \mu\text{m}$ [189].

At the maximum repetition rate of 10 kHz the idler energy dropped to 2.4 μJ , Fig. 19b (related to residual linear and nonlinear pump absorption as well as to slight deterioration of the pump beam spatial profile), but the average power reached its maximum of 24 mW. In this set-up the number of cavity round trips was less than 3 for the signal (having in mind the refractive index of CSP which is > 3). Thus, the experiment shows that in this regime, applying highly nonlinear NLCs the difference between pulsed OPO and OPG is smeared – indeed such an OPO can be

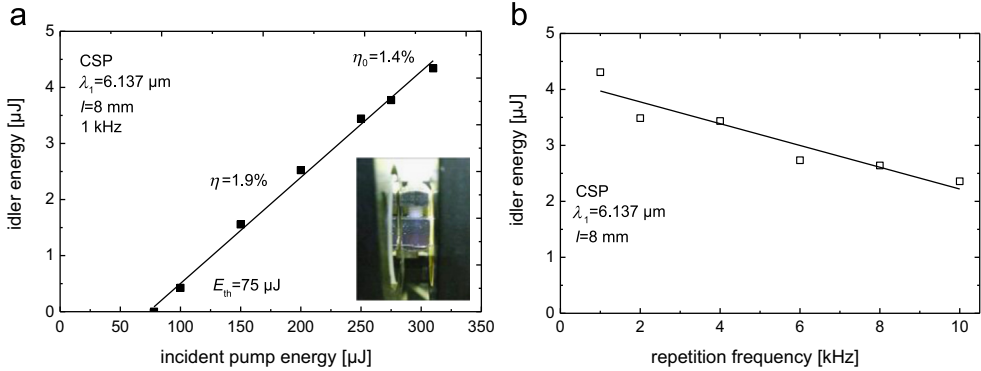


Fig. 19. Idler energy at $6.137 \mu\text{m}$ vs. pump energy at a repetition rate of 1 kHz (a) and vs. repetition frequency at a pump energy of $310 \mu\text{J}$ (b). The inset in (a) shows the CSP crystal between the two SRO cavity mirrors.

considered as a 3-stage combination of OPG and OPAs. On the other hand such a regime with short pump pulses obviously helps to avoid the surface damage problems in CSP.

In general, from Table 5, it can be seen that most $1\text{-}\mu\text{m}$ pumped OPOs were operated at 10 Hz, in rare cases up to 100 Hz, and damage-free operation at kHz repetition rates has only been achieved with pump pulse durations of few ns or less.

Only marginal improvement of the idler beam quality was observed when the RISTRA cavity concept was tested with CSP which can be attributed to the lack of spatial walk-off under NCPM [190]. More recently, a RISTRA OPO based on type-II HGS and operating at 10 Hz was compared with linear and planar ring cavities whose parameters were as close as possible and the effect of the spatial walk-off was studied by changing the pump beam diameter [180]. The pump source was the same as in [179], see Fig. 14b, with 8 ns pulse duration, but to improve its spatial beam profile (eliminate diffraction rings producing hot spots) a vacuum diamond pinhole was installed in the focus of a telescope. The M^2 parameter of the pump measured behind the telescope amounted to ~ 2 . The pump beam size was reduced by a second telescope to $2w_3 = 2.25 \text{ mm}$ (small diameter, corresponding to an OPO Fresnel number of 30) for the first series of measurements. The pump beam size was kept at $2w_3 = 5.35 \text{ mm}$ (large diameter, comparable to the crystal aperture, corresponding to a Fresnel number of 175) without this telescope, for the second series of measurements. All cavities studied were SP-SROs for the signal at $\lambda_2 \sim 1.28 \mu\text{m}$. However, the angles of incidence on the mirrors and polarizations differed in the three cases. Since all mirrors were designed for the monolithic RISTRA cavity (Fig. 8b) this led to some differences in the mirror characteristics at the three wavelengths which were unavoidable. In comparison to the other cavities, the RISTRA configuration contained also a half-wave plate for compensation of the polarization rotation of the signal. The physical length of the RISTRA cavity was $l = 128 \text{ mm}$ but what was kept almost equal for the three cavities was the round trip optical length. Two similar type-II HGS crystals for $6.3 \mu\text{m}$ generation were studied at normal incidence. The first one was 13.44-mm long with an aperture of $10 \text{ mm} \times 10 \text{ mm}$, cut at $\theta = 50.26^\circ$ and $\varphi = 0^\circ$ (used in the first series of experiments) and the second one was 17.88-mm long with an aperture of $8.57 \text{ mm} \times 7 \text{ mm}$, cut at $\theta = 50.25^\circ$ and $\varphi = 0^\circ$ (used in the second series of experiments). Both were AR-coated with a single layer for signal and pump.

Due to the above mentioned differing cavity losses, the OPO threshold was different for the three types of cavities studied but the slope efficiencies were very close. Thus, the idler M^2 factor

in the two planes was compared at 2–3 times threshold operation for the two different pump diameters. Since in HGS, type-II (eoe) PM is dictated by maximum d_{eff} (lowest threshold) considerations the idler is walk-off decoupled only from the resonated signal but not from the low quality pump which is neither SF nor TEM₀₀. This is the worst scenario for RISTRA. Moreover, the number of round trips is not very large for the 8 ns pump pulse duration (~ 16 and 15.5 for the first and second series of measurements, respectively), i.e., cavity modes are less established. The spatial walk-off amounted to 10.3% and 5.8% of the pump beam diameter for small and large pump diameter, respectively.

For $2w_3 = 2.25$ mm, the obtained M^2 values were of the order of 3 (3.1 in the critical and 3.5 in the uncritical plane for RISTRA measured at 0.36 mJ idler output). The RISTRA cavity made the idler spatial profile slightly more symmetric but did not in fact improve M^2 . Increasing the pump diameter to $2w_3 = 5.35$ mm led to larger M^2 values which was more pronounced for the linear and planar ring cavities. For the RISTRA cavity M^2 amounted to 4.8 and 5.4 in the critical and uncritical plane, respectively, at the maximum output energy of 0.8 mJ obtained. From the two series of experiments, no evidence for the significance of the walk-off effect on the idler beam quality was seen: although in linear cavities in most cases M^2 was slightly lower in the critical plane, in the planar ring cavities the idler beam was more divergent in this plane and the ellipticity was more pronounced. The RISTRA image rotation made the picture more symmetric assuming the better M^2 value but this was for the uncritical direction. Nevertheless, the focal fluences that could be achieved with the improved idler beam quality are much higher compared to the results in Fig. 14b [179]. For instance, assuming a collimated idler beam at $6.3 \mu\text{m}$ with a diameter of $0.5''$ focused by a 100 mm lens, axial focal fluence of 2 J/cm^2 is calculated both for $2w_3 = 2.25$ and 5.35 mm with the RISTRA output energies. This value is only 0.2 J/cm^2 for the large Fresnel number linear cavity in [179] where the output energy reached 3 mJ but $M^2 \sim 30$, see Fig. 14b. In any case, the RISTRA cavity had pronounced advantages over the other cavities at high idler energies (large pump diameters), providing not only lower M^2 values but also symmetric beam shape and equal focal distance in the two planes.

In 2015, the first OPGaP OPO pumped by a Nd:YVO₄ laser was demonstrated with a 0.15 mm thickness of the periodic structure, Table 5 [193]. The threshold amounted to 50 μJ . Temperature tuning (20–100 °C) produced idler wavelengths in the 4.591–4.876 μm range.

6.2.2.2. OPOs pumped between 1 and 2 μm . Since no suitable laser pump sources exist, there are only sporadic demonstrations of ns OPOs (all of them SROs) pumped between 1 and 2 μm , see Table 6. The situation might change, however, in the near future with development of powerful LD-pumped Er-lasers.

The NLC that can be utilized at pump wavelengths above 1 μm without TPA, for higher FM, is AGSe (Fig. 9). AGSe was pumped by $\sim 1.3 \mu\text{m}$ Nd-lasers, also in NCPM but angle tuning was then limited to 6.7–6.9 μm (Table 6) [198]. This pump wavelength is slightly too short and some TPA occurred [199]. Er:YLF laser operating near 1.73 μm [194] is a better alternative for AGSe and high idler energies were achieved with such an OPO albeit at low repetition rates (Table 6). The advantage of using type-I AGSe is mainly the broader tuning achievable with a single cut. AGSe was also pumped at 1.9 μm by a Raman shifted Nd:YAG laser [201] and again > 1 mJ energies were obtained with the potential to cover the entire transparency range with the idler. Similarly, CdSe (here $d_{\text{eff}} \neq 0$ only for type-II PM) based OPO was pumped at 1.833 μm by a Nd:YAG laser with the idler between 9.8 and 10.4 μm , tuned by angle tilt near the NCPM point [201]: Also in CdSe, broader tuning would require longer pump wavelengths.

All SRO results in Table 6 refer to resonated signal wave. In [202], SRO regime resonating the idler wave was also demonstrated in order to avoid the optical damage to the CdSe surface. In this case, however, the threshold was reached only with a partial double pass for the pump.

6.2.2.3. OPOs pumped near 2 μm . Pumping mid-IR OPOs near 2- μm ensures higher conversion efficiency to the idler simply because the quantum limit set by the ratio λ_3/λ_1 can be much higher. In addition, few applications (such as counter-measures in defense) are possible with broadband radiation and both signal and idler outputs can be utilized together. Thus, demonstrated $\sim 2\text{-}\mu\text{m}$ pumped OPOs were often DROs, outcoupling both signal and idler near degeneracy.

AGSe was the first NLC studied under Ho-laser/amplifier pumping but it showed thermal lensing problems [203], related to its low thermal conductivity [204] and residual absorption near 2 μm . Initially, lamp-pumped Ho:YLF laser systems emitting at 2.05 μm were employed. Idler energy in excess of 3 mJ (single pulses) at $\sim 4.8\text{ }\mu\text{m}$ with tuning from degeneracy up to 9.02 μm was reported in the first such SP-SRO using type-I AGSe ($L=21\text{ mm}$) with 50-ns pump pulses [198]. The tuning range was extended to 12.05 μm in [205]. Combined (signal and idler) average power of 170 mW near degeneracy was achieved at 100 Hz with a type-I AGSe ($L=33\text{ mm}$) SP-DRO pumped by 55 ns pulses at 2.06 μm [206]. Surface damage limited, however, long term operation. The same restriction on the achievable idler energy near 6- μm was observed comparing 20-mm long type-I and type-II AGSe crystals in a DP-SRO pumped by a LD-pumped Q-switched Tm,Ho:YAG ceramic laser at 10 Hz [207]. The longest wavelengths ($\lambda_1=12.6\text{ }\mu\text{m}$) were demonstrated with a type-II (i.e. higher d_{eff}) AGSe ($L=25\text{ mm}$) crystal, pumped at 2.088 μm by a LD-pumped Tm:YLF/Q-switched Ho:YAG laser system [208]. The idler energy reached 360 μJ at 8.18 μm but dropped to 50 μJ at 12.21 μm . This DP-SRO was pumped by relatively short (10 ns) pulses at 100 Hz and the idler was resonated aiming at better beam quality (lower Fresnel number) [208]. AGSe DROs were operated also at kHz repetition rates [203,209] but additional damage problems were detected related to the above mentioned thermal limitations. Such a SP-DRO with type-I AGSe ($L=30\text{ mm}$) was studied at 2.5 and 5 kHz with 2.05 μm pump pulses of 15 and 30 ns duration, respectively, from a LD-pumped Q-switched Tm, Ho:YLF oscillator amplified in lamp-pumped Er,Tm,Ho:YLF. Combined average output power of 740 mW was obtained at 2.5 kHz [209]. The parametric gain measured at 3.39 μm using a He–Ne laser probe beam with ns 2 μm pump sources indicated superior potential of ZGP compared to AGSe [210,211]. Thus ZGP, with its much higher FM (Fig. 9) and thermal conductivity (35–36 W/mK [204]) became the crystal of choice at such pump wavelengths.

Table 6

OPOs based on non-oxide NLCs pumped between 1 and 2 μm . SP: single pump pass, NA: not available.

Crystal-type, θ_{cut}	L [mm]	Pump source: λ_3 , Duration, Repetition rate, Pump mode	λ_1 [μm]	Idler energy @ Wavelength	Refs.
AGSe-I, $\sim 90^\circ$	20	$\sim 1.34\text{ }\mu\text{m}$, 23 ns, 10 Hz, SP, TEM ₀₀	6.7–6.9, incl. NCPM	80 μJ @ 6.9 μm	[198]
AGSe-I, 66.5°	30, 20	1.319 μm , 70 ns, NA, SP, TEM ₀₀	9.5	<60 μJ @ 9.5 μm	[199]
AGSe-I, 64.5°	25	1.732 μm , > 150 ns, 5 Hz, SP	3.5–5.1	1–1.2 mJ @ 3.8 μm	[200]
AGSe-I, 55°	20	1.906 μm , 10 ns, 10 Hz, SP, SF	3.8–4.7	1.2 mJ @ 4.5 μm	[201]
CdSe-II, $\sim 90^\circ$	21	1.833 μm , 300 ns, 5 Hz, SP	9.8–10.4, incl. NCPM	$\sim 0.1\text{ }\mu\text{J}$ @ 9.8 μm	[202]

Pumping ns OPOs near 2 μm has produced so far the best results in terms of output energy and/or average power mainly because an excellent, damage-resistant material, ZGP, is available. However, besides its relatively short long-wave limit, ZGP shows defect related residual absorption from the band-gap region up to $\sim 2 \mu\text{m}$. This is the reason why the first such OPO was pumped at 2.8 μm (see next section) and later on, Ho-lasers emitting slightly above 2 μm were preferred against Tm-lasers emitting slightly below 2 μm . LD in-band pumping of Ho-lasers was developed only recently and has not been employed yet for pumping OPOs. Typically, Ho-lasers/amplifiers used to pump ZGP OPOs were co-doped with Tm as sensitizer or pumped by LD-pumped Tm bulk or fiber lasers. ZGP based OPOs were operated often near degeneracy as DROs to combine the signal and idler output. This regime is only possible for ZGP in type-I (eo) PM. For this reason, so far only type-I ZGP was employed in 2- μm pumped OPOs though away from degeneracy (e.g. at $\lambda_1=6.45 \mu\text{m}$) type-II PM shows the same magnitude of d_{eff} .

The first such ZGP ($L=12 \text{ mm}$) OPO was pumped at 2.05 μm by a LD-pumped Q-switched Tm,Ho:YLF oscillator in conjunction with a lamp-pumped Er,Tm,Ho:YLF amplifier [212], similar to [209]. The pump pulse duration varied between 23 and 28 ns for repetition rates between 2.5 and 10 kHz. Operating close to degeneracy this SP-DRO produced energies of 155 μJ at 4 kHz and 73 μJ at 10 kHz, recalculated here only for the idler at 4.46 μm [212]. Such co-doped pump systems were exclusively employed for ZGP in the 1990s but they suffer from the requirement for cryogenic cooling (necessary for power scaling) related to up-conversion losses. With LD-pumped amplifier stages based on cryogenically cooled Tm,Ho:YLF (pump pulse duration of $\sim 10 \text{ ns}$), a similar SP-DRO with ZGP ($L=14 \text{ mm}$), operating close to degeneracy produced idler energy of $\sim 0.5 \text{ mJ}$ at 10 kHz which is equivalent to $> 10 \text{ W}$ of combined (signal and idler) average power [213]. Operation away from degeneracy (λ_1 from 7.8 to 8.4 μm) was also demonstrated with ZGP ($L=12.5 \text{ mm}$) pumped by 15-ns pulses [214] but this was again a SP-DRO; the idler energy at 8.2 μm reached 42 μJ for a repetition rate of 10 kHz. A ring DRO employing a walk-off compensating pair of ZGP ($L=14 \text{ mm}$) crystals was explored in [215], eliminating the back conversion in backward direction and the need of Faraday isolator to protect the pump system from feedback. Similarly, LD-pumped Tm,Ho:GdVO₄ lasers were introduced later in the 2000s as pump sources but this co-doped laser system also requires cryogenic cooling. In [216] the Q-switched at 10 kHz Tm,Ho:GdVO₄ laser emitting at 2.049 μm produced pulses of 20–30 ns duration, depending on the power level. The SP-DRO based on ZGP ($L=15 \text{ mm}$) operated near degeneracy and generated combined average output power of 14.1 W, corresponding to idler energy of $\sim 650 \mu\text{J}$ at 4.45 μm . Total slope efficiency of 64.8% was reported in [217] with an $L=18 \text{ mm}$ ZGP. The M^2 factor could be improved from 3.6 to 1.7 lengthening the cavity, however, at lower output [218]. With a similar laser pump system (18 ns, 8 kHz), a DP-SRO with ZGP ($L=16 \text{ mm}$) delivered idler energy of 21 μJ at 8.3 μm [219].

A different concept for pump power scaling was adopted in [220] based on in-band laser pumping into the upper laser level (i.e. with small quantum defect and minimum heat generation) of the Ho-ion, realized by combining a LD-pumped Tm:YLF and a Q-switched Ho:YAG laser emitting at 2.09 μm . With pump pulse duration of 29 ns and SP-DRO based on ZGP ($L=14 \text{ mm}$), idler energy of $\sim 200 \mu\text{J}$ at 4.65 μm was achieved for a repetition rate of 10 kHz [220]. The same pump concept was power scaled in [221] with a near-degenerate DP-DRO based on ZGP ($L=16 \text{ mm}$) pumped by 14-ns pulses: the idler energy at 4.6 μm amounted to ~ 500 , ~ 300 , and $\sim 200 \mu\text{J}$ at 10, 15 and 20 kHz, respectively, which is equivalent to combined average output power of the order of 10 W. More recently ring and linear SP-DROs with ZGP ($L=18 \text{ mm}$) were compared using a similar pump source (31 ns, 5–20 kHz) [222]. The

maximum idler energy near 4.6 μm reached $\sim 500 \mu\text{J}$ at 5 kHz and the ring cavity which performed better delivered at 20 kHz up to 17 W of combined (signal and idler) average power near degeneracy, corresponding to a total slope efficiency of 57.6%. A Ho:LuAG (Lu-analog of YAG) Q-switched laser, again pumped by Tm:YLF lasers, was employed as a pump source for the same ring ZGP SP-DRO in [223], with similar results at 5 kHz. Very recently, power scaling of the Tm:YLF/Ho:YAG pump source (2.09 μm , 23 ns, 20 kHz) with a ring SP-DRO containing two ZGP ($L=23 \text{ mm}$) crystals produced record high combined average power of 41.2 W ($\lambda_2=3.94 \mu\text{m}$ and $\lambda_1=4.5 \mu\text{m}$) with $M^2=3.83$ for the idler [224]. Another similar pump system (23 ns, 10 kHz) was used to pump a non-degenerate DP-SRO ($\lambda_1=8\text{--}9.1 \mu\text{m}$) based on ZGP ($L=17 \text{ mm}$) that delivered single pulse energy of 96 μJ at 8.08 μm which translates into an average power of 0.96 W [225]. A passively Q-switched Ho:YAG ceramic laser was employed as a pump source in [226].

The use of Tm-fiber lasers, in which the thermal load is distributed over a much larger volume, for pumping Q-switched Ho-lasers, was introduced for a ZGP OPO in 2003. With such a Q-switched Ho:YAG laser generating 24-ns pulses at 2.096 μm , near-degenerate operation of a SP-DRO containing two walk-off compensated ZGP ($L=14 \text{ mm}$) crystals produced idler ($\lambda_1 \sim 4.63 \mu\text{m}$) pulse energies in excess of 100 μJ at 20 kHz [227]. This corresponds to 58% total (signal and idler) conversion efficiency and 70% slope efficiency. About 20% increase in the output was due to matching the OPO cavity length to the pump laser cavity length which was shown to be important for DROs pumped by multi-longitudinal mode lasers (similar cavity matching effects with a Tm,Ho:GdVO₄ laser pump were studied later in [228]). Enhancement was observed also in an almost SRO operating away from degeneracy ($\lambda_1=7.9\text{--}9.8 \mu\text{m}$) with similar single pass pump and double crystal parameters [229]: idler energy of 47.5 μJ at 20 kHz (0.95 W corresponding to 10.7% conversion efficiency to idler) was obtained at 8 μm . This work presented also the longest idler wavelengths achieved with 2- μm laser-pumped ZGP OPO demonstrating an average power of $\sim 0.2 \text{ W}$ at 9.8 μm . Higher idler energies from a SRO (200 μJ albeit at 4.72 μm) were demonstrated at 10 kHz with a similar pump system and folded linear cavity with four pump passes through a single ZGP ($L=15 \text{ mm}$) crystal with walk-off compensation [230]. Power-scaling of the pump source (38 ns, 25 kHz) with a near-degenerate SP-DRO employing single ZGP ($L=15 \text{ mm}$) crystal produced combined average output power of 12.6 W for the idler at 4.57 μm [231]. With 32-ns pump pulses at 2.09 μm and near-degenerate SP-DRO containing two walk-off compensated ZGP ($L=12 \text{ mm}$) crystals, operation with a repetition rate of 40 kHz was reported in [232]; with an idler energy of $\sim 110 \mu\text{J}$ at 4.8 μm this scheme delivered similar average power (of the order of 10 W for signal and idler together). The same pump concept was explored also for an intracavity ZGP DRO, delivering $> 1 \text{ W}$ of combined average power near degeneracy at 10 kHz [233].

The concept of Tm-fiber laser in-band pumped Q-switched Ho-lasers, resolving thermal issues in both lasers, seems at present most promising for OPO power scaling due to the commercial availability of Tm-fiber lasers with steadily increasing power level. In [234], combined average power of 30 W (signal and idler) was extracted from a near-degenerate ZGP DRO with 56% total conversion efficiency and 66% slope efficiency. An original, relatively short V-ring cavity extending in the uncritical plane was proposed in [235] which helps realize DRO with double but non-overlapping pump pass in a single crystal for reduced optical damage risk and to avoid any feedback to the pump laser. The Ho-laser pump source delivered 32 ns pulses at 45 kHz. Utilizing cavity length matching for near-degenerate operation the total conversion efficiency with $L=8.5 \text{ mm}$ ZGP reached 58% (slope of 75%) which corresponds to a combined average power of 22 W (with $M^2 \sim 1.4$) or single pulse energy of $> 200 \mu\text{J}$ at $\lambda_1 \sim 4.5 \mu\text{m}$. The same idea

was also applied to a non-degenerate SRO achieving $\sim 40 \mu\text{J}$ at 38 kHz with $M^2 < 2$ for the idler at $8.05 \mu\text{m}$ [236]. Two walk-off compensated ZGP ($L=16 \text{ mm}$) crystals in a DRO pumped in single and double pass by 50-ns pulses at $2.09 \mu\text{m}$ and 35 kHz were studied in [237]. The DP version produced idler energy $\sim 360 \mu\text{J}$ at $4.5 \mu\text{m}$ in near-degenerate operation, equivalent to combined average power of 27.1 W with $M^2=4$ measured at maximum level. The total conversion efficiency was 62% with a slope of 67%. With a similar pump system (37 ns, 26 kHz) but a ring DRO containing two ZGP ($L=12 \text{ mm}$) crystals, idler energy of $\sim 540 \mu\text{J}$ at $4.5 \mu\text{m}$ was obtained very recently, which translates into combined average power of 30.2 W [238]. The total conversion efficiency was 56% with a slope of 63% and $M^2 \sim 1.3$.

Improvement of the ZGP optical quality enabled direct pumping at slightly shorter wavelengths by LD-pumped room-temperature Tm-lasers. A Q-switched Tm:YAP (YAIO₃) laser (50 ns, 10 kHz, $1.99 \mu\text{m}$) directly pumped a ZGP ($L=20\text{--}25 \text{ mm}$) SP-DRO in [239], generating combined (signal and idler) average output power of 3.1 W near degeneracy. A Tm-fiber gain-switched oscillator – power amplifier system (all-fiber based robust pump approach) emitting at $1.995 \mu\text{m}$ (30 ns, 30 kHz) was employed in [240] to pump a near-degenerate ZGP ($L=15 \text{ mm}$) SP-DRO, producing idler pulse energy of $\sim 9 \mu\text{J}$, up-scaled to $\sim 13.5 \mu\text{J}$ in a subsequent report on SP-SRO at 100 kHz, which corresponds to combined (signal and idler) average power of 2 W near degeneracy [241]. With a similar pump system at $2.044 \mu\text{m}$ and SP-DRO based on two walk-off compensated ZGP ($L=16 \text{ mm}$) crystals, combined average power of $\sim 3 \text{ W}$ was achieved at 75 kHz [242]. The highest combined (signal and idler) average power reported very recently with Tm-fiber laser ($\sim 2.024 \mu\text{m}$) pumped near-degenerate ZGP ($L=18 \text{ mm}$) SP-DRO was 6.5 W at 40 kHz [243–245]. Higher energies were achieved at 4 kHz [246] with 7 and 100 ns pulses at $1.98 \mu\text{m}$ pumping a near-degenerate ZGP ($L=12 \text{ mm}$) SP-DRO. The more efficient (49% total slope) 100 ns version delivered combined energy of $\sim 280 \mu\text{J}$.

All the ZGP OPOs described above operated at kHz repetition rates. Pumping at lower repetition rates to produce energies $> 1 \text{ mJ}$ is much more challenging, related to the development of the pump source, the necessity of larger crystal apertures, the higher Fresnel number, and the optical damage risk. A LD-pumped Tm:YLF/Q-switched Ho:YLF laser system (12–15 ns, 50–400 Hz, $2.05 \mu\text{m}$) was employed as a pump source in [247]. The combined output of the ZGP ($L=10 \text{ mm}$) DP-SRO exceeded 4 W at 400 Hz with a slope efficiency of 63%. At 50 Hz, the combined output energy reached $\sim 11.6 \text{ mJ}$ with a slope of 60%, which means at least 4.2 mJ in the idler at $5.7 \mu\text{m}$ which was completely out-coupled [247]. A Tm:YLF/Q-switched Ho:YAG laser system (14 ns, 60 Hz, $2.09 \mu\text{m}$) was employed to pump a near-degenerate ZGP ($L=15 \text{ mm}$) SP-DRO in [248]: The combined output energy reached $\sim 20 \text{ mJ}$ for a total conversion efficiency of 42% with initial slope of 57%. A LD-pumped, Q-switched, water-cooled Tm,Ho:LuLiF₄ (LLF) laser (150 ns, 6 Hz, $2.05 \mu\text{m}$, SF) pumped a ZGP ($L=25 \text{ mm}$) ring SRO in [249]: the idler was tunable from 4.3 to $10.1 \mu\text{m}$ with an energy of 17.3 mJ at $4.8 \mu\text{m}$ (conversion efficiency to idler of 27.5%) and $> 4 \text{ mJ}$ up to $8.3 \mu\text{m}$. This SRO was injection seeded (as was the pump laser) at $3.39 \mu\text{m}$ to reduce the idler bandwidth from $\sim 20 \text{ nm}$ to below the spectral resolution of $\sim 1 \text{ nm}$ and produce narrowband pulses of $\sim 2.5 \text{ mJ}$ at $5.2 \mu\text{m}$ [249]. At such low repetition rates, lamp-pumped, water-cooled Cr:Tm:Ho:YAG pump lasers present a simpler concept and though initial OPO results were inferior [250] substantial up-scaling of the idler energy can be expected [251].

Also for high energy operation, the power scaling concept based on Tm-fiber lasers pumping Ho-lasers is at present most promising. A Q-switched Ho:YLF laser ($\sim 25 \text{ ns}$, 500 Hz, $2.05 \mu\text{m}$) was employed to pump a RISTRA type ZGP ($L=10 \text{ mm}$) SRO emitting at $\lambda_1=5.163 \mu\text{m}$ [252].

Signal energy of 10 mJ at $\lambda_2=3.4\ \mu\text{m}$ was extracted but unfortunately the idler was not investigated. Power scaling included the pump system ($\sim 20\ \text{ns}$, 100–500 Hz) and the OPO, both with MOPA designs [253]. In this particular case the dimensions and conditions for pumping the OPO and OPA ZGP crystals were similar and thus the main purpose of the OPA stage seems to be the reduction of the damage risk in the OPO. The parametric gain is modest in OPAs pumped by ns pulses, ~ 3 in [253], and the maximum signal energy achieved from the OPA at 100 Hz was 31 mJ but again the system was only optimized for the signal while idler output was not characterized. A MOPA concept was employed also in [254]; in this case, however, the SRO provided good output beam quality using smaller fraction of the available pump energy at tighter focusing while the main part of the pump energy was used for the OPA stage. Nevertheless, the pump fluence was higher in the OPA, to ensure sufficient single pass parametric gain. The pump source was a Q-switched cryogenic Ho:YLF laser (16 ns, 1 Hz, $2.05\ \mu\text{m}$) and the SRO was with V-ring type cavity and two ZGP ($L=6\ \text{mm}$) crystals in double pump pass. The OPA was seeded with 12 mJ OPO output (signal and idler) and investigated with 1, 2, and 3 ZGP crystals of 6-mm length. The combined OPA output for 380 mJ of pump energy was 136, 207, and 212 mJ in near-degenerate ($3.5\text{--}4.9\ \mu\text{m}$) operation with $M^2=2.7, 2.9, 3.3$, respectively [254,255].

In some cases the efforts were focused on specific idler wavelengths, like the already mentioned $\lambda_1=6.45\ \mu\text{m}$ for medical (surgical) applications. A Tm-fiber laser pumped Q-switched Ho:LLF laser/amplifier system (38 ns, 100–200 Hz, $2.053\ \mu\text{m}$) was employed in [256] to pump a RISTRA ZGP ($L=16\ \text{mm}$) SRO. The non-resonated idler energy reached 5.67 mJ at 100 Hz and 4.76 mJ at 200 Hz [256]. After optimization, idler energies at $6.45\ \mu\text{m}$ of 6.4 and $\sim 5.5\ \text{mJ}$ at 100 and 200 Hz, respectively, were achieved (Fig. 20), with an average idler power of 1.09 W in the latter case. This value represents the highest average power achieved in this wavelength range for single pulse energies on the mJ level.

Close to degeneracy, with a similar pump (30 ns, 100 Hz, $2.053\ \mu\text{m}$) and RISTRA set-ups, the idler energy reached 9.8 mJ, corresponding to conversion efficiency of 21.5% with a slope of 27.6% [257], Fig. 21a. The combined average power was 2.38 W, corresponding to total conversion efficiency of 52.2%. The idler beam showed almost equal M^2 values of 1.91 and 1.94 in the two planes at energy of 8.2 mJ; the dependence on the pump level is shown in Fig. 21b. Strategies for further enhancement of the output beam quality of this scheme by generalization of

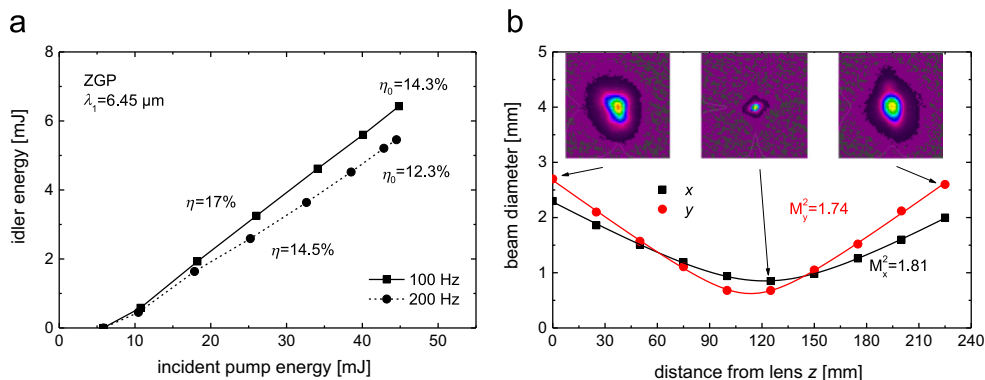


Fig. 20. Idler energy at $6.45\ \mu\text{m}$ vs. pump energy (a) and diameter of idler beam in the critical (y) and non-critical (x) planes vs. distance after focusing, measured at an idler energy of 5.67 mJ at 100 Hz (b). The insets show the idler beam profile at the indicated positions. (a) presents an unpublished result kindly provided by G. Stoepler, ISL. (b) is modified from [256] (Courtesy of G. Stoepler, M. Schellhorn, and M. Eichhorn, ISL).

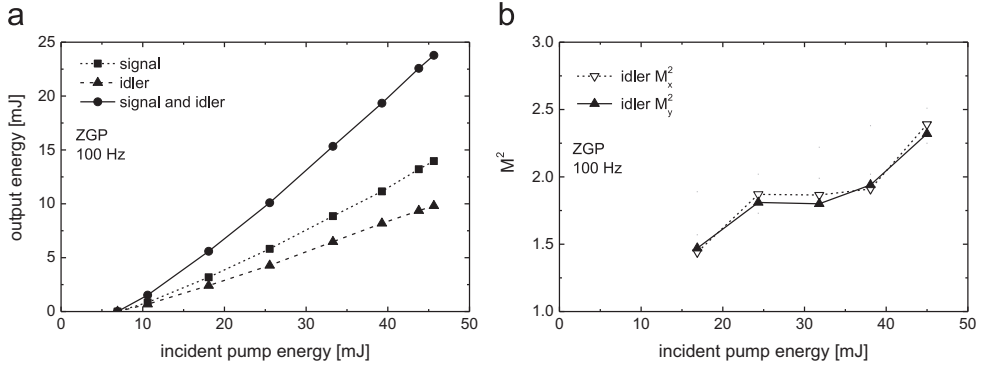


Fig. 21. Signal and idler energy of the near-degenerate ZGP RISTRA SRO vs. pump energy (a) and idler M^2 parameter in the two planes in dependence on the pump level (b). Both figures are modified from [257] (Courtesy of G. Stoeppler, M. Schellhorn, and M. Eichhorn, ISL).

the RISTRA principle based on fractional image rotation were presented in [258,259]. Comparison with a RISTRA cavity indicated improved beam quality at the 20 mJ (signal and idler near-degeneracy) output energy level.

The first OPO (SP-DRO) realized with the recently developed CSP ($L=12.3$ mm) using type-I (ooe) PM was in fact pumped at $\lambda_3=1.99$ μm by a LD-pumped Tm:YAP laser (140 ns, 20 kHz) [260]. The PM is critical at this pump wavelength, FM is not much higher than ZGP (Fig. 9) but the advantage of CSP is the lower residual absorption in the 2- μm spectral range and the possibility of temperature tuning, demonstrated near degeneracy in [260].

Recently, OPGaAs, presenting few essential advantages (Table 3), such as NCPM, extended mid-IR transmission, higher thermal conductivity, and lower residual absorption, emerges as a serious competitor to ZGP in 2- μm pumped OPOs. Because of the (still) limited aperture (thickness) of OPGaAs, this concerns more average power than energy scaling of such OPOs. Consequently, all demonstrated OPGaAs OPOs operated at repetition rates of 0.5 kHz and higher.

The first laser pumped OPGaAs OPO utilized a cryogenic Tm,Ho:YLF MOPA system ($\lambda_3=2.055$ μm) with a pulse duration of 28 and 54 ns at 10 and 20 kHz, respectively, [261]. The ~ 0.4 mm thick OPGaAs ($L=16$ mm, $\Lambda=62$ μm) generated idler ($\lambda_1=5.18$ μm) energy of >17 and ~ 7 μJ at 10 and 20 kHz, respectively, in a SP-DRO which operated near degeneracy (up to ~ 5.5 μm) and could be temperature tuned. The corresponding combined (signal and idler) average power amounted to 443 and 350 mW. A SP-SRO yielded very similar results at 20 kHz. Some improvement of these results in terms of energy was reported in [262] with a near degenerate SP-DRO pumped by a similar laser system (43 ns, 500 Hz). The idler energy at 4.4 μm exceeded 35 μJ using thicker OPGaAs ($L=15$ mm, $\Lambda=60.5$ μm) samples. A Tm,Ho:YAG laser (45 ns, 20 kHz, 2.09 μm) was employed in [263] to pump a ~ 0.5 mm thick OPGaAs ($L=20$ mm, $\Lambda=60$ μm) in single and double pass. The DP-DRO produced combined average output power of 1.2 W near degeneracy, which corresponds to total conversion efficiency of 37.5% with a slope of 57%. A SF Tm:YAP laser (36 ns, 100 Hz, 1.9385 μm) was used in [264] to pump a 0.5 mm thick OPGaAs ($L=10$ mm, $\Lambda=72.6$ μm). This DP-DRO employed a special cavity with different optical lengths for the signal and idler whose control enabled SF operation with 10.3 to 10.9 μm idler temperature tuning and maximum energy of 2 μJ at 10.3 μm .

Further power scaling was studied using Tm-fiber/Q-switched Ho:YAG laser pump systems ($\lambda_3=2.09\ \mu\text{m}$) operating at 20–100 kHz [265–268]. These SP-DROs were based on a $\sim 0.45\ \text{mm}$ thick OPGaAs ($L=20\ \text{mm}$, $\Lambda=63\ \mu\text{m}$). Highest output levels near degeneracy were reported in [268]: the combined average power at 40, 70, and 100 Hz reached 4, 6.4 and 7.7 W at pump pulse duration of 32, 51, and 70 ns, respectively (Fig. 22a). At 100 kHz, the limiting factor was the pump power available. M^2 measurement results for the idler are shown in Fig. 22b.

With a similar pump system (40 ns, 50 kHz, $2.096\ \mu\text{m}$) a $\sim 0.5\ \text{mm}$ thick OPGaAs ($L=22\ \text{mm}$, $\Lambda=63.8\ \mu\text{m}$) was studied in a SP-DRO in [269]. This near-degenerate DRO delivered combined average power exceeding 3 W at slope efficiency of $\sim 53\%$, and $M^2 \sim 1.4$ for the idler. The idler was tunable from 4.5 to $4.9\ \mu\text{m}$ when the temperature was adjusted from 30 to $60\ ^\circ\text{C}$.

In [266,267] an externally Q-switched Tm,Ho-fiber laser at $\sim 2.1\ \mu\text{m}$ was used to pump the same OPGaAs in a SP-DRO at 40–75 kHz. The pump pulse duration varied from 49 to 105 ns depending on the repetition rate. In the best case, a combined average output power of $\sim 2.2\ \text{W}$ with 62% slope efficiency was reached at 40 kHz in near-degenerate operation.

In few cases the performance of OPGaAs was compared to that of ZGP in DROs at kHz repetition rates and the two crystals showed remarkably close slope efficiencies (e.g. 50–60% in [258,265]) and OPO thresholds. In [270] OPGaAs was compared to ZGP and CSP under identical conditions pumping with the Tm:YAP laser at $1.99\ \mu\text{m}$ and the performance of OPGaAs and ZGP was again very similar, and superior to that of CSP.

In [271] an OPGaAs DP-SRO ($L=15.4\ \text{mm}$, $\Lambda=76, 82,$ and $84\ \mu\text{m}$) was studied for long wavelength operation pumped by a LD-pumped cryogenically cooled Tm,Ho:YLF laser (60–65 ns, 500 Hz, $2.054\ \mu\text{m}$). Idler range extended from $\sim 8.8\ \mu\text{m}$ ($\sim 35\ \mu\text{J}$) up to $\sim 11.5\ \mu\text{m}$ ($\sim 16\ \mu\text{J}$). M^2 , measured at $8.8\ \mu\text{m}$, amounted to 1.13 and 1.21 in the two planes. A NRO was also investigated to suppress back conversion but this increased the OPO threshold and reduced the efficiency.

Very recently, highly efficient intracavity (in a Tm:YAP laser) OPGaAs OPO was demonstrated [272], generating 120 mW of average idler power at $4.6\ \mu\text{m}$ for a repetition rate of 130 kHz. At fixed period Λ , this OPO was tunable through the pump wavelength.

The effect of the pump polarization and the possibility to pump ns OPGaAs OPOs by unpolarized lasers (in particular fiber based sources) were studied and discussed in [265,266].

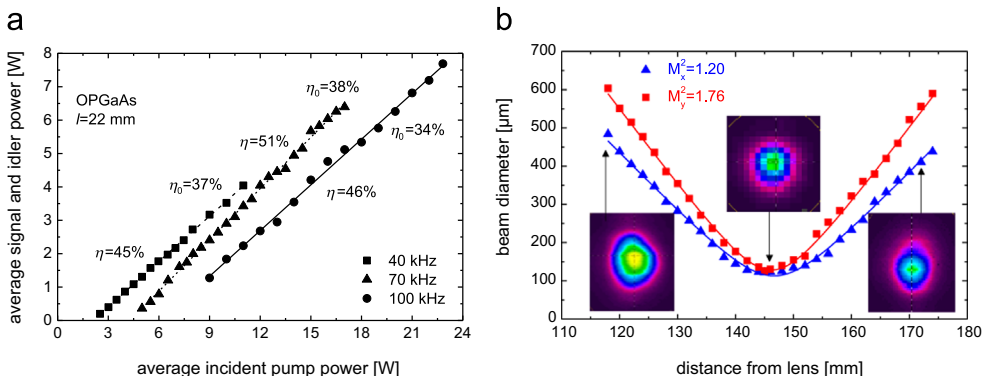


Fig. 22. Combined (signal and idler) output power of the near-degenerate OPGaAs OPO vs. average pump power (a) and diameter of idler in the two planes after focusing, measured at 40 kHz for an output power of 3.5 W (b). (Courtesy of A. Hildenbrand, C. Kieleck, and M. Eichhorn, ISL, from [268]).

Due to its high FM, OPGaAs can be also employed in OPAs pumped by ns laser sources near 2 μm . One motivation for this is to achieve narrowband operation. A SF cw distributed-feedback (DFB)-QCL at $\lambda_1=4.5 \mu\text{m}$ was amplified in [273] using a Tm-fiber/Q-switched Ho:YAG laser system (30 ns, 20 kHz, 2.09 μm). OPGaAs samples 0.5 mm thick were investigated ($L=32$ and 41 mm, $\Lambda=63.8 \mu\text{m}$). With the 41-mm-long crystal, maximum single pass idler gain of ~ 53 dB (580 W peak power at 4.5 μm) was achieved at an idler conversion efficiency of 12.4%. Another reason to use OPA, as already mentioned for ZGP, is to reduce the optical damage risk in an OPO. Such a MOPA based on OPGaAs ($\Lambda=60.5 \mu\text{m}$) crystals was pumped in [274] by a Q-switched Tm,Ho:YLF laser (71 ns, 1 kHz, 2.052 μm). The DP-DRO stage ($L=16.4$ mm) delivered idler energy of 11 μJ at $\lambda_1=4.39 \mu\text{m}$. The OPA stage ($L=25$ mm) was seeded at λ_2 and delivered idler energy of 44 μJ at $\lambda_1=4.39 \mu\text{m}$ with a gain factor of ~ 7 .

The first OPO (and in general nonlinear frequency conversion) based on bulk OPGaP was demonstrated in 2015 with Tm-fiber/Q-switched Ho:YAG pump system (12.6 ns, 20 kHz, 2.09 μm) [275]. The ~ 0.8 mm thick OPGaP sample ($L=16.5$ mm, $\Lambda=92.7 \mu\text{m}$) was used in a linear SP-DRO generating idler at 5.1 μm . The threshold pump intensity was 44 MW/cm² and the combined (signal and idler) average power reached 350 mW with slope efficiency of 16%.

6.2.2.4. OPOs pumped above 2 μm . Non-oxide NLCs were employed also in OPOs pumped by laser systems above 2- μm , Table 7. CdSe is useful for extension to longer idler wavelengths and in one of the first OPOs based on non-oxide NLCs, it was pumped by a Q-switched Dy²⁺:CaF₂ laser at 2.36 μm , achieving angle tunability between 7.88 and 13.7 μm [277], with the short λ_1 limit in the NCPM configuration. Temperature tuning was narrow. Broadest idler angle tuning requires for CdSe that $\lambda_3 \sim 2.5 \mu\text{m}$. Longer idler wavelengths with CdSe were achieved pumping by the discretely tunable (2.7–3 μm) HF gas laser. With a HF MOPA system at 2.87 μm , the CdSe OPO showed angle tuning from 14.1 to 16.4 μm [279] and > 2 mJ idler energies were obtained at 16 μm using a grating coupled cavity [280]. In this case the observed idler bandwidth of $\sim 0.3 \text{ cm}^{-1}$ was completely controlled by the signal bandwidth because the pump bandwidth was much narrower.

Er-lasers operating near 3- μm were used for pumping CdSe OPO for the first time in 1974 [281]. Cr,Er:YSGG near 2.8 μm [283–285,289] and Er:YAG lasers near 2.9 μm [286,287] became the main choice. Idler tuning from 8.4 to 12.3 μm and total (signal plus idler) conversion efficiency of 39% with a slope of 59% were reported in [284,285]. In fact the first ZGP OPO was demonstrated with 2.8 μm pumping using the second Stokes of Raman shifted (in methane) Nd:YAG laser [282]. Under identical conditions [284,285], ZGP, though much shorter, showed lower OPO threshold and higher output energies than CdSe (the values in Table 7 were measured in both directions for CdSe but only in forward direction for ZGP), however, above 8 μm its transmission is decreasing which affected the OPO efficiency. Nevertheless, with a similar pump laser, ZGP SROs yielded idler tuning up to 12.4 μm with 12.8% pump-to-idler conversion efficiency at 8.1 μm [288]. Compared to the FM (Fig. 9) and transparency range of CdSe and ZGP, AGSe occupies an intermediate position for application in such OPOs [286,287].

The Er-lasers discussed above as pump sources were lamp-pumped systems operating at low (1–25 Hz) repetition rates. A tunable (2.2–2.7 μm) gain-switched Cr²⁺:ZnSe laser, pumped by a LD-pumped Q-switched Tm:YAP laser, was employed for pumping ZGP and CdSe OPOs at kHz repetition rates [290–293]. Such pump wavelengths are compatible with NCPM for type-II (oeo) interaction in ZGP [291,293] for which total slope efficiency of 53% (signal at 4.7 μm plus idler at 5.6 μm) was achieved with $\lambda_3=2.55 \mu\text{m}$ at 1 kHz [291]. In [290], longer idler wavelengths were reported and NCPM in CdSe was presented, too, for which the total slope efficiency reached 64%. In [292,293] the energy with both crystals was up-scaled and the

repetition rate increased to 5 kHz, using intracavity pumping of the OPO. The idler average power reached 1 W at 5.6 μm (ZGP) and 0.8 W at 8.2 μm (CdSe). In contrast to angle/temperature tuning, rapid and random change of the idler wavelength is possible in this case using an AOTF in the pump laser [292,293]. Such tuning in the high energy regime at 10 Hz was demonstrated in [294,295] with ZGP OPOs, reaching idler energy of 4.6 mJ at 6.1 μm . The Cr^{2+} :ZnSe laser pumped OPOs represent the only all-SSL systems in Table 7.

Finally, CGA has also been employed in a ns OPO pumped by the SH of a CO_2 laser, see Table 7 [296]. As already mentioned, such long pump wavelengths are necessary for CGA in order to avoid residual absorption and TPA.

6.2.2.5. Cascaded OPOs. OPOs based on non-oxide NLCs can be pumped also in cascaded schemes (tandem OPO). Most often the first stage uses an oxide material and serves to shift the

Table 7

ns OPOs based on non-oxide NLCs laser-pumped above 2 μm . “+” means 2 crystals, SP: single pump pass, DP: double pump pass, IC: intracavity, TT: temperature tuning, DL: discrete lines, NA: not available.

Crystal-type, θ_{cut}	L [mm]	Pump source: λ_3 , Duration, Repetition rate, Pump mode	λ_1 [μm]	Idler energy @ Wavelength	Refs.
CdSe-II, $\sim 90^\circ$	25–30	2.36 μm , 30–60 ns, 1 Hz, SP, TEM_{00}	7.86–13.7, SRO, incl. NCPM and TT	765 μJ @ 7.88 μm	[276, 277]
CdSe-II, 85°	28	~ 2.87 μm (DL), 350 ns, 3 Hz, SP, TEM_{00}	8.1–8.3 (DL), SRO	NA (≤ 60 μJ)	[278]
CdSe-II, 72°	41–46	2.87 μm , 150 ns, < 1 Hz, DP	14.1–16.4, SRO	2.46 mJ @ 16 μm	[279, 280]
CdSe-II, NA	NA	2.76 μm , 30 ns, 1 Hz, NA, TEM_{00}	8–13, SRO	NA	[281]
ZGP-I, 45°	13	2.8 μm , 8–12 ns, NA, SP	5.6–6.9, DRO	< 70 μJ @ 5.94 μm	[282]
CdSe-II, 73°	51	2.79 μm , 35 ns, 10 Hz, DP	8.4–12.6, SRO	500 μJ @ 10 μm	[283]
CdSe-II, 73°	51	2.79 μm , 50 ns, 10 Hz, DP, TEM_{00}	8.4–12.3, SRO	2.4 mJ @ 9 μm	[284]
ZGP-II, 65°	25		6.9–9.9, SRO	2.4 mJ @ 7.6 μm	[285]
CdSe-II, 72°	46	2.936 μm , 50–100 ns, 2–6 Hz, SP, TEM_{00}	8–14, SRO	NA	[286]
AGSe-II, 62.5°	20		6–7, SRO	~ 2 mJ @ 6.45 μm	[287]
ZGP-I, 49.5°	20	2.93 μm , 100–110 ns, 10 Hz, DP, TEM_{00}	5.9–12.4, SRO	1.2 mJ @ 6.6 μm	[288, 289]
ZGP-II, 70°	20	2.80 μm , 100 ns, 25 Hz, DP, TEM_{00}	6.1–10, SRO	1 mJ @ 8.1 μm	
CdSe-II, 90°	30	2.45 μm , ~ 100 ns, 1 kHz, SP, TEM_{00}	~ 8 , SRO, \sim NCPM	~ 77 μJ @ 8 μm	[290]
ZGP-II, 62.5°	24	2.28–2.49 μm , ~ 100 ns, 1 kHz, SP, TEM_{00}	7.91–8, SRO	~ 50 μJ @ 8 μm	
ZGP-I, 49.5°	15	2.2–2.7 μm , ~ 100 ns, 1 kHz, SP, TEM_{00}	4.7–5.3, DRO	~ 40 μJ @ 4.7 μm	[291]
ZGP-II, 90°	15		5.55–5.66, DRO, NCPM	~ 35 μJ @ 5.6 μm	
CdSe-II, 82°	25+25	2.15–2.55 μm , < 125 ns, 5 kHz, IC, TEM_{00}	8.2–8.8, SRO	200 μJ @ 8.2 μm	[292]
ZGP-II, 90°	15	2.35–2.6 μm , < 125 ns, 5 kHz, IC, TEM_{00}	~ 5.6 , SRO, NCPM	200 μJ @ 5.6 μm	[293]
ZGP-I, $\sim 50^\circ$	15	2.15–2.31 μm , < 160 ns, 10 Hz, SP	6–9, DRO	1.2 mJ @ 6 μm	[294]
ZGP-I, 49°	15	2.34–2.44 μm , < 160 ns, 10 Hz, DP	4.9–8.2, SRO	4.6 mJ @ 6.1 μm	[295]
CGA-I, 33°	13	4.775 μm , 85 ns, 2 Hz, SP	10.5–10.9, DRO	~ 90 μJ @ 10.5 μm	[296]

1- μm wavelength of Nd-laser based systems to the 1.5–3.7 μm range (signal or idler can be utilized). Tuning through the pump wavelength of the second stage offers the possibility of NCPM, e.g. for type-I AGSe utilizing the signal from the first stage, or for narrow bandwidth type-II CdSe and ZGP, utilizing the idler as a pump. In addition, as already mentioned, rapid tuning can be performed independent of the PM type [297,298]. Degenerate or near-degenerate operation of the first stage enables pumping the second stage by both signal and idler. On the other hand the signal and idler from the first stage could pump two independently tunable OPOs [299]. Even more diversity to circumvent the quantum limit when pumping near 1 μm is possible by combining more than two OPOs and/or OPAs [168]. Apart from these new opportunities, however, the output quality from the first stage (in particular spatial profile and spectral bandwidth) becomes crucial when pumping a second OPO. The pump parameters for the second stage, including pulse duration, are not always specified in the literature because often only its output was characterized.

AGSe was employed in the first cascaded OPOs of this type in combination with type-I LiNbO₃ in the first stage [300,301]. In [300] type-I (ooe) AGSe ($L=25$ mm) was pumped by 15 ns, 50 Hz pulses at the signal wavelength of 1.82 μm and in [301] type-II (eoe) AGSe ($L=29$ mm) was pumped by 10 ns, 10 Hz pulses at the idler wavelength of 2.54 μm from the LiNbO₃ OPO. The efficiency of these SP-SROs was rather low due to the mentioned dependence on the pump quality. Special attention was paid to the beam quality of the first stage type-II NCPM KTP OPO (6 ns, 5 Hz, 1.57 μm) in [302] and the DP-SRO with type-I AGSe ($L=35.3$ mm), tunable from ~ 6 to 14 μm for the idler, delivered an energy exceeding 1 mJ at 9 μm . Upgrades of this system including a type-II NCPM KTiOAsO₄ (KTA, isomorph of KTP) OPO (10 ns, 5 Hz, 1.54 μm) led to idler energies as high as ~ 3.25 mJ at 7.75 μm and idler slope efficiency of 9% with a type-I AGSe ($L=25$ mm) crystal in optical contact with AR-coated ZnSe windows [303]. NCPM first stage OPOs based on KTP or KTA appear to be very suitable as pump sources also because wavelengths near 1.5 μm are available from mature systems developed for the purpose of obtaining the signal output in the eyesafe region. Further improvements of such tandem OPOs were directed towards power scaling at good idler beam quality from the AGSe SRO [304,305]. Idler energy as high as 6.8 mJ at 8.5 μm and 10 Hz and slope efficiency of 10.9% were achieved in [305] with two walk-off compensated type-I AGSe ($L=12$ mm) crystals pumped at 1.574 μm in single pass. Despite the large diameter beams, low divergence was obtained for both stages by using unstable confocal resonators that reduce the divergence of the oscillating beams each round trip, and the idler beam at 8.5 μm had $M^2=5.5$.

Type-I AGSe can be used at such pump wavelengths also in NCPM. In [306] with a 33-mm long crystal in a SP-SRO, idler wavelengths between 3.679 and 5.71 μm were demonstrated under the NCPM condition tuning the pump wavelength from 1.398 to 1.54 μm (idler from SH-pumped type-I KNbO₃ OPO). With a NCPM KTP OPO pump source at 1.54 μm the same NCPM AGSe SP-SRO produced energy of 120 μJ for the resonated idler at 3.71 μm which translates into an average power of 300 mW at 2.5 kHz [306]. Similar idler average power of 280 mW at 15 kHz ($\lambda_1 \sim 4$ μm), corresponding to 18% slope efficiency, was obtained in [307] with a DP-SRO based on type-I AGSe ($L=30$ mm) and analogous pump source. In [308], in order to satisfy the NCPM condition in AGSe for a specific idler wavelength ($\lambda_1=5.764$ μm), a pump wavelength of 1.401 μm was required which was generated by a NCPM RbTiOAsO₄ (RTA, another KTP isomorph) pumped at the SH of the Nd-laser at 532 nm. This DP-SRO employing a 20-mm long AGSe crystal delivered idler energy of ~ 1.3 mJ at 30 Hz [308].

Pumping AGSe below 2 μm in tandem OPOs helped to avoid the absorption feature observed in this crystal in the 2- μm spectral range. CdSe is another NLC studied in tandem OPOs which

requires longer pump wavelengths for broad tuning in the mid-IR. CdSe OPOs can be also tuned by the pump wavelength in NCPM configuration. Such CdSe ($L=35$ mm) DP-SRO was presented in [309,310]: Tuning the KTA OPO idler output from 2.99 to 3.45 μm produced $\lambda_1=8.31\text{--}10.58$ μm from the CdSe OPO with an estimated energy of ~ 2.2 mJ at 10.58 μm . Under critical PM and at lower energy levels, walk-off compensation can be applied as demonstrated in [311] with two CdSe ($L=25$ mm) crystals pumped at 2.596 μm by a KTA OPO.

Most of the recent work on cascaded OPOs has focused on ZGP. Similar to laser pumping, ZGP can be pumped by oxide-crystal based OPOs emitting near 2- μm or at longer wavelengths. Pumping near 2- μm offers the opportunity to utilize both signal and idler from a near-degenerate first stage OPO, whereas pumping at longer wavelengths is compatible with NCPM in type-II ZGP. LiNbO₃, KTP, KTA, PPLN, and PPKTP were used in the first stage of tandem OPOs with ZGP in the second one. The target has been to obtain high overall conversion efficiency from the 1- μm pump source at high energy levels or high average power (using more compact and flexible LD-pumped systems at kHz repetition rates). Most of the research was performed with near-degenerate DROs pumped near 2- μm , characterizing the combined signal and idler output.

The first such tandem OPO employed type-II KTP intracavity pumped in a Nd:YLF laser and one of its output beams of 2-ns pulse duration for pumping type-I ZGP ($L=13$ mm) [312]. The ZGP SP-DRO could be angle tuned between 4.1 and 5 μm simultaneously with the pump wavelength (2.05–2.5 μm) maintaining degeneracy, and delivered energy of 67 μJ at 4.4 μm which translates into an average power of 670 mW at 10 kHz.

Using the idler output of a NCPM type-II KTA OPO (7 ns, 5 Hz, 3.47 μm) a NCPM DP-DRO was demonstrated in [168,313] with type-II (oeo) ZGP ($L=12$ mm) which generated more than 1.5 mJ energy at 7.8 μm with a bandwidth of 8 cm^{-1} . Apart from this early work, type-II ZGP pumped above 2- μm was only rarely studied [314]. NCPM is attractive for low power systems because the threshold can be greatly reduced with focused beams. Using the tunable idler output from a PPLN OPO (~ 10 ns, 1 kHz, 2.3–3.7 μm) a DP-SRO based on type-II ZGP ($L=38$ mm) showed tunability from 5.6 to 10.2 μm with bandwidth of 5–6 cm^{-1} for the idler under NCPM and maximum energy of 23 μJ at 6.6 μm [315]. The threshold with a 24 mm long ZGP crystal was as low as 2 μJ corresponding to an axial fluence of 8.2 mJ/cm^2 (peak intensity of 0.82 MW/cm^2). In [316] critical PM in type-II ZGP ($L=14$ mm) in a DP-SRO pumped by the idler beam from a LiNbO₃ OPO (12 ns, 10 Hz, 2.55 μm) was studied in combination with spectral narrowing elements (grating substituting one of the OPO mirrors and an interactivity etalon) to achieve narrow spectral bandwidth for the resonated wave with broad spectral acceptance for the pump radiation. Bandwidths of the order of 0.1 cm^{-1} were reported in the 3.7 to 8 μm wavelength range, resonating either the signal or the idler, at an energy level > 10 μJ . The improvement due to the spectral selective elements was about two orders of magnitude. Note that the spectral bandwidths in conventional type-I ZGP OPOs range from hundreds of cm^{-1} near degeneracy to few cm^{-1} far from degeneracy.

In near-degenerate type-I ZGP OPOs, the conversion efficiency from the KTP OPO output to the ZGP OPO signal and idler can be quite high: In [317] total (signal and idler) conversion efficiency of 32% with slope of 42.5% was reported for a ZGP ($L=10$ mm) DP-DRO operating at 5 Hz. A similar ZGP ($L=18$ mm) DP-DRO operating at 8 kHz provided a total conversion efficiency of 38% with a slope of 46.6% resulting in combined average output power of 5.7 W [318]. A SP-DRO with a 16-mm long ZGP showed a total efficiency of 46.5% with slope of 73% and combined energy (signal and idler) of 2.65 mJ at 10 Hz near degeneracy [319]. This translates into an overall conversion efficiency of 10.3% with respect to the 1.064 μm pulse energy. Away from degeneracy ($\lambda_1=5.5\text{--}9.3$ mm), a ZGP ($L=10$ mm) DP-SRO showed a

conversion efficiency of 8.25% from the KTP OPO signal pulses (6 ns, 30 Hz, 2.02 μm) to the mid-IR idler at 8 μm [320]. The ZGP OPO idler energy (1.3 mJ) and conversion efficiency were much higher compared to a type-I AGSe crystal of $L=20$ mm under identical conditions.

The ZGP OPO itself can be pumped intracavity. Coupled cavities with one of the polarizations near 2.1 μm of a near-degenerate type-II KTP OPO were used in [321]. The type-I ZGP ($L=10$ mm) DRO/SRO idler was tunable from 4.2 to 8 μm . For $\lambda_1=4.3$ μm ($\lambda_2=3.8$ μm), a combined energy of 0.95 mJ was generated at 5 Hz equivalent to an overall (signal and idler) conversion efficiency of 5.2% with respect to the 1.064 μm pulse energy but the slope was 35%. Comparison at 5 kHz showed, however, that intracavity pumping of this DRO yields the same combined average output power near degeneracy (~ 2.5 W) as double pass pumping [322,323].

The effect of cavity matching was also investigated and exploited in tandem OPOs. When the ZGP DRO was pumped by a multilongitudinal-mode output of a KTP OPO, its output energy could be significantly increased when the optical lengths of the two OPOs were matched [324]. Utilizing this effect with only the signal beam from a KTP OPO (~ 20 ns, 20 Hz, 2.06 μm) and pumping a type-I ZGP ($L=15$ mm) SP-DRO, near-degenerate operation with 1.4 mJ combined (signal and idler) energy was achieved with overall conversion efficiency of 14% from 1.064 μm to the 3–5 μm range [325]. Weaker cavity matching effect was predicted also for SROs [326] and experimentally observed with a similar ZGP SP-SRO operating in the $\lambda_1=8$ –11.3 μm range (the longest wavelengths achieved with tandem ZGP OPO) [327]. Simulation of such systems taking into account all relevant effects such as dispersion, diffraction, absorption, spatial and temporal walk-off, multilongitudinal modes with large signal and idler bandwidths, spectral dependence of the resonator mirrors, and heating of the ZGP crystals is, however, a complex task [227].

Few methods were developed to utilize both the signal and idler from the first stage or to have single output from the first OPO stage near degeneracy. In principle type-I or QPM crystals in the first stage would provide a single polarization but near degeneracy the bandwidths will be too large for pumping ZGP in the second stage. In type-II PM, the polarization dependence of the mirror reflectivity in a ring OPO can be used to select one of the polarizations [325] or a thin film polarizer can be used in a linear cavity [328] but such dielectric coatings show reduced damage resistivity. With a ZGP ($L=11$ mm) DP-DRO pumped by the single output of the KTP OPO obtained by intracavity polarization beam splitter, 3.25 W of combined average output power were obtained at 10 kHz with a slope efficiency of 57% with respect to the 2- μm radiation [328]. In [329], using intracavity quarter-wave plate and polarization beam splitter the 2.128 μm output of a degenerate type-II KTP DRO (in fact NRO) was generated in a single beam without the instabilities associated with double resonance and this source was used to pump a ZGP OPO. In [330], a wavelength-dependent polarization rotator was developed to transform the orthogonal polarizations at the KTP-OPO output into a common polarization state when operating near degeneracy: The type-I ZGP ($L=12$ mm) DP-DRO produced a combined average output power of 5.5 W at 15 kHz, however, pumping at two slightly different λ_3 (2.08 and 2.14 μm), this power was distributed among two couples of signal and idler wavelengths near degeneracy.

PPKTP OPOs provide single polarization output but to reduce its bandwidth, VBG were employed which ensured near-SF operation for the signal [331–333]. Since the idler spectrum was also rather narrow the combined output (signal and idler) could be spectrally confined in only ~ 2 nm near 2.128 μm . Pumping a ZGP ($L=14.3$ mm) DP-DRO within its pump spectral acceptance delivered combined average output power (signal and idler between 3.7 and 5 μm) of ~ 3.2 W at 20 kHz; in this case the spectra of the two signal-idler pairs had almost merged [333]. The overall conversion efficiency was 12% relative to the 1.064 μm pulses. The same idea and DP-DRO were exploited also at low repetition rates and the combined energy achieved was

250 μJ at 10 Hz [332]. Another option to generate narrowband pump pulses with QPM materials near 2 μm is to operate the first stage away from degeneracy with a different pump laser, as described in [334] with a PPLN OPO in the first stage pumped by a 1.342 μm Nd:YVO₄ laser.

In [335] the signal and idler from a degenerate type-II KTP OPO at 2.013 μm were separated by a polarizer to pump two type-I ZGP ($L=12$ mm) DP-DROs: a combined average power of 24 W at 20 kHz with $M^2\sim 4$ was obtained at $\lambda_2=3.7\text{--}4.1$ μm and $\lambda_1=4.4\text{--}4.8$ μm from ~ 50 W of input power at 2.13 μm . The orthogonal output polarizations of such near-degenerate KTP OPO (2.128 $\mu\text{m}\pm 0.5$ nm) were also used to pump separately a ZGP ($L=16$ mm) DP-DRO and a ZGP OPA (two walk-off compensated crystals of $L=8$ mm) seeded by both signal and idler [336] with an overall (signal and idler in the 3.8–4.8 μm range) conversion efficiency of $\sim 14\%$ with respect to the 1.064 μm pump. A similar set-up in the high energy regime (10 Hz) was described in [337] using 15-mm long type-I ZGP in the DP-DRO and OPA stages: the combined output energy near degeneracy (4.256 μm) reached 26 mJ but similar to [336], the gain in the OPA stage was < 2 . The ZGP OPO alone when operated as SRO was tunable up to 12 μm (1 mJ) [337].

Tandem OPOs have produced so far inferior average powers and pulse energies in comparison with 2- μm laser pumped OPOs but at present both concepts are quite comparable in their overall potential with the limits in both cases set by available average pump power and thermal lensing effects in the kHz regime or by optical damage when high energy is targeted. A very nice review on the design consideration and interrelations between different parameters and criteria can be found in [338]. The pump beam quality becomes even more critical for energy scaling of tandem OPOs. To this aim, a MOPA approach was adopted in [339] for the first stage KTP OPO whose signal output at 2.08 μm was used to pump a near-degenerate type-I ZGP ($L=6$ mm) SP-DRO. The maximum output energy of 28 mJ (signal and idler) obtained at 10 Hz corresponds to 33% total conversion efficiency, but with a short plane-plane resonator and wide pump beam, the ZGP OPO beam quality was poor ($M^2 > 100$). The beam quality was improved to $M^2\sim 15$ at an energy level of 21 mJ by using a MOPA approach also for the ZGP stage, pumping the OPO with the idler at 2.18 μm and the OPA with the signal at 2.08 μm from the first stage.

As discussed before, in high energy OPOs, the pump beam diameter must be large to avoid damage in the NLC but with short cavities this may lead to a high Fresnel number resulting in poor beam quality due to a large number of transverse modes. One possible solution is the use of confocal unstable resonators [340], another possibility is the RISTRA cavity which was recently demonstrated also in a tandem OPO [341]. In this work the pump laser was a LD-pumped, 100 Hz, Q-switched SF Nd:YAG delivering 80 mJ, 10 ns pulses at 1.064 μm . The laser output was split into two channels, one powering a master PPKTP OPO with a VBG as an output coupler for spectral narrowing, while the other was used to pump a Rb-doped PPKTP OPA. Such a MOPA configuration was employed for the first stage of the cascade for better control over the beam quality and the spectral width of the output. The output of the 2.128 μm MOPA with pulse duration of 8 ns was used for pumping the second stage which employed type-I ZGP ($L=14$ mm).

The RISTRA design enabled output wavelength tuning by simply rotating the cavity without any additional adjustments. For $\pm 1^\circ$ -rotation from the collinear position the idler was tunable from 6.27 and 8.12 μm with the corresponding signal in the 3.22–2.88 μm range. The measured signal ($\lambda_2=3.176$ μm) and idler ($\lambda_1=6.45$ μm) output energies as a function of the 2.128 μm pump energy after the RISTRA incoupling mirror are shown in Fig. 23. The maximum idler energy here was 0.91 mJ at the pump energy of 21.3 mJ and the pulse duration was 5 ns. Note that the repetition rate of 100 Hz (desirable for surgical applications) is quite challenging for LD-pumped laser systems, and these results are unique in terms of energy level at such repetition rate.

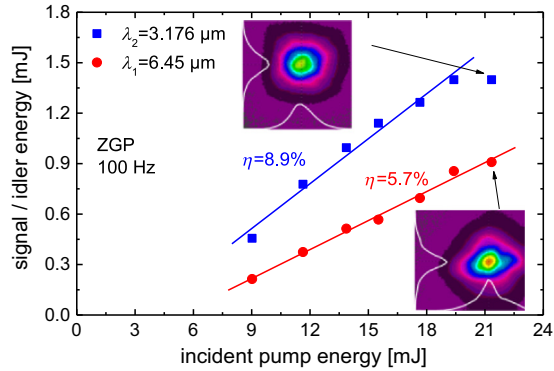


Fig. 23. Signal and idler energy of the ZGP RISTRA OPO vs. pump energy with the insets showing the spatial intensity profiles measured at a distance of ~ 47 cm from the ZGP crystal. (Courtesy of G. Stoeppler, M. Eichhorn, ISL, and N. Thilmann, V. Pasiskevicius, KTH, from [341]).

An alternative solution for high energy with good beam quality is the MOPA approach in which a master OPO is pumped with a low-energy, narrow pump beam, to suppress higher order transverse modes and the signal or idler from the master OPO seeds the OPA, where the pump diameter is large but this does not affect substantially the beam quality. As already mentioned, this approach was presented in [339] achieving gain of ~ 38 in the OPA stage. However, it is not necessary that both stages rely on ZGP. Even higher energies were obtained with ZGP used only in the final OPA [342]: In this system, starting from a 500 mJ, 6-ns, SF Nd:YAG laser operating at 10 Hz, the pump arm at $2.08 \mu\text{m}$ comprised KTP MOPA (using its signal output) and the signal arm – a KTA OPO whose idler was tunable between 2.8 and $3.7 \mu\text{m}$. The final type-I ZGP ($L=10$ mm) OPA, pumped by 75 mJ and seeded with ~ 0.1 mJ at the signal wave, generated idler between 4.7 and $8 \mu\text{m}$ with a maximum energy of > 8 mJ at $8 \mu\text{m}$ and combined energy near degeneracy (signal and idler in the 3–5 μm range) of 33 mJ [342]. These values emphasize the OPA regime in contrast to DFG experiments with ZGP described previously. The measured beam quality factors were in the range $M^2=2-4$ for both wavelength ranges. Surface damage of the ZGP crystal limited the achievable energy and also parasitic OPO effect due to imperfect AR-coatings was observed in the near-degenerate case.

Amplified ns pulses with sufficient energy can be used to pump separate OPAs based on highly nonlinear crystals such as ZGP to obtain sufficient gain even in the ns regime. This is similar to the OPA experiments with OPGaAs described before with laser pumping near $2 \mu\text{m}$. Such a SF near-IR MOPA (11 ns, 30 Hz, $2.21 \mu\text{m}$) was employed in [343] to pump type-I ZGP ($L=15$ mm) OPA which was seeded at the idler wavelength ($\lambda_1=7.8-8.4 \mu\text{m}$) by a tunable SF QCL. Gain in excess of 100 was achieved for pump energy of 7.5 mJ at $2.21 \mu\text{m}$ [343].

Finally, OPGaAs with its intrinsic NCPM directly profits from the tunable nature of the pump in tandem OPO configurations. Employing a 0.5 mm thick OPGaAs ($L=11$ mm, $\Lambda=61.2 \mu\text{m}$) and tuning either the pump from the first stage PPLN OPO, whose signal output between 1.75 and $2.01 \mu\text{m}$ (6 ns, 10 Hz) was spectrally narrowed near degeneracy by an intracavity etalon, or the OPGaAs temperature, the first ever OPGaAs OPO operated in the 5.8–11.1 μm idler spectral range with a single grating period [344,345]. This DP-SRO had a very low threshold and its total (signal plus idler) efficiency reached 26% with a slope of 54%. A > 1 mm thick sample of OPGaAs ($L=20$ mm, $\Lambda=150 \mu\text{m}$) was studied in a DP-SRO pumped by the idler pulses from a

PPLN OPO (20 ns, 2 kHz, 2.99–3.15 μm) for narrowband operation [346]. The bandwidth of the PPLN OPO was narrowed through an etalon while the operation of the OPGaAs OPO around degeneracy and the retracing point (Fig. 3) enabled broad tuning for signal and idler with combined energy of 7 μJ at 6 μm . Tuning was achieved by rotation of a cavity grating which acted on the signal and to a lesser extent by the pump wavelength, at a fixed period of the OPGaAs structure. The output bandwidth measured was between 2 and 6 cm^{-1} for the entire 4–14.2 μm range of the orthogonally polarized signal and idler.

As already mentioned, an interesting property of OPGaAs is that due to its high, cubic symmetry it can be also pumped with two orthogonal polarizations [347]: This was confirmed by converting the output polarization of a first stage PPLN OPO into circular or pseudo-depolarized, observing that in both cases the threshold of the OPGaAs OPO stage remained low and almost unchanged. This work demonstrated some of the diverse polarization combinations offered by GaAs and related zincblende NLCs such as GaP and ZnSe.

6.3. Down-conversion of ultrashort pulses

DFG is the simplest method for down-conversion of ps and fs laser pulses but again it requires two input wavelengths, at least one of them in the form of ultrashort pulses. Since idler photons are only produced by annihilation of pump photons, obviously it is more important to have high intensity (ultrashort pulse) at λ_3 but preferably also at λ_2 . DFG is a low gain process but the conversion efficiency is normally higher than in single stage OPG, in particular when the OPA regime can be reached using powerful (amplified) pump pulses at low (up to ~ 1 MHz, but in most cases not more than few kHz) repetition rate. OPG and SPOPO require just a single pump source. Ultrafast OPG is often then combined with OPA. High conversion efficiency is typical for SPOPOs which down-convert low-energy pulses at high (~ 100 MHz) repetition rates.

6.3.1. DFG of ps and fs pulses

DFG of ultrashort pulses is a universal method for down-conversion that can be applied with energetic low repetition rate laser oscillators or amplifiers and with low-energy mode-locked laser oscillators or SPOPOs operating at high repetition rates. More recently fiber based pump systems become available which encompass amplification at high repetition rates.

6.3.1.1. DFG of low energy ultrashort pulses at high repetition rates. Before the advent of the mode-locked Ti:Sa laser, the primary source of cw trains of ultrashort (ps or fs) pulses were synchronously-pumped or passively mode-locked dye lasers. The output power of the latter was too low for efficient DFG. Synchronously-pumped dye lasers could be mixed with their pump laser which had the same repetition rate but at substantially longer pulse duration.

In [348] such a ps dye laser pumped at the SH (532 nm) of a mode-locked Nd:YAG laser was mixed in type-I AGS with the residual fundamental, which was compressed with a fiber-grating compressor. This complex set-up produced average power of only 18 μW at 5 μm , see Table 8, and pulse durations of the order of 2 ps.

With the advancement of Ti:Sa laser technology in the 1990s, mode-locked oscillators became commercially available with average power on the watt level at ~ 100 MHz, generating both ps and fs pulses around 800 nm. Such average powers were roughly 1 and 2 orders of magnitude higher compared to synchronously-pumped and passively mode-locked dye lasers, respectively. However, the emission wavelength of these ultrafast SSLs is too short for pumping non-oxide NLCs because of the TPA limitation especially taking into account the tight focusing necessary

Table 8

DFG of ultrashort (ps and fs) laser sources in non-oxide NLCs at high (~ 100 MHz) repetition rates. CD: cavity dumping, RS: Raman soliton, SC: supercontinuum, FC: frequency comb generation.

Crystal-type, $\theta(\varphi)_{\text{cut}}, \Delta$	L [mm]	Pump and Signal sources/Repetition rate	λ_1 [μm]	Idler energy @ Wavelength	Refs.
AGS-I, 53.2°	1.65	Nd:YAG+SH:dye/76 MHz	3.4–7	~ 0.24 pJ @ $5 \mu\text{m}$	[348]
AGS-I, 40°	1	Ti:Sa:SPOPO (signal+idler)/82 MHz	2.5–5.5	~ 6 pJ @ $4.03 \mu\text{m}$	[349]
AGS-I, 50°	2	Ti:Sa:SPOPO (signal+idler)/80 MHz	2.6–5.3	5 pJ @ $3.4 \mu\text{m}$	[350]
AGS-I, 33°	2	Ti:Sa:SPOPO (signal+idler)/76 MHz	5.2–14.5 ^a	17.1 pJ @ $8.5 \mu\text{m}$	[351]
GaSe-I, 0°	1		5.2–18 ^a	26.3 pJ @ $8.5 \mu\text{m}$	
AGSe-II, 66°	1	Ti:Sa:SPOPO (signal+idler)/84 MHz	8–18	12 fJ @ $10\text{--}18 \mu\text{m}$	[352]
AGS-I, 44°	1	Dual-wavelength Ti:Sa/85 MHz	9	30 fJ @ $9 \mu\text{m}$	[353]
AGS-I, 39°	1	Dual-wavelength Ti:Sa/82 MHz	7.5–12.5	61 fJ @ $10 \mu\text{m}$	[354]
GaSe-I, 0°	1	Ti:Sa+Ti:Sa/100 MHz	7.5–12.5	~ 150 fJ @ $>9 \mu\text{m}$	[355]
GaSe-I, 0°	1	Broadband Ti:Sa/88 MHz	9–18	11 fJ @ $15 \mu\text{m}$	[356]
	0.5	CD broadband Ti:Sa/2 MHz	7–20	2.5 pJ @ $14 \mu\text{m}$	[357]
GaSe-I, 0°	0.2	Broadband Ti:Sa/125 MHz	9–12, FC	~ 80 fJ @ $10 \mu\text{m}$	[358]
GaSe-I, 0°	10	Nd:YVO ₄ +SC/2 MHz	5–12	500 pJ @ $6 \mu\text{m}$	[359]
CdSe-II, 70°	15	Nd:YAG: SPOPO (signal+idler)/25 Hz in bursts of 100 pulses @ 100 MHz	10–21	2.8 μJ @ $11 \mu\text{m}$ 0.8 μJ @ $15 \mu\text{m}$	[360]
GaSSe-I, 0°	1.6	Ti:Sa:SPOPO (signal+idler)/80 MHz	4–12	70 pJ @ $7.2 \mu\text{m}$	[361]
LiSe-II, 35°	4		4–11.5	130 pJ @ $7.2 \mu\text{m}$	[362]
GaSe-II, 0°	1	Yb:KGd(WO ₄) ₂ : dual-wavelength	10.6–16.2	29 pJ @ $12 \mu\text{m}$	[363]
GaSe-II, 0°	2	SPOPO (signal+signal)/41.7 MHz	12.7–14.3	50 pJ @ $13.5 \mu\text{m}$	
AGSe-II, 49°	3		12.7–14.3	103 pJ @ $13.2 \mu\text{m}$	
GaSe-I, 0°	2	Yb:KGd(WO ₄) ₂ +SC/41.7 MHz	4.85–9.33	20 pJ @ $6.46 \mu\text{m}$	[364]
AGSe-I, 57°	2	Yb-fiber:SPOPO (signal+idler)/53 MHz	5–17	1.3 nJ @ $\sim 6 \mu\text{m}$	[365,366]
LiSe-II, 35°	4	Yb-fiber:SPOPO (signal+idler)/53 MHz	5–12	1.25 nJ @ $6.2 \mu\text{m}$	[367]
		Yb-fiber:SPOPO (signal+idler)/80 MHz	5–12	0.21 nJ @ $6.1 \mu\text{m}$	
AGSe-I, 52°	10	Yb-fiber:SPOPO (signal+idler)/80 MHz	5–18	1.75 nJ @ $6 \mu\text{m}$	[366,368]
GaSe-NA, 0°	1	dual-wavelength Yb-fiber (RS or SC)/ 50 MHz	~ 18 17.5 16–20	0.4 pJ @ $18 \mu\text{m}$ 8 pJ @ $17.5 \mu\text{m}$ 30 pJ @ $18 \mu\text{m}$	[369] [370] [371]
AGSe-II, 59.6°	5	Er-fiber+RS/37 MHz	9.7–14.9, FC	~ 40 fJ @ NA	[372]
GaSe-II, 0°	1		FC		
GaSe-I, 0°	1	Er-fiber+RS/100 MHz	5–12, FC	~ 1.6 pJ @ $6.3 \mu\text{m}$	[373]
GaSe-I, 0°	1	Er-fiber+RS/250 MHz	8–14, FC	16 pJ @ $7.8 \mu\text{m}$	[374]
GaSe-I, 0°	0.5	Yb-fiber+RS/151 MHz	3–10, FC	~ 10 pJ @ $4.7 \mu\text{m}$	[375]
AGS-II, 50°	2	Yb-fiber+SC/40 MHz	5.3–6, FC	75 pJ @ $5.5 \mu\text{m}$	[376]
AGS-II, 50°	2	Yb-fiber: (SC+SC)/40 MHz	4.2–9, FC	16 pJ @ $4.5 \mu\text{m}$	[377,378]
GaSe-NA, 0°	1	Er-fiber+SC/40 MHz	4–17, FC	25 pJ @ NA	[379]
GaSe-NA, 0°	0.5	Er-fiber+SC/80 MHz	8–12, FC	~ 0.1 pJ @ $9 \mu\text{m}$	[380]
CSP-I, 66.5°	1.5	dual-wavelength Er,Tm,Ho-fiber/100 MHz	6.5, FC	150 pJ @ $6.5 \mu\text{m}$	[381]
AGS-II, 37.5°	2	dual-wavelength Er,Tm-fiber/40 MHz	7.5–11.6, FC	39 pJ @ $9.2 \mu\text{m}$	[382]
OPGaAs, $52\text{--}82 \mu\text{m}$	2	Tm-fiber+RS/72 MHz	6.7–12.7, FC	18 pJ @ $10.3 \mu\text{m}$	[383]
LGS-I, NA	0.5	broadband Yb:YAG (after compressor)/ 100 MHz	10, FC 10, FC	0.45 nJ @ $10 \mu\text{m}$ 1.03 nJ @ $10 \mu\text{m}$	[384]

^aUpper wavelength limits specified at $\sim 1\%$ of maximum energy level.

or the fs regime. Thus, the best results in terms of average power in the mid-IR were obtained by first pumping a near-IR SPOPO which can be a very efficient process and then mixing its signal and idler which are tunable around the degeneracy point near 1.6 μm . Note that (i) such SPOPOs became practical also only after the advent of the mode-locked Ti:Sa laser and the simultaneous development of few oxide NLCs with improved properties (LiB_3O_5 , KTP), and (ii) mixing simultaneously tunable signal and idler from the first stage offers easy access to a very broad tuning range for the mid-IR idler from the second stage DFG. Two NLCs were very useful for DFG with such SPOPOs: AGS and GaSe, Table 8. The longest idler wavelength achieved with AGS (14.5 μm [351]) is already in the phonon absorption range. GaSe is normally chosen above 12 μm . Below 12 μm , AGS is preferable because GaSe, though with much higher FM, shows additional problems; specific for such low energy DFG is the large spatial walk-off due to its large birefringence. As can be seen from Table 8, pJ pulse energies and broad tunability were achieved with such DFG using fs near-IR SPOPOs as an intermediate stage [349–351]. AGSe also exhibits higher FM and wider transparency compared to AGS but DFG is limited to long wavelengths [352] because of birefringence and TPA restrictions (Table 8).

DFG based directly on mode-locked Ti:Sa lasers (broadband, dual-wavelength, or two synchronized lasers) produced only fJ energies, Table 8. In addition to the mentioned limitations, the idler was restricted to $\lambda_1 > 7.5 \mu\text{m}$ because of the small separation of λ_3 and λ_2 .

All the systems based on direct or indirect pumping by Ti:Sa lasers operated in the fs regime for better efficiency although there are no principle restrictions to start with a ps Ti:Sa laser if narrower bandwidths are desirable. However, the mid-IR pulse durations obtained were often of the order of few hundred fs because a trade-off with the efficiency is always necessary in such DFG: Roughly speaking Δ_{32} will determine the efficiency of the process and Δ_{31} – the duration of the idler pulses, and very thin crystals maintaining the input pulse durations will result in low efficiency and vice versa. The mid-IR pulse energies in earlier experiments correspond to very low average powers, in the best case $> 1 \text{ mW}$ in the 8 μm range, using either GaSe or AGS [351].

The energy can be increased using more complex setups but at the expense of the repetition rate. Cavity dumping [357] or long cavity [359] of the mode-locked pump laser was realized at a repetition rate of 2 MHz. Pulsed (burst mode) operation of the mode-locked laser is also possible. In [360] the Nd:YAG laser/amplifier was mode-locked at 100 MHz but emitted macropulses at 25 Hz – the SPOPO maintains the temporal structure and μJ micropulse energies were generated in the mid-IR, Table 8. In this work also the longest idler wavelengths (21 μm with CdSe) were demonstrated. OPA regime is possible at high pump intensities [359].

Recently, the results obtained with SPOPOs pumped by Ti:Sa lasers were substantially improved achieving continuous tuning from 4 μm ($> 12 \text{ mW}$) to 12 μm ($> 0.5 \text{ mW}$) with almost bandwidth limited mid-IR pulses of $\sim 200 \text{ fs}$ duration (similar to the input pulses) using $\text{GaS}_{0.4}\text{Se}_{0.6}$ (GaSse in Table 8) which exhibits some advantages over GaSe, see Section 5 [361]. To a great extent this improvement was due to the use of commercial ultrafast systems (4 W Ti:Sa laser and SPOPOs based on QPM materials). The wide band-gap LISe with its superior thermal conductivity and damage resistivity was also tested in this set-up [362], achieving continuous tuning from 4 μm (16.7 mW) to 11.5 μm (2.3 mW) and almost 2 times higher conversion efficiency. The mid-IR pulses were ~ 2 times longer because of the relatively long crystal but the pulse spectra were narrower.

The next stage in the development of such DFG systems is connected to the use of Yb-lasers emitting in the 1- μm spectral range as pump sources which, in contrast to Ti:Sa lasers, are power scalable by direct LD-pumping. Their longer pump wavelength offers additional advantages. It is more suitable for pumping SPOPOs built with oxide QPM materials such as PPLN which then

emit at longer wavelengths (degeneracy point near 2 μm), compatible with DFG schemes based on smaller band-gap NLCs possessing higher FM. In particular AGSe can be employed with such SPOPO output wavelengths [365,366], with which average power of up to 69 mW near 6 μm and more than 1 mW at 17 μm was achieved in the fs regime, Table 8 and Fig. 24.

Bulk Yb-lasers can also be applied [363] but fiber based pump systems can be power scaled by Yb-fiber amplifiers, including chirped-pulse amplification, maintaining the high repetition rate. If NLCs with larger band-gap are used, such as LISe [367], then they can be longer because the GVM is reduced at such input wavelengths. With the same (non-optimized) sample length LISe showed good performance also in the ps regime, Table 8 and Fig. 24, which provides narrower spectral bandwidths in the mid-IR for better resolution in spectroscopy, Fig. 25. The Yb-fiber laser/amplifier pump systems used to obtain the results in Fig. 24 had maximum average power of 5 and 11 W in the fs and ps regime, respectively.

From the autocorrelation function (ACF) FWHM in Fig. 26a one can conclude that the fs pulses produced at 7.2 μm by DFG in LISe [367] have a Gaussian FWHM (intensity) of 313 fs, only slightly exceeding the pump pulse duration of the Yb-fiber laser. With the corresponding spectral FWHM of $\sim 360 \text{ nm}$ (69 cm^{-1}) this gives a time-bandwidth product (TBP) of ~ 0.65 . The much narrower bandwidths obtained in the ps regime (Fig. 25b) and the pulse duration of

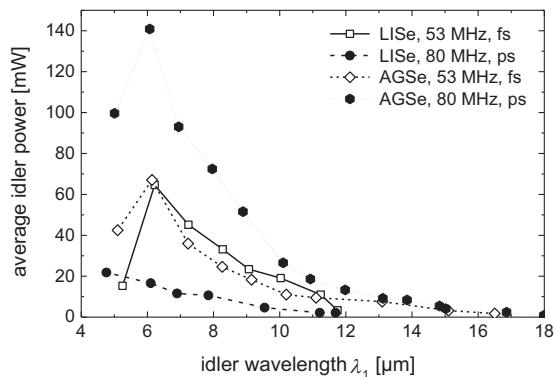


Fig. 24. Average DFG power at 53 MHz in the fs regime and average DFG power at 80 MHz in the ps regime using LISe and AGSe crystals [365–367].

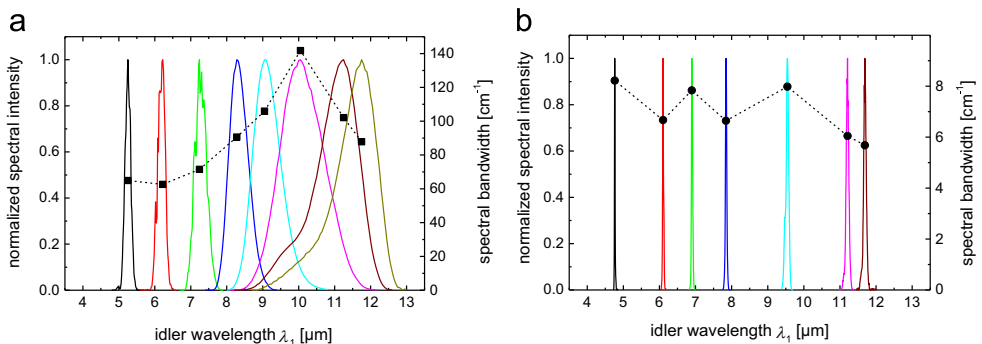


Fig. 25. Recorded DFG spectra demonstrating the achieved spectral tunability with LISe in the fs (a) and ps (b) regimes [367]. The dashed lines refer to the right scale and show the spectral bandwidth.

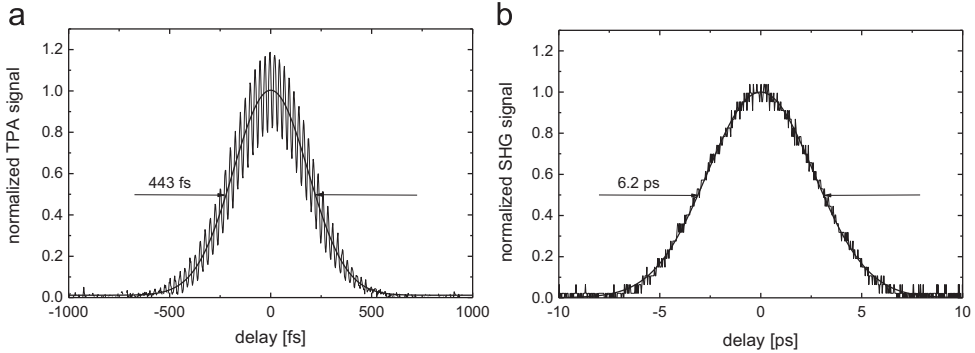


Fig. 26. Recorded ACFs of the fs DFG pulses at $7.2\ \mu\text{m}$ (a) and the ps DFG pulses at $4.8\ \mu\text{m}$ (b) generated with LISe [367]. Fringes in (a) result from imperfect noncollinearity in the autocorrelator. The ACFs were measured utilizing either TPA in a HgCdTe photodetector (a) or SHG in a 1-mm thick type-I AGSe crystal (b).

4.4 ps (Fig. 26b), which also reproduces more or less the value for the pump pulses near $1\ \mu\text{m}$, lead to a $\text{TBP}=1.08$. In both cases the TBP is also close to the value estimated for the corresponding Yb-fiber based pump sources [367]. AGSe yielded record high average power (140 mW) in the ps regime with single pulse energy of 1.75 nJ at $\lambda_1=6\ \mu\text{m}$ [366], see Table 8 and Fig. 24.

With pump sources emitting near $1\text{-}\mu\text{m}$ or beyond, instead of using SPOPO, DFG can be performed with the pump source and a frequency shifted pulse or between amplified parts of supercontinuum generated in highly nonlinear and photonic crystal fibers (PCFs) [359,364, 369–371]. Direct mixing with supercontinuum parts yielded relatively low energies [364]. Amplification in Yb-fibers before the DFG stage is feasible for power scaling since the gain spectrum is broad enough to accommodate two wavelengths of sufficient separation but the tuning range of the idler is then limited [369–371]. However, such an approach has further important implications in relation to frequency comb generation in the mid-IR [385]. In the case of fs pulse durations, such frequency combs can be viewed as a collection of $\sim 10^5$ phase-locked narrow-bandwidth cw sources, which can be applied to massively parallel high resolution spectroscopy. Direct generation of mid-IR frequency combs is challenging due to a lack of suitable fs laser sources but DFG between phase-correlated pulses, where the generated centre frequency is determined by the spectral separation of the pump and signal pulses, is a viable alternative. Thus it is important that, when the pump and signal pulse trains originate from the same oscillator (e.g., by self-frequency shifted Raman solitons or continuum generation [372,373]), they share the same carrier-envelope offset (CEO) which is canceled in the DFG process automatically [385], leaving only stabilization of the repetition rate to produce a stable optical comb.

The frequency comb generation systems presented in [372,373] were based on Er-fiber lasers near $1.5\ \mu\text{m}$ combined with amplification stages. In [375] an average power of 1.5 mW at $4.7\ \mu\text{m}$ was reported with an Yb-fiber frequency comb generator. In both cases GaSe, through its large birefringence, seems the ideal candidate for such DFG covering broad spectral ranges. The highest average power of 4 mW at $7.8\ \mu\text{m}$ was demonstrated at 250 MHz [374] but the output energies were in general limited when relying on Raman solitons, Table 8. More recently, with a special PCF design for continuum generation the seed signal level could be drastically increased leading to maximum idler energy of 75 pJ at $5.5\ \mu\text{m}$ obtained using AGS [376], Table 8. Nevertheless, broader wavelength range in the mid-IR could be covered using GaSe, pumped

with an Er-fiber laser system [379]. In [381] a dual-wavelength all-fiber system comprising an Er-fiber mode-locked oscillator with Er-fiber and Tm,Ho-fiber amplifier arms was used to investigate broadband DFG in CSP under noncollinear PM, producing average powers of 15 mW (50 times higher than AGS) and spectra supporting 2.3 optical cycles at 6.5 μm . AGS was studied in a similar scheme in [382], generating longer idler wavelengths. OPGAs offers further opportunities for frequency comb generation in the mid-IR, with attractive FM and spectral coverage, but has to be pumped by Tm-fiber fs laser systems near 2 μm [373].

Note that phase-matched DFG between frequency components of extremely broad spectra, as those emitted by ultimately short pulse lasers [356], can also be exploited for efficient frequency comb generation as demonstrated in [358] with GaSe pumped by 10-fs Ti:Sa lasers emitting 100 nm broad spectra. The problem with GaSe is that it will experience TPA losses at 800 nm and also in the 1- μm spectral range. Recently LGS, the non-oxide NLC with the widest band-gap according to Table 2 (3.76 eV correspond to ~ 330 nm) was employed for broadband frequency comb generation pumped near 1 μm [384], Table 8. The pump system comprised a high power thin-disc Yb:YAG oscillator followed by a nonlinear compression stage to obtain 50 W of average power in 24-fs pulses. The average power converted to the 10- μm range in sub-2 cycle pulses reached 103 mW with the 1-mm LGS.

6.3.1.2. DFG and OPA with high energy ultrashort pulses at low repetition rates. When pump intensity is much higher than signal intensity, it is often difficult to distinguish between DFG and OPA because the exact seed level is unknown. DFG of high energy pulses works at lower pump intensities compared to OPG (no seed signal) and in this way optical damage can be avoided especially in temporal regimes affected by large GVM (i.e., fs pulses) which require short NLCs (exactly when OPGs are plagued by complex spatio-spectral distribution of the output if noncollinear PM exhibits lower GVM).

DFG or seeded OPA not only helps to avoid damage problems and suppress noncollinear processes in OPGs, it provides better spectral control for generation of Fourier-limited pulses in the opposite limit, i.e., for ps pulses. This is problematic in OPGs when the pump pulses are too long with respect to the (maximum available) NLC length and the parametric gain bandwidth is much larger than the pump pulse bandwidth.

The first report on ps DFG with a non-oxide NLC dates back to 1979 [386]. Signal and idler from a 1- μm pumped LiNbO₃ OPG-OPA were mixed in CdSe, Table 9. The idea is the same as discussed for DFG with SPOPOs and became one of the standard approaches for tunable DFG of energetic pulses, using also other laser sources and NLCs, Fig. 27a. In another approach, demonstrated almost simultaneously with Ag₃AsS₃, the fundamental of a mode-locked Nd:glass laser acting as a pump was mixed with the idler from a SH-pumped OPG (acting as a signal for the DFG process) [387], Table 9. This scheme, Fig. 27b, was also often used in the following years for DFG and OPA when it was impossible to reach the OPG threshold without damage. Many other alternatives exist to derive a synchronized in time seed signal. Since the pump pulse is always derived from a mode-locked laser by picking pulses at lower repetition rate and eventually amplifying them, the available high repetition-rate pulse train or burst can be used to pump a SPOPO whose output serves as a seed at low repetition rate, too.

As in DFG based on SPOPO, AGS became soon the NLC of choice also in DFG with energetic pulses at low repetition rates, Table 9. In the ps regime, most often Nd-laser pump radiation was mixed with seed signal from some laser or parametric source pumped by the same Nd-laser, or its second or third harmonic, such as traveling-wave or short cavity dye lasers, DFG, OPG, OPA, and SPOPO [388–395]. In many of those experiments in fact the OPA regime was

realized, Table 9. Multiple DFG stages were also applied as walk-off compensation schemes [390,391,394], however, intermediate seeding by both signal and idler or too long crystals turned out to lengthen the output pulses due to GVM [390,394]. Of course this effect depends on the pump pulse duration [393,394]. In [391], suppressing the idler by filters between the multiple AGS crystals resulted in roughly 3-times shorter pulses in the mid-IR (down to 0.5 ps). The longest wavelength reached in high energy DFG with AGS was 12.9 μm [394].

Subsequent DFG studies in the ps regime were directed towards extension to longer idler wavelengths using GaSe or CdSe [395–399]. Pulses of the order of 1 ps and even of sub-ps duration were obtained starting with mode-locked Nd:glass pump lasers [395,396]. However, longer ps pulses provide better spectral resolution: at DFG pulse duration ~ 100 ps, the achieved spectral bandwidths were $\sim 0.5 \text{ cm}^{-1}$ which corresponds to about 3 times the Fourier limit [398]. This work was also the only demonstration of ps DFG at kHz repetition rate. The longest idler wavelengths ($\lambda_1 \sim 28 \mu\text{m}$) were achieved with GaSe and Er-doped GaSe which shows reduced phonon absorption [397].

Few other crystals were investigated for pumping with 1- μm ps sources including LIS and BGSe, Table 9. Both of them delivered one of the highest energies in the mid-IR from such devices. Of special interest is also the substitution of GaSe by S-doped GaSe in order to avoid TPA at 1.064 μm [400], see Fig. 28. The performance of GaS_{0.4}Se_{0.6} (GaSSe) was superior for this pump wavelength although its nonlinear coefficient is lower compared to undoped GaSe.

CGA and DBGaAs (third order QPM) were also studied in the ps regime, mixing signal and idler from OPG-OPA pumped by 2.8 μm mode-locked Cr,Er:YSGG lasers [404,405], however, judging from the results, such pump sources seem not to offer some specific advantages.

Summarizing, ps DFG mostly relied on mode-locked and amplified Nd:YAG pump lasers and one of the sets-ups depicted in Fig. 27. The output idler energies in the mid-IR were typically on the 10- μJ level, only in few cases above 100 μJ , and energies above 1 mJ have not been demonstrated, yet. Note that tunable ps pulses can be produced by DFG employing the scheme in Fig. 27a also on the basis of ultrafast Ti:Sa laser systems [406], as discussed below for the fs regime, see Table 10.

The first fs DFG in the mid-IR was demonstrated with AGS [407], pumping with a dye amplifier at 620 nm and seeding with continuum generated in water. Soon after that, however, Ti:Sa regenerative amplifiers emerged as most adequate primary pump sources with stable operation and pulse to pulse reproducibility at kHz repetition rate. Traveling-wave dye lasers were used at first to generate a synchronized in time seed signal [408,409] but direct pumping at Ti:Sa wavelengths (as at 620 nm) strongly limits the output energy from AGS due to TPA. Mixing the signal and idler from a Ti:Sa pumped near-IR OPG-OPA in AGS was first reported in [410], see Table 10. Continuous tunability from 3.3 to 10 μm was achieved at 1 kHz with pulse durations ~ 160 fs, starting with sub-100 fs signal and idler pulses. This approach based on Fig. 27a and using AGS or GaSe not only became widespread but was implemented in commercial products with BBO employed in the intermediate stage as well. The longest mid-IR wavelength achieved with AGS was 15 μm [446] and with GaSe it was 20 μm , see Table 10.

In [420] HGS generated $> 9 \mu\text{J}$ near 4 μm and $> 1 \mu\text{J}$ in the entire tuning range up to 12 μm , Fig. 29a. It showed superior performance compared to AGS while in both crystals type-II PM was selected due to its higher d_{eff} . With shorter pump pulses and crystal length, 84 fs (5 optical cycles) Fourier-limited idler pulses were obtained near 5 μm (Fig. 29b) using the quaternary crystal AgGaGe₅Se₁₂ (Table 10) in the DFG stage [421]. This solid solution has sufficiently large band-gap to avoid TPA and, as a selenide, higher nonlinearity but larger GVM compared to AGS.

Table 9

DFG of ps pulses in non-oxide NLCs at low repetition rates. In this table OPG sources always contain OPA stage, i.e. OPG in the third column always means OPG-OPA, while lasers in most cases include amplification stage. “+” means more crystals in series, TH: third harmonic pumped, NA: not available.

Crystal-type, $\theta(\varphi)_{\text{cut}}, \Lambda$	L [mm]	Pump and Signal sources/ Repetition rate	λ_1 [μm]	Idler energy @ Wavelength	Refs.
CdSe-II, 64.35°	10	OPG (signal+idler)/10 Hz	14.8–18.5	2 μJ	[386]
Ag ₃ AsS ₃ -I, 30.5°	13	Nd:glass+SH:OPG (idler)/1 Hz	3.7–10.2	25–50 μJ	[387]
AGS-I, 45°	15	Nd:YAG+dye/4/min.	3.9–9.4	few μJ	[388]
AGS-I, 49°	10	Nd:YAG+DFG (idler)/10 Hz	5.2–6.4	38 μJ @ 5.55 μm	[389]
AGS-I, 45°	7+7	Nd:YLF+SH:SPOPO (idler)/50 Hz (100 MHz SPOPO in burst mode)	2.7–7 ^a	10 μJ @ 2.86–4 μm 3 μJ @ 6.45 μm	[390]
	3+3+3+3		2.6–7 ^a	2 μJ @ 2.7 μm	[391]
AGS-I, 42°	10	Nd:YAG+SH:SPOPO (idler)/26 Hz (50 MHz SPOPO in burst mode)	2.5–11.1 ^a	100 μJ @ 2.5 μm , 5 μJ @ 10 μm	[392]
AGS-I, 41°	20	Nd:YAG+OPG (SH idler)/10 Hz	4.5–8.7 ^a	90 μJ @ 5.4 μm	[393]
AGS-I, 45.2°	18+18	Nd:YAG+TH:OPG (idler)/10 Hz	2.13–12.9 ^a	320 μJ @ 3 μm , 110 μJ @ 5 μm , 46 μJ @ 10 μm	[394]
AGS-I, NA	10	Nd:glass+dye/1 Hz	4–10 ^a	> 1 μJ @ 5 μm	[395]
GaSe-I, 0°	10		6–18 ^a	0.2 μJ @ 15 μm	
GaSe-I, 0°	4	SH:OPG (signal+idler)/4 Hz	5–17	2.5 μJ @ 7 μm	[396]
	4	Nd:glass+SH:OPG (idler)/4 Hz	4–21 ^a	> 25 μJ @ 10 μm	
	1.7	Nd:glass+SH:OPG (idler)/4 Hz	4–21 ^a	~ 13 μJ @ 10 μm	
GaSe-I, 0°	3.3	Nd:YAG+TH:OPG (idler)/10 Hz	2.4–28	~ 13 μJ @ 3.5 μm	[397]
GaSe-I, 0°	3.5	OPA (signal+idler)/1 kHz	3.4–19	40 μJ @ 4 μm , 1 μJ @ 18.7 μm	[398]
GaSe-I, 0°	10		6.2–18	16 μJ @ 7 μm , 0.3 μJ @ 18 μm	
CdSe-II, 67°	12		9–24.1	21 μJ @ 11 μm , 0.3 μJ @ 24.1 μm	
CdSe-II, 70°	10	OPA (signal+idler)/26 Hz	9–22	40 μJ @ 10 μm , 6 μJ @ 19 μm	[399]
GaSe-II, 0°	3.9	Nd:YAG+SH:OPG (idler)/10 Hz	6.45 ^a	3.4 μJ @ 6.45 μm	[400]
GaSSe-II, 0°	4.7		5–11 ^a	9.1 μJ @ 6.45 μm	
LIS-II, 38.9°	12	Nd:YAG+SH:OPG (idler)/10 Hz	5–7 ^a	170–370 μJ	[401]
BGSe-I, 54.7°	8.7	Nd:YAG+SH:OPG (idler)/10 Hz	3–5 ^a	830 μJ @ 3.9 μm , 300 μJ @ 5 μm	[402]
BGSe-I, 44°	8	Nd:YAG+SH:OPG (idler)/10 Hz	6.4–11 ^a	125 μJ @ 7.8 μm , 38 μJ @ 11 μm	[403]
DBGaAs, 504 μm	~6	OPG (signal+idler)/3 Hz	15.6–17.6	~ 12 nJ @ 16.6 μm	[404]
CGA-I, 41°	5.8	OPG (signal+idler)/3 Hz	6.8–20.1	~ 0.3 μJ @ 10–13 μm	[405]

^aIn these experiments the regime was OPA.

The data summarized in Table 10 show the trend towards higher efficiency and mid-IR energy but this depends on the pulse duration. Nearly Fourier-limited pulses as short as 55 fs at 3 μm were reported in [412]. While very thin AGS crystal had to be used to suppress the GVM effects in the DFG process, measuring such pulses or their spectroscopic application require consideration of GVD effects in the subsequent optical elements [410,412,414]. Almost Fourier-limited pulses of 54 fs were obtained in [419] at 5.5 μm close to the zero-GVD point of

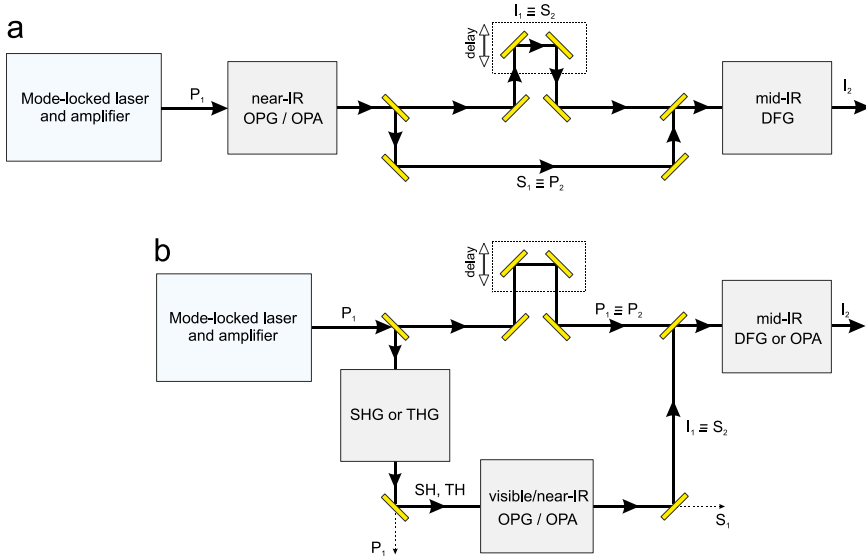


Fig. 27. Ultrafast mid-IR DFG of high energy pulses with an intermediate OPG/OPA stage (a) and mixing the pump with the idler output of a SH or TH pumped OPG/OPA (b). P, S, I designate pump, signal, and idler for the intermediate (1) and final (2) stage. THG: TH generation. Note that in a different form, i.e., employing SPOPOs or OPOs, both schemes are used for ultrafast DFG of low-energy pulses or DFG of ns pulses (see previous sections).

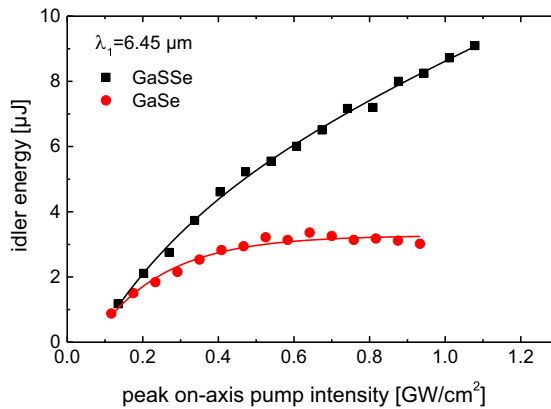


Fig. 28. Idler energy at $6.45 \mu\text{m}$ vs. pump intensity for $\text{GaS}_{0.4}\text{Se}_{0.6}$ (GaSSe) and GaSe OPAs pumped at $1.064 \mu\text{m}$ by ps pulses from a mode-locked Nd:YAG laser/amplifier and seeded by the idler from a SH pumped OPG/OPA based on oxide materials [400]. At such pump intensities GaSe already suffers from TPA.

GaSe. An order of magnitude higher energies ($> 15 \mu\text{J}$ in the entire tuning range of AGS and GaSe and $> 100 \mu\text{J}$ near $4 \mu\text{m}$) could be obtained with more powerful Ti:Sa amplifiers operating at 1 kHz , albeit at $\sim 130 \text{ fs}$ pulse durations [422]. On the other hand, the same approach is applicable also to Ti:Sa amplifiers operating up to their 250 kHz limit, although the idler energy was $\sim 60 \text{ nJ}$ at maximum when using AGS [423].

DFG in AGS in the presence of TPA was studied in [426,427] using dual-wavelength fs Ti:Sa amplifiers operating at 10 Hz . The idea was to utilize high input energies with large beam sizes

Table 10

DFG of fs pulses in non-oxide NLCs at low repetition rates. In the third column OPG sources, when used according to the scheme in Fig. 27a, always contain OPA stage, i.e. OPG means OPG-OPA in these cases. OPA in the third column means continuum seeding instead of OPG stage while “lasers” denote ultrafast amplifiers. “+” means two crystals and “2 ×” means double pass through one crystal. AgGaGeS₄ is Ag_xGa_xGe_{1-x}S₂ (x=0.5) and AgGaGe₅Se₁₂ is Ag_xGa_xGe_{1-x}Se₂ (x=0.17). NA: not available.

Crystal-type, $\theta(\varphi)_{\text{cut}}$	L [mm]	Pump and Signal sources/ Repetition rate	λ_1 [μm]	Idler energy @ Wavelength	Refs.
AGS-I, 60°, 70°	0.5, 3	dye+continuum/8.5 kHz	~10	~1 pJ @ ~10 μm	[407]
AGS-I, 45°	1, 0.5	Ti:Sa+dye/1 kHz	4.5–11.5	~10 nJ @ ~6.7 μm	[408, 409]
AGS-I, 40°	2	OPG (signal+idler)/1 kHz	3.3–10	50 nJ @ 5 μm	[410]
AGS-I, NA	1.5	OPA (signal+idler)/1 kHz	3–6	1–2 μJ	[411]
AGS-I, 39°	0.3	OPG (signal+idler)/1 kHz	2.7–8	~5 μJ @ 3.5 μm	[412]
AGS-II, NA	2+2	OPG (signal+idler)/1 kHz	6–12	7 μJ @ 8 μm, >4.5 μJ @ 6–12 μm	[413]
AGS-II, 50°	1	OPA (signal+idler)/1 kHz	~5	6 μJ @ 5 μm	[414]
AGS-II, NA	1	OPA (signal+idler)/1 kHz	3–10	1 μJ @ 5 μm	[415, 416]
AGS-II, 50.4°	0.5	OPA (signal+idler)/1 kHz	4.9	~5 μJ @ 4.9 μm	[417]
AGS-I, NA	2	OPA (signal+idler)/1 kHz	3.3–10.5	0.4 μJ @ ~4.5 μm	[418]
GaSe-I, 0°	1	OPA (signal+idler)/1 kHz	3–20	1 μJ @ 5 μm	[419]
AGS-II, 42°	2	OPA (signal+idler)/1 kHz	3.7–12	7.7 μJ @ 3.7 μm, 1.2 μJ @ 12 μm	[420]
HGS-II, 46°	2		3.7–12	9.2 μJ @ 3.7 μm, 1.4 μJ @ 12 μm	
AgGaGe ₅ Se ₁₂ -I, 61°	0.48	OPG (signal+idler)/1 kHz	4–7.5	0.5 μJ @ 5 μm	[421]
AGS-NA, NA	1	OPG (signal+idler)/1 kHz	2.6–14	>70 μJ @ 2.6–10 μm	[422]
GaSe-NA, 0°	0.46		3–20	>70 μJ @ 3–10 μm	
AGS-I, 50°	1.1	OPA (signal+idler)/250 kHz	2.4–12.7	>60 nJ @ 4 μm	[423]
AGS-I, 50°	1	OPA (signal+idler)/100 kHz	2.4–12	16.5 nJ @ 4 μm	[424]
AGS-II, 40°	1	OPA (signal+idler)/100 kHz	2.4–12	24 nJ @ 4 μm	[424]
GaSe-II, 0°	0.5, 3	dual-wavelength Ti:Sa/500 Hz	10–20	175 nJ, 600 nJ @ ~14 μm	[425]
	0.5	OPA (signal+idler)/500 Hz	3–10	>2.3 μJ @ ~4 μm	
AGS-II, NA	1	dual-wavelength Ti:Sa/10 Hz	8.3–11	7.4 μJ @ 10 μm	[426, 427]
AGS-I, 45°	1	dual-wavelength Ti:Sa/NA	8.4–11.8	<1 μJ	[428]
AGS-II, 45°	1		~11	NA	
LIS-II, 41°	1.5	Ti:Sa+continuum/1 kHz	4.8–9 ^a	~2 nJ @ 4.8–9 μm	[429]
	5		5–12 ^a	92 nJ @ 12 μm	[62, 430]
LIS-II, 41°	3	Ti:Sa+continuum/1 kHz	3.8–11 ^a	33 nJ @ 11 μm	[64]
LGS-II, 41°	3		3.8–11 ^a	99 nJ @ 11 μm	
LISe-II, 52°	3		3.8–11 ^a	2 nJ @ 11 μm	
LGSe-II, 42°	3		3.8–11 ^a	12 nJ @ 11 μm	
AgGaGeS ₄ -I, 53°	2.8		3.8–11 ^a	~25 nJ @ 7.1 μm	[431]
Cd _{0.48} Hg _{0.52} Ga ₂ S ₄ -I, 87°	3	Ti:Sa+continuum/1 kHz	6.6–11 ^a	2 μJ @ 6.6 μm	[432]
AGS-I, 36.5°	2	Cr:forsterite+SH:OPG (idler)/1 kHz	4.7 ^a	0.14 μJ @ 4.7 μm	[433]
AGS-II, 42°	2		4.7–8 ^a	0.35 μJ @ 4.7 μm	
AGS-I, 36.5°	2	Cr:forsterite+SH:OPG (idler)/1 kHz	5.5 ^b	0.12 μJ @ 5.5 μm	[434]
AGS-II, 42°	2		5.5–7.8 ^a	0.48 μJ @ 5.5 μm	
HGS-I, 40°	2		5.5–9 ^a	0.81 μJ @ 5.5 μm	
HGS-II, 46°	2		5.5–9 ^a	1.1 μJ @ 5.5 μm	

Table 10 (continued)

Crystal-type, $\theta(\varphi)_{\text{cut}}$	L [mm]	Pump and Signal sources/ Repetition rate	λ_1 [μm]	Idler energy @ Wavelength	Refs.
AGS-I, 48°	4.5	Cr:forsterite+SH:OPG (idler)/	6.5–8 ^a	1.6 μJ @ 6.5 μm	[435]
HGS-I, 55°	4.5	1 kHz	6.5–8 ^a	4.1 μJ @ 6.5 μm	
HGS-I, 40°	2	Cr:forsterite+SH:OPG (idler)/	5.5–8 ^a	0.3–0.7 μJ	[436]
Cd _{0.65} Hg _{0.35} Ga ₂ S ₄ -I, 78.1°	2	1 kHz	5.5–8 ^a	0.3–0.7 μJ	
LIS-II, 35°	3	Cr:forsterite+SH:OPA (idler)/NA	8.1–10.8 ^a	1 μJ @ 9.5 μm	[437]
AGS-II, 55°	2 × 2	Yb:KGd(WO ₄) ₂ +SH:OPA (idler)/ 2 kHz	3.5–9.2 ^a	6.5 μJ @ 4.5–5 μm	[438]
LGSe-II, NA	2	CPOPA (signal+idler)/1 kHz	3.2 ^a	11.1 μJ @ 3.2 μm	[439]
ZGP-I, 57.1°	12	OPA (idler)+OPA (idler)/500 Hz	6 ^a	6 μJ @ 6 μm	[440]
ZGP-I, NA	NA	Ho:YAG+SH:OPA (idler)/500 Hz	6 ^a	5 μJ @ 6 μm	[441]
ZGP-I, NA	5+5	Ho:YLF+DFG/100 Hz	~7 ^a	260 μJ @ ~7 μm	[442]
GaSe-I, 0°	1	broadband Ti:Sa (+compressor)/ 310 Hz	~12.5	10 nJ @ ~12.5 μm	[443]
AGS-II, NA	0.8	OPA (signal)+OPA (signal)/	4.2	NA	[444]
GaSe-II, 0°	0.14	1 kHz	5–30	1.7 μJ @ 10 μm	
GaSe-II, 0°	1		10	19 μJ @ 10 μm	
GaSe-II, 0°	0.2	OPA (signal)+OPA (signal)/1 kHz	17	2.5 μJ @ 17 μm	[445]

^aIn these experiments the regime was OPA.

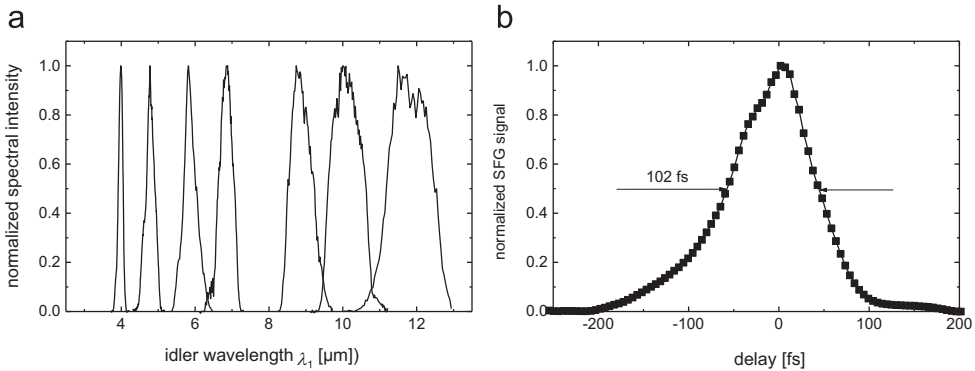


Fig. 29. Idler tuning obtained by fs DFG with HGS [420] (a) and cross-correlation trace recorded by SFG with 50-fs 800-nm pulses in 0.2 mm thick LiIO₃ crystal for estimation of the idler pulse duration under Gaussian shape assumptions in DFG performed with AgGaGe₅Se₁₂ (b) [421].

and still generate appreciable energy in the mid-IR at moderate intensities. However, the tuning achieved was confined to the 10 μm spectral range and the maximum idler energy was only 7.4 μJ , starting with a total energy of ~5 mJ while the pulse duration was of the order of 500 fs. The performance of GaSe, covering wavelengths up to 20 μm , only confirmed in direct comparison that the intermediate near-IR OPG-OPA stage, though technically more involved, permits higher input beam intensities and results in shorter mid-IR pulses and higher conversion efficiency [425]. All such experiments [425–428] also emphasized the detrimental role of TPA especially when performing DFG with amplified fs pulses. DFG with chirped pulses to

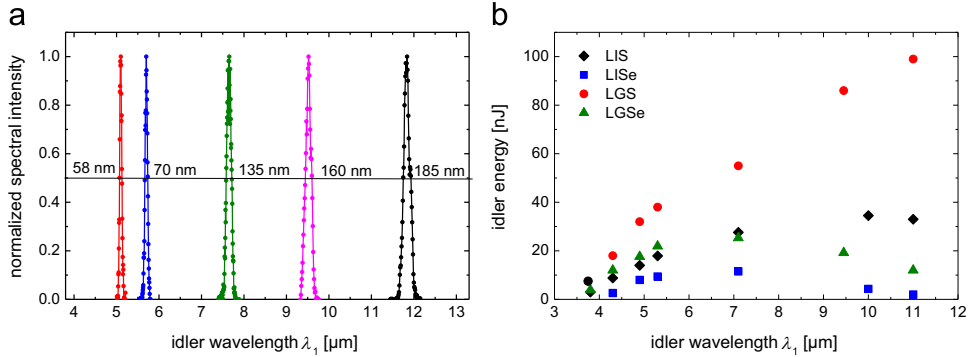


Fig. 30. Mid-IR DFG spectra recorded with LIS showing tuning up to 12 μm [62] (a) and idler energies obtained with 3-mm samples of the four lithium chalcogenide NLCs compared in [64] (b).

circumvent this effect, with subsequent idler compression, was extensively simulated in [447]. Noncollinear PM in AGS in order to generate extended bandwidths in the mid-IR with such dual-wavelength Ti:Sa amplifiers was demonstrated in [428].

One would expect that the output of fs Ti:Sa amplifiers could be directly employed for pumping DFG schemes with non-oxide NLCs possessing sufficiently large band-gap to avoid TPA near 800 nm, see Section 5. White light continuum was generated in a 2 mm thick sapphire plate to serve as a seed signal [62,64,429,430]. LIS OPA showed idler tuning up to 12 μm (Fig. 30a) but the conversion efficiency was low ($<0.1\%$) and the idler energy strongly depended on the crystal length which affected the pulse duration. In fact, comparison of different NLCs showed that besides the FM, the band-gap and the related TPA, the GVM is essential for the conversion efficiency [64,431,432], see Fig. 30b. Higher parametric gain due to lower GVM resulted in higher output energy and shorter idler pulse durations at the corresponding wavelength. Mixed quaternary crystals can be engineered to increase the band-gap and the damage resistivity, to increase d_{eff} and to reduce the GVM (Section 5). Crystals of AgGaGeS_4 (Table 10) [431] and $\text{Cd}_{0.48}\text{Hg}_{0.52}\text{Ga}_2\text{S}_4$ [432] were tested in the same arrangement. The latter one, with its much higher FM, delivered the highest output energy, 2 μJ at 6.6 μm , corresponding to pump to idler conversion efficiency of $\sim 1\%$, and also the shortest pulses, FWHM ~ 215 fs estimated from cross correlation measurements under Gaussian shape assumptions (Fig. 31a).

Cr:forsterite fs laser systems are analog of Ti:Sa but operate at longer wavelengths around 1.25 μm . Before the emergence of Yb-laser technology they were the only other SSL systems providing amplified fs pulses at wavelengths above 800 nm. This opened the way to explore for DFG/OPA different NLCs with higher FM whose band-gaps are too small for Ti:Sa laser pumping [448]. The approach adopted in [433–436] was based on Fig. 27b. Type-I and type-II AGS and HGS crystals were compared, with type-II HGS yielding the best performance [434]. Even in the absence of TPA, GVM posed a serious limitation for the efficiency and the pulse duration with both crystals. The output energies were substantially increased by using noncollinear interaction, Table 10, which improves the parametric gain bandwidth and enables the use of longer crystals [435]. In this case matching all 3 group velocities was targeted and this was possible in a broader spectral range for type-I interaction. If the PM angle could be increased (the birefringence reduced) to approach the non-critical geometry, then type-I PM would combine lower GVM with maximized d_{eff} . Thus, pulses of <200 fs FWHM, at improved efficiency, were generated with the mixed $\text{Cd}_{0.65}\text{Hg}_{0.35}\text{Ga}_2\text{S}_4$ crystal [436], Fig. 31b. LIS was

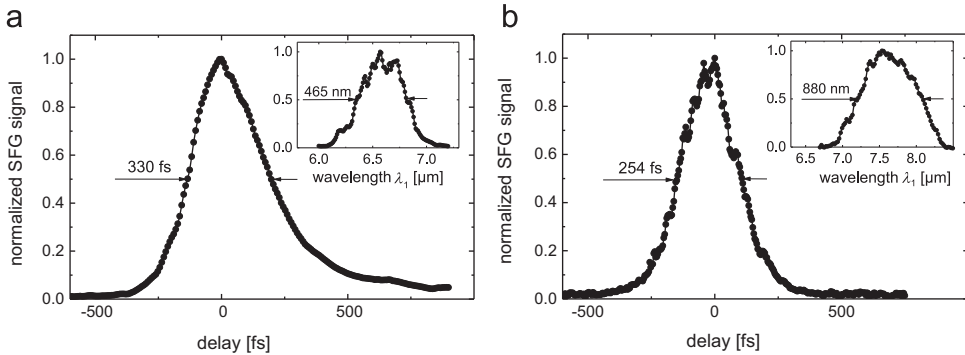


Fig. 31. Cross-correlation trace of the idler pulses at 6.6 μm from the $\text{Cd}_{0.48}\text{Hg}_{0.52}\text{Ga}_2\text{S}_4$ Ti:Sa laser pumped OPA obtained by SFG with 220-fs pulses at 820 nm in a 0.3 mm type-I AGS crystal (a) and the corresponding spectrum (inset), giving a TBP=0.7 [432], and cross-correlation trace of the idler pulses at 7.5 μm from the $\text{Cd}_{0.65}\text{Hg}_{0.35}\text{Ga}_2\text{S}_4$ Cr:forsterite laser pumped OPA obtained by SFG with 160-fs pulses at 1.25 μm in the same AGS crystal (b) and the corresponding spectrum (inset), giving a TBP=0.9 [436].

also investigated in a similar experimental set-up but did not show essential advantages at a pump wavelength of 1.25 μm [437], presumably because of its low FM.

As can be seen from Table 10, fs DFG experiments relying on the scheme in Fig. 27a produced higher idler output although the OPA regime was more typical for the scheme in Fig. 27b while similar numbers of pump and signal photons as in Fig. 27a are not the best prerequisite for high parametric gain. The main reason as explained above are NLC limitations when using fs laser amplifiers as pump sources. Thus, it is obviously attractive to try longer pump wavelengths. While Cr:forsterite laser systems have their intrinsic limitations with respect to output energy and average power, the Yb-laser systems developed later rely on direct LD pumping and are power scalable. Such a pump system with a DFG set-up according to Fig. 27b was employed in [438]. The AGS crystal was used in double pass with the major part of the pump energy in the second pass, Table 10. Recent experiments at longer pump wavelengths look more like proof of principle because the pump sources are still based on nonlinear frequency conversion. In [439] the pump (at 1.6 μm) and seed signal (near 3.1 μm) were the compressed (to 140 fs) and uncompressed (50 ps) signal and idler outputs of a KTA CPOPA, respectively. Due to the very different intensities, the energy gain with a 2-mm long LGSe crystal in the DFG stage exceeded 700 and the idler energy was over 10 μJ at 1 kHz. The idea in [440] was to simulate a future CPOPA based on broadband type-I ZGP pumped by ultrafast Ho-laser system employing OPAs to produce the pump (at 2.1 μm) and the seed signal (at 3.2 μm), Table 10. The generated in ZGP idler spectrum spanned over an octave [440]. Pumping of such an OPA with ~ 700 fs pulses at 2.09 μm from a Ho:YAG regenerative amplifier was then demonstrated in [441]. A CPOPA system with a ps Ho:YLF amplifier chain in the pump arm was realized in [442] using CSP-based fs DFG to produce a frequency comb seed at λ_1 [381]. With two 5-mm long ZGP crystals for CPOPA, idler energy of 260 μJ was obtained pumping the 2nd stage by 8 mJ. The spectral width near 7 μm indicates potential for compression to < 90 fs which means sub-4-fs duration [442], Table 10.

As already mentioned, an important issue when dealing with very short (< 100 fs) mid-IR pulses is the GVD effect both in the crystal used for DFG and in the optical elements behind it. Compensation or pre-compensation of this effect is necessary in order to compress the output pulses and achieve bandwidth-limited durations [414,419,438]. In [419] compression of the idler

pulses generated at 12.5 μm in GaSe was demonstrated for the first time using a grating compressor introducing positive dispersion (because optical elements and NLCs introduce negative GVD at such wavelengths). The pulse duration could be reduced from 360 to 115 fs and the pulses became Fourier-limited containing only ~ 3 optical cycles. Amplitude shaping of the mid-IR pulse by introducing a mask in the Fourier space was demonstrated with the same compressor after the DFG stage. Such pulse shaping can be performed more comfortably in the near-IR prior to the DFG process and can be used then for programmable generation of amplitude and phase-modulated fs pulses in the mid-IR, interesting for molecular vibrational spectroscopy and motivated in particular by the expectation that such pulses will enable coherent control of excitations in molecular and solid-state systems. In [449] such programmable amplitude and phase shaping was demonstrated by a liquid-crystal modulator array located in a zero-dispersion stretcher unit at the output of the cavity-dumped broadband Ti:Sa laser employed for DFG near 14 μm in GaSe [357]. In [415,416] the 80-fs signal output of the near-IR OPA was shaped with a liquid-crystal mask before mixing in AGS with a temporally stretched idler pulse, following the DFG scheme in Fig. 27a. In this experiment, spectral and amplitude modulation of the mid-IR pulse generated in the AGS crystal, control over linear chirp, adjustable double- and triple-pulse sequences, and more complex shapes were demonstrated. More recently, however, pulse shaping directly in the mid-IR after the DFG AGS crystal, was also demonstrated, using a Ge acousto-optic modulator with high efficiency and resolution [417].

Chirping of the pump pulses can increase the DFG conversion efficiency through the increased interaction length and precompensation of opposite sign GVD effects in the DFG crystal while pump and signal chirp of equal sign can be canceled and the generated idler remains Fourier-limited [438]. On the other hand, using Fourier-limited pump pulses might produce larger idler bandwidths but the overall GVD effects induce chirp and the idler pulses had to be compressed after the DFG [438]. Pulse shaping of the input pulses can be used for spectral narrowing of the output idler pulses in the mid-IR, producing higher spectral density. In [418] Si prism pairs were employed to positively chirp the two output pulses from the near-IR OPA before mixing them in AGS. While the chirp is canceled in the DFG process and the generated idler has almost the same TBP, its pulse duration becomes of course longer. Such a spectral narrowing scheme profits, however, from the more efficient operation of the near-IR OPA intermediate stage in the fs regime and the longer AGS crystal that could be used.

DFG with signal and idler from an intermediate OPA produces mid-IR pulses that are not phase-locked (the electric field oscillation is randomly phased from shot to shot) because the relative phase of the input pulses is not fixed. In contrast, DFG from a single optical pulse produces mid-IR pulses that have a defined carrier-envelope phase and that also are perfectly phased with respect to the envelope of the pulse from which they are generated. Such phase-matched DFG with 15-fs, 800 nm pulses in GaSe was demonstrated in [443] generating 100-fs pulses at $\sim 12.5 \mu\text{m}$ with energy of 10 nJ (or 50 nJ pulses when negative linear chirp was introduced on the input pulse). The process is very inefficient because only the wings of the spectrum participate and different input polarizations cannot be selected without losses. Seeding two OPAs by the same white-light continuum is also expected to preserve mutual phase lock and since both OPAs share the same frequency comb, the CEO will cancel in the DFG process. This was realized in [444] with the signal outputs. Extremely broad tunability was achieved mixing them, Table 10, while the resulting mid-IR pulse energy reached unprecedented 19 μJ at 10 μm . Moreover, this work demonstrated precise control of the carrier-envelope phase of the transient via the delay time between the two input pulses and the first electro-optic characterization of carrier-envelope phase stable pulses from such an OPA-based source revealing pulse durations of

2.4 optical cycles at 10 μm . A simple scheme for single shot monitoring and slow correction of absolute-phase drifts of such mid-IR pulses was presented in [445].

6.3.2. SPOPOs

SPOPO is a very attractive concept for down-conversion of low energy ultrashort pulses because only a single pump source is required and the efficiency can be much higher compared to the single pass DFG. SPOPOs are normally singly resonant for the signal wave. However, at the tight focusing required, residual absorption, TPA, thermo-mechanical properties and damage resistivity become crucial for reaching the threshold. Thus, e.g., SPOPO with non-oxide NLCs have never been demonstrated with the most popular fs mode-locked lasers based on Ti:Sa which emit near 800 nm and the shortest pump wavelength used so far was in the 1 μm range, Table 11.

The first SPOPO based on a non-oxide NLC operated in the burst mode [456]. This was the key to achieving extremely high overall efficiency in this tandem SPOPO (7.5% for the idler alone) because in such a way the peak powers are very high but the energy was spread over 20 individual pulses which minimized optical damage risks. In addition, this was a NRO (high OC transmission for both signal and idler and high reflection of the other cavity mirrors for both waves) pumped at 2.128 μm in double pass, see Table 11. Even if TPA could be avoided in AGSe at 2.128 μm [456] or in AGS at 1.064 μm [450–452], the main problem with these NLCs are the poor thermo-mechanical properties. Three concepts to reduce the thermal load to AGS in SPOPOs pumped at 1.064 μm by flash-lamp pumped Nd:YAG lasers were initially implemented: mechanical chopper [424], Q-switching in addition to mode-locking of the cw-pumped Nd-laser [451], as in [456], and pulsed operation (pumping) of the Nd:YAG oscillator-amplifier system [452]. Note that in the case of Q-switching or amplification of the mode-locked pump laser the energies of the micropulses constituting the idler burst (macropulse) can be on the μJ level, Table 11, i.e. comparable to what is typically achievable in DFG with high energy ps pulses at low repetition rates. None of the three concepts for burst mode operation mentioned above became practical with 1.064 μm pumping because of cumulative damage problems in AGS. However, more recently the last approach was implemented with type-I (ooe) CSP in NCPM and no damage imposed limitation was observed [453,454]. No signs of TPA were evident in that experiment until strong pump depletion (typically $>40\%$) occurred.

Under NCPM, normal incidence and slightly noncollinear geometry, the idler wavelength was $\sim 6.4 \mu\text{m}$, its pulse duration was 12.6 ps (FWHM) while the signal bandwidth amounted to 8 cm^{-1} [453]. Slight heating of the CSP sample shifted λ_1 to 6.45 μm maintaining NCPM while some tuning to longer wavelengths was possible by tilting [453,454]. Direct comparison with AGS under identical conditions (Fig. 32) clearly demonstrated the advantages of CSP with its higher FM but the upper limit of the idler tuning range was inferior due to multi-phonon absorption [454] (Table 11).

The burst mode of operation continues to be an attractive SPOPO regime also with modern LD-pumped laser systems and competes directly with ns pulse down-conversion in OPOs with regard to the macropulse energy. Apart from the mentioned reduced damage susceptibility of the NLC this regime is interesting for special (including programmable) time structures required in some applications. The burst can be picked out from a stable cw mode-locked pulse train using acousto-optic devices and then amplified at lower repetition rate to serve as a pump source. In [455] this was realized with a Nd:YVO₄ oscillator mode-locked at 450 MHz (for more compact SPOPO arrangement and ultimate stability) and Nd:YVO₄/Nd:YAG amplifiers. Tuning of the NCPM CSP SPOPO (Table 11 and Fig. 33a) was accomplished by changing the crystal temperature from 30 to 180 °C. The generated idler burst energy was $>1.2 \text{ mJ}$ over $>68\%$ of

Table 11

SPOPOs based on non-oxide NLCs. AMP: amplifier(s), “+” means two crystals, TT: temperature tuning, IC: intracavity pumping, DP: double pump pass, ND: near-degenerate or degenerate operation, FC: frequency comb generation.

Crystal-type, θ_{cut} , Λ	L [mm]	λ_3 , Pump source, Duration, Repetition rate	λ_1 [μm]	Idler energy @ Wavelength	Refs.
AGS-II, 48°	10+10	1.064 μm , Nd:YAG, 100 ps, 76 MHz, 1/32 duty cycle modulated at 40 Hz (quasi-cw)	5.505, SRO	~ 2.5 nJ ^a	[450]
AGS-I, 48°	30	1.064 μm , Nd:YAG, 145 ps, 76 MHz, Q-switched at 2 kHz, 260 ns burst duration	3.95–4.15, SRO	~ 16 μJ @ 4.06 μm ^a	[451]
AGS-I, 45°	10	1.064 μm , Nd:YAG+AMP, 12.5 ps, 100 MHz, pulsed at 25 Hz, 1 μs burst duration	4–9, SRO	6.8 μJ @ 5 μm ^a	[452]
AGS-I, 49°	10	1.064 μm , Nd:YAG+AMP, 15–20 ps, 100 MHz, pulsed at 25 Hz, 2 μs burst duration	2.9–7.1, SRO	1.2 μJ @ 6.5 μm ^a	[453,
AGS-II, 47°	10		4.4–8.6, SRO	2.6 μJ @ 6.5 μm ^a	454]
CSP-I, 90°	9.5		6.4–7, SRO, NCPM, TT	5.5 μJ @ 6.5 μm ^a	
CSP-I, 90°	12.1	1.064 μm , Nd:YVO ₄ +AMP, 8.6 ps, 450 MHz, 1 μs long burst picked and amplified at 20 Hz	6.091–6.577, SRO, NCPM, TT	3.3 μJ @ 6.275 μm ^a	[455]
AGSe-I, 46°	30+30	2.128 μm , KTP SPOPO (signal+idler), < 100 ps, 100 MHz, pulsed at 10 Hz, 200 ns burst duration	4.8, DP-NRO	~ 110 μJ @ 4.8 μm ^a	[456]
AGSe-I, 70°	6	1.551 μm , KTP SPOPO (signal), 40 ps, 75.4 MHz	4.04–7.75, SRO	2.5 nJ @ ~ 4.6 μm	[457]
AGSe-I, 80°	6		3.95–5.04, SRO	2.4 nJ @ 4.34 μm	
AGSe-I, 70°	2	1.55 μm , CTA SPOPO (signal), 120 fs, 82 MHz	4.1–7.9, SRO	0.43 nJ @ ~ 4.6 μm	[458]
AGSe-I, 70°	2	1.54–1.577 μm , PPLN SPOPO (signal), 450 fs, 42 MHz	4.57–5.121, SRO	2.7 nJ @ 4.857 μm	[459]
CdSe-II, 90°	20	1.85–1.97 μm , PPLN SPOPO (signal), ~ 5 ps, 120 MHz	9.1–9.7, SRO, NCPM	90 pJ @ 9.1 μm	[460]
ZGP-II, 90°	15, 20	2.25–2.5 μm , PPLN SPOPO (idler), ~ 8 ps, 76 MHz	5.65–5.7, SRO, NCPM	NA (< 100 pJ)	[461]
CSP-I, 90°	0.5	1.053 μm , Yb:KY(WO ₄) ₂ +Yb-fiber AMP, 130 fs, 100 MHz	6.2, SRO, NCPM	NA	[462]
CSP-I, 90°	0.5	1.023 μm , PPLN SPOPO, ~ 210 fs, 76 MHz, IC	5.947–8.109, SRO, NCPM	0.84 pJ @ 6.75 μm	[463]
CSP-I, 90°	1	1.029 μm , Yb:KGd(WO ₄) ₂ , ~ 560 fs, 43.1 MHz	6.76–7, SRO, NCPM	2.55 nJ @ ~ 7 μm	[464]
OPGaAs, 92 μm	0.5	2.45 μm , Cr:ZnSe, 100 fs, 182 MHz	4.9–5.4, DRO, NCPM, FC	~ 30 pJ, ND ^b	[465]
OPGaAs, 92 μm	0.5	2.38 μm , Cr:ZnS, 130 fs, 175 MHz	3.6–5.6, DRO, NCPM, FC	~ 300 pJ, ND ^b	[466]
OPGaAs, 60.5 μm	0.5	2.05 μm , Tm-fiber+AMP, 93 fs, 75 MHz	2.6–6.1, DRO, NCPM, FC	~ 250 pJ, ND ^b	[467]
OPGaAs, 60.5 μm	0.5	2 μm , Tm-fiber+AMP, 70 fs, 98.56 MHz	3–6, DRO, NCPM, FC	~ 50 pJ, ND ^b	[468]
OPGaAs, 51.5 μm	0.5	1.93 μm , Tm-fiber+AMP, 90 fs, 115 MHz	2.5–7.5, DRO, NCPM, FC	~ 300 pJ, ND ^b	[469]
OPGaAs, 53 μm	0.5	1.95 μm , Tm-fiber+AMP, 100 fs, 418 MHz	3–5.5, DRO, NCPM, FC	~ 50 pJ, ND ^b	[470]
AGSe-I, NA	1	1.95 μm , Er-fiber+Tm-fiber AMP, 180 fs, 100 MHz	3–5, DRO	~ 250 pJ, ND ^b	[471]

^aThe idler energies specified for the burst mode refer to the single ultrashort (micro)pulses.

^bIn ND SPOPOs for FC generation the idler energy was roughly estimated simply from half of the specified output power; note that tuning limits or FC spectral extent are defined at different levels in the corresponding literature.

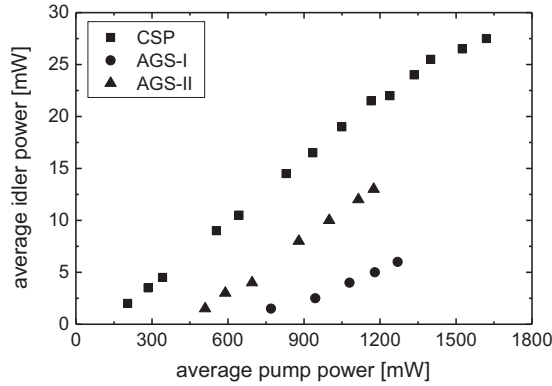


Fig. 32. Average idler power at $6.5 \mu\text{m}$ from the burst mode SPOPO using type-I and type-II AGS, and CSP crystals. The output consists of 200 micropulses of ps duration separated by 10 ns, constituting macropulses of $2 \mu\text{s}$ duration which follow at 25 Hz [454].

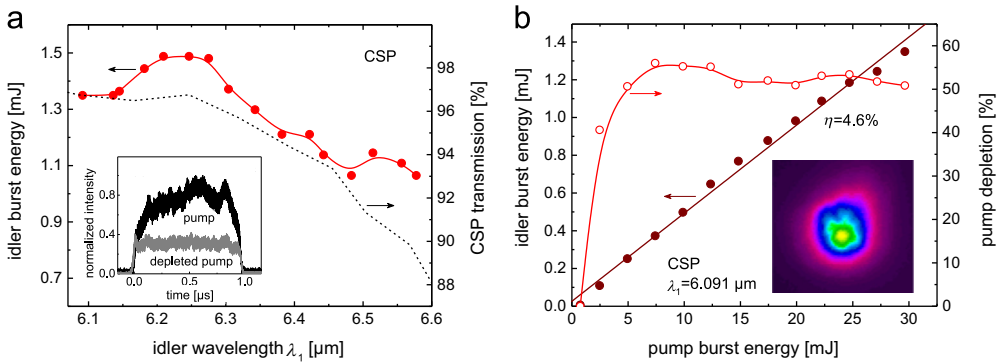


Fig. 33. Idler burst energy recorded at 30 mJ pump burst energy and CSP transmission across the tuning range (a). *Inset*: Macropulse envelope of the input pump and depleted pump for $\lambda_1 = 6.091 \mu\text{m}$ at $30 \text{ }^\circ\text{C}$. Idler energy scaling and pump depletion vs. pump energy (b). *Inset*: The corresponding idler spatial beam profile recorded at the full output energy showing TEM_{00} mode (Courtesy of M. Ebrahim-Zadeh, ICFO and A. Agnesi, University of Pavia [455]).

the tuning range with maximum idler conversion efficiency of $\eta_0 = 5\%$ [455]. The drop in the idler energy towards the longer wavelengths was attributed to the water absorption in air and multi-phonon absorption in the CSP crystal, resulting in reduced transmission, as evident from Fig. 33a. The macropulse envelope of the input and the depleted pump shown in the inset clearly indicate $>50\%$ depletion. The variation of the idler energy and pump depletion vs. pump energy, obtained at $30 \text{ }^\circ\text{C}$, corresponding to $\lambda_1 = 6.091 \mu\text{m}$, is shown in Fig. 33b [455]. The peak efficiency in this experiment was limited by the low surface damage threshold of CSP. Unfortunately, TPA was encountered in CSP in these ps experiments [455].

In the steady state SPOPO regime, pump focusing is tighter, alignment more difficult and the cavity length mismatch more critical, in particular for fs pulses. In order to avoid additional losses, ring cavity configuration can be used [460] since SPOPOs are usually pumped in single pass. Steady-state operation of mid-IR SPOPOs based on non-oxide NLCs was first demonstrated with longer pump wavelengths in cascaded (tandem) set-ups [457,458], see

Table 11. As in tandem OPOs, the spectral extent and spatial quality of the output beam from the first stage play crucial role for the achievable conversion efficiency in the second stage and special measures might be required in particular to generate close to Fourier-limited pulses from the first stage. In [457], a NCPM KTP SPOPO pumped by a mode-locked Nd:YLF laser served as a pump source for AGSe in the ps regime. A NCPM CsTiOAsO₃ (CTA, another KTP isomorph) SPOPO pumped by a mode-locked Ti:Sa laser was employed as a pump source for AGSe in the fs regime [458]. In both cases pump depletion of the order of 40% was observed in the AGSe SPOPO. The actual total conversion efficiency was of course lower, due to the additional losses present, especially for the non-resonated idler. Idler pulse durations in the 300–640 fs range were estimated for the fs AGSe SPOPO [458]. Complex dependence of the signal and idler pulse durations and chirp on the pump power was observed in the fs regime, accounted for by the effects of pump pulse chirp, self-phase and cross-phase modulation. In principle, tandem SPOPOs could be tuned by the pump wavelength for the second stage but in the above experiments the NCPM condition in the first stage could be maintained only in the fs regime thanks to the tunability of the Ti:Sa laser. In any case tuning by the pump wavelength is more important when angle tuning of the second stage is limited near the NCPM configuration. Such a SPOPO based on NCPM in type-II CdSe pumped and tuned by the signal output from a Nd:YLF MOPA pumped PPLN SPOPO was demonstrated in [460]. No thermal effects occurred in this SPOPO (CdSe shows lower residual losses and better thermal conductivity compared to AGSe) but the achieved tunability in the mid-IR was rather limited. More recently, NCPM type-II ZGP was also employed in a tandem SPOPO [461]. The idler output from a Nd:YVO₄ laser pumped PPLN SPOPO served as a pump for the ZGP SPOPO in which the idler was resonated. Tuning of the ZGP SPOPO was achieved by the pump wavelength but the idler was unfortunately not extracted [461]. The highest idler pulse energies from an ultrafast mid-IR SPOPO were achieved with AGSe pumped by the signal from a PPLN SPOPO, pumped in turn by a mode-locked Yb:KGd(WO₄)₂ laser [459], Table 11. Tuning by tilting the AGSe crystal, by changing the pump wavelength or by adjusting the cavity length mismatch was demonstrated. As mentioned in Section 4, the last option is characteristic only for SPOPOs because it is related to the dependence of the group velocity of the resonated wave on the wavelength.

More recently CSP was also employed in steady-state fs SPOPOs pumped for the first time near 1 μm , either directly or intracavity in a near-IR SPOPO [462,463]. 0.5-mm thin samples, possible due to the very high FM, permit the generation of relatively long idler wavelengths but the initial output energy levels reported were extremely low, Table 11, and TPA is even more pronounced in the fs regime [462]. Nevertheless, average idler powers exceeding 100 mW near 7 μm were demonstrated in [464] with a 1-mm thick CSP under NCPM pumped by ~ 560 fs pulses at 1.029 μm from a 43.1 MHz mode-locked Yb:KGd(WO₄)₂ laser. Tuning (6.76–7 μm) was achieved by variation of the cavity length. In the near future, more robust set-ups of this type using either CSP or OPGaP will obviously become preferable to the complex tandem SPOPOs which require synchronization of three cavities leading to undesirable instabilities.

As explained in Section 4, if the threshold could be reached with a SRO, DROs are avoided because of their intrinsic instabilities. Thus degenerate type-I PM in SPOPOs has been avoided for the same reason. However, such devices exhibit special properties related to self-phase-locking which are useful for broadband down-conversion of frequency combs into the mid-IR with low threshold and high efficiency. A SPOPO automatically inherits the repetition rate (mode spacing) of the pump laser but the CEO frequencies have to be determined and controlled in the general case. A doubly resonant SPOPO only oscillates in a discrete set of cavity length detunings with widely different output spectra [467]. For the degenerate case when signal and

idler are undistinguishable, it was shown that their CEO frequency is locked to half the value of the pump [472]. Thus, such a subharmonic or divide-by-2 SPOPO is phase and frequency locked to the pump laser and its coherence properties, i.e. CEO frequency and its stability are determined by the latter. It not only shifts the spectrum of the pump source to longer wavelengths but also broadens it. In [465] an OPGaAs based subharmonic ring SPOPO pumped by a fs Cr^{2+} :ZnSe laser generated broadband frequency combs (roughly twice the pump bandwidth in frequency units) with very low threshold (~ 40 mW of average pump power) and high efficiency (60% pump depletion). Even better performance was reported recently with a Cr^{2+} :ZnS pump laser increasing the output level by one order of magnitude to 110 mW [466]. A thin CaF_2 plate served to compensate the positive GVD of GaAs and as an OC in two beams. A similar ring SPOPO with a thin intracavity YAG plate was pumped in [467] by a mode-locked Tm-fiber laser, Table 11. The achieved spectral extent was more than an octave, limited by higher-order dispersion effects, the mirror coatings and the parametric gain bandwidth. Non-degenerate operation has the potential of further extending the SPOPO tuning range, however, the signal and idler CEO frequencies are not equal. Nevertheless, it was shown in [468] that in a doubly-resonant SPOPO they are locked to the pump wave and, e.g. the CEO frequency of the signal wave is a linear function of the CEO frequency of the pump laser, with a slope determined by the signal to pump carrier-frequency ratio. In this case the OPGaAs SPOPO was pumped by a fully stabilized frequency comb from a fs Tm-fiber laser system and non-degenerate operation was achieved by cavity length detuning. Threshold as low as 7 mJ was reported in [469] with a record broad spectral extent (2.5–7.5 μm at -50 dB level). Increasing the comb frequency spacing facilitates the measurement while tuning the pump system repetition rate, can still ensure continuous scanning of the comb teeth position in the mid-IR [470].

6.3.3. OPGs

OPGs based on non-oxide NLCs are difficult to realize in the ps regime and even more difficult with fs pulses. The major restriction comes not only from the TPA. Powerful fs laser amplifiers operate mainly near 800 nm (Ti:Sa) and powerful ps laser sources – mainly near 1 μm (Nd-lasers). More recently powerful fs sources emerge also near 1 μm (Yb-lasers). Other ultrashort pulse SSLs exist, e.g. Cr^{4+} :forsterite or Cr^{4+} :YAG near 1.25 and 1.5 μm , respectively, or Cr^{2+} lasers above 2 μm but, with few exceptions, the average output power is low and in most cases these systems do not include amplification. Er-lasers and amplifiers slightly below 3 μm until now have been mainly lamp-pumped and operated at very low repetition rates. For pumping near 1 μm or down to 800 nm, even if TPA can be avoided (pump photon energy $< E_g/2$), λ_3 will not be far enough from the short-wave cut-off wavelength of the NLC and consequently strong dispersion (GVM) will lead to temporal walk-off of the interacting pulses, short interaction length and consequently low parametric gain. Obviously, only thin NLCs can be used with fs lasers. Thus, the parametric gain achievable with amplified pump sources is normally not sufficient for OPG, and to overcome the damage limit DFG/OPA is used instead, as presented in Section 6.3.1.2. This is especially true for fs pulses because the dependence on interaction length is stronger compared to the dependence on peak intensity, see Eqs. (10),(11). Alternatively, cascaded schemes could be employed to transform λ_3 to spectral ranges of lower dispersion. As explained in Section 3, when the NLC length is selected shorter than the temporal walk-off lengths determined by the GVM parameters and pump pulse duration, parametric amplification in high gain OPG may be accompanied by pulse compression due to the temporal gain narrowing effect, i.e. the output pulses can be shorter than the pump pulse.

The first OPG experiments consisted in observation of spontaneous parametric fluorescence and the first non-oxide material studied with pulsed radiation around 1970 was Ag_3AsS_3 [163,473]. With ruby laser excitation, idler wavelengths as long as $14.6\ \mu\text{m}$ were calculated from the measured signal wavelength under type-I PM and even temperature tuning could be demonstrated in this early work [473]. The first report on ps OPG was again with proustite in 1980 [387] but the tunability extended only up to $5\ \mu\text{m}$, Table 12.

Double stage arrangements (OPG-OPA) employing two type-I (oo-e) Ag_3AsS_3 or AGS crystals pumped by low repetition rate $\sim 20\ \text{ps}$ Nd:YAG amplifiers were presented in [474,475]. The two crystals were simply in series without delay compensation which is not necessary in the ps regime. A pair of crystals served not only to compensate spatial walk-off [474], the separation between the two stages is a simple approach for spatio-spectral selection in order to obtain spectrally narrow and low-divergence output. Idler wavelengths as long as $10\ \mu\text{m}$ were reached with AGS, at pulse duration $\sim 8\ \text{ps}$ (shorter than the pump pulses) and typical idler bandwidths of $10\ \text{cm}^{-1}$, which corresponds roughly to 5 times the Fourier limit [475]. The difficulties in controlling the spectral bandwidth across the entire tuning range became evident already in those early OPG experiments. Moreover, although pump depletion near degeneracy reached 10% in [475], roughly 10 times higher than in [387], rapid drop away from degeneracy was observed in both set-ups. At such idler wavelengths the conversion efficiency of the AGS OPG-OPA was few times lower compared to DFG performed with the same pump source [388]. Higher total conversion efficiency (of the order of 1% away from degeneracy) and an order of magnitude increase in the idler pulse energy were reported in [476], Table 12. Longer pump pulses and longer AGS crystals were employed in this more recent experiment, separate pump beams were used in the two stages and the PM was noncollinear for easy separation/recombination of the beams which implies seeding the OPA only by the signal wave from the OPG.

Pumping of ZGP based OPGs became possible due to the availability of mode-locked ps Er:YAG and Cr,Er:YSGG lasers. Like the Nd-lasers used before, these were lamp-pumped systems operating at very low repetition rates including amplifiers for the single pulses in the case of Cr,Er:YSGG. The OPGs employing a single crystal in single pass were tunable up to $10\ \mu\text{m}$ with ZGP and $18\ \mu\text{m}$ with GaSe, see Table 12. Not far from degeneracy, a 42-mm long type-II ZGP showed a threshold as low as $350\ \text{MW}/\text{cm}^2$ (peak intensity) and maximum total conversion efficiency of 17.6% [478–480] which represents an improvement of about an order of magnitude compared to the AGS based OPGs in the same spectral range [476]. At such λ_3 , Type-II ZGP is close to the NCPM configuration with maximum d_{eff} but temperature tuning turned out to be very limited [481]. Type-I interaction in ZGP and GaSe provided much broader tunability but for a single stage OPG the spectral bandwidth varied by almost 2 orders of magnitude between degeneracy and far from degeneracy. With type-II ZGP the measured bandwidth was of the order of $10\ \text{cm}^{-1}$ at $6.7\ \mu\text{m}$ [479,480]. Few hundreds of cm^{-1} bandwidths in type-I ZGP or GaSe correspond to full extension of the spectrum over almost an octave, i.e. continuum generation. Even for $10\ \text{cm}^{-1}$ bandwidth the deviation from the Fourier limit is huge, about 50 times, though some compression of the pulses takes place in the OPG. In this case the generated mid-IR pulse consists of noisy spikes with duration $\sim 1\ \text{ps}$.

Further development of the Er-laser pumped OPGs focused on a double pass through the NLC, comparison of type-I and type-II ZGP and GaSe crystals, and extension to longer wavelengths with type-II CdSe [482–486], see Table 12. The double pass was realized with a total reflector for the three waves, without splitting the pump or introducing delay stages. Thus the primary goal was again to improve the beam divergence and spectrally narrow the output. With a 40-mm long type-II ZGP, the OPG threshold (peak intensity) near degeneracy was as low

Table 12

OPGs based on non-oxide NLCs. AMP: laser amplifier(s), TT: temperature tuning, “+” and “ \times ” indicate OPG-OPA arrangements with two separate crystals or one crystal in double pass, respectively. FEL: free-electron laser, ND: near degeneracy, NA: not available.

Crystal-type, $\theta_{\text{cut}}, \Lambda$	L [mm]	λ_3 , Pump source, Duration, Repetition rate	λ_1 [μm]	Idler energy @ Wavelength	Refs.
Ag ₃ AsS ₃ -I, 30.5°	13	1.054 μm , Nd:glass+AMP, 8.5 ps, 1 Hz	2.1–5	< 10 μJ , ND	[387]
Ag ₃ AsS ₃ -I, NA	10+10	1.064 μm , Nd:YAG+AMP, \sim 20 ps,	2.13–6	8.6 μJ @ 4.6 μm	[474]
AGS-I, 45°	15+30	few Hz (single pulses)	2.13–10	3 μJ @ 6.7 μm	[475]
AGS-I, 47.5°+48.7°	33.6+36.7	1.064 μm , Nd:YAG+AMP, 35–40 ps, (single pulses)	4.1–5.3	130 μJ @ 5.3 μm	[476]
AGS-I, 38.2°	2 \times 61.8		5.2–7.4	30 μJ @ 7.4 μm	
ZGP-II, 84°	42	2.94 μm , Er:YAG, \sim 80 ps, 1 Hz (burst of 25 pulses at 149 MHz)	6.29–6.46	\sim 10 μJ ^a	[477]
		2.79 μm , Cr,Er:YSGG+AMP, 100–150 ps, 1–2 Hz	5.9–6.3 (6.2–6.7)	\sim 35 μJ @ \sim 6 μm	[478– 480]
		2.79 μm , Cr,Er:YSGG, 100 ps, 1–2 Hz	5.86–6.04, TT	NA	[481]
ZGP-I, 47°	11–12	2.94 μm , Er:YAG, 100–110 ps, 1–2 Hz	6–10	\sim 6 μJ @ 6 μm	[479,480]
GaSe-I, 0°	12		6–18	\sim 2 μJ @ 6 μm	
GaSe-I, 0°	10+10	2.8 μm , Cr,Er:YSGG+AMP, 100 ps, 3 Hz	6–14	> 5 μJ	[482]
GaSe-II, 0°			6–10	NA	
ZGP-I, 47–48°	2 \times 11	2.8 μm , Cr,Er:YSGG+AMP, 100 ps, 3 Hz	5.6–10	\sim 100 μJ @ 8 μm	[483,484, 485]
ZGP-II, 63.5°	2 \times 30		6–10	similar	
GaSe-I, 0°	2 \times 14		5.6–19	\sim 50 μJ @ 8 μm	[484,485]
GaSe-II, 0°	2 \times 14		5.6–10	similar	
CdSe-II, 76°	2 \times 50		8–13	\sim 100 μJ @ 8 μm	[485,486]
ZGP-I, 52.5°	2	1.89–2.07 μm , BBO OPA (idler), 140 fs, 1 kHz	6–8	\sim 70 nJ @ 6.15 μm	[487,488]
ZGP-I, 56.1	1+1+1.5	2.05 μm , BBO OPA (idler), 63 fs, 10 Hz	\sim 5	58 μJ @ \sim 5 μm	[489]
ZGP-II, 80°	2 \times 10	2.9–3.5 μm , LiNbO ₃ OPA (idler), 2.7 ps, 10 Hz	6–11	1.4 μJ @ 6.9 μm	[490]
OPGaAs, 166.6 μm	17.5	3.1–3.3 μm , DFG (idler), 1 ps, NA (1 kHz)	6.56–10.7, NCPM	< 40 nJ	[491]
CGA-I, 33°	7	\sim 5 μm , FEL, \sim 600 fs, 10 Hz (burst of 100 pulses at 25 MHz)	10–18	< 100 nJ @ 10 μm ^a	[492]
CSP-I, 90°	8	1.064 μm , Nd:YVO ₄ +AMP, 8.7 ps, 100 kHz	6.204, NCPM	1.54 μJ @ 6.204 μm	[493,494]
CSP-I, 90°	12.1	1.064 μm , Nd:YAG+AMP, 20 ps, 5 Hz	6.153–6.731, NCPM, TT	33 μJ @ 6.153 μm	[495,496]
CSP-I, 90°	2 \times 21.4	1.064 μm , Nd:YAG+AMP, 8 ns, 100 Hz	6.125, NCPM	523 μJ @ 6.125 μm	[497]
CSP-I, 90°	2 \times 21.4	1.064 μm , Nd:YAG+AMP, 500 ps, 1–10 kHz, SF	6.102, NCPM	8.7 μJ @ 6.102 μm	[498]
CSP-I, 90°	21.4	1.064 μm , Nd:YVO ₄ +AMP, 120 ps, 230 kHz, SF	6.1, NCPM	510 nJ @ 6.1 μm	[499]
CSP-I, 90°	2 \times 21.4	1.198 μm , Ba(NO ₃) ₂ Raman shifter, 150 ps, 1 kHz, SF	4.64, NCPM	6 μJ @ 4.64 μm	[500]
HGS-II, 50.2°	10.76	1.064 μm , Yb-fiber+AMP, 16 ps, 250 kHz	3.85–10	192 nJ @ \sim 6.1 μm	[501]

^aThe idler energies specified for the burst mode refer to a single ultrashort micropulse.

as 90 MW/cm^2 [485]. The idler tunability was extended with GaSe to wavelengths as long as $19 \mu\text{m}$, Table 12. With all NLCs which were uncoated the total conversion efficiency of the double pass scheme was typically two times lower compared to a single pass but the output quality (close to diffraction limited beams and narrower spectral bandwidths) was improved. Nevertheless, near-degenerate operation with type-I PM again produced continuum-like spectra. While the role of the two passes was basically to suppress noncollinear processes, such were observed in type-I PM far from degeneracy when the idler wavelength entered the phonon absorption region [483]. From comparison of different NLCs, ZGP was superior in terms of threshold and efficiency up to $8 \mu\text{m}$, GaSe – above $12 \mu\text{m}$ and CdSe was superior (in the sense of efficiency and bandwidth) in the $8\text{--}12 \mu\text{m}$ range [485]. All these experiments demonstrated that high OPG efficiency and output energies are possible if pump wavelength, pulse duration, and NLCs are properly selected and optical damage can be avoided.

As can be seen from Table 12, the actively mode-locked, pulsed (mostly Q-switched) Er-lasers used as pump sources at 2.8 or $2.94 \mu\text{m}$ generated relatively long pulse durations ($80\text{--}150 \text{ ps}$). To obtain shorter idler pulses from OPGs cascaded schemes could be employed, first transforming λ_3 , e.g. of ultrafast Ti:Sa amplifiers operating in the 800-nm spectral range. For long time, the only demonstration of such a fs OPG was with a 2-mm type-I ZGP in a single pass arrangement [487,488], Table 12. Whereas $\sim 100 \text{ ps}$ pulses profit from longer NLCs and the OPG threshold can be very low in terms of peak intensity, the main problem is that for reasonable crystal lengths (L values up to few cm in Table 12) the parametric gain bandwidth is still too large to obtain Fourier-limited pulses. This is not so in the fs regime where thin crystals have to be chosen which correspond to the actual interaction length determined by GVM and no additional spectral broadening of the generated waves is expected in collinear interaction if higher order nonlinear effects are negligible. With a 140-fs pump pulse at $2.07 \mu\text{m}$ (idler from a BBO OPG-OPA at 1 kHz), the OPG threshold in [487] amounted to 25 GW/cm^2 (peak pump intensity). At 60 GW/cm^2 , the uncoated ZGP OPG emitting at $\lambda_1 = 6.15 \mu\text{m}$ showed a total (signal plus idler) conversion efficiency of $> 1.3\%$. The recorded spectra are reproduced in Fig. 34a. Assuming the same TBP for the idler as for the pump (~ 0.5), idler pulse duration of $\sim 200 \text{ fs}$ was predicted at $6.15 \mu\text{m}$ from the spectral bandwidth, in accordance with the temporal walk-off value between pump and idler. Type-I PM was chosen in this experiment for lower threshold and to test ultimately short λ_3 far from degeneracy. However, the OPG threshold could not be reached at much shorter pump wavelengths (e.g., for $> 100 \text{ GW/cm}^2$ at $\lambda_3 = 1.66 \mu\text{m}$) before other higher order nonlinear effects occurred such as self-phase modulation, induced spectral broadening and self-focusing of the pump pulses, as well as non-phase-matched SHG. Nonlinear and linear losses pose indeed a limitation for ZGP but even if they can be minimized with a thin crystal, GVM rapidly increases for $\lambda_3 < 1.9 \mu\text{m}$ and this makes fs OPG a challenging task at such pump wavelengths. Longer pump wavelengths on the other hand may lead to continuum generation in type-I PM which makes the generation of Fourier-limited pulses impossible because the retracing point in ZGP is near $\lambda_3 = 2.5 \mu\text{m}$ [17,488], see Fig. 3. Recently, a similar OPG with two OPA stages ($\lambda_3 \sim 2.05 \mu\text{m}$) was studied as a proof of principle for a future fs pulse laser system, generating idler energies as high as $58 \mu\text{J}$ at 10 Hz near $5 \mu\text{m}$ [489].

Another cascaded scheme employed a ps Ti:Sa regenerative amplifier operating at 10 Hz and a LiNbO₃ OPA as a first stage [490]. The 2.7 ps idler pulses from this OPA, tunable near $3.15 \mu\text{m}$, were used to pump type-II ZGP in double pass, see Table 12. The pump threshold for detection of parametric fluorescence was less than 200 MW/cm^2 (peak intensity). Tunability between 5 and $11 \mu\text{m}$ (at the 10% energy level) was achieved by tilting the NLC and varying λ_3 . Typical spectral bandwidths measured were $\sim 35 \text{ cm}^{-1}$ and the generated mid-IR idler pulses were only

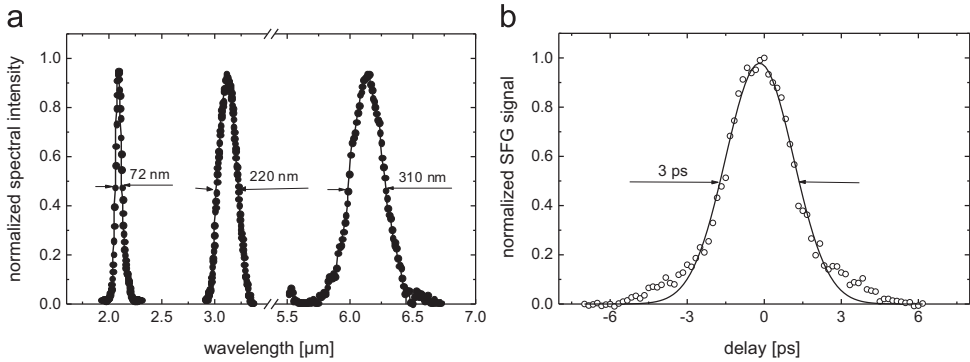


Fig. 34. Spectra of the pump, signal, and idler from the fs ZGP OPG [488] (a). Cross-correlation trace of the idler ($\lambda_1 = 7.6 \mu\text{m}$) from the ps ZGP OPG obtained by SFG with 2.7-ps pulses at 795 nm in a 1-mm type-I AGS [490] (b).

~ 2 times above the Fourier limit ($\text{TBP} \sim 1$). Their pulse durations were estimated from cross-correlation measurements and Fig. 34b reproduces the result for $\lambda_1 = 7.6 \mu\text{m}$ with $\lambda_3 = 3.34 \mu\text{m}$. From deconvolution of such traces, pulse durations ~ 1 ps (FWHM) were estimated for the entire tuning range (signal and idler). The pulse shortening was attributed to the temporal gain narrowing effect at high parametric gain [490]. This ps OPG was characterized by high total conversion efficiency, $\sim 17\%$ in single pass (collecting the entire radiation behind the crystal) and about 6% in the double pass (with non-optimized extraction) used to obtain the above results.

OPGaAs was also employed in a single pass degenerate OPG pumped above $3 \mu\text{m}$ in order to achieve extreme bandwidths (combined signal and idler spectra) by operating at λ_3 close to the retracing point [491]. The threshold peak intensity was $0.6 \text{ GW}/\text{cm}^2$ (55 nJ pump energy) and the maximum total conversion efficiency observed was 15%. The entire spectrum spanned $4.5\text{--}10.7 \mu\text{m}$ with a combined (signal and idler) energy of 80 nJ for 1.4 μJ of pump energy, well over an octave wide. This experiment was a nice illustration of continuum generation by a three-wave mixing process. The output showed a divergence just two times above the diffraction limit. However, parasitic nonlinear processes were observed also in OPGaAs at the intensities applied. As explained in Section 3 the efficiency of such continuum generation in QPM materials will be affected more severely by the GVM with the pump in comparison to birefringent NLCs.

Sub-ps OPG was demonstrated also with the high gain material CGA but this required yet longer pump wavelengths. A Free-Electron Laser (FEL) at $\sim 5 \mu\text{m}$ operating in the burst mode (~ 100 micropulses of ~ 600 fs pulse duration separated by 40 ns in a $\sim 4 \mu\text{s}$ long macropulse) was employed to pump CGA in single pass [492]. With an uncoated type-I CGA ($L = 7$ mm), the threshold was about $3 \text{ GW}/\text{cm}^2$ (peak intensity). Idler tuning from degeneracy ($10 \mu\text{m}$) up to $18 \mu\text{m}$ was achieved with typical total conversion efficiency of $\sim 1.5\%$.

The interest in ultrafast OPGs pumped near $1 \mu\text{m}$ was revived after the discovery of CSP. In [493,494] a single pass NCPM OPG was pumped by amplified 8.7 ps Nd:YVO₄ laser pulses from a LD-pumped and very stable pump system at 100 kHz. Pump to idler conversion efficiency $\sim 2.5\%$ was achieved for $\lambda_1 = 6.204 \mu\text{m}$ at average pump power of 6.1 W, resulting in an average idler power of 154 mW (Fig. 35), however, thermal lensing effects occurred beyond this pump level caused by the still relatively high residual absorption of CSP at $1.064 \mu\text{m}$. The idler beam profile had relatively uniform, near-Gaussian energy distribution [493]. With

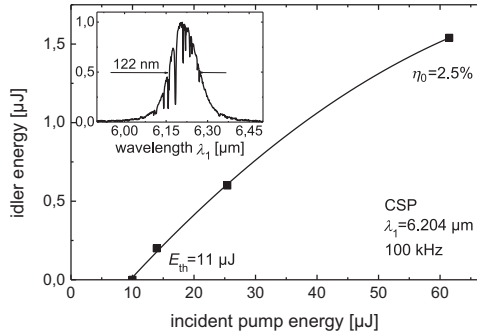


Fig. 35. Idler pulse energy of the ps NCPM CSP OPG operating at 100 kHz. The inset shows idler spectrum centered at 6.204 μm with the sharp features corresponding to water absorption lines (Courtesy of M. Ebrahim-Zadeh and J. Biegert, ICFO) [494].

TBP ~ 9.3 measured for the signal the pulses were also far from Fourier-limited. Energy scaling at low (5 Hz) repetition rate and temperature tuning were demonstrated in [495,496].

In [497] a relatively long ($L=21.4$ mm) CSP crystal was employed in a NCPM OPG pumped by 8 ns pulses at 1.064 μm . This represents a unique OPG regime which is of practical importance because commercial Q-switched pump lasers normally deliver pulses with duration of the order of 10 ns or longer and are much more robust and compact compared to ultrafast laser systems. On the other hand, ns OPG could provide much narrower spectral bandwidths. Such a regime, possible only with high FM NLCs, can be directly compared to OPOs: The advantage is that OPG seeding with a SF source is much easier to apply for narrowband SF operation. Indeed, narrowband seeding with simple cw laser sources or MOPO have not been demonstrated yet with ns OPOs based on non-oxide NLCs. The pump source in [497] was the same as the one used in few of the OPO experiments described in Section 6.2.2.1, see Table 5. The pump beam was first expanded and then a nearly flat-top spatial profile was obtained by a circular aperture which reduced the beam diameter to ~ 3.8 mm, matching the limited CSP aperture (4.1 mm along the c -axis \times 6.1 mm). The CSP sample was AR-coated with a single layer only for pump and signal. The double pass OPG threshold was extremely low, corresponding to intensity ~ 0.23 MW/cm² at the detection limit or 0.55 MW/cm² if extrapolated from linear fit, see Fig. 36a. At the maximum applied pump energy of 12 mJ (axial fluence ~ 100 mJ/cm²), the combined output energy exceeded 4 mJ, from which ~ 0.52 mJ were at 6.125 μm (idler). As expected the signal and idler pulse durations (4.4 and 5.8 ns, respectively) were shorter than the pump. The measured M^2 values for the idler were 7.1 and 7.8 in the two planes, better than for an OPO pumped with a similarly shaped beam [497].

With 8-ns pump pulses, residual reflections may contribute to an OPO feedback effect. This was indeed established by tilting the crystal in order to facilitate noncollinear interaction: surface reflections formed a low-finesse cavity for the idler. Therefore, this experiment corresponds more or less to quasi-OPG or weakly-resonant OPO operation. Nevertheless, it shall be outlined that the conversion efficiency, e.g., from pump to idler was roughly two times higher compared to an analogous OPO [187], see Fig. 17b. Thus the same idler energy was extracted from the double pass CSP OPG (practically an OPO without output coupler) at more than two times lower pump intensity which shows a route how to avoid the damage problem in CSP.

The feedback effect was totally eliminated in a subsequent experiment using a different pump source (again based on Q-switching) with 500-ps pulse duration [498]. In this experiment the low

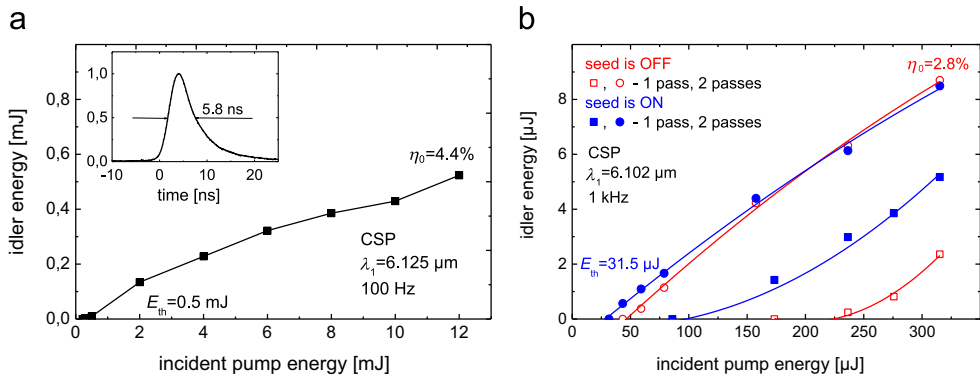


Fig. 36. Idler output energy of the double pass ns CSP OPG vs. incident pump energy at 1.064 μm [497] (a). The inset shows the idler temporal profile recorded at maximum output energy, possibly affected by the 2.6 ns response time of the HgCdTe photoconductive detector. Idler output energy of the sub-ns CSP OPG vs. incident pump energy at 1.064 μm in single and double pass, and with and without seeding [498] (b).

energy but kHz repetition rate and SF pump source beam was down collimated to $2w_3 \sim 1.38$ and ~ 1.15 mm in the two planes and a fiber-coupled wavelength stabilized DFB LD near 1.29 μm served as a seed. About 0.5 mW of cw seed power were incident on the CSP crystal with proper polarization. While in single pass OPG operation the threshold for seeded operation was more than two times lower and the output energies drastically increased in the presence of seeding, in double pass operation the input-output characteristics were almost independent of the seed (Fig. 36b). The threshold for unseeded double pass OPG operation corresponded to axial fluence of 6.9 mJ/cm^2 or peak intensity of 13.8 MW/cm^2 . When the seed LD was switched on it decreased to 5 mJ/cm^2 and 10 MW/cm^2 , respectively. The total conversion efficiency of the double pass arrangement (seeded or not) got saturated at $\sim 20\%$. The idler energy changed only slightly when increasing the repetition rate, because of slight degradation of the pump beam spatial profile but nevertheless maximum average idler power of 79 mW was obtained at 10 kHz. Seeding at the signal wavelength with the DFB LD enabled ~ 10 fold narrowing of the idler bandwidth down to < 1 nm at ~ 6.1 μm , leading to a Fourier product of ~ 2.3 (from the estimated pulse duration of ~ 300 ps), which, in terms of spectral resolution, is an improvement of ~ 130 times compared to results obtained with sub-10 ps pump pulses [494], see inset in Fig. 35. This OPG was studied with even shorter pulses (120 ps) from a microchip Q-switched laser [499], see Fig. 37. This pump source operated at 230 kHz and at the low energy level the pump beam was focused to $2w_3 = 0.62$ and 0.53 mm in the position of the CSP crystal. The maximum average idler power reached 117 mW in single pass and the total conversion efficiency - 21%. No damage occurred to the CSP sample up to 150 MW/cm^2 . Note, however, that this is equivalent to 18 mJ/cm^2 , or roughly 20 times lower than the fluence at which surface damage was observed in ns OPO experiments [187], see Fig. 17b. The cw seed level necessary was extremely low, about 20 μW with the proper polarization. Seeding resulted in almost Fourier-limited output pulses with TBP=0.53 measured for the signal.

As already mentioned at $\lambda_3 = 1.064$ μm CSP exhibits residual absorption and for pulse durations below 10 ps some TPA became also evident [494]. Both effects can be avoided by slightly shifting the pump wavelength. Small wavelength shifts are problematic in three-wave interactions because the idler will normally lie outside the transparency range, however, stimulated Raman scattering fills in exactly this gap. In [500] the Raman active crystal $\text{Ba}(\text{NO}_3)_2$

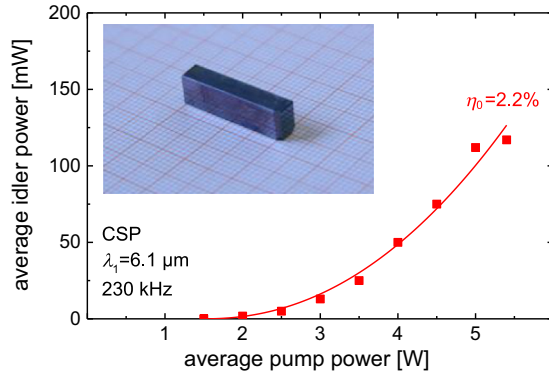


Fig. 37. Average idler power at 230 kHz of the single pass sub-100 ps CSP OPG vs. average incident pump power at 1.064 μm [499]. The inset shows the CSP sample used in [497–500].

was used to convert the wavelength of the 500-ps Nd-laser pump source to 1.198 μm, simultaneously shortening the duration to ~150 ps. These pulses were then used to pump the double pass CSP OPG with a corresponding DFB LD seed near 1.615 μm for narrowband operation, Table 12.

The NCPM condition in type-I CSP fixes the idler wavelength to ~4.64 μm at room temperature. The threshold for unseeded double pass OPG operation corresponded to peak intensity of 26 MW/cm² or axial fluence of ~4 mJ/cm², Fig. 38. When the OPG was seeded the threshold dropped to ~18 MW/cm² (~2.8 mJ/cm²). In seeded operation, the maximum total conversion efficiency (signal and idler) was clamped to ~30% from ~40 μJ pump energy. Seeding at the signal wavelength enabled ~25 fold narrowing of the signal/idler bandwidths down to 10 GHz (~0.7 nm at λ₁=4.64 μm), leading to a TBP~1, estimated from the measured by SHG pulse durations (FWHM~100 ps at full power), Fig. 38 (inset).

The mid-IR transmission cut-off and tuning range under NCPM are limiting factors in the case of CSP. According to Fig. 9 and Table 2, HGS is the candidate with the second best FM for OPG pumped near 1 μm. Such a single pass experiment was performed in [501], Table 12. As already mentioned, novel mode-locked Yb-fiber lasers with subsequent amplification can be used

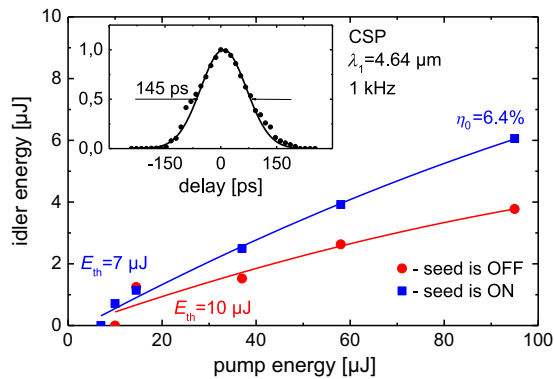


Fig. 38. Idler output energy of the double pass CSP OPG vs. incident pump energy at 1.198 μm [500]. Inset: ACF of the idler pulses at 4.64 μm with corresponding Gaussian fit, measured by SHG in 4-mm long type-I GaSe.

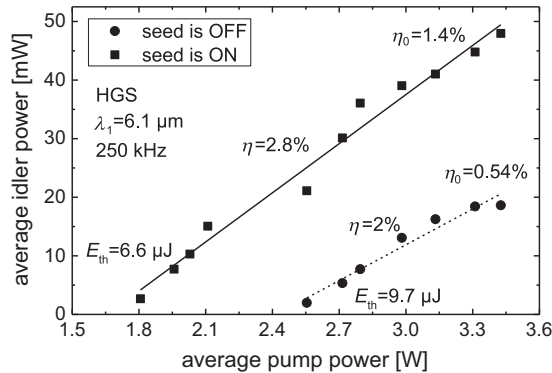


Fig. 39. Average idler power of the single pass ps HGS OPG vs. average incident pump power at 1.064 μm with and without cw SF seeding at the signal wave [501].

nowadays as pump sources, Table 12. Broad tunability up to 10 μm was achieved by tilting the HGS crystal. Seeding at the signal wavelength by a cw SF source was employed in order to maintain the TBP of the 15 ps pump pulses. As can be seen from Fig. 39, seeding reduced the threshold and increased the output power; it also improved the idler spatial quality [501].

7. Miscellaneous down-conversion using non-oxide nonlinear materials

The previous sections presented detailed history, trends and latest results on down-conversion of laser radiation to the mid-IR using non-oxide NLCs. There is clear correspondence between the type of device and the temporal regime although the borderline appears nowadays somewhat smeared due to the availability of NLCs with very high figure of merit. Examples are the sub-ns OPOs and the ns OPGs. In this concluding section it is important to outline which related topics remained outside the scope of the present text and explain why.

The first important issue concerns the generation of far-IR or THz radiation in the 30–3000 μm (0.1–10 THz) spectral range. There are few reasons why this topic is closely related to the present review. First of all, one of the methods (in fact one out of many) for generation of THz radiation is based on second-order nonlinear frequency down-conversion, i.e. DFG or optical rectification which is a particular case of DFG [1,3,6]. The other important reason is that the same non-oxide NLCs (few of them widely discussed here) are one of the best selections for the far-IR, too. The third reason is that strictly speaking it is impossible to draw a borderline between down conversion to the mid-IR and far-IR and the adopted here border wavelength of 30 μm is simply a convention.

Optical rectification is equivalent to DFG when the two input fields have equal carrier frequencies, i.e., $\omega_3 = \omega_2$ and they coincide. The resulting idler field from a single input is then DC or transient DC which typically creates THz radiation for ultrashort excitation pulses. The linear electro-optic (Pockels) effect when a DC field acts on an optical field is the reverse process and it can be shown that under full permutation symmetry the two processes are governed by the same nonlinear coefficient which is proportional to the electro-optic coefficient [1,6]. The crystallographic symmetry properties remain unchanged. However, there are different resonant contributions to the second-order nonlinear susceptibility tensor when the optical frequencies lie above and the DC field below the reststrahlen band. Therefore the nonlinear coefficients are different from those discussed in Section 3, they cannot be derived from them and Miller's rule

cannot be applied [502]. Moreover, the requirements to the NLCs are different, e.g., good transmission in the THz range is desirable and can be equally important as the nonlinear coefficient, hence, the FM shall be redefined. These differences are the main reason why THz generation is outside the scope of the present review which is to a great extent material oriented, apart from the fact that a lot of review articles on the subject already exist. In fact THz generation has developed into a broad field of its own with impressive publication activity in recent years – a nice overview on second-order nonlinear down-conversion for THz generation with emphasis on ultrashort pulses and use of QPM can be found in [503].

Many of the theoretical aspects presented in the initial sections are relevant also to DFG of THz radiation when the generated wave is low-frequency (i.e. close to DC with $\omega_1 \ll \omega_3, \omega_2$) or optical rectification with a single ultrashort pulse when DFG occurs among its frequency components. For instance, the DFG efficiency will be intrinsically limited to very low values according to Eq. (5) due to the $(\lambda_1)^{-2}$ dependence and linear absorption shall be taken into account as in Eq. (14) because it can be detrimental. Similar laser sources (e.g., dual-wavelength lasers, cw SF lasers for monochromatic THz generation, mode-locked lasers or SPOPOs generating broadband ps or fs pulses at high repetition rates, amplified ultrafast systems at low repetition rate, etc.) and similar devices and methods (e.g., DFG including intracavity DFG or optical rectification, OPO or SPOPO with non-resonated THz wave or DFG of signal and idler from OPO/SPOPO, etc.) can be used for THz generation again on temporal scales from cw to ultrafast, at different repetition rates and different energy/power levels. Similar problems such as residual absorption, TPA, damage limitations etc. are also encountered in THz generation.

After quartz, the highly nonlinear InSb was one of the first NLCs employed for THz generation at $\sim 99 \mu\text{m}$ [504]. The choice of such cubic zincblende compounds was motivated by transparency both near $10 \mu\text{m}$ (CO_2 laser) and in the THz range, i.e. narrow lattice resonances that permit transmission both $> 1000 \text{ cm}^{-1}$ and $< 100 \text{ cm}^{-1}$. They are still widely used, on the first place ZnTe which transmits also in the visible and was studied for the first time with the R_1 and R_2 lines of the ruby laser [505], but also GaAs, CdTe, InP, GaP, etc. The zincblende NLCs show good transparency below their lowest phonon resonance, e.g. $< 8 \text{ THz}$ for GaAs. PM is again desirable but the coherence lengths can be pretty large for THz generation in such semiconductors, of the order of 1 mm, comparable to the interaction length determined by absorption, and further, noncollinear PM may occur [505,506]. In contrast, non-phase-matched DFG was mentioned few times in the present review in relation to first demonstrations but was not systematically discussed because, apart from some rare occasions [133] and for extreme bandwidths (see below), it has lost its importance in the mid-IR. Even if non-phase-matched DFG looks simple for realization in the far-IR, in the absence of PM other nonlinear processes cannot be suppressed and this limits the power levels, e.g., in ZnTe. In fact it can be shown that the PM condition for low-frequency idler generation is equivalent to the equality of the phase velocity of the THz wave and the (average) group velocity of the two optical pulses with close frequencies [507]. Birefringent PM is impossible in the optically isotropic semiconductors although in some of them the optical group index and the THz refractive index are very close (ZnTe, GaP). Input optical and THz wavelengths for which this situation might occur in GaAs, CdTe, InP, GaP, and ZnTe were computed in [508]. Some more exotic methods such as magneto-optic PM [509] or anomalous dispersion by manipulation of the absorption bands [510] were developed but they required operation at low temperatures. Thus, chalcopyrites, such as ZGP which also show relatively narrow lattice band, were introduced for phase-matched DFG into the far-IR [511]. GaSe is another non-oxide NLO that is attractive for collinear phase-matched DFG in the THz range because it exhibits rather low absorption losses [135,503].

The ns DFG experiment in GaSe discussed in Section 6.2.1 [135] is a good illustration how mid-IR and far-IR generation is possible by the same phase-matched process and the same set-up: the one extended up to 38.4 μm (7.81 THz) and the other started from 58.2 μm (5.15 THz) with the gap caused by lattice absorption. However, this gap differs from crystal to crystal and the role of resonant contributions to the nonlinearity in the region of strong absorption is in general unknown. QPM is also possible and a lot of results were obtained with OPGaAs [503]. In contrast to non-phase-matched optical rectification which typically generates single pulses, optical rectification in QPM crystals gives rise to multi-cycle narrowband THz radiation [503].

Strictly speaking optical rectification requires no PM. In centrosymmetric bulk semiconductors this condition is anyway not satisfied. Extremely short pulses can be then produced, but at the expense of efficiency since only the entrance and exit interfaces of the material contribute to the nonlinear process. This technique was adapted from the far-IR to the mid-IR in [512] using the entrance surface of GaAs which absorbs the input 800 nm radiation to generate quasi-single-cycle mid-IR pulses whose spectrum extended from 7 to 15 μm . Reaching such (short) wavelengths relied on the fact that input pulses with 15-fs duration possess near-zero frequency components which encompass the production of light in the mid-IR. In crystals that in principle permit PM such as GaSe, single-cycle regime was possible only violating it, i.e., in pure optical rectification when the conversion efficiency is much lower [356,513]. In other words interaction within a coherence length is necessary for extremely broad idler bandwidths because PM selects spectral components and narrows the idler spectrum [356,443]. In [514], broadband shaping of mid-IR pulses generated by optical rectification in GaAs was demonstrated by shaping the input pulses.

Nevertheless, using a very thin (90 μm) GaSe crystal, pulses as short as 55 fs were obtained at 12 μm through phase-matched DFG of the broad input spectrum [515]. Tuning is possible by PM [356] and such was demonstrated in [515] from 0.1 to 60 THz (3 mm to 5 μm) with a gap at 5–7 THz corresponding to the reststrahlen band of GaSe. These limits also illustrate the smeared border between mid-IR and far-IR DFG with respect to the generation method and sources used.

Besides the inorganic NLCs considered in this review, it should be mentioned that organic materials can also be employed for mid-IR generation. One of the most popular and widely studied organic NLC is DAST [516]. Such crystals show much higher nonlinearities than the inorganic materials, at lower refractive index but also, apart from their inferior mechanical and chemical stability, absorption features within the transparency window. One of the primary application fields of such NLCs is THz generation by optical rectification, however, PM for DFG of THz radiation is also possible [516]. DFG was realized in DAST in the far-IR but also in the mid-IR by practically the same methods as discussed in previous sections although the material shows some resonances in the spectral range of both idler and input waves. In [517] the idler waves from a dual-wavelength ns KTP OPO were mixed in DAST to generate radiation from 2 to 30 THz (150–10 μm). In [518], the signal and idler from a fs near-IR OPA pumped by a fs Ti:Sa regenerative amplifier at 1 kHz were mixed in a 0.5 mm DAST crystal. To utilize the highest d_{eff} , the polarizations of all three waves were parallel, nevertheless it was possible to achieve PM also in the mid-IR under noncollinear propagation. The idler spectra recorded covered the 8–30 THz (37.5–10 μm) spectral range. Thus fs pulses were generated at record-long idler wavelengths if one compares with Table 12.

As emphasized in many places, damage resistivity is one of the major limitations of non-oxide NLCs. In Section 5 some important relations between damage susceptibility and other material properties such as band-gap or thermal conductivity were outlined. Still, some non-oxide NLCs remained excluded from the consideration. One example is the polytype SiC characterized by

wide band-gap and high thermal conductivity but modest nonlinearity. Recently, extremely high damage threshold of $>3 \text{ GW/cm}^2$ for 5 ns pulses at $1.064 \mu\text{m}$ was reported for two of the hexagonal polytypes [519]. Tunable DFG was obtained with broadband 5-fs pulses from a Ti:Sa amplifier using 4H-SiC. Moreover, the material seems usable also in OPA pumped at 800 nm – seeded operation in the fs regime was demonstrated with the idler at $3.75 \mu\text{m}$ [520]. However, the practical upper transmission limit for a 3-mm thick sample is around $4 \mu\text{m}$. Therefore, the extent of the transparency of SiC is similar to the best oxide NLCs, just like GaN which is under development for QPM applications [70].

It should be outlined that the present review on down-conversion of laser radiation in non-oxide NLCs was limited to birefringent PM and QPM. With some exceptions, basically some pioneering work and the THz generation by optical rectification discussed in this section, non-phase-matched DFG was not considered, although it is most relevant to the cubic semiconductors. The main reason is the low efficiency, e.g., some more recent experiments with non-phase-matched DFG in the 8–12 μm range using the cubic GaAs and ZnSe led to pJ energy levels [521] which is too low for ns pulses at low repetition rates (see Section 6.2.1). Still, some related aspects can be mentioned here. As explained in Section 5, the predecessors of OPGaAs were diffusion bonded stacks. Experimental results with DBGaAs were mentioned in Sections 6.2.1 and 6.3.1.2 although they relied on third order QPM which reduces d_{eff} , see Section 2. Some preliminary DFG experiments with small number of diffusion bonded plates which just served to demonstrate the principle utilizing yet higher order QPM were, however, discarded [522]. The so-called random PM is known in fact from the early period of nonlinear optics and such effects were described for DFG between 4 and 21 μm in ZnSe in 1975 [523]. It can be placed somewhere between non-phase-matched and QPM processes, the conversion efficiency is still too low for practical applications and maybe sufficient only for temporal diagnostics. A more recent review contains experimental results on mid-IR DFG in polycrystalline ZnSe [524].

Finally, some more exotic PM schemes applicable to the cubic zincblende NLCs will only be mentioned here. Total internal reflection was in fact proposed by the pioneers of nonlinear optics in their seminal work [3], together with QPM. This technique was recently employed for DFG in ZnSe slabs but the conversion efficiency was very low and deviated substantially from theoretical expectations [525]. Due to the small mode size and strong modal overlap, the DFG efficiency can be extremely high in waveguides. Form-birefringent PM (FBPM) uses highly asymmetric, sub-wavelength waveguides or waveguide layers to engineer sufficient birefringence to counteract the material dispersion. DFG from 5.2 to 5.6 μm based on FBPM was demonstrated in cw regime in AlGaAs/AlAs selectively oxidized waveguides [526]. Substantial improvement in conversion efficiency and cw idler power was achieved recently with ultrahigh index-contrast waveguides - subwavelength GaAs rib waveguides suspended in air [527]. Obviously, waveguide geometries are also interesting for down-conversion by QPM in OPGaAs [528].

Acknowledgments

The author acknowledges fruitful collaboration, contributions, numerous discussions, and generous provision of materials and unpublished information for this paper from P. Schunemann (Nashua, USA), M. Eichhorn, G. Stöppler, A. Hildenbrand and C. Kieleck (Saint Louis, France), V. Badikov, D. Badikov, G. Shevyrdyaeva and V. Panyutin (Krasnodar, Russia), M. Beutler, F. Noack, G. Marchev and A. Kwasniewski (Berlin, Germany), K. Mitin (Moscow, Russia), M.

Ebrahim-Zadeh and A. Esteban-Martin (Barcelona, Spain), K. Miyata and T. Suzuki (Tokyo, Japan), L. Isaenko, A. Yelissev, A. Tyazhev, V. Vedenyapin, M. Starikova and D. Kolker (Novosibirsk, Russia), K. Kato and N. Umemura (Chitose, Japan), J.-J. Zondy (Paris, France), A. Agnesi, F. Pirzio and M. Reza (Pavia, Italy), H. Giessen (Stuttgart, Germany), D. Guyer (Bellevue, USA), V. Pasiskevicius (Stockholm, Sweden), F. Rotermund (Suwon, Korea), A. Peremans and N. Hendaoui (Namur, Belgium), P. Segonds and B. Boulanger (Grenoble, France).

References

- [1] R.W. Boyd, *Nonlinear Optics*, 3rd ed., Academic Press, Orlando, 2008.
- [2] P.A. Franken, A.E. Hill, C.W. Peters, G. Weinreich, *Phys. Rev. Lett.* 7 (1961) 118.
- [3] J.A. Armstrong, N. Bloembergen, J. Ducuing, P.S. Pershan, *Phys. Rev.* 127 (1962) 1918.
- [4] R.L. Sutherland, *Handbook of Nonlinear Optics*, 2nd ed., Marcel Dekker, New York, 2003.
- [5] V.G. Dmitriev, G.G. Gurzadyan, D.N. Nikogosyan, *Handbook of Nonlinear Optical Crystals*, 3rd ed., Springer, Berlin, 1999.
- [6] G. New, *Introduction to Nonlinear Optics*, Cambridge University Press, New York, 2011.
- [7] F. Zernike, J.E. Midwinter, *Applied Nonlinear Optics*, Wiley, New York, 1973.
- [8] V.G. Dmitriev, L.V. Tarasov, *Applied Nonlinear Optics*, 2nd ed., Fizmatlit, Moscow, 2004 (in Russian).
- [9] H. Ito, H. Naito, H. Inaba, *J. Appl. Phys.* 46 (1975) 3992.
- [10] P. Tzankov, V. Petrov, *Appl. Opt.* 44 (2005) 6971.
- [11] G.D. Boyd, D.A. Kleinman, *J. Appl. Phys.* 39 (1968) 3597.
- [12] M.M. Fejer, G.A. Magel, D.H. Jundt, R.L. Byer, *IEEE J. Quantum Electron.* 28 (1992) 2631.
- [13] R.A. Baumgartner, R.L. Byer, *IEEE J. Quantum Electron.* 15 (1979) 432.
- [14] R. Danielius, A. Piskarskas, A. Stabinis, G.P. Banfi, P. Di Trapani, R. Righini, *J. Opt. Soc. Am. B* 10 (1993) 2222 (errata 12 (1995) 2321).
- [15] V. Petrov, M. Ghotbi, O. Kokabee, A. Esteban-Martin, F. Noack, A. Gaydardzhiev, I. Nikolov, P. Tzankov, I. Buchvarov, K. Miyata, A. Majchrowski, I.V. Kityk, F. Rotermund, E. Michalski, M. Ebrahim-Zadeh, *Laser Phot. Rev.* 4 (2010) 53.
- [16] A.P. Piskarskas, A.P. Stabinis, V. Pyragaite, *IEEE J. Quantum Electron.* 46 (2010) 1031.
- [17] S.I. Orlov, E.V. Pestryakov, Y.N. Polivanov, *Quantum Electron.* 34 (2004) 477.
- [18] A. Birmontas, A. Piskarskas, A. Stabinis, *Sov. J. Quantum Electron.* 13 (1983) 1243 (transl. from *Kvantovaya Elektron. (Moscow)* 10 (1983) 1881).
- [19] X. Liu, D. Deng, M. Li, D. Guo, Z. Xu, *J. Appl. Phys.* 74 (1993) 2989.
- [20] M.S. Webb, D. Eimerl, S.P. Velsko, *J. Opt. Soc. Am. B* 9 (2007) 1118.
- [21] K. Kato, F. Tanno, N. Umemura, *Appl. Opt.* 52 (2013) 2328.
- [22] G. Cerullo, S. De Silvestri, *Rev. Sci. Instrum.* 74 (2003) 1.
- [23] A.V. Smith, *Opt. Lett.* 26 (2001) 719.
- [24] S. Witte, K.S.E. Eikema, *IEEE J. Sel. Top. Quantum Electron.* 18 (2012) 296.
- [25] S.A. Akhmanov, A.S. Chirkin, K.N. Drabovich, A.I. Kovrigin, R.V. Khokhlov, A.P. Sukhorukov, *IEEE J. Quantum Electron.* 4 (1968) 598.
- [26] J.-C. Diels, W. Rudolph, *Ultrashort Laser Pulse Phenomena*, 2nd ed., Academic Press, Elsevier Inc., Amsterdam, 2006.
- [27] J.A. Armstrong, S.S. Jha, N.S. Shiren, *IEEE J. Quantum Electron.* 6 (1970) 123.
- [28] V. Petrov, F. Noack, R. Stolzenberger, *Appl. Opt.* 36 (1997) 1164.
- [29] S.A. Akhmanov, V.A. Vysloukh, A.S. Chirkin, *Optics of Femtosecond Laser Pulses*, AIP, New York, 1992.
- [30] A.P. Sukhorukov, *Nonlinear Wave Interactions in Optics and Radiophysics*, Nauka, Moscow, 1988 (in Russian).
- [31] R.L. Byer, in: H. Rabin, C.L. Tang (Eds.), *Quantum Electronics: A Treatise*, Vol. I *Nonlinear Optics*, Part B, Academic Press, New York, 1975, pp. 587–702.
- [32] J.A. Giordmaine, R.C. Miller, *Phys. Rev. Lett.* 14 (1965) 973.
- [33] R.G. Smith, in: A.K. Levine, A.J. DeMaria (Eds.), *Lasers*, vol. 4, Marcel Dekker, New York, 1976, pp. 189–306.
- [34] M. Ebrahimzadeh, M.H. Dunn, Chapter 22 of *OSA Handbook of Optics*, Vol. IV, *Fiber Optics & Nonlinear Optics*, McGraw Hill, New York, 2001, pp. 22.01–22.72.

- [35] S.J. Brosnan, R.L. Byer, *IEEE J. Quantum Electron.* 15 (1979) 415.
- [36] A.V. Smith, M.S. Bowers, *J. Opt. Soc. Am. B* 18 (2001) 706.
- [37] A.V. Smith, D.J. Armstrong, *J. Opt. Soc. Am. B* 19 (2002) 1801.
- [38] E.C. Cheung, J.M. Liu, *J. Opt. Soc. Am. B* 7 (1990) 1385.
- [39] A.A. Kaminskii, *Laser Photon. Rev.* 1 (2007) 93.
- [40] S.B. Mirov, V.V. Fedorov, D. Martyshekin, I.S. Moskalev, M. Mirov, S. Vasilyev, *IEEE J. Sel. Top. Quantum Electron.* 21 (2015) 1601719.
- [41] J. Faist, *Quantum Cascade Lasers*, Oxford University Press, 2013.
- [42] P.S. Bechthold, S. Haussühl, *Appl. Phys.* 14 (1977) 403.
- [43] M. Hagemann, H.-J. Weber, *Appl. Phys. A* 63 (1996) 67.
- [44] L. Kang, D.M. Ramo, Z. Lin, P.D. Bristowe, J. Qin, C. Chen, *J. Mater. Chem. C* 1 (2013) 7363.
- [45] D.N. Nikogosyan, *Nonlinear Optical Crystals: A Complete Survey*, Springer, New York, 2005.
- [46] A.G. Jackson, M.C. Ohmer, S.R. LeClair, *Infrared Phys. Technol.* 38 (1997) 233.
- [47] G.D. Boyd, E. Buehler, F.G. Storz, J.H. Wernick, *IEEE J. Quantum Electron.* 8 (1972) 419.
- [48] W. Jantz, P. Koidl, W. Wettling, *Appl. Phys. A* 30 (1983) 109.
- [49] D. Haertle, M. Jazbinsek, G. Montemezzani, P. Günter, *Opt. Express* 13 (2005) 3765.
- [50] Yu.V. Voroshilov, V.Yu. Slivka, *Anoksidnye Materialy dlya Elektronnoi Tekhniki, Vishcha shkola, L'vov*, 1989 (in Russian).
- [51] J.L. Shay, J.H. Wernick, *Ternary Chalcopyrite Semiconductors: Growth, Electronic Properties, and Applications*, Pergamon Press, Oxford, 1975.
- [52] L. Isaenko, P. Krinitsin, V. Vedenyapin, A. Yelissev, A. Merkulov, J.-J. Zondy, V. Petrov, *Cryst. Growth Des.* 5 (2005) 1325.
- [53] K.T. Zawilski, P.G. Schunemann, T.C. Pollak, D.E. Zelmon, N.C. Fernelius, F. Kenneth Hopkins, *J. Cryst. Growth* 312 (2010) 1127.
- [54] V. Petrov, V. Badikov, V. Panyutin, in: M. Ebrahim-Zadeh, I. Sorokina (Eds.), *Mid-Infrared Coherent Sources and Applications. NATO Science for Peace and Security Series – B: Physics and Biophysics*, Springer, Dordrecht, NL, 2008, pp. 105–147.
- [55] P.G. Schunemann, *MRS Bull.*, July (1998) 23–27.
- [56] R.S. Caldwell, H.Y. Fan, *Phys. Rev.* 114 (1959) 664.
- [57] H. Iijima, R. Nagai, N. Nishimori, R. Hajima, E.J. Minehara, *Rev. Sci. Instrum.* 80 (2009) 123106.
- [58] S. Avanesov, V. Badikov, A. Tyazhev, D. Badikov, V. Panyutin, G. Marchev, G. Shevyrdyaeva, K. Mitin, F. Noack, P. Vinogradova, N. Schebetova, V. Petrov, A. Kwasniewski, *Opt. Mater. Express* 1 (2011) 1286.
- [59] V. Petrov, V.L. Panyutin, A. Tyazhev, G. Marchev, A.I. Zagumennyi, F. Rotermund, F. Noack, K. Miyata, L.D. Iskhakova, A.F. Zerrouk, *Laser Phys.* 21 (2011) 774.
- [60] V. Badikov, K. Mitin, F. Noack, V. Panyutin, V. Petrov, A. Seryogin, G. Shevyrdyaeva, *Opt. Mater.* 31 (2009) 590.
- [61] J.-J. Zondy, V. Petrov, A. Yelissev, L. Isaenko, S. Lobanov, in: M. Ebrahim-Zadeh, I. Sorokina (Eds.), *Mid-Infrared Coherent Sources and Applications. NATO Science for Peace and Security Series – B: Physics and Biophysics*, Springer, Dordrecht (NL), 2008, pp. 67–104.
- [62] S. Fossier, S. Salauin, J. Mangin, O. Bidault, I. Thenot, J.-J. Zondy, W. Chen, F. Rotermund, V. Petrov, P. Petrov, J. Henningsen, A. Yelissev, L. Isaenko, S. Lobanov, O. Balachninaite, G. Sleky, V. Sirutkaitis, *J. Opt. Soc. Am. B* 21 (2004) 1981.
- [63] V. Petrov, J.-J. Zondy, O. Bidault, L. Isaenko, V. Vedenyapin, A. Yelissev, W. Chen, A. Tyazhev, S. Lobanov, G. Marchev, D. Kolker, *J. Opt. Soc. Am. B* 27 (2010) 1902.
- [64] V. Petrov, A. Yelissev, L. Isaenko, S. Lobanov, A. Titov, J.-J. Zondy, *Appl. Phys. B* 78 (2004) 543.
- [65] V. Badikov, D. Badikov, G. Shevyrdyaeva, A. Tyazhev, G. Marchev, V. Panyutin, V. Petrov, A. Kwasniewski, *Phys. Stat. Sol. RRL* 5 (2011) 31.
- [66] J. Xu, G.M.H. Knippels, D. Oepts, A.F.G. Van der Meer, *Opt. Commun.* 197 (2001) 379.
- [67] P.S. Kuo, M.M. Fejer, in: M. Ebrahim-Zadeh, I. Sorokina (Eds.), *Mid-Infrared Coherent Sources and Applications. NATO Science for Peace and Security Series – B: Physics and Biophysics*, Springer, Dordrecht, NL, 2008, pp. 149–168.
- [68] A. Grisard, E. Lallier, B. Gérard, *Opt. Mater. Express* 2 (2012) 1020.
- [69] C. Lynch, D.F. Bliss, M. Snure, V. Tassev, G. Bryant, C. Yapp, D.B. Fenner, M.G. Allen, K. Termkoa, J. Li, S. Vangala, W. Goodhue, *J. Cryst. Growth* 353 (2012) 152.
- [70] P.G. Schunemann, S.D. Setzler, *Proc. SPIE* 7917 (2011) 79171F.
- [71] P. Klocek (Ed.), *Handbook of Infrared Optical Materials*, Marcel Dekker, New York, 1991.
- [72] V. Tassev, D. Bliss, M. Snure, G. Bryant, R. Peterson, R. Bedford, C. Yapp, W. Goodhue, K. Termkoa, *J. Eur. Opt. Soc. – Rapid Publ.* 6 (2011) 11017.

- [73] V. Tassev, M. Snure, S. Vangala, M. Kimani, R. Peterson, P. Schunemann, *Proc. SPIE* 9253 (2014) 925318.
- [74] H. Kildal, J.C. Mikkelsen, *Opt. Commun.* 9 (1973) 315.
- [75] H. Kildal, J.C. Mikkelsen, *Opt. Commun.* 10 (1974) 306.
- [76] M.S. Piltch, J. Rink, C. Tallman, *Opt. Commun.* 15 (1975) 112.
- [77] T.J. Bridges, V.T. Nguyen, E.G. Burkhardt, C.K.N. Patel, *Appl. Phys. Lett.* 27 (1975) 600.
- [78] P. Canarelli, Z. Benko, R. Curl, F.K. Tittel, *J. Opt. Soc. Am. B* 9 (1992) 197.
- [79] A. Vitcu, R. Ciurylo, R. Wehr, J.R. Drummond, A.D. May, *Appl. Opt.* 43 (2004) 4965.
- [80] A.H. Hielscher, C.E. Miller, D.C. Bayard, U. Simon, K.P. Smolka, R.F. Curl, F.K. Tittel, *J. Opt. Soc. Am. B* 9 (1992) 1962.
- [81] U. Simon, F.K. Tittel, L. Goldberg, *Opt. Lett.* 18 (1993) 1931.
- [82] U. Simon, C.E. Miller, C.C. Bradley, R.G. Hulet, R.F. Curl, F.K. Tittel, *Opt. Lett.* 18 (1993) 1062.
- [83] U. Simon, S. Waltman, I. Loa, F.K. Tittel, L. Hollberg, *J. Opt. Soc. Am. B* 12 (1995) 323.
- [84] K.P. Petrov, S. Waltman, U. Simon, R.F. Curl, F.K. Tittel, E.J. Dlukencky, L. Hollberg, *Appl. Phys. B* 61 (1995) 553.
- [85] F.J. Effenberger, G.J. Dixon, *CLEO 1994*, paper CThQ5.
- [86] E.J. Canto-Said, M.P. McCann, P.G. Wigley, G.J. Dixon, *Opt. Lett.* 20 (1995) 1268.
- [87] W. Chen, J. Burie, D. Boucher, *Rev. Sci. Instrum.* 67 (1996) 3411.
- [88] W. Chen, J. Burie, D. Boucher, *Spectrochim. Acta A* 55 (1999) 2057.
- [89] W. Schade, T. Blanke, U. Willer, C. Rempel, *Appl. Phys. B* 63 (1996) 99.
- [90] A. Khorsandi, U. Willer, P. Geiser, W. Schade, *Appl. Phys. B* 77 (2003) 509.
- [91] B. Sumpf, T. Kelz, M. Nägele, H.-D. Kronfeldt, *Appl. Phys. B* 64 (1997) 521.
- [92] T. Kelz, A. Schumacher, M. Nägele, B. Sumpf, H.-D. Kronfeldt, *J. Quant. Spectrosc. Radiat. Transfer* 61 (1999) 591.
- [93] H.-D. Kronfeldt, G. Basar, B. Sumpf, *J. Opt. Soc. Am. B* 13 (1996) 1859.
- [94] D. Lee, T. Kaing, J.-J. Zondy, *Appl. Phys. B* 67 (1998) 363.
- [95] M. Maleki, S.G. Sabouri, A. Khorsandi, *Opt. Laser Technol.* 56 (2014) 436.
- [96] V. Petrov, C. Rempel, K.-P. Stolberg, W. Schade, *Appl. Opt.* 37 (1998) 4925.
- [97] L. Wang, Z. Cao, H. Wang, H. Zhao, W. Gao, Y. Yuan, W. Chen, W. Zhang, Y. Wang, X. Gao, *Opt. Commun.* 284 (2011) 358.
- [98] K.P. Petrov, R.F. Curl, F.K. Tittel, L. Goldberg, *Opt. Lett.* 21 (1996) 1451.
- [99] B. Sumpf, D. Rehle, T. Kelz, H.-D. Kronfeldt, *Appl. Phys. B* 67 (1998) 369.
- [100] W. Chen, G. Mouret, D. Boucher, *Appl. Phys. B* 67 (1998) 375.
- [101] W. Chen, F. Cazier, F. Tittel, D. Boucher, *Appl. Opt.* 39 (2000) 6238.
- [102] W.C. Eckhoff, R.S. Putnam, S. Wang, R.F. Curl, F.K. Tittel, *Appl. Phys. B* 63 (1996) 437.
- [103] R.S. Putnam, D.G. Lancaster, *Appl. Opt.* 38 (1999) 1513.
- [104] W. Chen, E. Pouillet, J. Burie, D. Boucher, M.W. Sigrist, J.-J. Zondy, L. Isaenko, A. Yelissev, S. Lobanov, *Appl. Opt.* 44 (2005) 4123.
- [105] D. Levi, T.J. Pinguet, T. Skauli, L.A. Eyres, K.R. Parameswaran, J.S. Harris Jr., M.M. Fejer, T.J. Kulp, S.E. Bisson, B. Gerard, E. Lallier, L. Becouarn, *Opt. Lett.* 27 (2002) 2091.
- [106] S.E. Bisson, T.J. Kulp, O. Levi, J.S. Harris, M.M. Fejer, *Appl. Phys. B* 85 (2006) 199.
- [107] S. Vasilyev, S. Schiller, A. Nevsky, A. Grisard, D. Faye, E. Lallier, Z. Zhang, A.J. Boyland, J.K. Sahu, M. Ibsen, W.A. Clarkson, *Opt. Lett.* 33 (2008) 1413.
- [108] K. Devi, P.G. Schunemann, M. Ebrahim-Zadeh, *Opt. Lett.* 39 (2014) 6751.
- [109] U. Simon, F.K. Tittel, *Infrared Phys. Technol.* 36 (1995) 427.
- [110] U. Simon, Z. Benko, M.W. Sigrist, R.F. Curl, F.K. Tittel, *Appl. Opt.* 32 (1993) 6650.
- [111] A. Douillet, J.-J. Zondy, *Opt. Lett.* 23 (1998) 1259.
- [112] A. Douillet, J.-J. Zondy, A. Yelissev, S. Lobanov, L. Isaenko, *J. Opt. Soc. Am. B* 16 (1999) 1481.
- [113] J.-J. Zondy, A. Douillet, A. Clairon, A. Yelissev, L. Isaenko, S. Lobanov, *J. Mater. Sci.: Mater. Electron.* 12 (2001) 451.
- [114] L. Pomeranz, P. Schunemann, S. Setzler, C. Jones, P. Budni, *CLEO 2012*, paper JTh11.4.
- [115] M.D. Martin, E.L. Thomas, *Phys. Lett.* 19 (1966) 651.
- [116] D.C. Hanna, R.C. Smith, C.R. Stanley, *Opt. Commun.* 4 (1971) 300.
- [117] G.C. Bhar, D.C. Hanna, B. Luther-Davies, R.C. Smith, *Opt. Commun.* 6 (1972) 323.
- [118] R.L. Byer, M.M. Choy, R.L. Herbst, D.S. Chemla, R.S. Feigelson, *Appl. Phys. Lett.* 24 (1974) 65.
- [119] D. Andreou, *Opt. Commun.* 23 (1977) 37.
- [120] A. Bianchi, M. Garbi, *Opt. Commun.* 30 (1979) 122.
- [121] Ph. Kupecek, H. Le Person, M. Comte, *Infrared Phys.* 19 (1979) 263.

- [122] K.S. Abedin, S. Haidar, Y. Konno, C. Takyo, H. Ito, *Appl. Opt.* 37 (1998) 1642.
- [123] S. Haidar, K. Nakamura, E. Niwa, K. Masumoto, H. Ito, *Appl. Opt.* 38 (1999) 1798.
- [124] S. Haidar, H. Ito, *Opt. Commun.* 171 (1999) 171.
- [125] G. Mennerat, Ph. Kupecek, *ASSL* 1998, vol. 19 of OSA TOPS, pp. 269–272.
- [126] E. Lallier, L. Becouarn, M. Brévignon, J. Lehoux, *Electron. Lett.* 34 (1998) 1609.
- [127] W.R. Bosenberg, D.R. Guyer, *J. Opt. Soc. Am. B* 10 (1993) 1716.
- [128] R. Utano, M.J. Ferry, *ASSL* 1997, vol. 10 of OSA TOPS, pp. 267–269.
- [129] S. Haidar, K. Miyamoto, H. Ito, *J. Phys. D: Appl. Phys.* 37 (2004) 3347.
- [130] A. Godard, M. Raybaut, O. Lambert, J.-P. Faleni, M. Lefebvre, E. Rosencher, *J. Opt. Soc. Am. B* 22 (2005) 1966.
- [131] Y.-F. Geng, X.-L. Tan, X.-J. Li, J.-Q. Yao, *Chin. Phys. B* 19 (2010) 114209.
- [132] K. Zhong, J. Li, D. Xu, J. Wang, Z. Wang, P. Wang, J. Yao, *Optoelectron. Lett.* 6 (2010) 179.
- [133] W. Shi, Y.J. Ding, *Opt. Commun.* 207 (2002) 273.
- [134] W. Shi, Y.J. Ding, X. Mu, N. Fernelius, *Appl. Phys. Lett.* 80 (2002) 3889.
- [135] W. Shi, Y. Ding, *Appl. Phys. Lett.* 84 (2004) 1635.
- [136] G.B. Abdullaev, L.A. Kulevskii, P.V. Nikles, A.M. Prokhorov, A.D. Savel'ev, E.Yu. Salaev, V.V. Smirnov, *Sov. J. Quantum Electron.* 6 (1976) 88 (transl. from *Kvantovaya Elektron. (Moscow)* 3 (1976) 163).
- [137] J.L. Oudar, Ph.J. Kupecek, D.S. Chemla, *Opt. Commun.* 29 (1979) 119.
- [138] J.J. Jacob, *Proc. SPIE* 461 (1984) 11.
- [139] K. Kato, *IEEE J. Quantum Electron.* 20 (1984) 698.
- [140] D.S. Bethune, A.C. Luntz, *Appl. Phys. B* 40 (1986) 107.
- [141] M. Gerhards, *Opt. Commun.* 241 (2004) 493.
- [142] G.V. Mayer, T.N. Kopylova, Yu.M. Andreev, V.A. Svetlichnyi, E.N. Tel'minov, *Russ. Phys. J.* 52 (2009) 640 (Translated from *Izvestiya Vysshikh Uchebnykh Zavedenii, Fizika*, No. 6, (2009) 83).
- [143] K. Akagawa, S. Wada, A. Nakamura, H. Tashiro, *Appl. Opt.* 35 (1996) 2570.
- [144] A.O. Okorogu, S.B. Mirov, W. Lee, D.I. Crouthamel, N. Jenkins, A.Yu. Dergachev, K.L. Vodopyanov, V.V. Badikov, *Opt. Commun.* 155 (1998) 307.
- [145] H. Hazama, Y. Takatani, K. Awazu, *Proc. SPIE* 6455 (2007) 645507.
- [146] L.I. Stoychev, M.B. Danailov, A.A. Demidovich, I.P. Nikolov, P. Cinquergana, P. Sigalotti, D. Bakalov, A. Vacchi, *Proc. SPIE* 9135 (2014) 91350J.
- [147] S. Haidar, H. Ito, *Opt. Commun.* 202 (2002) 227.
- [148] S. Haidar, E. Niwa, K. Masumoto, H. Ito, *J. Phys. D: Appl. Phys.* 36 (2003) 1071.
- [149] S. Haidar, Y. Sasaki, E. Niwa, K. Masumoto, H. Ito, *Opt. Commun.* 229 (2004) 325.
- [150] S. Haidar, Y.K. Hsu, C.S. Chang, S.C. Wang, H. Ito, *Opt. Eng.* 41 (2002) 1932.
- [151] D. Zheng, L.A. Gordon, Y.S. Wu, R.K. Route, R.S. Feigelson, M.M. Fejer, R.L. Byer, M.S. Bowers, A. Drobshoff, D. Smith, *ASSL* 1998, vol. 19 of OSA TOPS, pp. 291–293.
- [152] J. Saikawa, M. Miyazaki, M. Fujii, H. Ishizuki, T. Taira, *Opt. Lett.* 33 (2008) 1699.
- [153] S.-C. Pei, S.-Y. Tu, A.H. Kung, *QELS* 2005, Paper JTUC4.
- [154] R.J. Seymour, F. Zernike, *Appl. Phys. Lett.* 29 (1976) 705.
- [155] S. Banerjee, K. Miyata, K. Kato, *Opt. Commun.* 277 (2007) 202.
- [156] S. Banerjee, K. Miyata, K. Kato, N. Saito, S. Wada, *Appl. Phys. B* 87 (2007) 101.
- [157] O.V. Budilova, A.A. Ionin, I.O. Kinyaevskiy, Yu.M. Klimachev, A.A. Kotkov, *Proc. SPIE* 9251 (2014) 92510P.
- [158] K. Furuki, M.-T. Horikawa, A. Ogawa, K. Miyamoto, T. Omatsu, *Opt. Express* 22 (2014) 26351.
- [159] N. Saito, K. Akagawa, S. Wada, H. Tashiro, *Appl. Phys. B* 69 (1999) 93.
- [160] N. Saito, M. Kato, S. Nakasaka, S. Wada, H. Tashiro, *Opt. Lett.* 31 (2006) 2024.
- [161] M. Yumoto, Y. Maeda, N. Saito, T. Ogawa, M. Yamashita, S. Wada, *Jpn. J. Appl. Phys.* 49 (2010) 010209.
- [162] V. Petrov, *IEEE J. Sel. Top. Quantum Electron.* 21 (2015) 1602914.
- [163] E.O. Ammann, J.M. Yarborough, *Appl. Phys. Lett.* 17 (1970) 233.
- [164] D.C. Hanna, B. Luther-Davies, H.N. Rutt, R.C. Smith, *Appl. Phys. Lett.* 20 (1972) 34.
- [165] D.C. Hanna, B. Luther-Davies, R.C. Smith, *Appl. Phys. Lett.* 22 (1973) 440.
- [166] Y.X. Fan, R.C. Eckardt, R.L. Byer, R.K. Route, R.S. Feigelson, *Appl. Phys. Lett.* 45 (1984) 313.
- [167] P.B. Phua, R.F. Wu, T.C. Chong, B.X. Xu, *Jpn. J. Appl. Phys.* 36 (1997) L1661.
- [168] T.H. Allik, S. Chandra, W.W. Hovis, C.G. Simi, J.A. Hutchinson, *Proc. SPIE* 3383 (1998) 58.
- [169] K.L. Vodopyanov, J.P. Maffetone, I. Zwieback, W. Ruderman, *Appl. Phys. Lett.* 75 (1999) 1204.
- [170] T.-J. Wang, Z.-H. Kang, H.-Z. Zhang, Q.-Y. He, Y. Qu, Z.-S. Feng, Y. Jiang, J.-Y. Gao, Y.M. Andreev, G.V. Lanskii, *Opt. Express* 14 (2006) 13001.

- [171] T.-J. Wang, Z.-H. Kang, H.-Z. Zhang, Z.-S. Feng, Y. Jiang, J.-Y. Gao, Y.M. Andreev, G.V. Lanskii, A.V. Shaiduko, *J. Phys. D: Appl. Phys* 40 (2007) 1357.
- [172] T.-J. Wang, H.-Z. Zhang, F.-G. Wu, Z.-S. Feng, H.-Y. Zang, Z.-H. Kang, Y. Jiang, J.-Y. Gao, *Laser Phys.* 19 (2009) 377.
- [173] E. Takaoka, K. Kato, CLEO 1998, Paper CWF39.
- [174] K. Kato, K. Miyata, *Proc. SPIE* 8604 (2013) 86041K.
- [175] V.V. Badikov, A.K. Don, K.V. Mitin, A.M. Seregin, V.V. Sinaiskii, N.I. Shchebetova, *Quantum Electron.* 33 (2003) 831.
- [176] V.V. Badikov, A.K. Don, K.V. Mitin, A.M. Seregin, V.V. Sinaiskii, N.I. Shchebetova, T.A. Shchetinkina, *Quantum Electron.* 37 (2007) 363.
- [177] A. Tyazhev, G. Marchev, V. Badikov, A. Esteban-Martin, D. Badikov, V. Panyutin, G. Shevyrdyaeva, S. Sheina, A. Fintisova, V. Petrov, *Laser Photon. Rev.* 7 (2013) L21.
- [178] J. Mangin, G. Mennerat, G. Gadret, V. Badikov, J.-C. de Miscault, *J. Opt. Soc. Am. B* 26 (2009) 1702.
- [179] A. Esteban-Martin, G. Marchev, V. Badikov, V. Panyutin, V. Petrov, G. Shevyrdyaeva, D. Badikov, M. Starikova, S. Sheina, A. Fintisova, A. Tyazhev, *Laser Photon. Rev.* 7 (2013) L89.
- [180] G. Marchev, M. Reza, V. Badikov, A. Esteban-Martin, G. Stöppler, M. Starikova, D. Badikov, V. Panyutin, M. Eichhorn, G. Shevyrdyaeva, A. Tyazhev, S. Sheina, A. Agnesi, A. Fintisova, V. Petrov, *Appl. Opt.* 53 (2014) 7951.
- [181] V.V. Badikov, A.K. Don, K.V. Mitin, A.M. Seryogin, V.V. Sinaiskii, N.I. Schebetova, *Quantum Electron.* 35 (2005) 853.
- [182] V. Badikov, A. Fintisova, V. Panutin, S. Sheina, S. Scherbakov, G. Shevyrdyaeva, A. Don, K. Mitin, N. Schebetova, A. Seryogin, V. Sinaisky, N. Kuzmin, V. Laptev, A. Malinovsky, E. Ryabov, J. Mangin, G. Gadret, J.-C. Jules, G. Mennerat, C. Pasquer, J.-C. de Miscault, CLEO 2004, paper CThT44.
- [183] J.-J. Zondy, V. Vedenyapin, A. Yelisseyev, S. Lobanov, L. Isaenko, V. Petrov, *Opt. Lett.* 30 (2005) 2460.
- [184] G. Marchev, A. Tyazhev, V. Vedenyapin, D. Kolker, A. Yelisseyev, S. Lobanov, L. Isaenko, J.-J. Zondy, V. Petrov, *Opt. Express* 17 (2009) 13441.
- [185] G. Marchev, A. Tyazhev, V. Vedenyapin, D. Kolker, A. Yelisseyev, S. Lobanov, L. Isaenko, J.-J. Zondy, V. Petrov, *Proc. SPIE* 7487 (2009) 74870F.
- [186] A. Tyazhev, G. Marchev, V. Vedenyapin, D. Kolker, A. Yelisseyev, S. Lobanov, L. Isaenko, J.-J. Zondy, V. Petrov, *Proc. SPIE* 7582 (2010) 75820E.
- [187] V. Petrov, P.G. Schunemann, K.T. Zawilski, T.M. Pollak, *Opt. Lett.* 34 (2009) 2399.
- [188] V. Petrov, G. Marchev, P.G. Schunemann, A. Tyazhev, K.T. Zawilski, T.M. Pollak, *Opt. Lett.* 35 (2010) 1230.
- [189] G. Marchev, F. Pirzio, A. Agnesi, G. Reali, V. Petrov, A. Tyazhev, P.G. Schunemann, K.T. Zawilski, *Opt. Commun.* 291 (2013) 326.
- [190] G. Marchev, A. Tyazhev, G. Stöppler, M. Eichhorn, P. Schunemann, V. Petrov, *Proc. SPIE* 8240 (2012) 82400E.
- [191] A. Tyazhev, V. Vedenyapin, G. Marchev, L. Isaenko, D. Kolker, S. Lobanov, V. Petrov, A. Yelisseyev, M. Starikova, J.-J. Zondy, *Opt. Mater.* 35 (2013) 1612.
- [192] A. Tyazhev, D. Kolker, G. Marchev, V. Badikov, D. Badikov, G. Shevyrdyaeva, V. Panyutin, V. Petrov, *Opt. Lett.* 37 (2012) 4146.
- [193] L.A. Pomeranz, P.G. Schunemann, D.J. Magarrell, J.C. McCarthy, K.T. Zawilski, D.E. Zelmon, *Proc. SPIE* 9347 (2015) 93470K.
- [194] V.V. Badikov, N.V. Kuzmin, V.B. Laptev, A.L. Malinovsky, K.V. Mitin, G.S. Nazarov, E.A. Ryabov, A.M. Seryogin, N.I. Shchebetova, *Quantum Electron.* 34 (2004) 451.
- [195] V. Petrov, G. Marchev, A. Tyazhev, M. Beutler, V. Panyutin, M. Starikova, A. Esteban-Martin, V. Badikov, G. Shevyrdyaeva, D. Badikov, M. Reza, S. Sheina, A. Fintisova, *Opt. Eng.* 52 (2013) 117102.
- [196] A. Hildenbrand, C. Kieleck, A. Tyazhev, G. Marchev, G. Stöppler, M. Eichhorn, P. Schunemann, V.L. Panyutin, V. Petrov, *Opt. Eng.* 53 (2014) 122511.
- [197] K. Kato, N. Umemura, V. Petrov, *J. Appl. Phys.* 109 (2011) 116104.
- [198] R.C. Eckardt, Y.X. Fan, R.L. Byer, C.L. Marquardt, M.E. Storm, L. Esterowitz, *Appl. Phys. Lett.* 49 (1986) 608.
- [199] S. Pearl, S. Fastig, Y. Ehrlich, R. Lavi, *Appl. Opt.* 40 (2001) 2490.
- [200] N. Barnes, K. Murray, *ASSL* 1990, vol. 6 of OSA Proc. Series, pp. 322–328.
- [201] S.T. Amimoto, R.W.F. Gross, M. Jupina, J. Machan, L. Garman-Duvall, CLEO 1990, post-deadline paper CPDP34.
- [202] R.L. Herbst, R.L. Byer, *Appl. Phys. Lett.* 21 (1972) 189.
- [203] C.L. Marquardt, D.G. Cooper, P.A. Budni, M.G. Knights, K.L. Schepler, R. DeDomenico, G.C. Catella, *Appl. Opt.* 33 (1994) 3192.

- [204] J.D. Beasley, *Appl. Opt.* 33 (1994) 1000.
- [205] G.J. Quarles, C.L. Marquardt, L. Esterowitz, in: Proc. of LEOS, IEEE, New York, 1990, paper EL7.1, pp. 128–129.
- [206] K.L. Schepler, M.D. Turner, P.A. Budni, *ASSL* 1991, vol. 10 of OSA Proc. Series, pp. 325–328.
- [207] A.H. Hazama, M. Yumoto, T. Ogawa, S. Wada, K. Awazu, *Proc. SPIE* 7917 (2011) 79170N.
- [208] S. Chandra, M. Wager, B. Clayton, A. Geiser, T.H. Allik, J.L. Ahl, C. Miller, P. Budni, P. Ketteridge, K. Lanier, E. Chicklis, J.A. Hutchinson, W.W. Hovis, *Proc. SPIE* 4036 (2000) 200.
- [209] P.A. Budni, M.G. Knights, E.P. Chicklis, K.L. Schepler, *Opt. Lett.* 18 (1993) 1068.
- [210] N.P. Barnes, D.J. Gettemy, J.R. Hietanen, R.A. Iannini, *Appl. Opt.* 28 (1989) 5162.
- [211] N.P. Barnes, K.E. Murray, M.G. Jani, P.G. Schunemann, T.M. Pollak, *J. Opt. Soc. Am. B* 15 (1998) 232.
- [212] P.A. Budni, P.G. Schunemann, M.G. Knights, T.M. Pollak, E.P. Chicklis, *ASSL* 1992, vol. 13 of OSA Proc. Series, pp. 380–383.
- [213] P.A. Budni, L.A. Pomeranz, M.L. Lemons, P.G. Schunemann, T.M. Pollak, E.P. Chicklis, *ASSL* 1998, vol. 19 of OSA TOPS, pp. 226–229.
- [214] P.A. Ketteridge, P.A. Budni, P.G. Schunemann, M. Lemons, T.M. Pollack, E.P. Chicklis, *ASSP* 1998, vol. 19 of OSA TOPS, pp. 233–235.
- [215] S.D. Setzler, G.A. Rines, P.A. Budni, D.M. Rines, *ASSL* 2002, vol. 68 of OSA TOPS, pp. 85–87.
- [216] G.-L. Zhu, Y.-L. Ju, T.-H. Wang, Y.-Z. Wang, *Chin. Phys. Lett.* 26 (2009) 034208.
- [217] S.X. Xia, C.H. Yang, G. Li, G.Li. Zhu, B.Q. Yao, Z.T. Lei, *Laser Phys.* 21 (2011) 1366.
- [218] G.L. Zhu, Y.L. Ju, C.H. Zhang, B.Q. Yao, Y.Z. Wang, *Laser Phys.* 20 (2010) 1341.
- [219] L.J. Li, B.Q. Yao, Y.L. Ju, Y.Z. Wang, *Laser Phys.* 19 (2009) 1957.
- [220] P.A. Budni, L.A. Pomeranz, M.L. Lemons, C.A. Miller, J.R. Mosto, E.P. Chicklis, *J. Opt. Soc. Am. B* 17 (2000) 723.
- [221] M. Schellhorn, M. Eichhorn, C. Kieleck, A. Hirth, *C. R. Phys.* 8 (2007) 1151.
- [222] B.Q. Yao, Y.J. Shen, X.M. Duan, W. Wang, Y.L. Ju, Y.Z. Wang, *J. Russ. Laser Res.* 34 (2013) 503.
- [223] Y.-J. Shen, B.-Q. Yao, Z. Cui, X.-M. Duan, Y.-L. Ju, Y.-Z. Wang, *Appl. Phys. B* 117 (2014) 127.
- [224] B.-Q. Yao, Y.-J. Shen, X.-M. Duan, T.-Y. Dai, Y.-L. Ju, Y.-Z. Wang, *Opt. Lett.* 39 (2014) 6589.
- [225] G. Li, B.-Q. Yao, X.-M. Duan, G.-L. Zhu, Y.-Z. Wang, Y.-L. Ju, *Chin. Phys. Lett.* 27 (2010) 014207.
- [226] B. Yao, J. Yuan, J. Li, T. Dai, X. Duan, Y. Shen, Z. Cui, Y. Pan, *Opt. Lett.* 40 (2015) 348.
- [227] E. Lippert, S. Nicolas, G. Arisholm, K. Stenersen, G. Rustad, *Appl. Opt.* 45 (2006) 3839.
- [228] G.L. Zhu, Y.L. Ju, P.B. Meng, B.Q. Yao, Y.Z. Wang, *Laser Phys.* 20 (2010) 1329.
- [229] E. Lippert, G. Rustad, G. Arisholm, K. Stenersen, *Opt. Express* 16 (2008) 13878.
- [230] X. Mu, H. Meissner, H.-C. Lee, *Proc. SPIE* 7917 (2011) 79170M.
- [231] I. Elder, *Proc. SPIE* 7325 (2009) 73250I.
- [232] A. Hemming, J. Richards, S. Bennetts, A. Davidson, N. Carmody, P. Davies, L. Corena, D. Lancaster, *Opt. Commun.* 283 (2010) 4041.
- [233] L.H. Tan, P.B. Phua, *Proc. SPIE* 7917 (2011) 79170O.
- [234] P.G. Schunemann, *Proc. SPIE* 6455 (2007) 64550R.
- [235] E. Lippert, H. Fonnum, G. Arisholm, K. Stenersen, *Opt. Express* 18 (2010) 26475.
- [236] E. Lippert, H. Fonnum, K. Stenersen, *Proc. SPIE* 7836 (2010) 78360D.
- [237] A. Hemming, J. Richards, A. Davidson, N. Carmody, S. Bennetts, N. Simakov, J. Haub, *Opt. Express* 21 (2013) 10062.
- [238] A. Hemming, J. Richards, A. Davidson, N. Carmody, N. Simakov, M. Hughes, P. Davies, S. Bennetts, J. Haub, *CLEO* 2013, paper CW1B.7.
- [239] L.A. Pomeranz, P.A. Ketteridge, P.A. Budni, K.M. Ezzo, D.M. Rines, E.P. Chicklis, *ASSP* 2003, vol 83 of OSA TOPS, pp. 142–146.
- [240] D. Creeden, P.A. Ketteridge, P.A. Budni, S.D. Setzler, Y.E. Young, J.C. McCarthy, K. Zawilski, P.G. Schunemann, T.M. Pollak, E.P. Chicklis, M. Jiang, *Opt. Lett.* 33 (2008) 315.
- [241] D. Creeden, M. Jiang, P.A. Budni, P.A. Ketteridge, S.D. Setzler, Y.E. Young, J.C. McCarthy, P.G. Schunemann, T.M. Pollak, P. Tayebati, E.P. Chicklis, *Proc. SPIE* 6952 (2008) 69520S.
- [242] N. Simakov, A. Davidson, A. Hemming, S. Bennetts, M. Hughes, N. Carmody, P. Davies, J. Haub, *Proc. SPIE* 8237 (2012) 82373K.
- [243] C. Kieleck, A. Berrou, C. Kneis, B. Donelan, M. Eichhorn, *Proc. SPIE* 9251 (2014) 92510C.
- [244] C. Kieleck, A. Berrou, B. Donelan, B. Cadier, T. Robin, M. Eichhorn, *Proc. SPIE* 9347 (2015) 93470O.
- [245] C. Kieleck, A. Berrou, B. Donelan, B. Cadier, T. Robin, M. Eichhorn, *Opt. Lett.* 40 (2015) 1101.
- [246] M. Gebhardt, C. Gaida, P. Kadwani, A. Sincore, N. Gehlich, C. Jeon, L. Shah, M. Richardson, *Opt. Lett.* 32 (2014) 1212.

- [247] A. Dergachev, P.F. Moulton, *ASSP* 2003, vol. 83 of OSA TOPS, pp. 137–141.
- [248] P.A. Budni, C.R. Ibach, S.D. Setzler, L.A. Pomeranz, M.L. Lemons, P.A. Ketteridge, E.J. Gustafson, Y.E. Young, P.G. Schunemann, T.M. Pollak, R.T. Castro, E.P. Chicklis, *ASSP* 2003, Post-deadline paper PD12.
- [249] H.R. Lee, J. Yu, N.P. Barnes, Y. Bai, *ASSP* 2006, Paper MC1.
- [250] A.F. Nieuwenhuis, C.J. Lee, P.J.M. van der Slot, I.D. Lindsay, P. Groß, K.-J. Boller, *Opt. Lett.* 33 (2008) 52.
- [251] L. Wang, J. Yang, X. Cai, J. Wang, H. Wu, X. Wu, H. Jiang, *Chin. J. Laser* 41 (2014) 0102008 (in Chinese).
- [252] A. Dergachev, D. Armstrong, A. Smith, T. Drake, M. Dubois, *Opt. Express* 15 (2007) 14404.
- [253] A. Dergachev, D. Armstrong, A. Smith, T. Drake, M. Dubois, *Proc. SPIE* 6875 (2008) 687507.
- [254] M.W. Haakestad, H. Fønnum, E. Lippert, *Opt. Express* 22 (2014) 8556.
- [255] E. Lippert, H. Fønnum, M.W. Haakestad, *Proc. SPIE* 9251 (2014) 92510D.
- [256] G. Stoeppler, M. Schellhorn, M. Eichhorn, *Laser Phys.* 22 (2012) 1095.
- [257] G. Stoeppler, M. Schellhorn, M. Eichhorn, *Proc. SPIE* 8604 (2013) 86040I.
- [258] C. Kieleck, A. Hildenbrand, M. Schellhorn, G. Stoeppler, M. Eichhorn, *Proc. SPIE* 8898 (2013) 889809.
- [259] S. Bigotta, G. Stöppler, J. Schöner, M. Schellhorn, M. Eichhorn, *Opt. Mater. Express* 4 (2014) 411.
- [260] P.G. Schunemann, L.A. Pomeranz, K.T. Zawilski, J. Wei, L.P. Gonzalez, S. Guha, T.M. Pollak, *AIOM* (2009) paper AWA3.
- [261] P.G. Schunemann, S.D. Setzler, L. Mohnkern, T.M. Pollak, D.F. Bliss, D. Weyburne, K. O’Hearn, *CLEO* (2005) paper CThQ4.
- [262] R.D. Peterson, D. Whelan, D. Bliss, C. Lynch, *Proc. SPIE* 7197 (2009) 719709.
- [263] D. Faye, E. Lallier, A. Grisard, B. Gerard, C. Kieleck, A. Hirth, *Proc. SPIE* 6875 (2008) 68750G.
- [264] Q. Clement, J.-M. Melkonian, J.-B. Dherbecourt, M. Raybaut, A. Godard, A. Grisard, E. Lallier, B. Gerard, B. Faure, G. Souhaite, *CLEO* (2015) paper SW3O.5.
- [265] C. Kieleck, M. Eichhorn, A. Hirth, D. Faye, F. Lallier, *Opt. Lett.* 34 (2009) 262.
- [266] C. Kieleck, M. Eichhorn, D. Faye, E. Lallier, S.D. Jackson, *Proc. SPIE* 7582 (2010) 758212.
- [267] C. Kieleck, A. Hildenbrand, M. Eichhorn, D. Faye, E. Lallier, B. Gérard, S.D. Jackson, *Proc. SPIE* 7836 (2010) 783607.
- [268] A. Hildenbrand, C. Kieleck, E. Lallier, D. Faye, A. Grisard, B. Gérard, M. Eichhorn, *Proc. SPIE* 8187 (2011) 81870H.
- [269] A. Grisard, F. Gutty, E. Lallier, B. Gerard, *Proc. SPIE* 7836 (2010) 783606.
- [270] P.G. Schunemann, K.T. Zawilski, L.A. Pomeranz, L. Mohnkern, *AIOM* 2011, Paper AIFA1.
- [271] R.K. Feaver, R.D. Peterson, P.E. Powers, *Opt. Express* 21 (2013) 16104.
- [272] D.J. Kane, J.M. Hopkins, M.H. Dunn, P. Schunemann, D.J.M. Stothard, *Europhoton* 2014, paper TuA-T1-O-03.
- [273] G. Bloom, A. Grisard, E. Lallier, C. Larat, M. Carras, X. Marcadet, *Opt. Lett.* 35 (2010) 505.
- [274] D. French, R. Peterson, I. Jovanovic, *Opt. Lett.* 36 (2011) 496.
- [275] P.G. Schunemann, L.A. Pomeranz, D.J. Magarrell, *Proc. SPIE* 9347 (2015) 93470J.
- [276] A.A. Davydov, L.A. Kulevskii, A.M. Prokhorov, A.D. Savel’ev, V.V. Smirnov, *JETP Lett.* 15 (1972) 513 (transl. from *Zh. Eksp. Teor. Fiz. Pis. Red.* 15 (1972) 725).
- [277] A.A. Davydov, L.A. Kulevskii, A.M. Prokhorov, A.D. Savel’ev, V.V. Smirnov, A.V. Shirkov, *Opt. Commun.* 9 (1973) 234.
- [278] J.A. Weiss, L.S. Goldberg, *Appl. Phys. Lett.* 24 (1974) 389.
- [279] R.G. Wenzel, G.P. Arnold, *Appl. Opt.* 15 (1976) 1322.
- [280] G.P. Arnold, R.G. Wenzel, *Appl. Opt.* 16 (1977) 809.
- [281] S.Kh. Batygov, L.A. Kulevskii, A.M. Prokhorov, V.V. Osiko, A.D. Savel’ev, V.V. Smirnov, *Sov. J. Quantum Electron.* 4 (1975) 1469 (transl. from *Kvantovaya Electron. (Moscow)* 1 (1974) 2633).
- [282] P.A. Budni, K. Ezzo, P.G. Schunemann, S. Minnigh, J.C. McCarthy, T.M. Pollak, *ASSL* 1991, vol. 10 of OSA Proc. Series, pp. 335–338.
- [283] D.M. Rines, G.A. Rines, P.F. Moulton, *ASSL* 1995, vol. 24 of OSA Proc. Series, pp. 184–186.
- [284] T.H. Allik, S. Chandra, D.M. Rines, P.G. Schunemann, J.A. Hutchinson, R. Utano, *Opt. Lett.* 22 (1997) 597.
- [285] T.H. Allik, S. Chandra, D.M. Rines, P.G. Schunemann, J.A. Hutchinson, R. Utano, *ASSL* 1997, vol. 10 of OSA TOPS, pp. 265–266.
- [286] R.K. Shori, N.S. Prasad, G. Catella, *CLEO* 1999, Paper CMG2.
- [287] R.K. Shori, O.M. Stafsudd, N.S. Prasad, G. Catella, P.G. Schunemann, *ASSL* 2000, vol. 34 of OSA TOPS, pp. 286–289.
- [288] K.L. Vodopyanov, F. Ganikhanov, J.P. Maffetone, I. Zwieback, W. Ruderman, *Opt. Lett.* 25 (2000) 841.
- [289] M.W. Todd, R.A. Provencal, T.G. Owano, B.A. Paldus, A. Kachanov, K.L. Vodopyanov, M. Hunter, S.L. Coy, J.I. Steinfeld, J.T. Arnold, *Appl. Phys. B* 75 (2002) 367.

- [290] C.B. Rawle, I.T. Mckinnie, G.J. Wagner, S.E. Christensen, T.J. Carrig, D.C. Senft, J.L. Ahl, C. Swim, NLO 2002, vol. 79 of OSA TOPS, pp. 437–439.
- [291] W.S. Pelouch, G.J. Wagner, T.J. Carrig, W.J. Scharpf, ASSL 2001, vol. 50 of OSA TOPS, pp. 670–674.
- [292] A. Zakel, G.J. Wagner, W.J. Alford, T.J. Carrig, ASSP 2005, vol. 98 of OSA TOPS, pp. 433–437.
- [293] A. Zakel, G.J. Wagner, W.J. Alford, T.J. Carrig, CLEO 2005, Paper CThY5.
- [294] N. Saito, M. Yamoto, T. Tomida, U. Takagi, S. Wada, Proc. SPIE 8526 (2012) 852605.
- [295] M. Yumoto, N. Saito, U. Takagi, S. Wada, NLO 2013, Paper NW4A.19.
- [296] A. Zakel, S.D. Setzler, P.G. Schunemann, T.M. Pollak, M. Burky, S. Guha, CLEO 2002, Paper CTuH4.
- [297] K. Miyamoto, H. Ito, Opt. Lett. 32 (2007) 274.
- [298] K. Miyamoto, K.M. Abedin, H. Ito, Proc. SPIE 6582 (2007) 65820U.
- [299] T.H. Allik, S. Chandra, Proc. SPIE 3082 (1997) 54.
- [300] J. Raffy, T. Debuisschert, J.-P. Pocholle, M. Papuchon, Appl. Opt. 33 (1994) 985.
- [301] J. Kirton, Opt. Commun. 115 (1995) 93.
- [302] S. Chandra, T.H. Allik, G. Catella, R. Utano, J.A. Hutchinson, Appl. Phys. Lett. 71 (1997) 584.
- [303] T.H. Allik, J.L. Ahl, S. Chandra, J.A. Hutchinson, W.W. Hovis, J. Fox, L. Newman, ASSL 1999, vol. 26 of OSA TOPS, pp. 525–528.
- [304] Y. Ehrlich, S. Fastig, S. Pearl, G. Cinader, Proc. SPIE 4484 (2002) 311.
- [305] Y. Ehrlich, S. Pearl, S. Fastig, ASSP 2004, vol. 94 of OSA TOPS, pp. 398–402.
- [306] H. Komine, J.M. Fukumoto, W.H. Long Jr., E.A. Stappaerts, IEEE J. Sel. Top. Quantum Electron. 1 (1995) 44.
- [307] T. Chuang, R. Burnham, R.B. Jones, ASSL 1997, vol. 10 of OSA TOPS, pp. 262–264.
- [308] T. Shido, T. Mikami, K. Kato, Proc. SPIE 7354 (2009) 73541C.
- [309] Y. Isyanova, G.A. Rines, D. Welford, P.F. Moulton, ASSL 1996, vol. 1 of OSA TOPS, pp. 174–176.
- [310] Y. Isyanova, A. Dergachev, D. Welford, P.F. Moulton, ASSL 1999, vol. 26 of OSA TOPS, pp. 548–553.
- [311] J.M. Fukumoto, ASSL 2002, vol. 68 of OSA TOPS, pp. 558–562.
- [312] L.R. Marshall, J. Earl, A. Johnson, T. Pollak, P. Schunemann, ASSL 1996, vol. 1 of OSA TOPS, pp. 171–173.
- [313] T.H. Allik, S. Chandra, P.G. Schunemann, P.A. Ketteridge, I. Lee, T.M. Pollak, E.P. Chicklis, J.A. Hutchinson, ASSL 1998, vol. 19 of OSA TOPS, pp. 230–232.
- [314] S. Das, Infrared Phys. Technol. 69 (2015) 13.
- [315] K.L. Vodopyanov, P.G. Schunemann, Opt. Lett. 28 (2003) 441.
- [316] F. Ganikhanov, T. Caughey, K.L. Vodopyanov, J. Opt. Soc. Am. B 18 (2001) 818.
- [317] P.B. Phua, K.S. Lai, R.F. Wu, T.C. Chong, Appl. Opt. 38 (1999) 563.
- [318] Y. Peng, X. Wei, W. Wang, Chin. Opt. Lett. 9 (2011) 061402.
- [319] R. Lebrun, G. Menerat, P. Georges, ASSL 2002, vol. 68 of OSA TOPS, pp. 198–200.
- [320] S. Haidar, K. Miyamoto, H. Ito, Opt. Commun. 241 (2004) 173.
- [321] P.B. Phua, K.S. Lai, R.F. Wu, T.C. Chong, Opt. Lett. 23 (1998) 1262.
- [322] R.F. Wu, K.S. Lai, E. Lau, H.F. Wong, W.J. Xie, Y.L. Lim, K.W. Lim, L. Chia, ASSL 2002, vol. 68 of OSA TOPS, pp. 194–197.
- [323] R. Wu, K.S. Lai, W.-P. E. Lau, H.F. Wong, Y.L. Lim, K.W. Lim, L.C.L. Chia, CLEO 2002, paper CTuD6.
- [324] G. Arisholm, E. Lippert, G. Rustad, K. Stenersen, Opt. Lett. 25 (2000) 1654.
- [325] G. Arisholm, E. Lippert, G. Rustad, K. Stenersen, Opt. Lett. 27 (2002) 1336.
- [326] G. Rustad, E. Lippert, K. Stenersen, G. Arisholm, ASSL 2001, vol. 50 of OSA TOPS, pp. 660–665.
- [327] G. Rustad, S. Nicolas, E. Lippert, K. Stenersen, G. Arisholm, ASSP 2003, vol. 83 of OSA TOPS, pp. 333–338.
- [328] B.J. Perrett, M.R. Harris, Proc. SPIE 5620 (2004) 84.
- [329] J.A.C. Terry, K.J. McEwan, M.J.P. Payne, ASSL 1998, vol. 19 of OSA TOPS, pp. 236–239.
- [330] P.B. Phua, B.S. Tan, R.F. Wu, K.S. Lai, L. Chia, E. Lau, Opt. Lett. 31 (2006) 489.
- [331] M. Henriksson, M. Tiihonen, V. Pasiskevicius, F. Laurell, Opt. Lett. 31 (2006) 1878.
- [332] M. Henriksson, M. Tiihonen, V. Pasiskevicius, F. Laurell, Appl. Phys. B 88 (2007) 37.
- [333] M. Henriksson, L. Sjöqvist, G. Strömqvist, V. Pasiskevicius, F. Laurell, Proc. SPIE 7115 (2008) 71150O.
- [334] D.E. Smith, M.S. Bowers, P.G. Schunemann, Proc. SPIE 4972 (2003) 78.
- [335] E. Cheung, S. Palese, H. Injeyan, C. Hoefler, J. Ho, L. Hilyard, H. Komine, J. Berg, W. Bosenberg, ASSL 1999, vol. 26 of OSA TOPS, pp. 514–517.
- [336] D.G. Lancaster, Opt. Commun. 282 (2009) 272.
- [337] T. Traub, G. Anstett, G. Goeritz, J. L’huillier, Proc. SPIE 9136 (2014) 913616.
- [338] E. Lippert, Proc. SPIE 8187 (2011) 81870F.
- [339] G. Rustad, S. Nicolas, O. Nordseth, G. Arisholm, Proc. SPIE 5989 (2005) 598904.
- [340] Y. Ehrlich, S. Pearl, S. Fastig, ASSP 2004, vol. 94 of OSA TOPS, pp. 398–402.

- [341] G. Stoepler, N. Thilman, V. Pasiskevicius, A. Zukauskas, C. Canalias, M. Eichhorn, *Opt. Express* 20 (2012) 4509.
- [342] M.W. Haakestad, G. Arisholm, E. Lippert, S. Nicolas, G. Rustad, K. Stenersen, *Opt. Express* 16 (2008) 14263.
- [343] Q. Clément, J.-M. Melkonian, J. Barrientos-Barria, J.-B. Dherbecourt, M. Raybaut, A. Godard, *Opt. Lett.* 38 (2013) 4046.
- [344] K.L. Vodopyanov, O. Levi, P.S. Kuo, T.J. Pinguet, J.S. Harris, M.M. Fejer, B. Gerard, L. Becouarn, E. Lallier, *Opt. Lett.* 29 (2004) 1912.
- [345] K.L. Vodopyanov, O. Levi, P.S. Kuo, T.J. Pinguet, J.S. Harris, M.M. Fejer, B. Gerard, L. Becouarn, E. Lallier, *Proc. SPIE* 5620 (2004) 63.
- [346] K.L. Vodopyanov, I. Makasyuk, P.G. Schunemann, *Opt. Express* 22 (2014) 4131.
- [347] P.S. Kuo, K.L. Vodopyanov, M.M. Fejer, X. Yu, J.S. Harris, D.F. Bliss, D. Weyburne, *Opt. Lett.* 32 (2007) 2735.
- [348] A.G. Yodh, H.W.K. Tom, G.D. Aumiller, R.S. Miranda, *J. Opt. Soc. Am. B* 8 (1991) 1663.
- [349] A. Lohner, P. Kruck, W.W. Rühle, *Appl. Phys. B* 59 (1994) 211.
- [350] J.D. Kafka, M.L. Watts, J.W. Pieterse, R.L. Herbst, *Appl. Phys. B* 60 (1995) 449.
- [351] S. Ehret, H. Schneider, *Appl. Phys. B* 66 (1998) 27.
- [352] J.M. Fraser, D. Wang, A. Hache, G.R. Allan, H.M. van Driel, *Appl. Opt.* 36 (1997) 5044.
- [353] M.R.X. de Barros, P.C. Becker, *Opt. Lett.* 18 (1993) 631.
- [354] M.R.X. de Barros, R.S. Miranda, T.M. Jedju, P.C. Becker, *Opt. Lett.* 20 (1995) 480.
- [355] S.M. Foreman, D.J. Jones, J. Ye, *Opt. Lett.* 28 (2003) 370.
- [356] R.A. Kaindl, D.C. Smith, M. Joschko, M.P. Hasselbeck, M. Woerner, T. Elsaesser, *Opt. Lett.* 23 (1998) 861.
- [357] R.A. Kaindl, F. Eickemeyer, M. Woerner, T. Elsaesser, *Appl. Phys. Lett.* 75 (1999) 1060.
- [358] A. Schliesser, M. Brehm, F. Keilmann, D.W. van der Weide, *Opt. Express* 13 (2005) 9029.
- [359] G.I. Petrov, K.L. Vodopyanov, V.V. Yakovlev, *Opt. Lett.* 32 (2007) 515.
- [360] A.A. Mani, Z.D. Schultz, A.A. Gewirth, J.O. White, Y. Caudano, C. Humbert, L. Dreesen, P.A. Thiry, A. Peremans, *Opt. Lett.* 29 (2004) 274.
- [361] M. Beutler, I. Rimke, E. Büttner, V. Panyutin, V. Petrov, *Laser Phys. Lett.* 10 (2013) 075406.
- [362] M. Beutler, I. Rimke, E. Büttner, V. Petrov, L. Isaenko, *Opt. Mater. Express* 3 (2013) 1834.
- [363] R. Hegenbarth, A. Steinmann, S. Sarkisov, H. Giessen, *Opt. Lett.* 37 (2012) 3513.
- [364] J. Krauth, A. Steinmann, R. Hegenbarth, M. Conforti, H. Giessen, *Opt. Express* 21 (2013) 11516.
- [365] M. Beutler, I. Rimke, E. Büttner, V. Badikov, D. Badikov, V. Petrov, *Proc. SPIE* 8964 (2014) 89640D.
- [366] M. Beutler, I. Rimke, E. Büttner, P. Farinello, A. Agnesi, V. Badikov, D. Badikov, V. Petrov, *Opt. Express* 23 (2015) 2730.
- [367] M. Beutler, I. Rimke, E. Büttner, V. Petrov, L. Isaenko, *Opt. Lett.* 39 (2014) 4353.
- [368] J. Michel, M. Beutler, I. Rimke, E. Büttner, P. Farinello, A. Agnesi, V. Petrov, *Proc. SPIE* 9347 (2015) 93470Q.
- [369] R. Romero-Alvarez, R. Pettus, Z. Wu, D. Strickland, *Opt. Lett.* 33 (2008) 1065.
- [370] A.M. Al-Kadry, D. Strickland, *Opt. Lett.* 36 (2011) 1080.
- [371] M. Hajjalamdari, D. Strickland, *Opt. Lett.* 37 (2012) 3570.
- [372] D.G. Winters, P. Schlup, R.A. Bartels, *Opt. Lett.* 35 (2010) 2179.
- [373] A. Gambetta, R. Ramponi, M. Marangoni, *Opt. Lett.* 33 (2008) 2671.
- [374] A. Gambetta, N. Coluccelli, M. Cassinero, D. Gatti, P. Laporta, G. Galzerano, M. Marangoni, *Opt. Lett.* 38 (2013) 1155.
- [375] A. Ruehl, A. Gambetta, I. Hartl, M.E. Fermann, K.S.E. Eikema, M. Marangoni, *Opt. Lett.* 37 (2012) 2232.
- [376] Y. Yao, W.H. Knox, *Opt. Express* 20 (2012) 25275.
- [377] Y. Yao, W.H. Knox, *Opt. Express* 21 (2013) 26612.
- [378] Y. Yao, W.H. Knox, *Proc. SPIE* 8964 (2014) 89640Q.
- [379] F. Keilmann, S. Amarie, *J. Infrared Milli. Terahz. Waves* 33 (2012) 479.
- [380] S. Liu, T.S. Mahony, D.A. Bender, M.B. Sinclair, I. Brener, *Appl. Phys. Lett.* 103 (2013) 181111.
- [381] D. Sanchez, M. Hemmer, M. Baudisch, K. Zawilski, P. Schunemann, H. Hoogland, R. Holzwarth, J. Biegert, *Opt. Lett.* 39 (2014) 6883.
- [382] D. Churin, K. Kieu, R.A. Norwood, N. Peyghambarian, *IEEE Phot. Technol. Lett.* 26 (2014) 2271.
- [383] C.R. Phillips, J. Jiang, C. Mohr, A.C. Lin, C. Langrock, M. Snure, D. Bliss, M. Zhu, I. Hartl, J.S. Harris, M.E. Fermann, M.M. Fejer, *Opt. Lett.* 37 (2012) 2928.
- [384] I. Pupez, D. Sánchez, O. Pronin, J. Zhang, N. Lilienfein, M. Seidel, I. Znakovskaya, V. Pervak, Z. Wei, F. Krausz, A. Apolonski, J. Biegert, *CLEO 2014*, Post-deadline paper STh5C.7.
- [385] A. Schliesser, N. Picqué, T.W. Hänsch, *Nat. Photonics* 6 (2012) 440.
- [386] A.J. Campillo, R.C. Hyer, S.L. Shapiro, *Opt. Lett.* 4 (1979) 325.

- [387] B. Bareika, G. Dikchys, E.D. Isyanova, A. Piskarskas, V. Sirutkaitis, *Sov. Tech. Phys. Lett.* 6 (1980) 301 (*Pis'ma Zh. Tekh. Fiz.* 6 (1980) 694).
- [388] T. Elsaesser, H. Lobentanz, A. Seilmeier, *Opt. Commun.* 52 (1985) 355.
- [389] K.G. Spears, X. Zhu, X. Yang, L. Wang, *Opt. Commun.* 66 (1988) 167.
- [390] R. Laenen, K. Simeonidis, C. Rauscher, *IEEE J. Sel. Top. Quantum Electron.* 2 (1996) 487.
- [391] R. Laenen, K. Simeonidis, A. Laubereau, *J. Opt. Soc. Am. B* 15 (1998) 1213.
- [392] P. Guyot-Sionnest, *J. Electron Spectr. Relat. Phenom.* 64/65 (1993) 1.
- [393] H.J. Bakker, J.T.M. Kennis, H.J. Kop, A. Lagendijk, *Opt. Commun.* 86 (1991) 58.
- [394] H.-J. Krause, W. Daum, *Appl. Phys. B* 56 (1993) 8.
- [395] T. Dahinten, U. Plödereder, A. Seilmeier, K.L. Vodopyanov, K.R. Allakhverdiev, Z.A. Ibragimov, *IEEE J. Quantum Electron.* 29 (1993) 2245.
- [396] I.M. Bayanov, R. Danielius, P. Heinz, A. Seilmeier, *Opt. Commun.* 113 (1994) 99.
- [397] C.-W. Chen, Y.-K. Hsu, J.Y. Huang, C.-S. Chang, J.-Y. Zhang, C.-L. Pan, *Opt. Express* 14 (2006) 10636.
- [398] K. Finsterbusch, A. Bayer, H. Zacharias, *Appl. Phys. B* 79 (2004) 457.
- [399] A. Dhirani, P. Guyot-Sionnest, *Opt. Lett.* 20 (1995) 1104.
- [400] K. Miyata, G. Marchev, A. Tyazhev, V. Panyutin, V. Petrov, *Opt. Lett.* 36 (2011) 1785.
- [401] R.L. York, G.J. Holinga, D.R. Guyer, K.R. McCrea, R.S. Ward, G.A. Somorjai, *Appl. Spectr.* 62 (2008) 937.
- [402] F. Yang, J. Yao, H. Xu, K. Feng, W. Yin, F. Li, J. Yang, S. Du, Q. Peng, J. Zhang, D. Cui, Y. Wu, C. Chen, Z. Xu, *Opt. Lett.* 38 (2013) 3903.
- [403] F. Yang, J.-Y. Yao, H.-Y. Xu, F.-F. Zhang, N.-X. Zhai, Z.-H. Lin, N. Zong, Q.-J. Peng, J.-Y. Zhang, D.-F. Cui, Y.-C. Wu, C.-T. Chen, Z.-Y. Xu, *IEEE Phot. Technol. Lett.* 27 (2015) 1100.
- [404] D. Zheng, L.A. Gordon, Y.S. Wu, R.S. Feigelson, M.M. Fejer, R.L. Byer, K.L. Vodopyanov, *Opt. Lett.* 23 (1998) 1010.
- [405] K.L. Vodopyanov, P.G. Schunemann, *Opt. Lett.* 23 (1998) 1096.
- [406] D.K. Hore, J.L. King, F.G. Moore, D.S. Alavi, M.Y. Hamamoto, G.L. Richmond, *Appl. Spectr.* 58 (2004) 1377.
- [407] P.C. Becker, D. Gershoni, A. Prosser, *Ultrafast Phenom.* VII (1990) 81.
- [408] P. Hamm, C. Lauterwasser, W. Zinth, *Opt. Lett.* 18 (1993) 1943.
- [409] P. Hamm, S. Wiemann, M. Zurek, W. Zinth, *Opt. Lett.* 19 (1994) 1642.
- [410] F. Seifert, V. Petrov, M. Woerner, *Opt. Lett.* 19 (1994) 2009.
- [411] P. Hamm, R.A. Kaindl, J. Stenger, *Opt. Lett.* 25 (2000) 1798.
- [412] H. Maekawa, K. Tominaga, D. Podenas, *Jpn. J. Appl. Phys.* 41 (2002) L329.
- [413] T. Imahoko, K. Takasago, T. Sumiyoshi, H. Sekita, K. Takahashi, M. Obara, *Appl. Phys. B* 87 (2007) 629.
- [414] N. Demirdöven, M. Khalil, O. Golonzka, A. Tokmakoff, *Opt. Lett.* 27 (2002) 433.
- [415] T. Witte, D. Zeidler, D. Proch, K.L. Kompa, M. Motzkus, *Opt. Lett.* 27 (2002) 131.
- [416] T. Witte, K.L. Kompa, M. Motzkus, *Appl. Phys. B* 76 (2003) 467.
- [417] S.-H. Shim, D.B. Strasfeld, M.T. Zanni, *Opt. Express* 14 (2006) 13120.
- [418] F.O. Koller, K. Haiser, M. Huber, T.E. Schrader, N. Regner, W.J. Schreier, W. Zinth, *Opt. Lett.* 32 (2007) 3339.
- [419] R.A. Kaindl, M. Wurm, K. Reimann, P. Hamm, A.M. Weiner, M. Woerner, *J. Opt. Soc. Am. B* 17 (2000) 2086.
- [420] F. Rotermund, V. Petrov, F. Noack, *Opt. Commun.* 185 (2000) 177.
- [421] V. Petrov, F. Noack, V. Badikov, G. Shevyrdyaeva, V. Panyutin, V. Chizhikov, *Appl. Opt.* 43 (2004) 4590.
- [422] A.B. Sugiharto, C.M. Johnson, H.B. De Aguiar, L. Alloati, S. Roke, *Appl. Phys. B* 91 (2008) 315.
- [423] M.K. Reed, M.K. Steiner Shepard, *IEEE J. Quantum Electron.* 32 (1996) 1273.
- [424] B. Golubovic, M.K. Reed, *Opt. Lett.* 23 (1998) 1760.
- [425] J.M. Fraser, I.W. Cheung, F. Legare, D.M. Villeneuve, J.P. Likforman, M. Joffre, P.B. Corkum, *Appl. Phys. B* 74 (Suppl. 1) (2002) S153.
- [426] J. Song, J.F. Xia, Z. Zhang, D. Strickland, *Opt. Lett.* 27 (2002) 200.
- [427] J.F. Xia, J. Song, D. Strickland, *Opt. Commun.* 206 (2002) 149.
- [428] A. Sugita, K. Yokoyama, H. Yamada, N. Inoue, M. Aoyama, K. Yamakawa, *Jpn. J. Appl. Phys.* 46 (2007) 226.
- [429] F. Rotermund, V. Petrov, F. Noack, L. Isaenko, A. Yelissev, S. Lobanov, *Appl. Phys. Lett.* 78 (2001) 2623.
- [430] L. Isaenko, A. Yelissev, S. Lobanov, V. Petrov, F. Rotermund, J.-J. Zondy, G.H.M. Knippels, *Mat. Sci. Semicond. Process* 4 (2001) 665.
- [431] V. Petrov, V. Badikov, G. Shevyrdyaeva, V. Panyutin, V. Chizhikov, *Opt. Mater.* 26 (2004) 217.
- [432] V. Petrov, V. Badikov, V. Panyutin, G. Shevyrdyaeva, S. Sheina, F. Rotermund, *Opt. Commun.* 235 (2004) 219.
- [433] F. Rotermund, V. Petrov, *Appl. Phys. B* 70 (2000) 731.
- [434] F. Rotermund, V. Petrov, *Opt. Lett.* 25 (2000) 746.
- [435] F. Rotermund, V. Petrov, *Jpn. J. Appl. Phys.* 40 (2001) 3195.

- [436] V. Petrov, F. Rotermund, *Opt. Lett.* 27 (2002) 1705.
- [437] V.M. Gordienko, S.S. Grechin, A.A. Ivanov, A.A. Podshivalov, E.V. Rakov, *Quantum Electron.* 36 (2006) 114.
- [438] V. Kozich, A. Moguilevski, K. Heyne, *Opt. Commun.* 285 (2012) 4515.
- [439] E. Pelletier, A. Sell, A. Leitenstorfer, R.J. Dwayne Miller, *Opt. Express* 20 (2012) 27456.
- [440] G. Andriukaitis, S. Ališauskas, A. Pugžlys, A. Baltuška, L. Tan, H.J. Lim, P.P. Boon, K. Balskus, A. Michailovas, *ASSL 2013*, Paper AM1A.6.
- [441] P. Malevich, T. Kanai, G. Gitzinger, R. Maksimenka, N. Forget, A. Baltuska, A. Pugzlys, *CLEO 2015*, Paper SM1P.3.
- [442] D. Sanchez, M. Hemmer, M. Baudisch, S.L. Cousin, K. Zawilski, P. Schunemann, V. Smirnov, H. Hoogland, R. Holzwarth, O. Chalus, C. Simon-Boisson, J. Biegert, *CLEO 2015*, Paper SW4O.5.
- [443] J.-P. Likforman, M. Mehendale, D.M. Villeneuve, M. Joffre, P.B. Corkum, *Opt. Lett.* 26 (2001) 99.
- [444] A. Sell, A. Leitenstorfer, R. Huber, *Opt. Lett.* 33 (2008) 2767.
- [445] C. Manzoni, M. Först, H. Ehrke, A. Cavalleri, *Opt. Lett.* 23 (2010) 757.
- [446] A.A. Lanin, A.B. Fedotov, A.M. Zheltikov, *J. Opt. Soc. Am. B* 31 (2014) 1901.
- [447] C. Erny, C.P. Hauri, *Appl. Phys. B* 117 (2014) 379.
- [448] V. Petrov, F. Rotermund, F. Noack, *J. Opt. A: Pure Appl. Opt.* 3 (2001) R1.
- [449] F. Eickemeyer, R.A. Kaindl, M. Woerner, T. Elsaesser, A.M. Weiner, *Opt. Lett.* 25 (2000) 1472.
- [450] E.C. Cheung, K. Koch, G.T. Moore, *Opt. Lett.* 19 (1994) 631.
- [451] K.J. McEwan, *Opt. Lett.* 23 (1998) 667.
- [452] A.A. Mani, L. Dreesen, Ph. Hollander, C. Humbert, Y. Caudano, P.A. Thiry, A. Peremans, *Appl. Phys. Lett.* 79 (2001) 1945.
- [453] A. Peremans, D. Lis, F. Cecchet, P.G. Schunemann, K.T. Zawilski, V. Petrov, *Opt. Lett.* 34 (2009) 3053.
- [454] N. Hendaoui, A. Peremans, P.G. Schunemann, K.T. Zawilski, V. Petrov, *Laser Phys.* 23 (2013) 085401.
- [455] S. Chaitanya Kumar, A. Agnesi, P. Dallochio, F. Pirzio, G. Reali, K.T. Zawilski, P.G. Schunemann, M. Ebrahim-Zadeh, *Opt. Lett.* 36 (2011) 3236.
- [456] D. Guyer, C. Hamilton, F. Braun, D. Lowenthal, J. Ewing, *CLEO 1991*, Post-deadline paper CPDP6.
- [457] Ch. Grässer, S. Marzenell, J. Döring, R. Beigang, R. Wallenstein, *ASSL 1996*, vol. 1 of OSA TOPS, pp. 158–163.
- [458] S. Marzenell, R. Beigang, R. Wallenstein, *Appl. Phys. B* 69 (1999) 423.
- [459] R. Hegenbarth, A. Steinmann, S. Mastel, S. Amarie, A.J. Huber, R. Hillenbrand, S.Y. Sarkisov, H. Giessen, *J. Opt.* 16 (2014) 094003.
- [460] M.A. Watson, M.V. O'Connor, D.P. Shepherd, D.C. Hanna, *Opt. Lett.* 28 (2003) 1957.
- [461] J.-B. Dherbecourt, A. Godard, M. Raybaut, J.-M. Melkonian, M. Lefebvre, *Opt. Lett.* 35 (2010) 2197.
- [462] Z. Zhang, D.T. Reid, S. Chaitanya Kumar, M. Ebrahim-Zadeh, P.G. Schunemann, K.T. Zawilski, C.R. Howle, *Opt. Lett.* 38 (2013) 5110.
- [463] V. Ramaiah-Badarla, A. Esteban-Martin, S. Chaitanya Kumar, K. Devi, K.T. Zawilski, P.G. Schunemann, M. Ebrahim-Zadeh, *CLEO 2015*, Paper SW4O.3.
- [464] S. Chaitanya Kumar, J. Krauth, A. Steinmann, K.T. Zawilski, P.G. Schunemann, H. Giessen, M. Ebrahim-Zadeh, *Opt. Lett.* 40 (2015) 1398.
- [465] K.L. Vodopyanov, E. Sorokina, I.T. Sorokina, P.G. Schunemann, *Opt. Lett.* 36 (2011) 2275.
- [466] V.O. Smolski, S. Vasilyev, P.G. Schunemann, S.B. Mirov, K.L. Vodopyanov, *CLEO 2015*, Paper SW4O.2.
- [467] N. Leindecker, A. Marandi, R.L. Byer, K.L. Vodopyanov, J. Jiang, I. Hartl, M. Fermann, P.G. Schunemann, *Opt. Express* 20 (2012) 7046.
- [468] K.F. Lee, J. Jiang, C. Mohr, J. Bethge, M.E. Fermann, N. Leindecker, K.L. Vodopyanov, P.G. Schunemann, I. Hartl, *Opt. Lett.* 38 (2013) 1191.
- [469] V.O. Smolski, K.L. Vodopyanov, *Proc. SPIE* 9347 (2015) 934702.
- [470] K.F. Lee, P. Maslowski, A. Mills, C. Mohr, J. Jiang, P.G. Schunemann, M.E. Fermann, *Proc. SPIE* 9355 (2015) 93550K.
- [471] D.L. Maser, L. Nugent-Glandorf, G. Ycas, F. Adler, K. Knabe, S.A. Diddams, *CLEO 2014*, Paper JT4A.110.
- [472] S.T. Wong, T. Plettner, K.L. Vodopyanov, K. Urbanek, M. Dignonet, R.L. Byer, *Opt. Lett.* 33 (2008) 1896.
- [473] A. Hordvik, H.R. Schlossberg, C.M. Stickley, *Appl. Phys. Lett.* 18 (1971) 448.
- [474] T. Elsaesser, A. Seilmeier, W. Kaiser, *Opt. Commun.* 44 (1983) 293.
- [475] T. Elsaesser, A. Seilmeier, W. Kaiser, P. Koidl, G. Brandt, *Appl. Phys. Lett.* 44 (1984) 383.
- [476] V.V. Badikov, P.S. Blinov, A.A. Kosterev, V.S. Letokhov, A.L. Malinovsky, E.A. Ryabov, *Quantum Electron.* 27 (1997) 523 (transl. from *Kvantovaya Elektron. (Moscow)* 24 (1997) 537).
- [477] K.L. Vodopyanov, V.G. Voevodin, A.I. Gribenyukov, L.A. Kulevskii, *Bull. Acad. Sci. USSR Phys. Ser.* 49 (1985) 146 (transl. from *Izv. Akad. Nauk SSSR, Ser. Fiz.* 49 (1985) 569).

- [478] K.L. Vodop'yanov, V.G. Voevodin, A.I. Gribenyukov, L.A. Kulevskii, *Sov. J. Quantum Electron.* 17 (1987) 1159 (transl. from *Kvantovaya Elektron.* (Moscow) 14 (1987) 1815).
- [479] K.L. Vodop'yanov, L.A. Kulevskii, V.G. Voevodin, A.I. Gribenyukov, K.R. Allakhverdiev, T.A. Kerimov, *Opt. Commun.* 83 (1991) 322.
- [480] K.L. Vodop'yanov, *J. Opt. Soc. Am. B* 10 (1993) 1723.
- [481] K.L. Vodop'yanov, Yu.A. Andreev, G.C. Bhar, *Quantum Electron.* 23 (1993) 763 (transl. from *Kvantovaya Elektron.* (Moscow) 20 (1993) 879).
- [482] K.L. Vodop'yanov, V.G. Voevodin, *Opt. Commun.* 114 (1995) 333.
- [483] K.L. Vodop'yanov, V.G. Voevodin, *Opt. Commun.* 117 (1995) 277.
- [484] K.L. Vodop'yanov, V. Chazapis, *Opt. Commun.* 135 (1997) 98.
- [485] K.L. Vodop'yanov, *J. Opt. Soc. Am. B* 16 (1999) 1579.
- [486] K.L. Vodop'yanov, *Opt. Commun.* 150 (1998) 210.
- [487] V. Petrov, F. Rotermund, F. Noack, P. Schunemann, *Opt. Lett.* 24 (1999) 414.
- [488] F. Rotermund, V. Petrov, F. Noack, P. Schunemann, *Fiber Integr. Opt.* 20 (2001) 139.
- [489] S. Wandel, G. Xu, I. Jovanovic, *J. Phys. B: At. Mol. Opt. Phys.* 47 (2014) 234016.
- [490] V. Petrov, Y. Tanaka, T. Suzuki, *IEEE J. Quantum Electron.* 33 (1997) 1749.
- [491] P.S. Kuo, K.L. Vodop'yanov, M.M. Fejer, D.M. Simanovskii, X. Yu, J.S. Harris, D. Bliss, D. Weyburne, *Opt. Lett.* 31 (2006) 71.
- [492] K.L. Vodop'yanov, G.M.H. Knippels, A.F.G. van der Meer, J.P. Maffetone, I. Zwieback, *Opt. Commun.* 202 (2002) 205.
- [493] O. Chalus, P.G. Schunemann, K.T. Zawilski, J. Biegert, M. Ebrahim-Zadeh, *Proc. SPIE* 7917 (2011) 79170L.
- [494] O. Chalus, P.G. Schunemann, K.T. Zawilski, J. Biegert, M. Ebrahim-Zadeh, *Opt. Lett.* 35 (2010) 4142.
- [495] S. Chaitanya Kumar, M. Jelínek, M. Baudisch, K.T. Zawilski, P.G. Schunemann, V. Kubeček, J. Biegert, M. Ebrahim-Zadeh, *Proc. SPIE* 8434 (2012) 84340F.
- [496] S. Chaitanya Kumar, M. Jelínek, M. Baudisch, K.T. Zawilski, P.G. Schunemann, V. Kubeček, J. Biegert, M. Ebrahim-Zadeh, *Opt. Express* 20 (2012) 15703.
- [497] G. Marchev, A. Tyazhev, V. Petrov, P.G. Schunemann, K.T. Zawilski, G. Stöppler, M. Eichhorn, *Opt. Lett.* 37 (2012) 740.
- [498] G. Marchev, F. Pirzio, R. Piccoli, A. Agnesi, G. Reali, P.G. Schunemann, K.T. Zawilski, A. Tyazhev, V. Petrov, *Opt. Lett.* 37 (2012) 3219.
- [499] A. Tyazhev, F. Pirzio, A. Agnesi, G. Reali, V. Petrov, G. Marchev, P.G. Schunemann, K.T. Zawilski, *Appl. Phys. B* 112 (2013) 453.
- [500] G. Marchev, F. Pirzio, R. Piccoli, A. Agnesi, G. Reali, P.G. Schunemann, K.T. Zawilski, A. Tyazhev, V. Petrov, *Opt. Lett.* 38 (2013) 3344.
- [501] R. Piccoli, F. Pirzio, A. Agnesi, V. Badikov, D. Badikov, G. Marchev, V. Panyutin, V. Petrov, *Opt. Lett.* 39 (2014) 4895.
- [502] W.L. Faust, C.H. Henry, *Phys. Rev. Lett.* 17 (1966) 1265.
- [503] K.L. Vodop'yanov, *Laser. Photon. Rev.* 2 (2008) 11.
- [504] F. Zernike, *Bull. Am. Phys. Soc.* 12 (1967) 687.
- [505] T. Yajima, K. Inoue, *Phys. Lett. A* 26 (1968) 281.
- [506] T.J. Bridges, A.R. Strnad, *Appl. Phys. Lett.* 20 (1972) 382.
- [507] T. Yajima, K. Inoue, *IEEE J. Quantum Electron.* 5 (1969) 140.
- [508] M. Bahoura, G.S. Herman, N.P. Barnes, C.E. Bonner, P.T. Higgins, *Proc. SPIE* 3928 (2000) 132.
- [509] N. Van Tran, C.K.N. Patel, *Phys. Rev. Lett.* 22 (1969) 463.
- [510] F. Zernike, *Phys. Rev. Lett.* 22 (1969) 931.
- [511] G.D. Boyd, T.J. Bridges, C.K.N. Patel, E. Buechler, *Appl. Phys. Lett.* 21 (1972) 553.
- [512] A. Bonvalet, M. Joffre, J.L. Martin, A. Migus, *Appl. Phys. Lett.* 67 (1995) 2907.
- [513] F. Keilmann, C. Gohle, R. Holzwarth, *Opt. Lett.* 29 (2004) 1542.
- [514] N. Belabas, J.-P. Likforman, L. Canioni, B. Bousquet, M. Joffre, *Opt. Lett.* 26 (2001) 743.
- [515] R. Huber, A. Brodschelm, F. Tauser, A. Leitenstorfer, *Appl. Phys. Lett.* 76 (2000) 3191.
- [516] M. Jazbinsek, L. Mutter, P. Günter, *IEEE J. Sel. Top. Quantum Electron.* 14 (2008) 1298.
- [517] H. Adachi, T. Taniuchi, M. Yoshimura, S. Brahadeeswaran, T. Higo, M. Takagi, Y. Mori, T. Sasaki, H. Nakanishi, *Jpn. J. Appl. Phys.* 43 (2004) L1121.
- [518] T. Satoh, Y. Toya, S. Yamamoto, T. Shimura, K. Kuroda, Y. Takahashi, M. Yoshimura, Y. Mori, T. Sasaki, S. Ashihara, *J. Opt. Soc. Am. B* 27 (2010) 2507.
- [519] S. Wang, M. Zhan, G. Wang, H. Xuan, W. Zhang, C. Liu, C. Xu, Y. Liu, Z. Wei, X. Chen, *Laser Photon. Rev.* 7 (2013) 831.

- [520] H.-T. Fan, C.-H. Xu, Z.-H. Wang, G. Wang, C.-J. Liu, J.-K. Liang, X.-L. Chen, Z.-Y. Wei, *Opt. Lett.* 39 (2014) 6249.
- [521] R. Haidar, A. Mustelier, Ph. Kupecek, E. Rosencher, R. Triboulet, Ph. Lemasson, G. Mennerat, *J. Appl. Phys.* 91 (2002) 2550 (Erratum 91 (2002) 6212).
- [522] A. Mustelier, E. Rosencher, Ph. Kupecek, A. Godard, M. Baudrier, M. Lefebvre, M. Poulat, G. Mennerat, C. Pasquer, Ph. Lemasson, *Appl. Phys. Lett.* 84 (2004) 4424.
- [523] C.F. Dewey Jr., L.O. Hocker, *Appl. Phys. Lett.* 26 (1975) 442.
- [524] M. Baudrier-Raybaut, R. Haidar, Ph. Kupecek, Ph. Lemasson, E. Rosencher, *Nature* 432 (2004) 374.
- [525] R. Haidar, N. Forget, Ph. Kupecek, E. Rosencher, *J. Opt. Soc. Am. B* 21 (2004) 1522.
- [526] A. Fiore, V. Berger, E. Rosencher, P. Bravetti, J. Nagle, *Nature* 391 (1998) 463.
- [527] T.H. Stievater, R. Mahon, D. Park, W.S. Rabinovich, M.W. Pruessner, J.B. Khurgin, C.J.K. Richardson, *Opt. Lett.* 39 (2014) 945.
- [528] M.B. Oron, P. Blau, S. Pearl, M. Katz, *Proc. SPIE* 8240 (2012) 82400C.